

Ductile Fracture by Void Growth to Coalescence

A. Amine Benzerga¹ and Jean-Baptiste Leblond²

¹ Department of Aerospace Engineering, Texas A&M University
College Station, TX 77843-3141, USA

² Université Pierre et Marie Curie, UMR CNRS 7190
4, place Jussieu, 75252 Paris cedex 05

August 21, 2010

Contents

1	Introduction	3
2	Experimental Facts	5
2.1	Macroscopic Aspects	5
2.2	Microscopic Mechanisms	10
2.3	Microscopic Measurements	16
3	Computational Cell Models	19
3.1	Void Nucleation	21
3.2	Void Growth and Coalescence	23
3.2.1	Elasto-Plastic Matrix	24
3.2.2	Elasto-Viscoplastic Matrix	33
4	Void Nucleation and Damage Initiation	35
5	Fundamentals for Porous Ductile Solids	42
5.1	Homogenization	42
5.1.1	Kinematic Approach	43
5.1.2	Static Approach	44
5.2	Limit Analysis	45
5.3	Viscoplastic Formulation	47
5.3.1	The Microscopic and Macroscopic Stress Potentials	47
5.3.2	The Gauge Surface, the Gauge Function and the Gauge Factor	47
5.4	Microstructure Evolution	49

6	Void Growth Models	51
6.1	Gurson Model	52
6.1.1	Synopsis of Derivation	52
6.1.2	Heuristic Extensions	54
6.2	GLD Model	58
6.3	Benzerga & Besson Model	65
6.4	Combined Plastic Anisotropy and Void Shape Effects	68
6.5	Viscoplastic Model	72
7	Void Coalescence Models	75
7.1	Coalescence in Layers	76
7.1.1	Thomason's Model	76
7.1.2	Benzerga's Model	80
7.1.3	Coalescence in Combined Tension and Shear	85
7.2	Coalescence in Columns	87
7.3	Closing Remarks on Void Coalescence	90
8	Top-Down Approach to Ductile Fracture	92
8.1	Synopsis of Integrated Model	92
8.2	Material Parameter Identification	95
8.2.1	Standard Procedure	96
8.2.2	Accounting for 3D Aspects	97
8.2.3	Accounting for Void Nucleation	98
9	Crack Initiation and Growth	98
9.1	Round Smooth Bars	98
9.2	Plane Strain Bars	101
9.3	Notched Bars	104
9.4	Cracked Specimens	106
10	Discussion	111
A	GLD Criterion Parameters	115
B	Finite Element Formulation	116

1 Introduction

An important failure mechanism in ductile metals and their alloys is by growth and coalescence of microscopic voids. In structural materials, the voids nucleate at inclusions and second-phase particles, by decohesion of the particle–matrix interface or by particle cracking. Subsequently, void growth is driven by plastic deformation of the surrounding matrix. Early micromechanical treatments of this phenomenon considered the growth of isolated voids (McClintock, 1968; Rice and Tracey, 1969). Later, constitutive equations for porous ductile solids were developed based on homogenization theory. Among these, the most widely known model is that developed by Gurson (1977) for spherical and cylindrical voids. His model was given in terms of a macroscopic yield criterion and an evolution law for a single microstructural variable, the void volume fraction. Since this model only accounted for void growth, heuristic additions were made to account for void nucleation and coalescence, notably based on micromechanical cell model studies. The previous review of ductile fracture due to Tvergaard (1990) has documented the salient features of the Gurson model and discussed various applications to predictions of material failure accounting for finite strain effects.

The dilatant plasticity models that were available at the time of the previous review on this topic made the simplifying assumptions that (i) voids were cylindrical or spherical; and (ii) the matrix was plastically isotropic. This included the Gurson model and a model due to Rousselier (1981, 1987). These assumptions may be reasonable, depending on the shape of inclusions from which voids nucleate, the polycrystalline texture of the matrix and on the stress state triaxiality. Over the past two decades, generalizations of the Gurson model have been developed, notably to account for the anisotropies associated with deformation of the matrix and shapes of the voids. This progress permits analyses of the effects of microstructural variables, other than the porosity, to be undertaken. Among the practically important microstructure–property relationships addressed by such analyses is the anisotropy in ductility and toughness and a rationale for why the ductility varies among materials having comparable purity, such as steels and aluminum alloys.

The micromechanical models for porous plastic solids, including those accounting for anisotropy, were developed on the basis that void growth is driven by some diffuse plastic flow in the matrix. As a consequence, predictions based on these models overestimate measured ductilities. Heuristic corrections aiming at improving quantitative predictions create difficulties of their own. Experimental observations suggest strong evidence for a termination to stable void growth by various mechanisms of flow localization in the intervoid matrix. Subsequent to that, the growth of voids is much more rapid. Among all possible mechanisms of this micro-scale flow localization, internal necking of the intervoid ligament is most common. It has been known in the materials science community for a long time; according to Argon et al. (1975), it had been invoked as early as 1855. Finite element cell model analyses, as pioneered by Needleman (1972b) and settled in (Koplik and Needleman, 1988), have essentially provided the micromechanical evidence of internal necking and the foundation for the development of new mathematical models. The key element of this new class of models is that they account for possible discontinuities in the velocity gradient within the elementary volume to be homogenized. Indeed, the onset of internal necking at the microscale involves the formation of regions of elastic unloading separated from regions of highly localized plastic flow (the ligaments). It is this process

that leads to the acceleration of void growth leading up to final failure by coalescence.

Fig. 1 depicts a ductile crack at the ultimate stage of rupture of a round notched bar of low alloy steel. The zig-zag crack goes “slant” as it approaches the free surfaces forming the shear lips that characterize cup-cone fracture. The background material is etched revealing a ferrite-pearlitic matrix with intact cementite particles and extensive damage in the form of voids, typically larger than $1\ \mu\text{m}$ in size. Reconstructing the history of that crack from an initial state with no crack and a fully dense material is an interesting exercise. A similar question could be asked about a body containing an initial crack. In all cases, the fundamental problem statement in ductile fracture boils down to the following: for a given constitutive description at the microscale, i.e., a scale at which each void is resolved, the question addressed is that of what relationship exists between stress and strain at the macroscale, i.e., one which contains many voids. Of particular importance is how microstructural information (usually void population attributes and matrix properties) enters the macroscopic constitutive laws and how it evolves in the context of porous ductile solids.

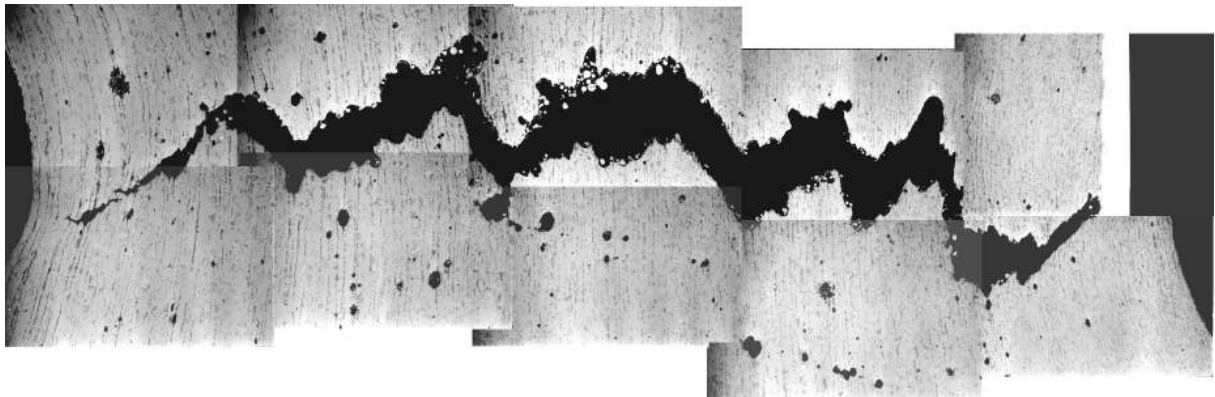


Figure 1: Ductile crack propagation by void growth and coalescence in an initially dense steel (Benzerga, 1999).

The cardinal facts about ductile fracture are summarized in the next section with experiments as sole basis. Lessons drawn from cell model studies, which are a major tool in understanding material behavior at intermediate scales, are gathered in Section 3. The micromechanical models of the various stages of ductile fracture are then presented in Sections 4–7, with Section 5 devoted to the fundamentals that are a pre-requisite for the beginner in this field to master the void growth and coalescence models. The integrated model is summarized for quick reference in Section 8 as an essential part of a top-down approach to ductile fracture¹. The section also contains details about material parameter identification. The following section is entirely devoted to applications: simulation of cup-cone and slant fracture; analyses of macroscopic plastic flow localization; quantitative prediction of fracture in notched bars; and crack growth simulations. The last section is devoted to a discussion of the state of the art, potential impact of progress made, and future directions.

¹Also known as “local approach”. We do not use this terminology in the context of this review to avoid confusion with “nonlocal approaches”.

2 Experimental Facts

2.1 Macroscopic Aspects

A variety of laboratory specimens are used to measure characteristic properties and determine essential features of the fracture process in ductile metals under quasi-static loadings. Broadly put, three categories of specimens are used: smooth, notched and cracked, Fig. 2. Defining the stress triaxiality T as the ratio of hydrostatic stress to the von Mises equivalent stress, T is effectively varied over a wide range covering most practical situations. The measured fracture property and observed macroscopic failure mode also vary from one type of specimen to the other.




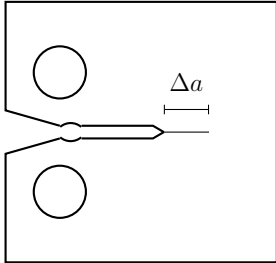
	Smooth		Notched	Cracked
	round	thick/thin		
				
Triaxiality	0.3–0.5	0.5–0.8	0.5–1.5	2.0–4.0
Measured	$\bar{\epsilon}_f$	$\bar{\epsilon}_f$	$\bar{\epsilon}_c, \bar{\epsilon}_f$	$J_{Ic}, dJ/da$

Figure 2: Specimens most commonly used in ductile fracture experiments, corresponding stress triaxiality levels and measured fracture properties.

In round smooth bars, the value of T is initially $1/3$ and increases subsequent to the onset of necking. Measured properties include the necking strain, which is determined by plastic instability, and a fracture strain $\bar{\epsilon}_f$ evaluated *post mortem* as the reduction of the cross-sectional area. The failure mode that is most commonly observed is the “cup–cone”. Exceptions include some aluminum alloys, which exhibit slant fracture when loaded in certain orientations (Achon, 1994). By way of contrast, the fracture surface of an initially smooth plane strain specimen almost invariably exhibits a slant character and a lower value of the fracture strain. In thin metal sheets, both slant and flat fracture modes are observed with the flat fracture surface presenting a bathtub-like aspect, Fig. 2.

Notched bars constitute a major experimental tool in fracture investigations. They were introduced by Hancock and MacKenzie (1976), and the Beremin group (Beremin, 1981b). They present some advantages over smooth bars in that the fracture process is decoupled from plastic instabilities such as necking and shear banding, the stress triaxiality range can be made wider by varying the notch radius and crack propagation can be controlled. As a consequence, two fracture strains can be measured: $\bar{\epsilon}_c$ at crack initiation and $\bar{\epsilon}_f$ at final failure. Furthermore, after a transient stage, the triaxiality T remains

on specimen geometry and plastic constraint, extra care should be taken for the latter as CTOA measurements are practically limited to the surface. A notable phenomenon in thick cracked specimens is that the ductile crack advances in the mid-section faster than near the free surfaces, Fig. 3. This phenomenon, commonly referred to as crack tunneling, is rooted in the stress-state triaxiality dependence of fracture since the triaxiality is a strongly decreasing function of position away from the mid-section across the thickness. Another macroscopic aspect of fracture in cracked specimens is the often observed transition from flat to slant fracture, as illustrated in Fig. 3. Crack tunneling and flat-to-slant fracture transition complicate further the analysis of macroscopic properties measured in cracked specimens.

While the effect of stress triaxiality on the fracture strain is strong, the question of whether it is sufficient to determine the fracture locus of ductile materials has been examined to more depth in recent years. Thus, Bao and Wierzbicki (2004) used “butterfly” specimens and Barsoum and Faleskog (2007a) used double notched tube specimens under tension/torsion to explore the effect of the Lode parameter μ . The latter is related to the third invariant of the stress tensor and will be defined formally in the next section. Because of the complexity of the stress states considered, recourse to numerical simulations was necessary to construct failure maps parameterized by both the stress triaxiality ratio T and the Lode parameter μ . Their results indicate a significant reduction in ductility under shear-dominated loadings ($\mu \approx 0$).

Figure 4 illustrates the two types of fracture properties measured in the laboratory, the fracture strain and J versus crack extension curves. The material is a hot-rolled C-Mn steel. As noted above, the fracture strain is much greater in round smooth bars than in plane strain bars. In this steel, the difference is in fact traceable to a stress

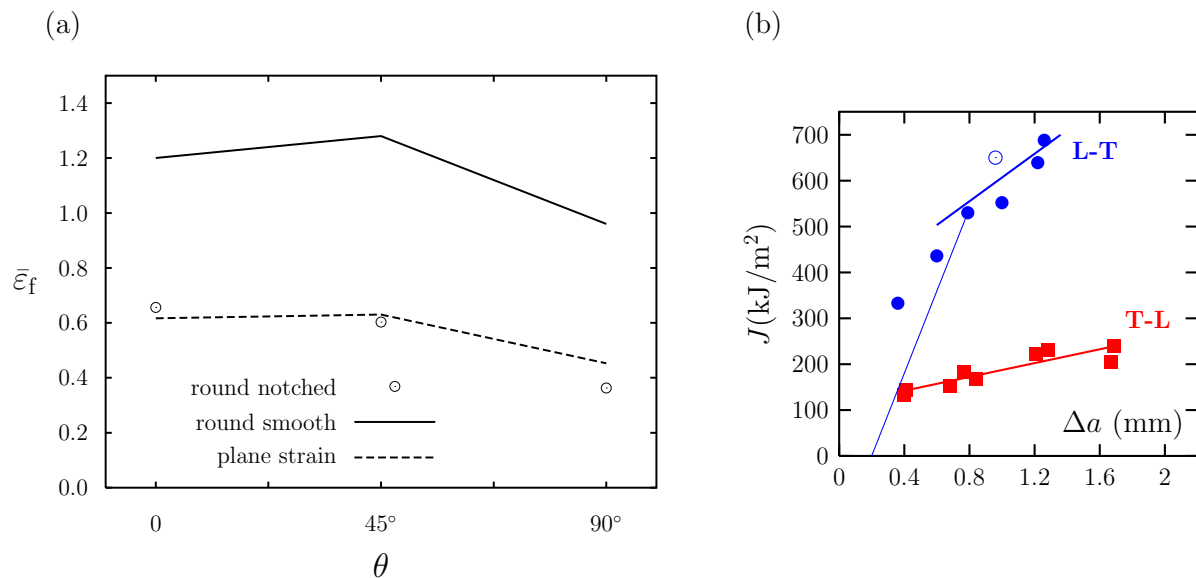


Figure 4: Macroscopic fracture properties. (a) Fracture strain versus loading orientation measured from the longitudinal direction L (Benzerga et al., 2002). (b) Crack growth resistance curves for two loading orientations (Benzerga, 2000).

triaxiality effect, not to the slanted fracture mode. Indeed, the plane strain ductility was compared by Benzerga et al. (2002) with the mean strain to failure initiation in moderately notched bars having roughly the same value of T as in the plane strain bar. As shown in Fig. 4a, the two fall nearly on top of each other, for three different loading orientations. On re-examination of the data, it appears that there is also a slight effect of the Lode parameter. Benzerga (2000) reported $J-\Delta a$ crack growth resistance curves for the same steel, Fig. 4b. Loss of constraint was prominent in the L-T orientation due to the extent of plastic deformation. In two instances, a slanted crack was formed (one is shown as open circle).

A noticeable feature in Fig. 4 is the anisotropy in fracture properties, which is typical of structural steels used in pressure vessels and naval applications. Hancock and MacKenzie (1976) reported similar anisotropic properties for notched bar ductility but indicated a trend of decreasing anisotropy with increasing stress triaxiality. This is in contrast with the trends shown in Fig. 4, which are consistent with most other measurements, e.g., (Lautridou and Pineau, 1981; Decamp et al., 1997). In recent years, the anisotropy in fracture properties of structural materials available as wrought products has been increasingly characterized, e.g., in aluminum alloys (Agarwal et al., 2002; Steglich et al., 2008) and zirconium alloys (Prat et al., 1998).

The fracture surface of a broken ductile specimen exhibits a rough topography. In

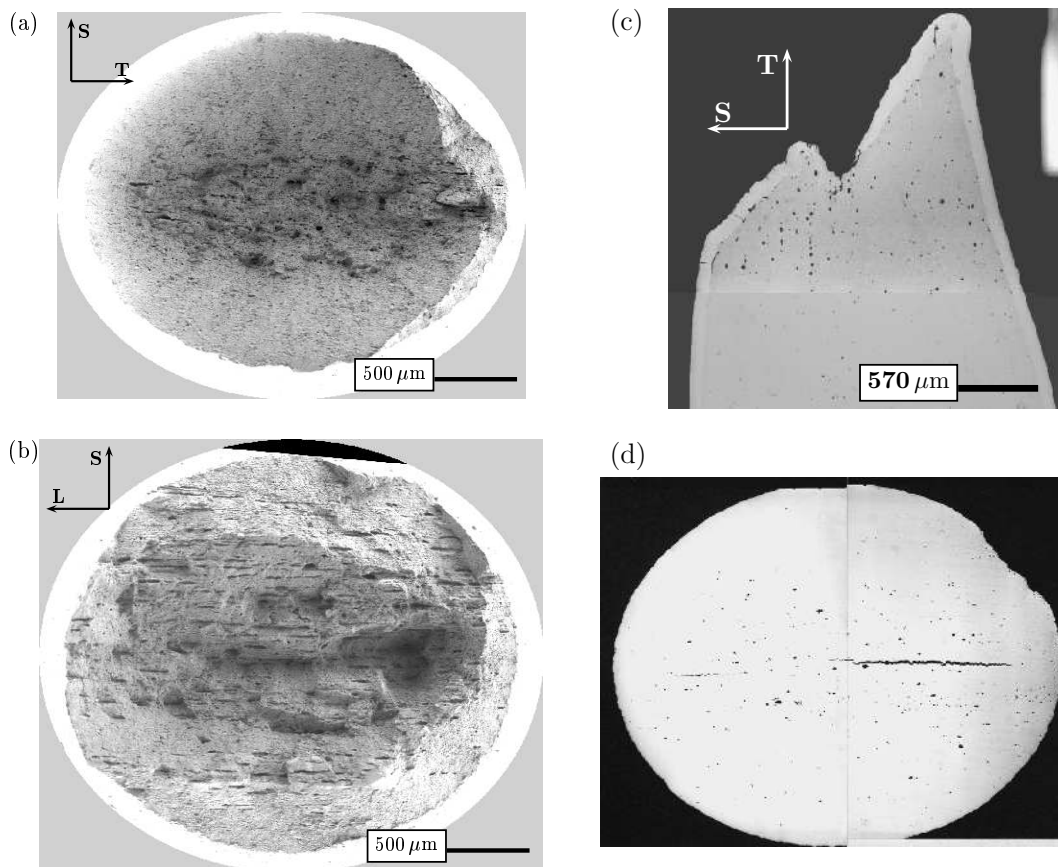


Figure 5: Topography of fracture surfaces. (a) Dimpled and (b) Fibrous (Benzerga et al., 2004a); (c) Slanted (Benzerga et al., 2002); (d) Delamination (Benzerga, 1999).

round bars, the “cup” and “cone” consist of a flat part, which is generally dimpled (Fig. 5a) or fibrous (Fig. 5b), and of shear lips with a lower degree of roughness. Similar aspects are observed in round notched bars (Fig. 1). In plane strain bars where slant fracture prevails, the shear lips cover almost the entire fracture surface, Fig. 5c. The fracture surfaces of certain steels exhibit some delamination, the extent of which depends on the stress state. This is illustrated in Fig. 5d showing the cross-section of a notched bar normal to the loading axis. The material is a pressure vessel steel (X65) with slightly higher strength than the one shown in Figs. 5a–c. The polishing of the fracture surface revealed a secondary ductile crack orthogonal to the main crack. Such delaminations can severely limit the ductility of some steels. In cracked specimens under mode I quasi-static loading, fracture is usually flat, presenting a bathtub-like aspect (Rivalin et al., 2001; Pardoen et al., 2004). However, transitions to slant fracture are commonly reported, especially under circumstances where the size of the plastic zone is greater than the specimen thickness, as is often the case in wide panels/plates or thin sheets (Fig. 3); see also (Asserin-Lebert et al., 2005).

Most of the macroscopic aspects of ductile fracture are generic and apply to high-rate and dynamic loadings to some extent. The Charpy V-notch impact test is commonly used to measure the material resilience (or impact energy absorbed per unit area) and its dependence upon temperature. As mentioned above, the initiation toughness J_{Ic} may be geometry dependent. This is even more so for resilience. Yet, the Charpy test is very useful for comparing different materials and most importantly for determining a reference ductile-to-brittle transition temperature. In the Charpy test, inertial effects are small and the high-rate loading reflects mostly through the rate-sensitivity of the material; see (Tanguy et al., 2005) for an overview.

Rivalin et al. (2001) investigated the effect of loading rate on fracture in pre-notched wide plates using a custom-made 4000 kN quasi-dynamic tensile machine. Nominal strain rates were in excess of 20 s^{-1} during the tearing phase of the test. They found important effects of loading rate on the fracture mode, slanted versus flat with the former being favored at high loading rates at fixed plate thickness. Benzerga (2000) carried out similar experiments on high-strength steel. Fig. 6 shows the transition from flat to slant mode I+III fracture. By way of contrast, fracture would occur in mode I under quasi-static loading conditions for the same $\approx 10 \text{ mm}$ plate thickness. A noticeable feature in Fig. 6 is the central line in the direction of crack propagation. This feature is commonly observed, notably on fracture surfaces of burst open pressurized tubes and pressure vessels. It suggests a certain order in which events take place, probably necking induced crack initiation in the mid-section, followed by shear localization and slant fracture.



Figure 6: Transition from flat to slant fracture in a “quasi-dynamic” ductile tearing experiment on a pre-notched wide plate of steel. From (Benzerga, 2000).

Under truly dynamic loadings, wave effects may enhance local stresses and/or af-

fect plastic flow localization in ways not necessarily encountered under quasi-static or low-velocity impact loadings. Zhang and Ravi-Chandar (2006) used the expanding ring experiment to study necking and fragmentation in an Al alloy with a low rate-sensitivity. Their results indicate an increase in the fracture strain with increasing expansion velocity. The range of nominal strain rates covered was $4000\text{--}10000\text{s}^{-1}$. Careful interpretation of unprecedented measurements indicated that the increase in ductility is not associated with an increase in strain-rate but with dynamic effects. The fracture strain is indeed affected by a large number of necks whose formation is favored by the slow propagation of unloading and release waves from individual necks and fractures. There is a need for more dynamic experiments, especially to explore more severe states of stress triaxiality.

Another set of dynamic experiments where ductile fracture plays an important role pertains to ballistic penetration. Three categories of failure mode are observed: adiabatic shear plugging, discing and ductile failure (Woodward, 1984). Adiabatic shearing is possible if the rate of thermal softening exceeds the rate of work hardening of the target material. The intersection of shear bands with a free surface lead to asymmetry in the deformation and this does not favor further propagation of adiabatic shear bands. Failure is then completed by discing, particularly if the target plate has a low through thickness toughness, or by ductile tearing. The penetration process is shear-dominated at initiation stages then combined tensile and shear contributions become equally important at later stages (Borvik et al., 1999). In addition, the ballistic limit velocity depends on the failure mode as, for example, affected by use of different projectile nose shapes (Borvik et al., 2002). Systematic studies of material microstructure effects are still lacking although there is some evidence from the early works, e.g., (Woodward, 1984) that material purity and plastic anisotropy affect qualitatively and quantitatively the penetration process and ballistic limit.

From what precedes it follows that typical fracture properties are the fracture strain and the material toughness and that typical ductile fracture experiments measure the effect of stress state on these properties. While different macroscopic failure modes may be observed, all fracture surfaces reveal a dimpled character which hints to a set of generic micromechanisms of damage initiation and accumulation. These mechanisms are addressed next.

2.2 Microscopic Mechanisms

The advent of scanning electron microscopy (SEM) has transformed our understanding of ductile fracture in metals and their alloys. Plateau et al. (1957) showed the first fractographs of dimpled fracture surfaces. It has long been known that room-temperature ductility of structural alloys is affected by their inclusion content. The most widely reported effect is that of the volume fraction of inclusions and second-phase particles (Edelson and Baldwin, 1962). This is so because ductile fracture mainly involves the growth and coalescence of voids nucleated at those micron scale particles, thus leading to the dimpled character of the fracture surface. Consistently, a strong effect of initial porosity on ductility has also been documented by Bourcier et al. (1986).

Early studies of ductile fracture (Argon and Im, 1975; Beremin, 1981a; Le Roy et al., 1981) have established the basic facts about void nucleation. The latter occurs by decohesion at the particle–matrix interface or by particle cracking. Also, particle fragmentation

is often reported for elongated inclusions when loaded along their length. Exceptions include multiphase material systems where damage can initiate in a brittle phase, e.g., (Joly et al., 1990; Bugat, 2000) or at interfaces. For given matrix–particle interface strength and particle brittle strength, factors favoring one mode of nucleation over the other include the matrix flow properties (yield strength and hardening capacity), the particle shape and relative loading orientation, the matrix–particle stiffness mismatch and the state of stress. Table 1 summarizes the trends as they are now widely accepted. These trends will be discussed and rationalized in Section 4.

Parameter	Type	Trend	
		Decohesion	Cracking
Matrix yield strength		\searrow	\nearrow
Matrix hardening exponent		\searrow	\nearrow
Particle elongation		\searrow	\nearrow
Particle stiffness		\nearrow	\nearrow
Load orientation	axial	\searrow	\nearrow
	transverse	\nearrow	\searrow
Load triaxiality		\nearrow	\searrow

Table 1: Key parameters in void nucleation and relative trends upon increasing the parameter for the microscopic mechanism.

Figure 7 illustrates the basic mechanisms for model Al based materials and a structural steel. Babout et al. (2004a) investigated the effect of matrix hardness on void nucleation in an Al matrix ceramic particle model composite under uniaxial loading ($T = 1/3$). Pure Al was used as the soft matrix and a structural Al alloy as the hard one. They used *in situ* X-ray computed micro-tomography and thus were able to detect the process of void nucleation. In the hard matrix, particle cracking was found to be the mechanism for damage initiation. Penny-shaped cracks then formed and blunted a little in the hard matrix before linking up together (Fig. 7a). By way of contrast, matrix–particle decohesion was favored in the case of a soft matrix (Fig. 7b). Also, in that case plastic deformation in the matrix promoted more substantial void growth. In the structural steel studied by Benzerga (2000) MnS stringers were identified as key damage initiation sites. Often longer than $100\mu\text{m}$, MnS inclusions can be thinner than 100 nm and thus fall below the current resolution of X-ray tomography. The damage processes were investigated to quite some detail using conventional metallography techniques and scanning electron microscopy. Fig. 7c illustrates the stages of void growth and coalescence in the neck of a notched bar beneath the main crack; see also (Benzerga et al., 2004a).

Under certain circumstances, void nucleation is not complete even in intensely strained, highly stressed regions. This is illustrated in Fig. 8a which shows that pieces of the inclusion were not torn free. The void in the micrograph was located just below the

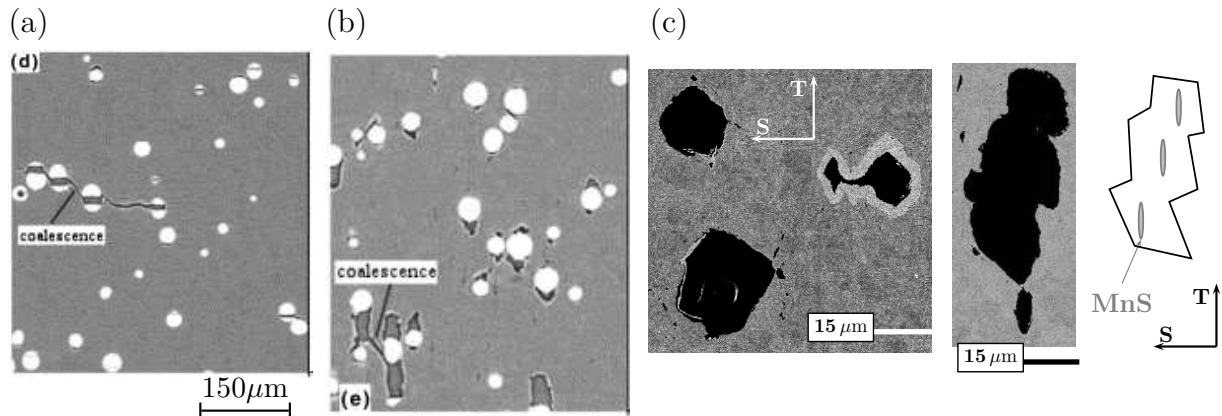


Figure 7: Micromechanisms of ductile fracture. (a) Particle cracking, formation of penny-shaped cracks and void coalescence in a model metal matrix composite (hard matrix). (b) Particle-matrix decohesion and void growth to coalescence in a model MMC (soft matrix); both from (Babout et al., 2004b). (c) Void growth and coalescence in a C-Mn steel (Benzerga, 2000). The Ni plating around the coalescing voids indicates that they are connected to the main crack.

macro-crack of a broken notched bar. This phenomenon may be referred to as void locking by the inclusion. An other example is found in Fig. 7b shown earlier. Void locking is prevalent at sufficiently low stress triaxiality, generally lower than about $2/3$. It is believed to play a more important role under predominantly deviatoric loadings, such as in tension/torsion experiments.

When void growth is substantial, it is usually terminated by void-linking or coalescence. This locally terminal process takes place in a variety of modes, depending on microstructural factors, loading conditions and matrix plastic flow properties. The most commonly observed mode of void coalescence is internal necking. It appears that this process was recognized to be responsible for fracture as early as the mid-19th century; for a brief historical perspective see (Argon et al., 1975) and references therein. Fig. 9a shows an example of internal necking. The second most commonly observed mode is void coalescence in a micro-shear band, also known as “void-sheet” coalescence (Cox and Low, 1974). This is illustrated in Figs. 9b and c. It is expected that this mode would entail a decrease in local—and perhaps global—ductility since the stable void growth is suddenly terminated while the voids are still quite apart. Evidently, coalescence in a shear-band is very much configuration-dependent so that the inclination of the micro-shear band depends on the relative positions of the voids. For example, the angle between the band in Fig. 9b and the vertical loading axis is higher than in Fig. 9c. It is possible, however, that the lower angle in Fig. 9c has resulted from subsequent straining. Real-time observations, such as tomography, will hopefully clarify such details in the future as they have emerged as a powerful probe of mechanisms over the past decade (Maire et al., 2005; Weck et al., 2008).

Yet a third mode of void coalescence is the formation of voided columns. It was called “necklace” coalescence by Benzerga (2000) who gathered multiple instances of the phenomenon. An example is shown in Fig. 9d. In fact, necklace coalescence is quite prominent

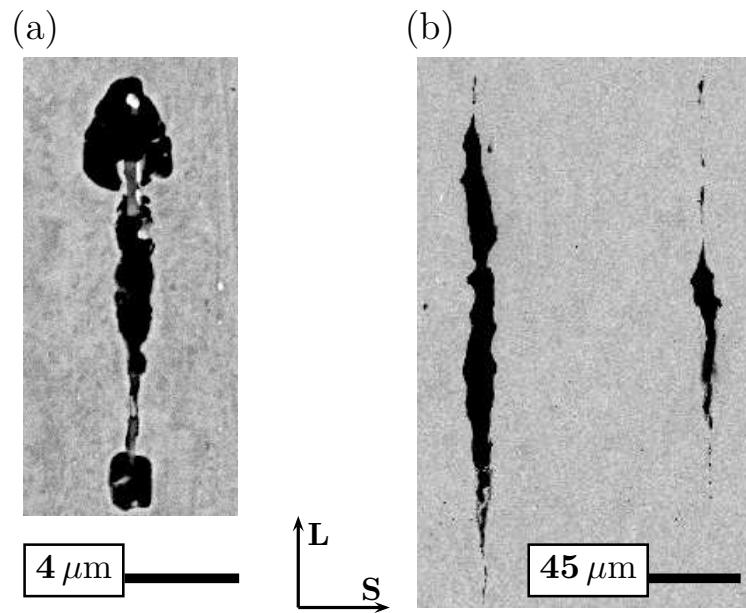


Figure 8: (a) Void locking by MnS inclusion at low stress triaxiality ($T < 0.8$). (b) Unimpeded void growth at higher triaxiality ($T > 1.2$). Adapted from (Benzerga, 2000; Benzerga et al., 1999).

in steels containing elongated MnS inclusions loaded along the rolling direction (denoted L in Fig. 9d). Statistically, it is by far the most dominant mode of void coalescence in these materials under uniaxial loading, either axisymmetric or plane strain (e.g. see Fig. III.59 in (Benzerga, 2000)). While it is favored at low stress triaxiality, it has repeatedly been observed in moderately notched bars (see Fig. 12 in (Benzerga et al., 2004a)) as well as in the neck of sharp notches as in Fig. 8b above. Yet, coalescence in columns had little effect on macroscopic ductility in this steel. However, it led to micro-delaminations (Fig. 5a) and it is believed to be a key mechanism in driving ductile delaminations as shown earlier in a similar steel of higher grade (Fig. 5d).

While isolated void-coalescence events such as those documented above shed light on the mechanisms, it is worth recalling that they do not have much to do with macroscopic crack initiation. This applies to most micrographs documented in the specialized literature, including the famous capturing of void-sheet coalescence by Cox and Low (1974). Figure 10 depicts how the above fundamental mechanisms affect, in an average sense, the macroscopic load-displacement response in a typical notched bar experiment. Here, the displacement corresponds to the diameter reduction at the notch root. Prior to point (c) in Fig. 10 damage accumulation takes place gradually through the processes of void nucleation and growth (as well as a few isolated and inconsequential void-coalescence events). The change in slope of the load-displacement curve at (c) corresponds to the onset of a macroscopic crack via the coalescence of the two or three largest voids; also see (Benzerga et al., 2004a). This change in slope can be more abrupt than shown in Fig. 10. The descending part of the curve corresponds to the stage of crack propagation inside the bar. In later stages, the faster load drop is in fact associated with the formation of shear lips, as illustrated in the inset. Although the two pieces seem separated in the

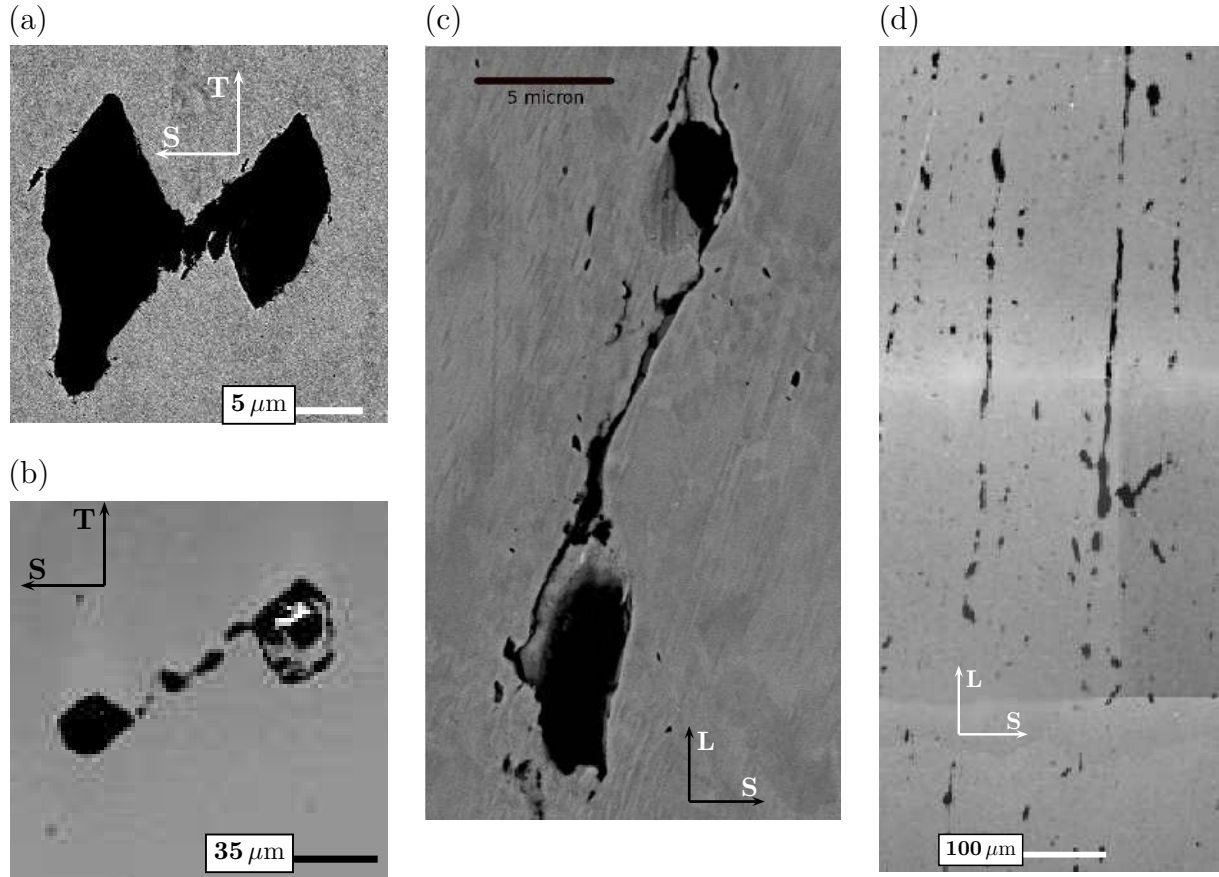


Figure 9: Modes of void coalescence. (a) Necking of intervoid ligament or coalescence in a layer (Benzerga et al., 1999). (b),(c) Coalescence in a micro-shear band (Benzerga, 2000). (d) “Necklace” coalescence or coalescence in columns (Benzerga, 2000). Major loading axis is vertical in all. Loading is axisymmetric in (a)–(c) and plane strain in (d).

2D view, they are in fact still connected by ligaments that are not visible, since the 3D crack has not reached all free surfaces. The final stage (f) in Fig. 10 corresponds to the micrograph in Fig. 1, which shows the actual specimen tested. The fracture surface of the shear lips contains dimples that are sheared off, just like in the cup-cone fracture of smooth bars, slant fractures or fracture surfaces of specimens under predominant shear loading (Barsoum and Faleskog, 2007a).

The fracture strains $\bar{\epsilon}_c$ and $\bar{\epsilon}_f$ mentioned in the previous section correspond to the stages shown as (c) and (f) in Fig. 10. It is clear from the figure that the two measures are substantially different in a notched bar. The difference between $\bar{\epsilon}_c$ and $\bar{\epsilon}_f$ in smooth round bars is negligibly small (Benzerga, 1999). It is also small in plane strain smooth bars (Benzerga et al., 2002). Therefore, care should be taken in interpreting certain published results, especially when data from smooth and notched bar experiments are plotted together.

The above mechanisms of micro-void nucleation and growth to coalescence apply under dynamic and impact loadings as well. Under low velocity impact the mechanisms are

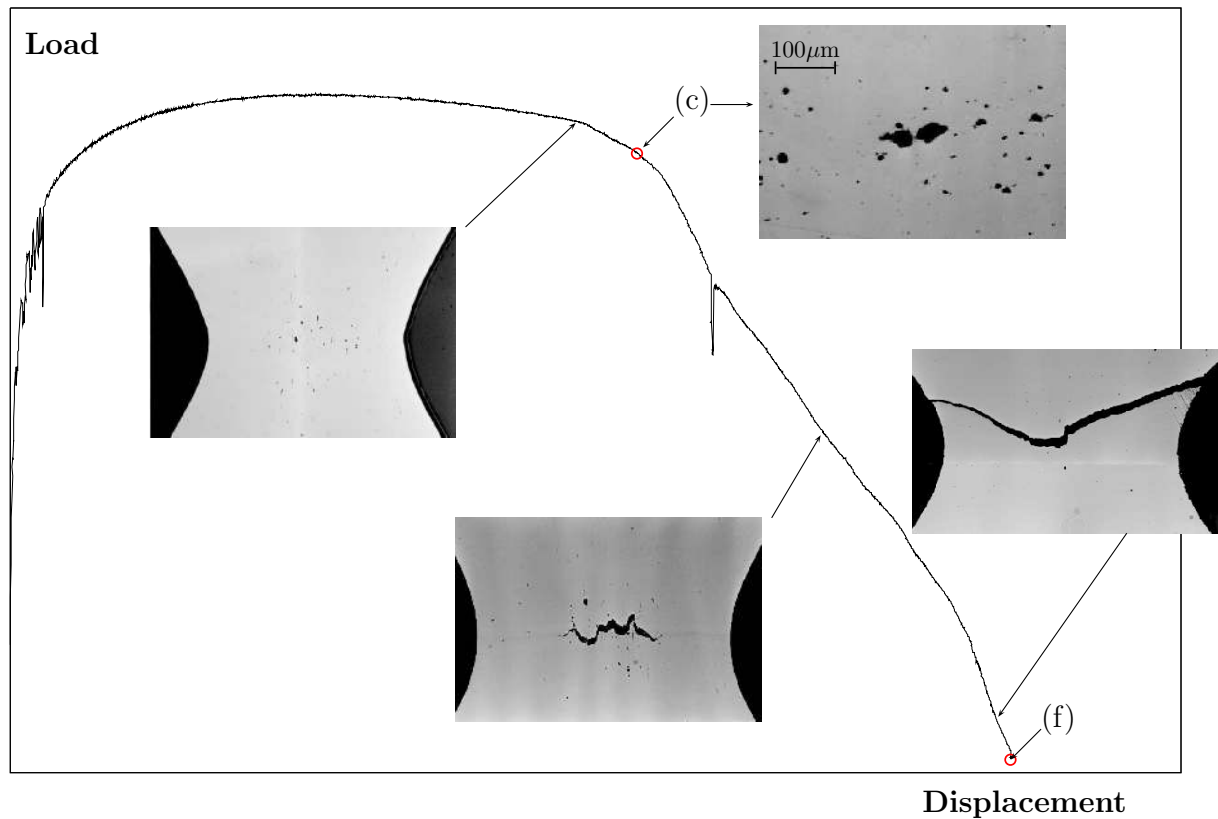


Figure 10: Phenomenology of ductile fracture in round notched bars of high strength steel: damage accumulation, initiation of macroscopic crack, crack growth and shear lip formation. Adapted from (Benzerga, 2000).

vastly similar and are well documented (Tanguy et al., 2005). Under dynamic loadings, conducting controlled experiments in which the damage process is interrupted at will is a very challenging task. Most observations tend to be *post mortem*. Recently, expansion ring/cylinder experiments were carried out on an Al alloy using rings of various aspect ratios (Zhang and Ravi-Chandar, 2009). The fragmentation process was followed in real-time using high magnification, high speed cameras. Interestingly, cylinders (or rings of high aspect ratio) were found to fail in localized bands on the surface, not through-thickness as in lower aspect-ratio rings. Also, it was found that voids are nucleated at intersections of micro-shear bands, which themselves initiate at round second phase particles. Void growth at particles was not found to be significant. However, the thickness of all rings was about 0.5 mm so that the prevailing plane stress conditions may have favored this nucleation mechanism. In ballistic penetration, ductile fracture by hole growth has also been observed. When available, metallurgical examination of the penetrated target clearly reveals void growth in the localized shear/tension zones (Borvik et al., 1999).

2.3 Microscopic Measurements

Within the large body of experimental investigations of fracture in ductile materials, reports on meaningful microscopic measurements remain unfortunately scarce. Thus, Argon and Im (1975) measured the effective interfacial strength of spherical inclusions in three different alloys, aided by analysis. Similarly, Beremin (1981a) developed an estimate of the local stress required for void nucleation, based on a hybrid experimental–analytical approach. For a given amount of overall strain, they unloaded the specimens and examined for damage all nonspherical MnS inclusions. The process was repeated several times, for three notched specimen geometries, two steels, two loading orientations at three test temperatures. Aided by finite element calculations of the specimens modeled as elasto-plastic, they mapped the local stress and strain fields onto the locations of damaged inclusions. Next, they used an extension of Eshelby’s theory for inhomogeneities to account for the polarization stresses arising in the inclusions due to plastic strain incompatibility between matrix and inclusion. The outcome of that process was a temperature-independent critical stress for void nucleation. The latter was found to be lower in the short transverse direction than in the longitudinal direction. The difference was associated with a change in nucleation mechanism, decohesion versus inclusion cracking, respectively.

Le Roy et al. (1981) developed an estimate of the strain (not stress) required for void nucleation in smooth tensile bars. They studied spheroidized plain carbon steels in which void nucleation was related to cementite Fe_3C particles. They pre-strained the specimens to various levels of deformation, heat-treated them to restore the material’s strain-hardening capacity and loaded them again up to fracture. An overall measure of nucleation strain was inferred as the pre-strain needed to cause a change in the fracture strain. Le Roy et al. (1981) did not investigate the effect of stress triaxiality on the so-determined nucleation strain. It is important to note that Fe_3C particles are very resistant to void nucleation, in comparison with MnS inclusions and oxide particles which constitute the main damage initiation sites in many steels. In addition, cementite particles directly affect the flow properties of the material, unlike sulfides and oxides.

More recently, Pardoen and Delannay (1998b) used the methodology of Le Roy et al. (1981) to measure the effect of triaxiality on the nucleation strain in copper. Also, Shabrov et al. (2004) followed a procedure similar to Beremin’s (1981a) to estimate effective strengths of TiC particles in a high strength steel. Babout et al. (2004b) and Maire et al. (2005) used X-ray tomography data combined with finite element analysis to infer the critical stress for particle cracking under remotely uniaxial loading of model metallic materials (see Fig. 7a,b). Although the analytical approach of Beremin (1981a) does not distinguish between decohesion and inclusion cracking, their experiments remain to this day the most thorough quantitative experimental investigation of the void nucleation process.

Early measurements of void growth rates are due to Marini et al. (1985); see (Garrison and Moody, 1987) for an account of earlier, rather inconclusive attempts. Round notched bars of model composite materials made of a sintered-forged steel and spherical alumina particles were pre-deformed at room temperature and subsequently broken at liquid nitrogen temperature. Since the interface between matrix and alumina particles had no cohesive strength, cavities were easily formed and dominated the composite ductility. Different pre-strain levels corresponded to different amounts of cavity enlargement,

averaged over 100 voids. By using bars with different notch radii, Marini et al. (1985) were able to correlate the average void size with both plastic strain and stress triaxiality. Their main finding is that the void growth rate increases exponentially with the triaxiality ratio T . Measurements of the same kind, but on structural steel, were made by Mudry (1982). In these experiments, void sizes were measured directly on fracture surfaces. Therefore, the void growth ratio was not measured in the direction of loading.

More recently, Pardoen and Delannay (1998a) carried out density measurements in copper bars containing copper oxide particles as main nucleation sites. The measurements were made at several overall strain levels and for two material conditions: as-received (strain hardening exponent $N = 0.1$) and annealed ($N = 0.3$). These measurements revealed two important facts: (i) overall porosity levels of about 0.01 to 0.015 were reached near failure; (ii) the rate of growth of porosity was found to be lower in the annealed material, that is, in the material with higher hardening capacity. Considering the fact that the porosity was averaged over some deformed volume, local values of the porosity were likely higher than the above figures.

Koss and co-workers (Jablokov et al., 2001; Chae and Koss, 2004) and Benzerga (2000) carried out a series of measurements of void dimensions on metallographically polished sections of broken notched round bars. When sections are prepared with care, void smearing is minimal and the error in underestimating the void area fraction due to polishing is less than that associated with employing a lower cutoff in void size measurements. Fig. 11 shows typical void distributions measured in SEM. The error is typically a few percent of the measured area. Chae and Koss (2004) used the general methodology of

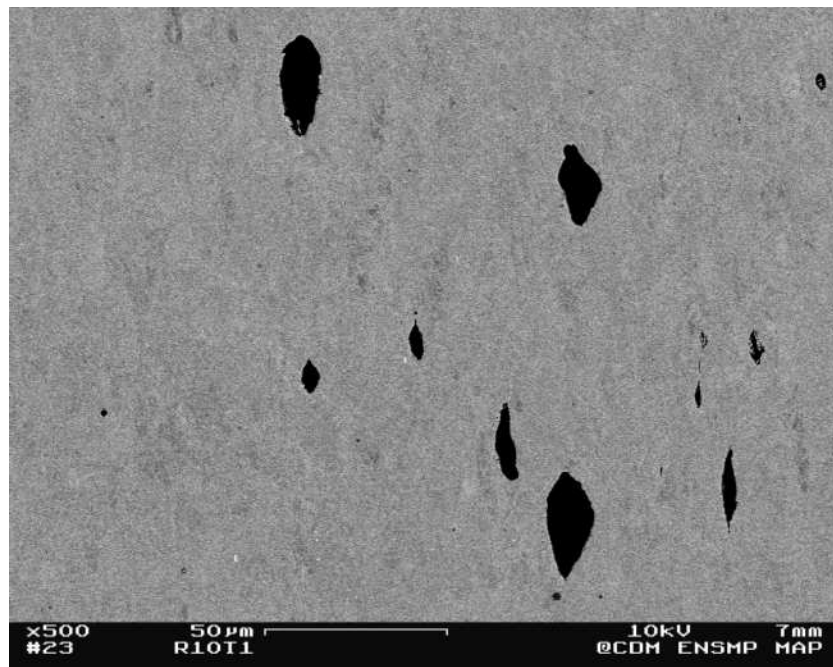


Figure 11: Distribution of voids underneath the fracture surface of a broken notched bar. Plane of view is T-S, with loading along the transverse direction T (vertical). Some voids which are elongated perpendicular to the section are viewed “end-on”. Actual measurements were made at a higher magnification, as reported by Benzerga et al. (2004a).

Beremin (1981a) and Marini et al. (1985) combining local measurements with finite element calculations for four different geometries. They mapped the local strains and stress triaxialities to the local porosities determined from void dimensions using a grid of fixed size. From their measurements, the values of local void area fraction at incipient coalescence are inferred to be about 0.005 ± 0.001 . However, these values should be considered as a lower bound because the use of a fixed-size grid inevitably leads to underestimating local porosities at or near the void coalescence stage.

Benzerga et al. (2004a) carried out void size and porosity measurements in a steel similar to the materials used by Beremin (1981a), Mudry (1982) and Jablokov et al. (2001) in terms of their inclusion content. Elongated MnS sulfides and Al oxides were the main void nucleation sites in this material. The void-size measurements were carried out for three notch geometries and two loading directions. For each loading orientation, void dimensions were measured in the axial loading direction as well as the two lateral directions on two perpendicular sections. A snapshot of one section is shown in Fig. 11. Given the extent of the measurements, the data was collected only in broken bars. Direct correlations with local strain and stress fields from FE calculations were not reported.

In addition, local void area fractions were measured in four bars. The method was different from the one used by Chae and Koss (2004). Dirichlet cell analysis was used to define gauges of neighborhood and determine local porosities in an objective manner (Benzerga et al., 2004a). In particular, a critical porosity for coalescence was estimated as the local porosity averaged over the ten largest values. The conclusions from this work are as follows. First, in the central region of the bars where void growth is maximum, void growth ratios varied between 3 and 10 under longitudinal loading and between 2 and 50 under transverse loading, depending on triaxiality level and growth direction. These values contrast with those inferred from the earlier measurements of Marini et al. (1985). Both measurements can be rationalized based on void growth models (Section 6). Second, void growth ratios larger than 10 are only realized for elongated voids in the short-transverse direction S. Most importantly, the critical porosity was found to be about 0.02 under longitudinal loading and a little below 0.01 under transverse loading.

3 Computational Cell Models

Finite-element micromechanical analyses have proven useful in guiding the development of improved ductile fracture models. A typical investigation focusses on a characteristic volume element containing a single void or particle. This includes the pioneering analyses by Needleman (1972a) and Tvergaard (1981) for a square array of cylindrical voids, those by Tvergaard (1982b) and Koplik and Needleman (1988) for spherical voids and those by Needleman (1987) for spherical particles initially bonded to a ductile matrix. Many more cell model studies have followed since. Here, a few such cell model analyses will be discussed which demonstrate the basic phenomenology of void nucleation and growth to failure. Focus is placed on the axisymmetric model problem illustrated in Fig. 12 to discuss the effects of stress state and those of microstructural variables on salient features of ductile fracture. The behavior of voids in a shear field will be addressed at the end.

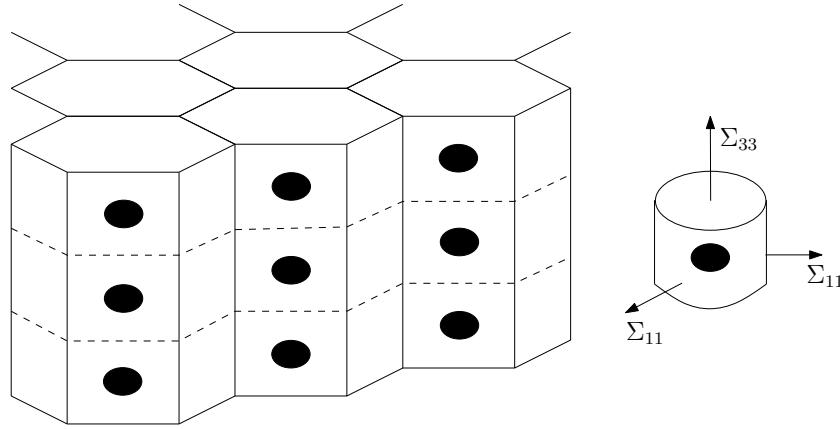


Figure 12: Axisymmetric cell model for doubly periodic array of spheroidal voids or void-nucleating particles. Adapted from (Tvergaard, 1990).

Unless otherwise noted, the computations shown here were carried out using the finite-element research code ZeBuLoN (Besson and Foerch, 1997) (Version 8.2) and a Lagrangian formulation of the field equations. A cylindrical matrix containing a particle or a void defines the unit cell, of which only one quadrant is modeled due to symmetries, Fig. 13. The meshes consist of sub-integrated quadratic quadrilateral elements. The cell boundaries are constrained to remain straight so that the unit cell is representative of a periodic array of voids. Special boundary conditions are formulated such that, in any given calculation, the ratio ρ of net lateral stress, Σ_{11} , to net axial stress, Σ_{33} , remains constant throughout. Stress triaxiality is measured by the ratio T of mean normal stress, Σ_m , to the von Mises effective stress, Σ_e , given by:

$$\Sigma_e = |\Sigma_{33} - \Sigma_{11}|, \quad \Sigma_m = \frac{1}{3}(\Sigma_{33} + 2\Sigma_{11}), \quad T = \frac{\Sigma_m}{\Sigma_e} = \frac{1}{3} \frac{2\rho + 1}{|1 - \rho|} \quad (1)$$

The matrix is modeled as an elastic-plastic or elastic-viscoplastic isotropically hardening material with the rate of deformation \mathbf{d} written as the sum of an elastic part, \mathbf{d}^e , and a plastic part, \mathbf{d}^p . The former is given by a hypoelastic law with elastic constants E and ν

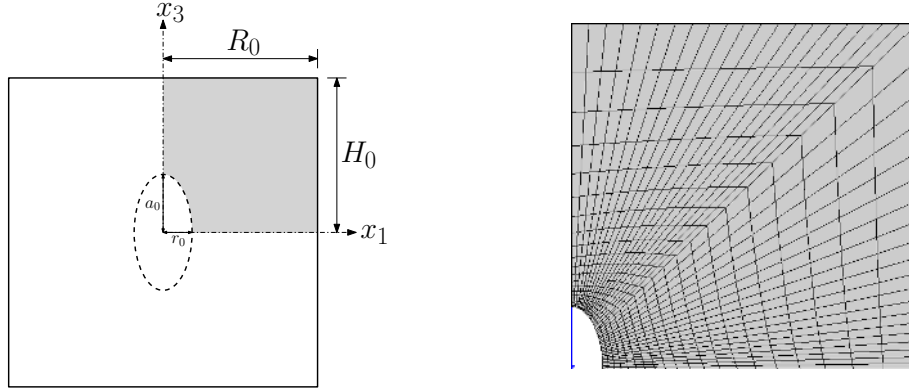


Figure 13: Geometry of the axisymmetric cell model and typical finite element mesh used in the calculations.

while the latter is described by the following flow rule:

$$\mathbf{d}^p = \frac{3}{2} \frac{\dot{\bar{\varepsilon}}}{\sigma_{\text{eq}}} \boldsymbol{\sigma}', \quad \dot{\bar{\varepsilon}} \equiv d_{\text{eq}} = \sqrt{\frac{2}{3} \mathbf{d}^p : \mathbf{d}^p} \quad (2)$$

In this expression $\boldsymbol{\sigma}'$ denotes the Cauchy stress deviator, d_{eq} the matrix equivalent plastic strain rate and σ_{eq} the equivalent stress. For a rate-independent matrix, Eqn (2) expresses normality to a von Mises yield function $\sigma_{\text{eq}} - \bar{\sigma}$ with:

$$\bar{\sigma}(\bar{\varepsilon}) = \sigma_0 (1 + \bar{\varepsilon}/\varepsilon_0)^N, \quad \varepsilon_0 = \sigma_0/E \quad (3)$$

where $\bar{\sigma}$ and $\bar{\varepsilon} \equiv \int \dot{\bar{\varepsilon}} dt$ are work-conjugate measures of matrix effective stress and plastic strain, respectively. Also, N is the strain hardening exponent and σ_0 is a reference yield strength. For a rate-dependent matrix, a Norton law is used such as

$$\dot{\bar{\varepsilon}} = \dot{\varepsilon}_0 \left(\frac{\sigma_{\text{eq}}}{\sigma_0} \right)^n \quad (4)$$

where σ_0 , $\dot{\varepsilon}_0$ and n are material constants; n is the Norton exponent. In some studies, plastic flow anisotropy is modeled using a quadratic Hill-like yield function. In such cases, Hill's tensor with respect to a deviatoric stress space is denoted \mathbf{h} and involves six parameters h_1 to h_6 ; see Section 6.3 below for details. The constitutive equations are integrated using a Newton–Raphson algorithm or a Riks algorithm (Riks, 1979) keeping the stress ratio ρ , and hence T , constant. The macroscopic response of the unit cell is defined in terms of the effective stress Σ_e above versus an effective strain, E_e , defined as follows:

$$E_e = \frac{2}{3} |E_{33} - E_{11}|; \quad E_{33} = \ln \left(\frac{H}{H_0} \right), \quad E_{11} = \ln \left(\frac{R}{R_0} \right) \quad (5)$$

where H and R are the current height and radius of the axisymmetric unit cell, respectively, and H_0 and R_0 their initial values (Fig. 13).

3.1 Void Nucleation

A few cell model analyses have been undertaken for matrix–particle systems. Some of these assume perfect bonding between matrix and particle and aim at examining local stress and plastic strain distributions that could not be obtained analytically (Thomson and Hancock, 1984; Babout et al., 2004b). Results are often limited to spherical inclusions and uniaxial loading. Fewer studies have examined the effect of cohesive separation at the interface (Needleman, 1987; Shabrov and Needleman, 2002) on the void nucleation process. Another type of analyses assumed no cohesion between matrix and particles and investigated the void–particle interaction as a function of stress state (Fleck et al., 1989; Siruguet and Leblond, 2004). Although the latter work focussed on the effect of void locking, it did provide some insight into the role of void–particle interaction in void nucleation.

In the analyses discussed below, the particle is modeled as rigid and the properties that remain fixed are given by $\sigma_0/E = 0.002$, $\nu = 0.3$, and the particle volume fraction $f_p = 0.0104$. In a fine study of void nucleation, Needleman (1987) analyzed the debonding of a spherical particle from the surrounding matrix. The latter was modeled using a variant of equation (4) and a rate-insensitive behavior was approached using $n = 100$. A traction–separation constitutive law was used to describe the gradual loss of cohesion at the interface. The parameters of the cohesive law are the maximum normal traction for separation, σ_{\max} , the displacement jump at complete separation, δ , and the ratio of shear to normal stiffness of the interface, α . The first two parameters are also known as the cohesive strength and cohesive length, respectively, and play a major role. For the axisymmetric loadings considered, the stress triaxiality ratio T was varied between $2/3$ and 2 . Fig. 14a shows a typical evolution of dilational plastic strain, which is related to the void volume fraction, with the axial strain E_{33} (solid line). The use of a cohesive law allows to follow the initiation and propagation of the debond along the interface. For a “ductile” interface ($\delta/r_0 = 0.04$), initial debonding occurs at an angle $\approx 30^\circ$ off the x_3 axis, more precisely at the end of the strain concentration nearest the symmetry axis. From that moment onward, the void volume fraction starts to increase (Fig. 14a). The crack then rapidly propagates to the axis of symmetry and a spherical void cap opens. Finally, the decohering region propagates toward the mid-section.

A detailed analysis such as Needleman’s (1987) shows that the void nucleation is a process with a beginning and, eventually, an end. As discussed by Needleman (1987), the nucleation strain can be identified with the strain at initial debonding or the strain at complete separation. In the example of Fig. 14a, these two measures take respectively the values of 0.068 and 0.34 , which are quite different from each other. Alternatively, Needleman (1987) defined the nucleation strain ϵ_N as that for which the curve of f versus E_{33} coincides at the larger volume changes with a similar curve obtained for an initial void having the same size as the inclusion, and shifted by ϵ_N . This procedure is illustrated in Fig. 14a and results in a value of $\epsilon_N = 0.19$, which is intermediate between strains at the initiation of debonding and complete separation.

Fig. 14b shows the strong dependence of the nucleation strain ϵ_N upon the stress triaxiality T for three different particle sizes and $\sigma_{\max}/\sigma_0 = 3$. There is predicted a particle size effect on void nucleation, since the interface model involves a characteristic length, which is the cohesive length δ . However, the dependence upon interface strength

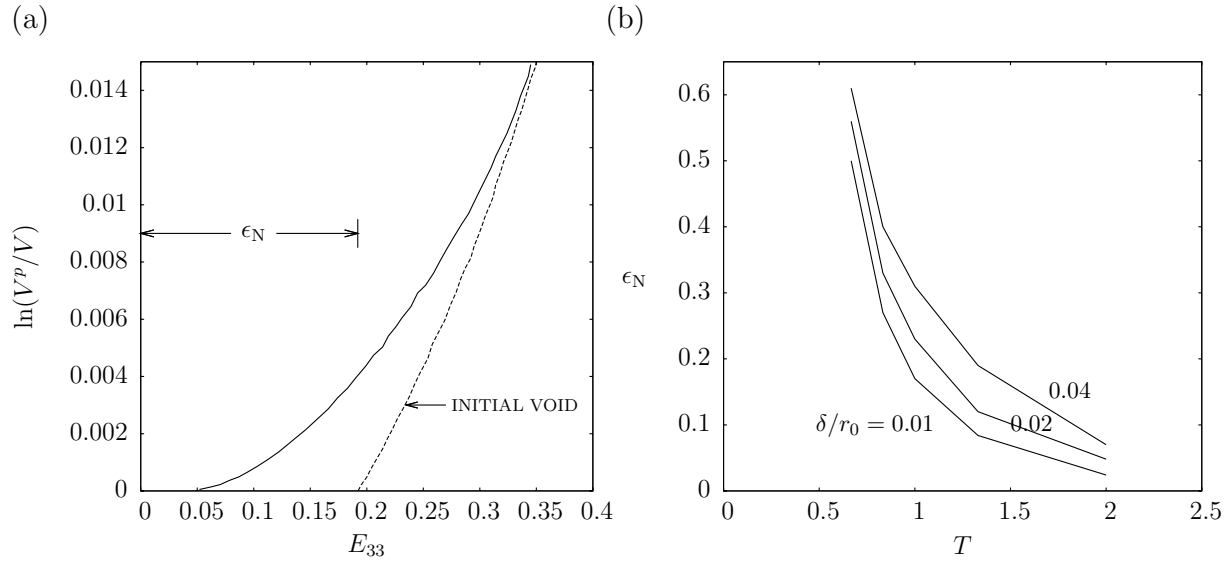


Figure 14: (a) Normalized logarithmic plastic volume change, $\ln(V^p/V)$, versus axial strain, E_{33} , for $f_p = 0.0104$, $N = 0.1$ with $T = 1.33$ and interface parameters $\sigma_{\max} = 3\sigma_0$, $\delta/r_0 = 0.04$ and $\alpha = 10$. The $\ln(V^p/V)$ versus E_{33} curve for a 1.04 percent volume fraction of initial void is shown shifted by an amount ϵ_N along the strain axis. (b) Nucleation strain, ϵ_N , versus the stress triaxiality ratio T for three values of δ/r_0 . Adapted from Needleman (1987).

σ_{\max} was found to be much stronger. In addition, although not analyzed by Needleman (1987), the size effect is expected to vanish or decrease in magnitude for particles greater than a few microns. Indeed, with parameter values representative of iron carbides in spheroidized carbon steels (i.e., $\sigma_{\max} = 1$ GPa and a work of separation about 10 J/m^2), δ is about 10 nm so that the particle sizes in Fig. 14b are 0.5 , 1 and $2 \text{ }\mu\text{m}$. The results in Fig. 14 are only indicative. In some cases, they tend to underestimate the nucleation strain since the actual values are expected to strongly depend on the interfacial properties used in the simulations. Carbides in steels, for instance, are known to be much more resistant to void nucleation than would be predicted on the basis of Fig. 14. Yet, the above definition of ϵ_N also leads to an overestimation of the nucleation strain at low triaxialities. In fact, that definition entails that $\epsilon_N \rightarrow \infty$ for $T < 2/3$. Because of compressive lateral stresses toward the midsection, void nucleation is never complete in that case.

Other cell model studies (Fleck et al., 1989; Kuna and Sun, 1996; Siruguet and Leblond, 2004) investigated the range of triaxialities below $2/3$, which was the cutoff in the analyses of Needleman (1987). Most such analyses assume, however, no bonding between particle and matrix and thus focus on the contact interaction. For $T < 2/3$ void nucleation is incomplete because the normal tractions are compressive near the mid-section. This is in keeping with the experimental observations in Fig. 7b and Fig. 8a. Fig. 15 shows the evolution of the void volume fraction f for $T = 0$, $1/3$ and $2/3$, as predicted in the computations of Siruguet and Leblond (2004) where the particle was modeled as rigid in a non-hardening matrix ($N = 0$) with no cohesion. In all cases, the void volume fraction steadily increases. By way of contrast, without void locking by the particle, f would have

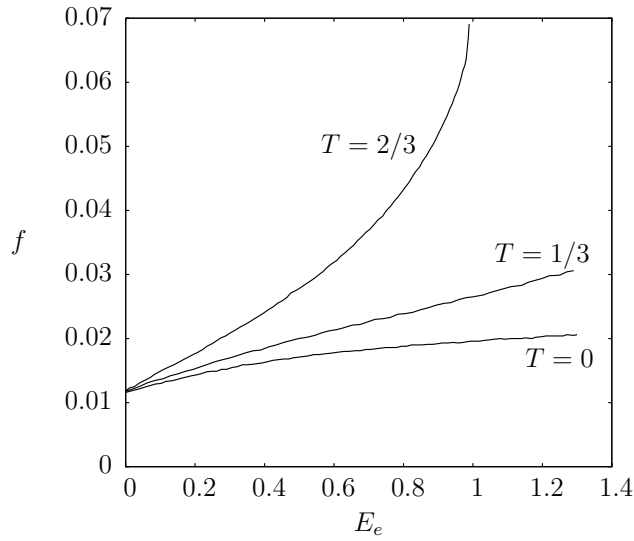


Figure 15: Effect of void locking by a rigid particle on the void volume fraction, f , versus effective strain, E_e , response. Cell model results for a spherical particle in an isotropic non-hardening matrix with no interfacial cohesion for three values of the stress triaxiality $T \leq 2/3$. Adapted from (Siruguet and Leblond, 2004).

decreased under $T = 0$ (void collapse) and saturated to a value close to f_0 under $T = 1/3$. At $T = 2/3$ the behavior with or without the particle is very similar since the mid-section normal stresses are small.

3.2 Void Growth and Coalescence

Many more cell model studies have been carried out for void growth to coalescence. In general, the geometry of the unit cell is characterized by the void volume fraction or porosity, f , the void aspect ratio, w , defined as the ratio of the axial to transverse semi-axes, and the cell aspect ratio, $\lambda = H/R$ (Fig. 13) with initial values denoted by the subscript 0. In what follows, the parameters varied are stress state triaxiality, initial void aspect ratio, initial cell aspect ratio, matrix material plastic anisotropy and matrix material rate sensitivity. The properties that remain fixed are given by $\sigma_0/E = 0.002$ and $\nu = 0.3$. Also, $N = 0.1$ and $f_0 = 0.001$ in the rate-independent case. Most analyses correspond to loadings with a major axial stress ($\rho < 1$) but a few analyses with $\rho > 1$ will be discussed in the broader context of stress state effects on void growth and coalescence.

3.2.1 Elasto-Plastic Matrix

We first illustrate the effect of stress triaxiality with $1/3 \leq T \leq 3$. These values cover the range from smooth cylindrical tensile bars to the triaxiality prevailing in crack tip fields. Figure 16 shows the cell model response with $w_0 = 1$, $\lambda_0 = 1$ and $\mathbb{h} = \mathbb{I}$. This case corresponds to an initially isotropic distribution of spherical voids in an isotropic matrix as first investigated by Koplik and Needleman (1988). Fig. 16a shows that the effect

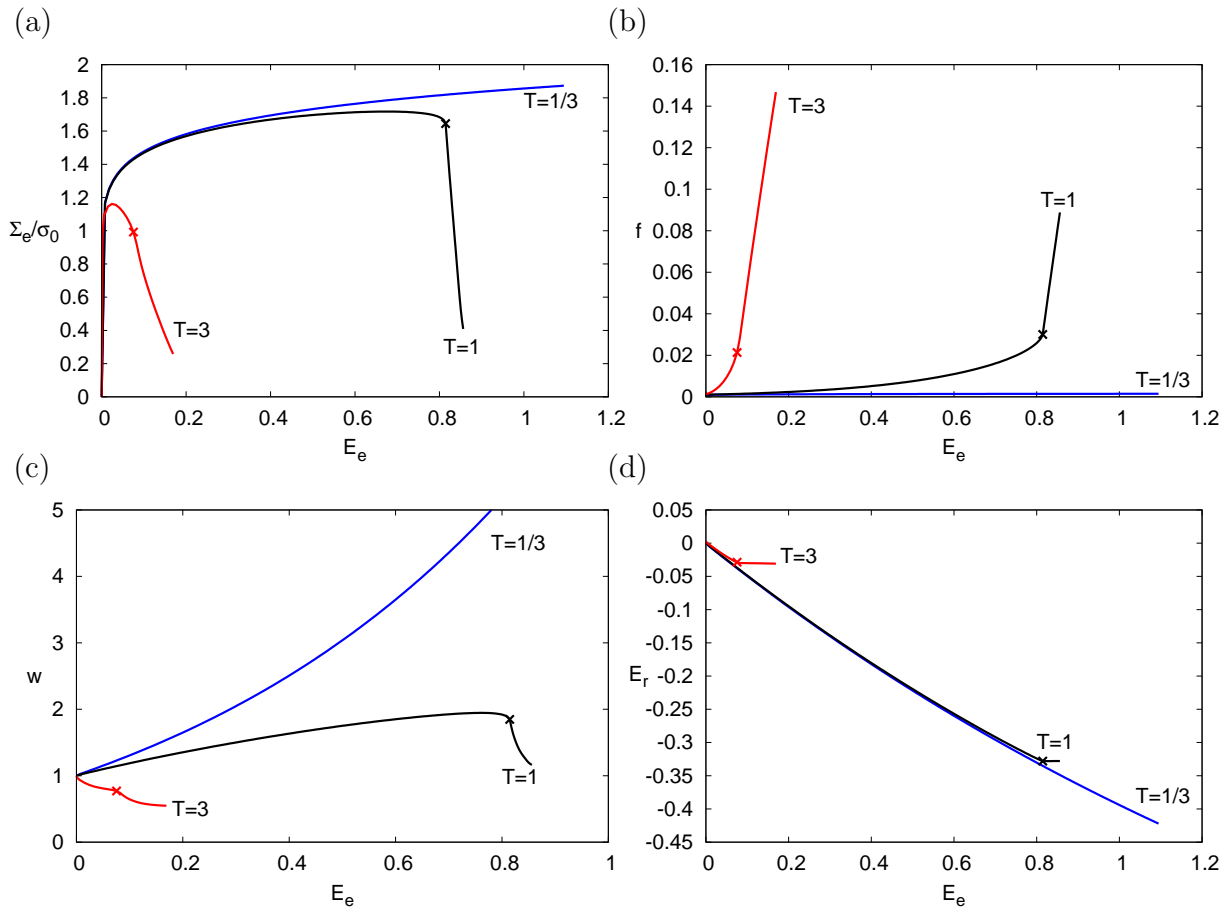


Figure 16: Effect of the stress triaxiality ratio T . Cell model results for an initially spherical void in an isotropic matrix for various values of T . (a) Effective stress, Σ_e , normalized by the matrix yield stress, versus effective strain, E_e . (b) Void volume fraction versus E_e . (c) Void aspect ratio versus E_e . (d) Net lateral strain, $E_r \equiv E_{11}$, versus E_e . The onset of void coalescence, i.e., the shift to a uniaxial straining mode, is marked by a symbol \times .

of stress triaxiality on the macroscopic effective stress versus effective strain response is paramount. Fig. 16b shows the corresponding porosity versus strain curves. Clearly, the macroscopic response in Fig. 16a is determined by the competition between matrix material strain hardening and porosity induced softening, with the latter effect being more prominent at high triaxialities. Under uniaxial tension ($T = 1/3$), the porosity does not evolve and consequently the macroscopic response is almost identical to the uniaxial response of the matrix. Fig. 16c also clearly indicates the effect of stress triaxiality on

the evolution of microstructural variable w , i.e., the void aspect ratio. For example, the void evolves into an oblate shape for $T = 3$ and toward a prolate shape for $T = 1$ and $T = 1/3$. The cavity flattening at high triaxiality is counter-intuitive since $\Sigma_{33} > \Sigma_{11}$. This typically nonlinear effect was first noticed by Budiansky et al. (1982).

Figure 16d shows the change in cell radius, or net lateral strain, as a function of effective strain. Except for $T = 1/3$, an effective strain is eventually reached beyond which deformation proceeds in a uniaxial straining mode, that is no further change in E_{11} occurs subsequently. This corresponds to flow localization in the intervoid ligament with elastic unloading taking place above and below the cavity. Since the pioneering work of Koplik and Needleman (1988) this transition to a localized deformation mode is referred to as the onset of void coalescence. In fact, at this point the porosity increases rapidly (Fig. 16b), the void aspect ratio (generally) decreases rapidly (Fig. 16c) and the load drops abruptly (Fig. 16a). These rapid changes are less noticeable at high triaxialities. The decrease in w is indicative of an acceleration in the lateral void growth, which is mainly responsible for the rapid increase in porosity.

Koplik and Needleman (1988) investigated the effect of initial porosity ($f_0 = 0.0013$ and $f_0 = 0.0104$), the effect of initial spacing ratio ($\lambda_0 = 1$ and $\lambda_0 = 8$) and that of the strain hardening exponent N (0, 0.1 and 0.2). They found that the rate of void growth is affected by f_0 and N . The rate of void growth decreases, and therefore the strain to coalescence increases, with decreasing f_0 or increasing N . Typically, a factor of 10 in f_0 and a 0.1 difference in N impart significant variations in ductility. The initial (relative) spacing λ_0 has no effect on void growth but a strong one on the strain to failure, measured by the effective strain at the onset of coalescence. This is illustrated in Fig. 17, which reveals that a multiplicative factor of 2 for λ_0 leads to strong variations in the strain to failure and that the effect is slightly more pronounced at the higher stress triaxiality of $T = 3$.

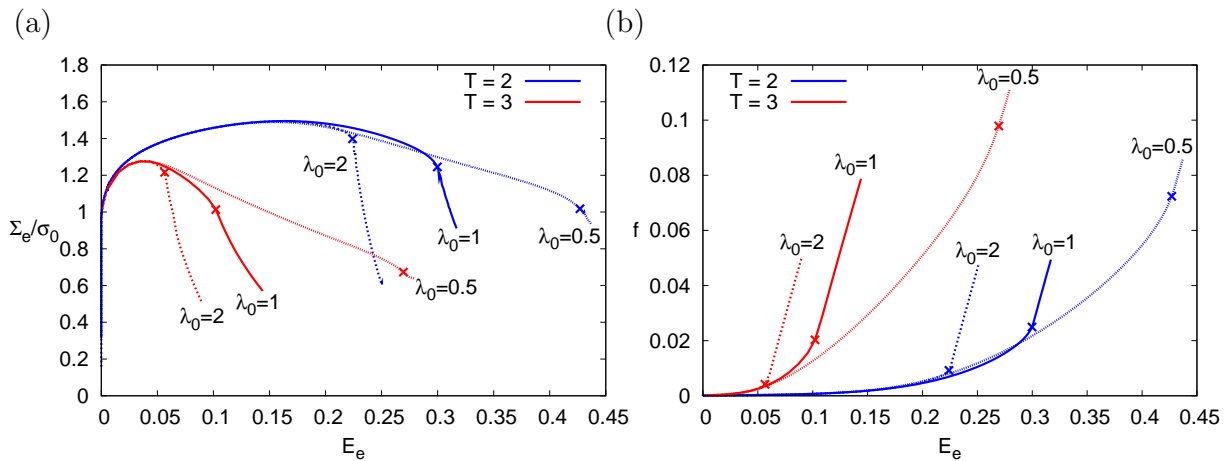


Figure 17: Effect of cell aspect ratio λ_0 . Cell model results for an initially spherical void in an isotropic matrix for $\lambda_0 = 1/2, 1$ and 2 and two values of the stress triaxiality ratio T . (a) Effective stress, Σ_e , normalized by the matrix yield stress, versus effective strain, E_e . (b) Void volume fraction versus E_e . The onset of void coalescence is marked by a symbol \times .

A series of other axisymmetric cell model studies have revealed additional aspects of behavior for an aggregate of initially spherical voids embedded in an isotropic matrix material. Among these the effects of boundary conditions, of a secondary porosity, and of the third invariant of the stress tensor deserve mention. Garajeu et al. (2000) compared the response of the cylindrical unit cell with that of a spherical shell subjected to uniform boundary deformations. They found little differences between the two responses indicating a negligible influence of remote boundary conditions on void growth rates, at least within the range of practical porosities². Brocks et al. (1995) and Fabregue and Pardoen (2008) modeled the effect of a second population of voids using a constitutive model for the matrix that accounted for compressibility and dilational effects. For wide ranges of cell model parameters, both studies showed evidence of a transition to the uniaxial straining mode. Under circumstances where the second population of voids is nucleated late, as may be expected in some cases, the effect of the secondary porosity on the strain to coalescence is relatively small. If voids are present from the outset, then the effect of the secondary porosity can be significant. Under such circumstances, the conditions that should be satisfied for separation of scales were recently discussed by Vincent et al. (2009). Compressibility aside, the behavior of a matrix with softening may be extrapolated from the behavior of power-law dense matrices with a hardening exponent N becoming negative. Some artefacts can emerge from representing the second population of voids through an effective porous medium. To avoid that, Tvergaard (1998) has explicitly modeled smaller voids interacting with bigger ones and showed some effects on localization patterns in plane strain. Similar studies are still lacking for spherical voids. The effect of the third stress invariant on void growth and coalescence was investigated by Gologanu et al. (1994b) and Benzerga and Besson (2001) and more specifically by Zhang et al. (2001) and Gao and Kim (2006). Under axisymmetric loadings, this effect is generally weak in comparison with that of the stress triaxiality and is more important at low values of T .

²The comparison between the two types of boundary conditions only makes sense for void growth prior to localization because the boundary conditions of uniform rate of deformation preclude localization, as will be reviewed below.

The voided cell model has also been employed in a number of investigations of initial and induced anisotropies and their effects on the growth and coalescence of voids. Broadly speaking, the analyses are of two types depending on whether the anisotropy is associated with the void shape or with the plastic flow of the matrix material. Void shape effects have been reported in several studies among which those of Sovik and Thaulow (1997) and Pardoën and Hutchinson (2000) are most comprehensive. An early study by Becker et al. (1989) focussed on a plane strain analysis of an elongated void having an elliptical cross-section and representing voids nucleated at MnS stringers in high strength steels. For spheroidal voids embedded in an isotropic matrix, it is generally found that the larger the initial aspect ratio, the slower void growth and the greater the strain to failure. This behavior is illustrated in Fig. 18 using three values of the initial aspect ratio $w_0 = 1/2$ (oblate void), $w_0 = 1$ (spherical void) and $w_0 = 2$ (prolate void). In all cases, the

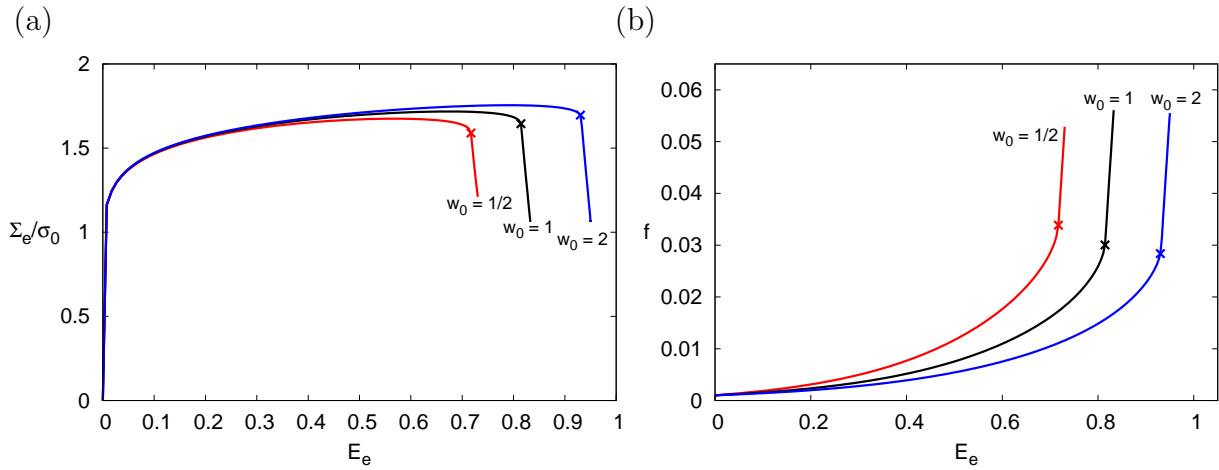


Figure 18: Effect of initial void shape. Cell model results for initially spherical ($w_0 = 1$), prolate ($w_0 = 2$) and oblate ($w_0 = 1/2$) voids in an isotropic matrix for $T = 1$. (a) Effective stress, Σ_e , normalized by the matrix yield stress, versus effective strain, E_e . (b) void volume fraction versus E_e . After (Keralavarma et al., 2010).

void distribution is initially isotropic ($\lambda_0 = 1$). The results in Fig. 18 indicate that a factor of 2 in the void aspect ratio can impart significant variations to the overall ductility. However, this effect of void shape decreases with increasing stress triaxiality and essentially disappears for T larger than about 2. This is in contrast with the effect of initial cell aspect ratio λ_0 , which persists at higher triaxialities, as shown earlier in Fig. 17.

Figure 19 illustrates the void and cell shapes at the onset of void coalescence in some of the calculations carried out by Pardoën and Hutchinson (2000) for two extreme porosities. The initial voids are also sketched so that the extent of void growth may be visually appreciated. The stress triaxiality is $T = 3$ so that the cell height to diameter ratio is close to unity in all cases, with $E_e^c \approx 0.1$ for $f_0 = 0.0001$ and $E_e^c \approx 0.05$ for $f_0 = 0.01$, irrespective of initial void shape. It is clear from Fig. 19 that neither a constant void growth ratio nor a constant void size to void spacing ratio are adequate representations of the state at the onset of void coalescence. A more complete tabulation of coalescence

states at other values of T and microstructural variables may be found in (Benzerga, 2002).

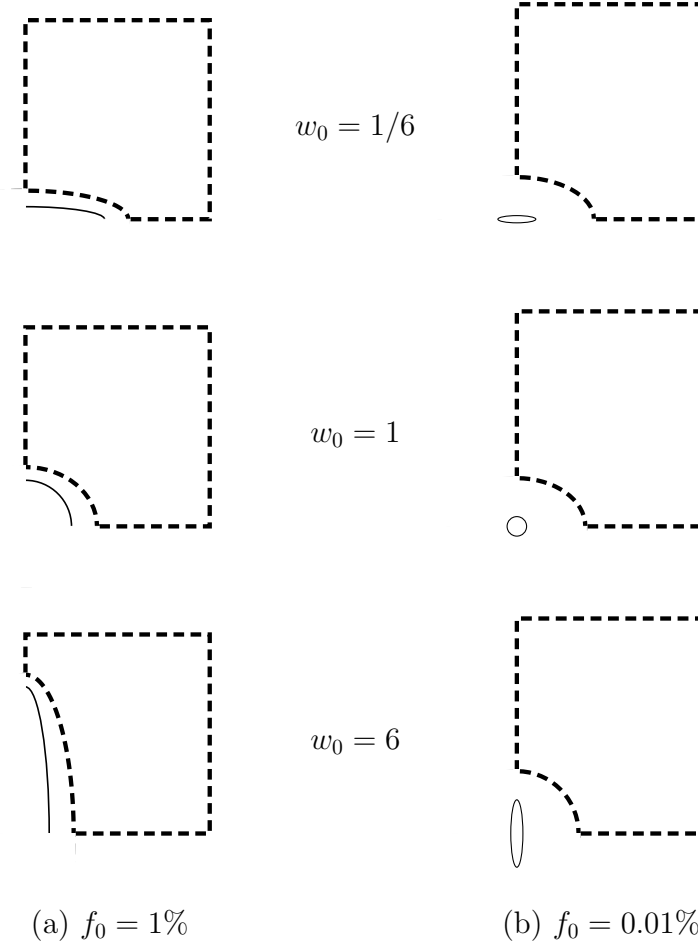


Figure 19: Initial and deformed states corresponding to actual cell model studies, showing the extent of void growth and relative void positions at the onset of localization. In all cases, $T = 3$ and $\lambda_0 = 1$. After (Benzerga, 2002).

Fewer studies have been devoted to understanding the role of matrix material plastic flow anisotropy in ductile failure. Benzerga and Besson (2001) used the cell model to analyze the growth of initially spherical voids in a Hill matrix. Invariance of material plastic flow properties about an axis \mathbf{e}_S was assumed. Their strain-hardening law amounted to replacing the reference strength σ_0 in $(3)_2$ with σ_S , the initial yield stress of the matrix material along \mathbf{e}_S . All material parameters were kept fixed except the Hill anisotropy factors that characterize plastic flow of the matrix material (Table 2). The applied loading was taken to be axially symmetric about \mathbf{e}_S . Benzerga and Besson (2001) identified categories of transverse isotropy that lead to important variations in the void growth rate. Figure 20 shows typical results corresponding to a relatively simple type of anisotropy considered by Benzerga and Besson (2001), except that the results here include the stage of void coalescence.

The fact that plastic anisotropy has an influence on void growth and coalescence is

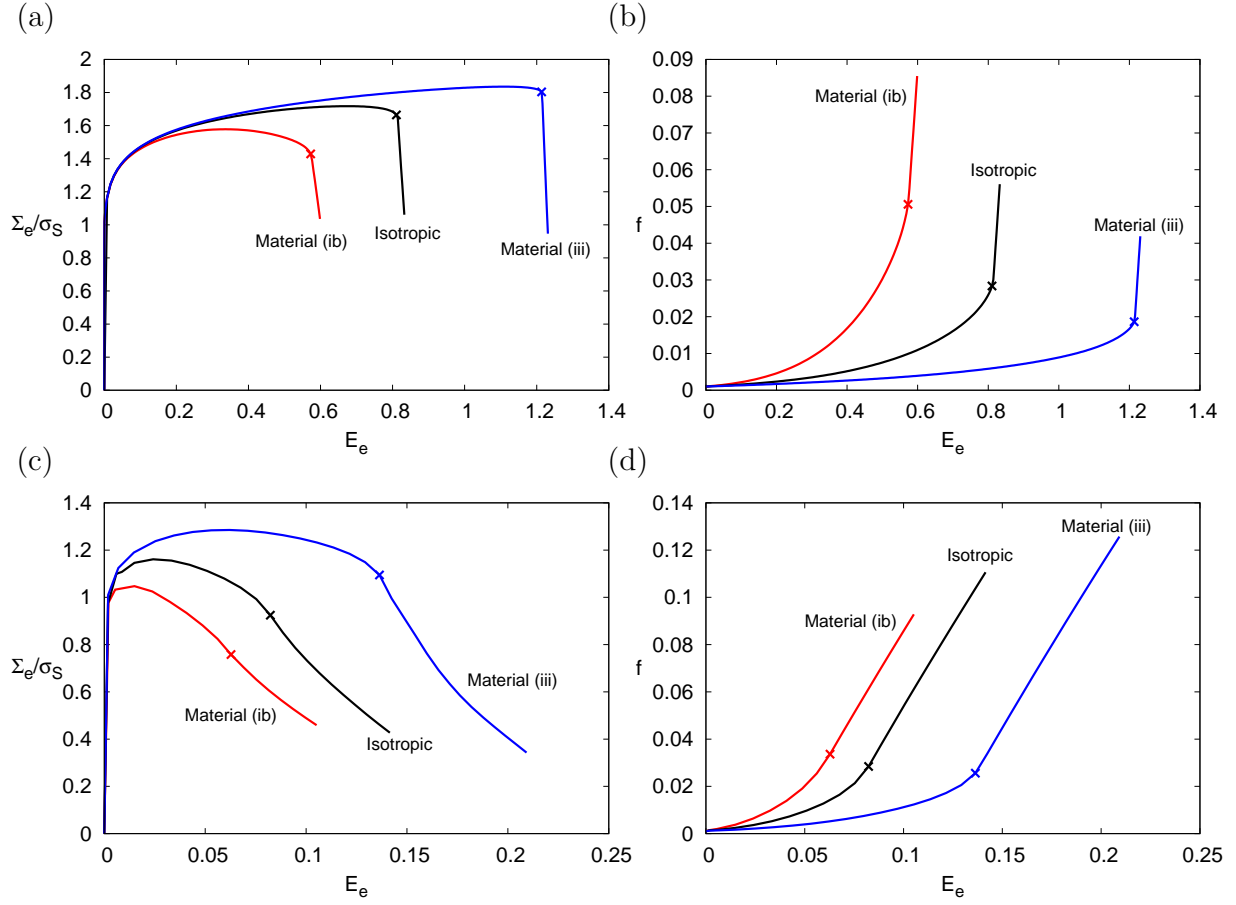


Figure 20: Effect of matrix plastic flow anisotropy. Cell model results for an initially spherical void in a transversely isotropic matrix material (Table 2) for $T = 1$ (top) and $T = 3$ (bottom). (a;c) Effective stress, Σ_e , normalized by the matrix yield stress in loading along \mathbf{e}_S , versus effective strain, E_e . (b;d) void volume fraction versus E_e .

expected, since void growth is merely the signature of plastic deformation of the surrounding matrix. However, the magnitude of the effect of matrix anisotropy shown in Fig. 20 is quite significant. This holds irrespective of the triaxiality provided that $T \neq 1/3$. In particular, it is remarkable that the effect of matrix anisotropy persists at high stress triaxiality. This is in contrast with the effect of void shape, which would be comparatively insignificant at $T = 3$ (Sovik and Thaulow, 1997; Pardoen and Hutchinson, 2000).

Recently, Benzerga and Keralavarma (2009) and Keralavarma et al. (2010) have carried out several cell model analyses to study the combined effects of void shape and matrix plastic flow anisotropy. They considered spheroidal voids embedded in a Hill matrix. In their simulations, the principal axes of the void, the axes of material orthotropy and the principal axes of the loading all coincided. The loading was taken to be axially symmetric about the void axis, which coincided with \mathbf{e}_S . For certain types of plastic anisotropy and initial microstructural variables (f_0 , w_0 and λ_0), the combined effect of void shape and matrix anisotropy qualitatively amounts to superposing the two separate effects. For

Name	h_1	h_2	h_3	h_4	h_5	h_6
Isotropic	1.000	1.000	1.000	1.000	1.000	1.000
Material (ib)	1.000	1.000	1.000	2.333	2.333	1.000
Material (iii)	1.000	1.000	1.000	0.500	0.500	1.000
Material Ti	1.650	0.778	0.893	1.378	0.943	1.627

Table 2: Material anisotropy parameters used in the computations reported in Figs. 20, 21 and 40–42.

other choices of the microstructural variables, however, the combined effect was found to be more subtle. Figure 21 illustrates some of the results found using material parameters from Table 2 and $T = 1$. In the material denoted (ib) (representative of aluminum alloys) the effect of void shape is as would be expected for the isotropic matrix material with the overall ductility being greater for initially prolate voids; compare with Fig. 18. However, in material (iii) (which is representative of a zirconium alloy), the effect of void shape essentially disappears, at least within the range of values of w_0 considered here. In this case, therefore, the combined effect of void shape and plastic flow anisotropy is not a simple superposition of separate effects. In examining the way in which plastic flow develops in

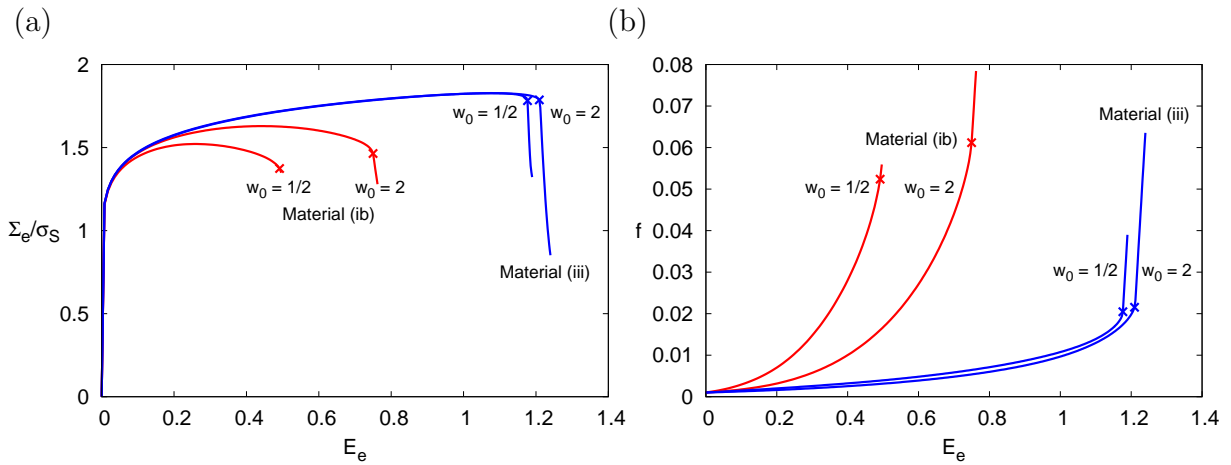


Figure 21: Combined effects of void shape and matrix anisotropy. Cell model results for initially prolate ($w_0 = 2$) and oblate ($w_0 = 1/2$) voids in a transversely isotropic matrix material (Table 2) for $T = 1$. (a) Effective stress, Σ_e , normalized by the matrix yield stress for uniaxial loading along \mathbf{e}_S , versus effective strain, E_e . (b) void volume fraction versus E_e . Adapted from (Keralavarma et al., 2010).

the matrix, the effect of plastic anisotropy was found to be even more subtle than discussed above. Keralavarma et al. (2010) identified certain types of plastic anisotropy that lead to plastic flow localization under the axisymmetric loading configurations considered. For pronounced anisotropies, localization was found to take place in inclined bands, i.e., in conical shear bands. The onset of the latter led to a faster decay of the stress bearing capacity of the unit cell but precluded the transition to the uniaxial straining deformation mode, which was invariably found in all previous cell model studies (with the known

exception for $T = 1/3$).

Cell model analyses have also been carried out with a more realistic description of matrix plasticity. Notable among these are the studies using crystal plasticity models by Orsini and Zikry (2001); Horstemeyer et al. (2000); Potirniche et al. (2006) and Yerra et al. (2010). In the latter two studies, the rate of void growth in single crystals was found to be strongly affected by the crystal orientation. In particular, the findings by Yerra et al. (2010) were generally consistent with the results above based on the phenomenological Hill criterion.

Most cell model studies conducted to date have concentrated on axisymmetric loadings with a major axial stress, i.e., $\Sigma_{33} > \Sigma_{11}$ or $\rho < 1$; see Eq. (1). In fact, the same stress triaxiality ratio T can be realized under axisymmetric conditions for a major radial stress, i.e., for a value of ρ greater than unity. Stress states of that type may be encountered in thick-walled pressure vessels with internal cracks parallel to the walls. Gologanu et al. (1994b) investigated the case $\rho > 1$ to quite some detail; also see (Gologanu et al., 2001a). They discovered that plastic flow localization in the cell occurs in the axial ligament, not the radial ones. As a consequence, void coalescence and plastic ruin takes place in columns, as opposed to layers in the case $\rho < 1$. Some of their results will be shown in Section 7. While this behavior is reminiscent of the observations of necklace coalescence (see Fig. 8b and Fig. 9d), there are important differences. In the cell model, this mode of coalescence in columns leads to significant reduction in the overall load bearing capacity of the cell. In the experiments, necklace coalescence is detrimental only if it leads to delamination, which is inherently a 3D process, or under strain path changes. Also, necklace coalescence was observed under a major axial stress $\rho < 1$ while the cell model predictions of Gologanu et al. (2001a) are for $\rho > 1$. Cell model studies for nonspherical cavities subjected to stress states with $\rho > 1$ would provide a broader perspective. It is likely indeed that the transition from coalescence in layers to coalescence in columns is not only affected by the stress state but also by the microstructure, namely the void aspect ratio, and its orientation relative to the loading.

In fact the distinction between the cases $\rho < 1$ and $\rho > 1$ amounts to investigating the effect of the third invariant of the stress tensor, or equivalently the Lode parameter. For arbitrary loadings, the latter is defined as:

$$\mu = \sqrt{3} \tan \theta = \frac{2\Sigma_{\text{II}} - \Sigma_{\text{I}} - \Sigma_{\text{III}}}{\Sigma_{\text{I}} - \Sigma_{\text{III}}} \quad (6)$$

where $\Sigma_{\text{I}} \geq \Sigma_{\text{II}} \geq \Sigma_{\text{III}}$ denote the principal stresses and θ is the Lode angle such that $\cos(3\theta) = (27/2) \det(\mathbf{\Sigma}'/\Sigma_e)$. Thus, the axisymmetric cell model results shown in Figs. 16–21 correspond to $\mu = -1$, irrespective of the stress triaxiality ratio T . On the other hand, the analyses of Gologanu et al. (2001a) correspond to the case $\mu = +1$, also known as generalized compression because it consists of a compressive axial load $\Sigma_{33} - \Sigma_{11}$ superposed onto a hydrostatic stress of magnitude Σ_{11} .

Cell model studies addressing the effect of the Lode parameter include those of Benzerga and Besson (2001) under axisymmetric loadings and the 3D analyses of Zhang et al. (2001) and Gao and Kim (2006) who considered 3D loadings and thus were able to explore values of μ other than ± 1 . Analyses accounting for superposed shear will be discussed below. In fact the trends obtained in the 3D calculations fall within the bounds of the axisymmetric calculations (see e.g., Fig. 9 of Gao and Kim (2006), where the bounds

$\theta = \pm 30^\circ$ correspond to $\mu = \pm 1$). It thus suffices to focus on the extremes $\mu = \pm 1$. Fig. 22 compares the cell model responses obtained by Benzerga and Besson (2001) for $\mu = +1$ with those corresponding to $\mu = -1$ for an isotropic matrix material and two anisotropic materials. The results for $\mu = -1$ were already shown in Fig. 20, except for the material labeled (i), which is similar to (ib) from Table 2 but with $h_4 = h_5 = 3.667$. For the isotropic matrix, the effect of the Lode parameter on void growth is not negligible.

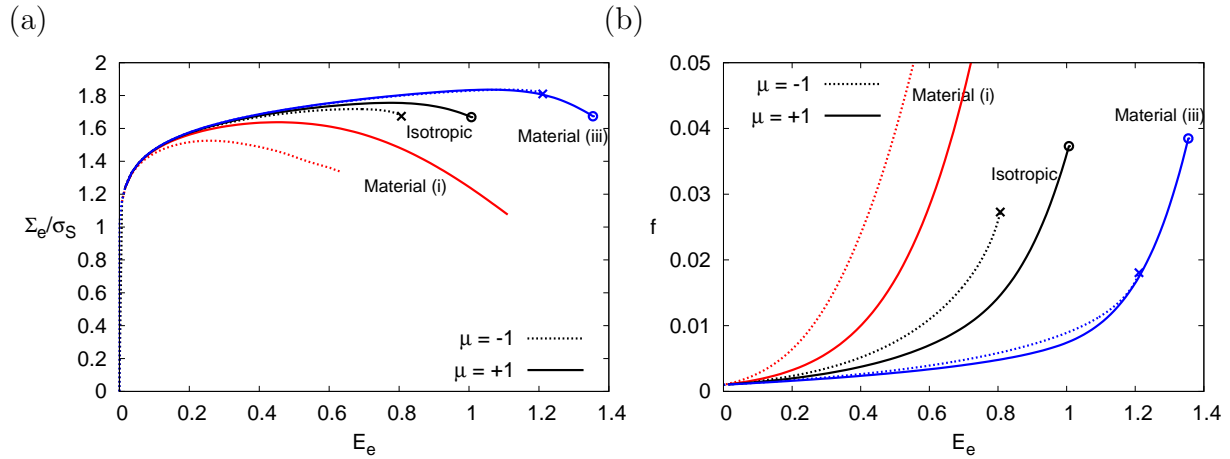


Figure 22: Effect of the Lode parameter μ . Cell model results for an initially spherical void in a transversely isotropic matrix material (Table 2; see text) for $T = 1$. (a) Effective stress, Σ_e , normalized by the matrix yield stress, versus effective strain, E_e . (b) Void volume fraction versus E_e . The onset of localization in the ligament is marked either by a symbol \times (coalescence in layers) or a symbol \circ (coalescence in columns). Replotted with corrections from Fig. 8 of (Benzerga and Besson, 2001).

Plastic anisotropy in matrix flow may exacerbate this effect, as in material (i), or annihilate it altogether, as in material (iii). The most important effect of the Lode parameter is on the mode of void coalescence, as first evidenced by Gologanu et al. (2001b,a). Their main findings is that void coalescence takes place in layers for $\mu = -1$ and in columns for $\mu = +1$. This applies to initially spherical voids and most likely to nonspherical voids, but to a limited extent. Also, their calculations were for isotropic distributions of voids, i.e., $\lambda_0 = 1$. It is likely that coalescence in columns would occur for $\lambda_0 < 1$, even if $\mu = -1$, i.e., for $\Sigma_{33} > \Sigma_{11}$.

The 3D cell model analyses of Barsoum and Faleskog (2007b) and Leblond and Mottet (2008) provide interesting trends under combined tensile and shear loadings and complete the above picture to some extent. They used periodic boundary conditions to accommodate the kinematics in shear. For instance, Barsoum and Faleskog (2007b) investigated the range $-1 \leq \mu \leq 0$ for fixed $T = 1$. Based on their main Fig. 6, the effect of the Lode parameter is weak for $-1 \leq \mu \leq -0.33$, at least when put in perspective of other effects due to the microstructural and loading parameters discussed so far. The most important finding corresponds to the case $\mu = 0$. There is little void growth in that case. However, plastic localization takes place in a narrow band and leads to softening in the overall response. Although their main results were derived for a high level of initial

porosity ($f_0 = 0.018$) and for a non-hardening material (thus promoting localization), their finding points to an important change in the localization of plastic flow, which is yet another mode of void coalescence. This change is effected by the Lode parameter μ . Similar trends were obtained by Leblond and Mottet (2008) using $f_0 = 0.02$. The effect of the Lode parameter on void growth and coalescence will be further analyzed in Section 7.

More recently, Tvergaard (2009) analyzed specifically the behavior of cylindrical voids in a shear field under plane strain loading. Using periodic boundary conditions and a remeshing technique, he simulated contact stresses arising from void closure representing frictionless sliding in an approximate way. Without contact stresses, the void would rotate and close into a penny-shaped crack so that the effective cell response would be identical to that of the dense matrix. However, with contact stresses included a maximum overall shear stress is predicted thus suggesting a mechanism for failure by plastic flow localization under shear dominated loadings. Scheyvaerts et al. (2010) also studied the behavior of initially spheroidal voids in a shear field for different initial orientations of the spheroid. In particular, they analyzed the evolution of void orientation induced by large plastic deformations.

In structural materials, voids originate from inclusions so that the behavior in a shear field is expected to be strongly affected by the void-inclusion interaction. Cell model analyses of this problem were carried out by Siruguet and Leblond (2004) for initially spherical voids under low stress triaxialities in the range $0 \leq T \leq 2/3$. Some of their results were given earlier in Fig. 15.

3.2.2 Elasto-Viscoplastic Matrix

We now briefly present some results obtained by Flandi and Leblond (2005b) in the viscoplastic case, using the SYSTUS FE software developed by ESI Group. The cell considered is a cylinder with circular basis and initially equal diameter and height ($\lambda_0 = 1$), containing an initially spherical void ($w_0 = 1$). The material behavior is described by plastic flow rule (2) along with the Norton law (4). The calculations use the values $\sigma_0 = 1$ and $\dot{\epsilon}_0 = 1$; this is equivalent to normalizing stresses and strain rates through division by σ_0 and $\dot{\epsilon}_0$ respectively. The elastic constants used are the same as above.

The loading is axisymmetric with predominant axial stress ($\Sigma_{11} = \Sigma_{22} < \Sigma_{33}$, other $\Sigma_{ij} = 0$). The values of the radial displacement on the lateral surface and the vertical displacement on the top are adjusted at each step so as to ensure a constant macroscopic triaxiality T and a constant macroscopic axial rate of deformation D_{33} . A value of unity is conventionally adopted for D_{33} ; results for other values can be obtained through use of the homogeneity property of the constitutive law.

Figure 23 presents typical results obtained for $T = 1$, $f_0 = 0.0104$, and three values of n , 3, 5 and 10, thus illustrating the influence of Norton's exponent. This figure shows the macroscopic equivalent stress Σ_e and the porosity f versus the macroscopic equivalent strain E_e . The figure also contains results of a predictive model, which will be presented in Section 6.5. The influence of the Norton exponent can be seen to be rather modest during the growth phase, but quite important during the coalescence phase, marked by a quick decrease of the equivalent stress and a quick increase of the porosity; the higher the value of n , the sharper (and earlier) the onset of coalescence. This can be qualitatively

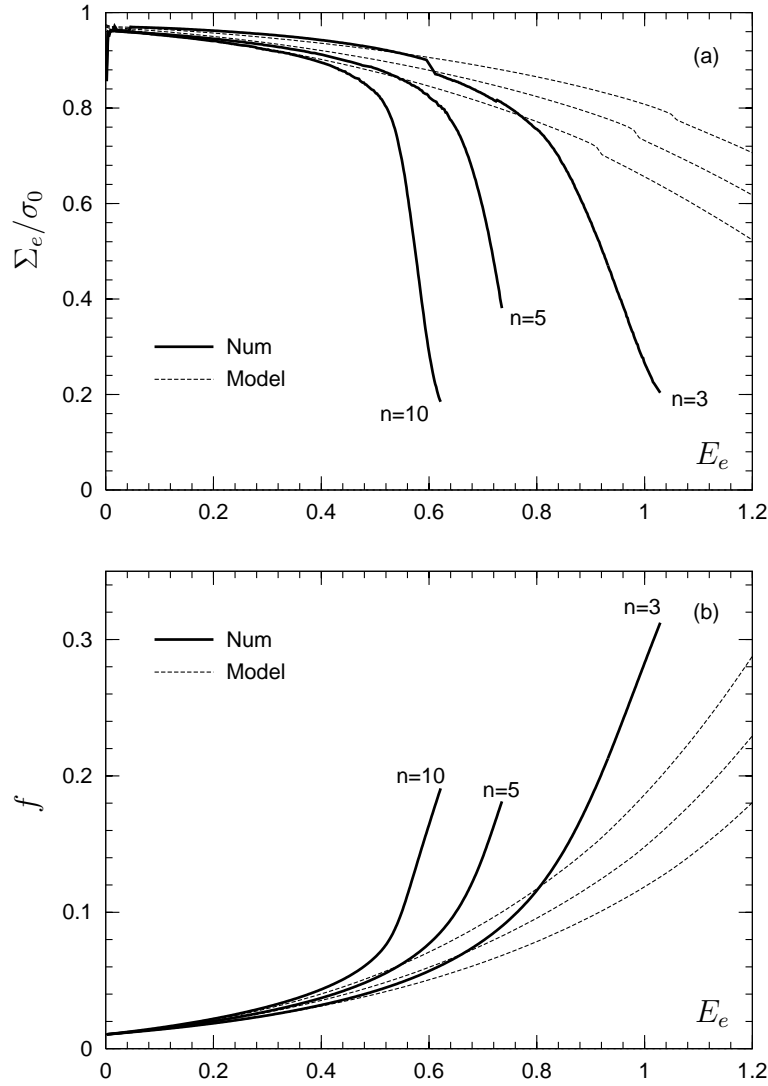


Figure 23: Influence of Norton's exponent. Cell model results (solid lines) for $T = 1$, $f_0 = 0.0104$ and $w_0 = 1$. (a) Normalized effective stress versus effective strain, E_e ; (b) porosity versus E_e . Adapted from (Flandi and Leblond, 2005b).

explained as follows. In the plastic case ($n = +\infty$), the onset of coalescence corresponds to a sudden concentration of the rate of deformation in the horizontal ligaments linking neighboring voids, the horizontal layers separating these ligaments in the vertical direction becoming suddenly elastic. As a result, the overall deformation mode becomes a vertical extension with almost no lateral shrinkage. In the viscoplastic case ($n < +\infty$), the same phenomenon occurs, but the transition from the pre-coalescence phase to the coalescence phase is more gradual because viscoplastic flow can never completely cease in the horizontal layers separating the inter-void ligaments, at least for the Norton law without threshold considered here.

4 Void Nucleation and Damage Initiation

With the experimental facts (Section 2) and cell model studies (Section 3) as background, we present in this and the next three sections general formulations of continuum models of void nucleation, growth and coalescence.

Within the range of applicability of a continuum approach to void nucleation, Argon and co-workers proposed the following criterion (Argon et al., 1975; Argon, 1976):

$$\sigma_I + \Sigma_m = \min(\sigma^d, \sigma^c) \quad (7)$$

where σ_I is the maximum principal (local) stress and Σ_m the mean normal (remote) stress as above. Argon (1976) developed approximate expressions for σ_I for various particle geometries under a remote shear stress, then assumed that the effect of Σ_m can be modeled through a simple superposition. Also, σ^d and σ^c are the interface strength and brittle strength of the particle, respectively. They do not directly represent the fundamental interface cohesive strength or ideal particle strength, rather some effective measures of strength. These material parameters can be inferred from experimental measurements such as those of Argon and Im (1975). For a summary of earlier works and views on void nucleation see (Argon et al., 1975).

Beremin (1981a) proposed an improved model that accounts for the plastic strain incompatibility between matrix and inclusion and, by the same account, for particle shape effects. The basic form of their criterion writes:

$$\sigma_I = \Sigma_I + \hat{\sigma}_I = \min(\sigma^d, \sigma^c)$$

where Σ_I may be viewed as the remote maximum principal stress and $\hat{\sigma}_I$ is a polarization stress arising in the inclusion due to strain incompatibility. Using an extension of Eshelby's theory for ellipsoidal inclusions in a plastically deforming matrix (Berveiller and Zaoui, 1979), the final, approximate form of their criterion is:

$$\Sigma_I + k(\Sigma_{eq} - \sigma_0) = \min(\sigma^d, \sigma^c) \quad (8)$$

where Σ_{eq} is the remote von Mises effective stress, σ_0 is the initial yield strength of the matrix and k is a factor that depends on particle shape and loading orientation. Defining w^p as the particle aspect ratio in the case of spheroidal particles, Fig. 24 depicts typical loading configurations for both prolate and oblate particles. Table 3 summarizes the expressions taken by $k(w^p)$ for some special limit cases.

It is implicit in both equations (7) and (8) that the stress fields are considered as homogeneous within the particle. As a consequence, these criteria distinguish between decohesion and particle cracking only through the material-dependent critical stresses σ^d and σ^c , not through the inhomogeneous distribution of mechanical fields. It is known, however, that for a matrix undergoing plastic deformation the stress and strain fields within the elastic particle are not uniform. Accurate numerical solutions have been derived by Wilner (1988) for spherical elastic particles and by Lee and Mear (1999) for prolate spheroidal particles in an infinite elasto-plastic strain-hardening matrix under axisymmetric proportional loadings. These authors used a procedure based on Hill's (1956) minimum principle for displacements, as modified by Budiansky et al. (1982) and a deformation theory of plasticity. Their approach is thus a kinematic one, as opposed to the

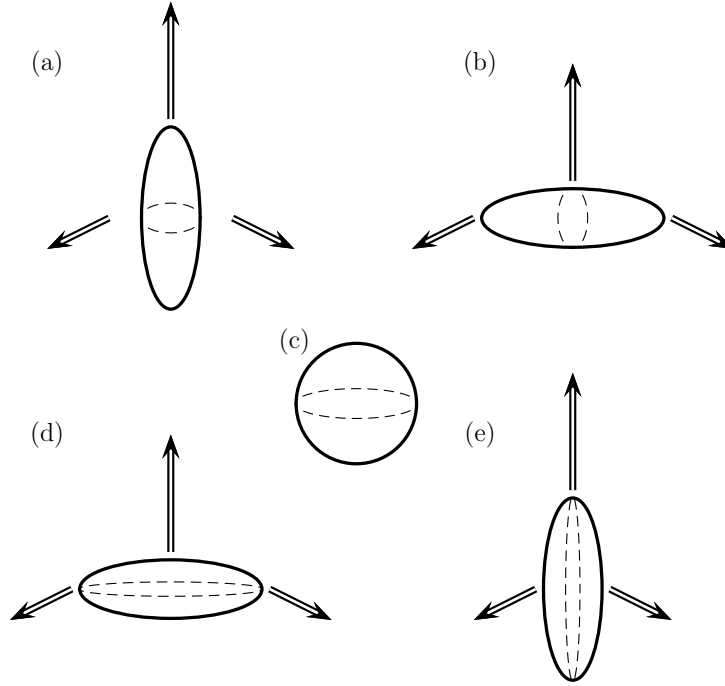


Figure 24: Loading configurations for (a),(b) prolate, (c) spherical and (d),(e) oblate particles corresponding to Table 3.

static approach of Berveiller and Zaoui (1979). The outcome of Lee and Mear's analysis may be summarized in terms of stress concentration factors at the interface and in the particle, respectively defined by:

$$\kappa^I = \frac{\max(\sigma_{\eta\eta}|_{\eta=\eta_0})}{\Sigma_{33}}; \quad \kappa^P = \frac{\max(\sigma_I^P|_{\eta \leq \eta_0})}{\Sigma_{33}} \quad (9)$$

Here, Σ_{33} is the remote axial stress, i.e., aligned with the x_3 -axis of the particle, $\sigma_{\eta\eta}$ is the normal stress in a spheroidal coordinate system (η, β, φ) , σ_I^P is the major principal stress in the particle and $\eta = \eta_0$ defines the matrix–particle interface. It is clear from (9) that κ^I is a measure of the maximum tensile normal traction acting at the interface while κ^P is a measure of the maximum normal stress acting within the particle.

Dimensional analysis indicates that κ^I and κ^P should depend on the particle aspect ratio w^P , the remote stress triaxiality T , the modulus mismatch E^P/E , the matrix strain-hardening exponent N , Poisson's ratios and the matrix yield strength through the ratio σ_0/E . Lee and Mear (1999) investigated the influence of all but the last parameter. Poisson's ratios play only a minor role. For reference, $\kappa^I = \kappa^P$ in the case of a linearly elastic matrix since the stress field is then uniform within the particle (Eshelby, 1957). The salient features of the analysis are as follows:

- The interface stress concentration factor κ^I is strongly affected by the modulus mismatch at low strains. However, at larger strains it asymptotes to a constant which depends on the matrix hardening exponent, the particle aspect ratio and the stress triaxiality, but not on E^P/E . This behavior is illustrated in Fig. 25 under uniaxial loading ($T = 1/3$).

Particle shape	w^P	Loading orientation	k	Sketch
Fiber	$\gg 1$	axial	$\frac{2}{3} \left(-1 + \frac{1}{3} \frac{1 + 2w^{P2}}{2 \ln(2w^P - 1) - 1} \right)$	(a)
		transverse	$\frac{1}{2} \left(1 + \frac{1}{9} \frac{1 + 2w^{P2}}{2 \ln(2w^P - 1) - 1} \right)$	(b)
Sphere	1		1	(c)
Disk	$\ll 1$	axial	$\frac{2}{3} \left(-1 + \frac{4}{3\pi} \frac{1}{w^P} \right)$	(d)
		transverse	$\frac{2}{3} \left(-1 + \frac{10}{3\pi} \frac{1}{w^P} \right)$	(e)

Table 3: Expressions taken by the shape factor $k(w^P)$ in (8) for some special cases of prolate and oblate particles, as sketched in Fig. 24.

- The asymptotic value of κ^I increases with increasing w^P , with decreasing T or with increasing N , the magnitudes of the effect being in that order. For example, the effect of particle aspect ratio is clear when comparing Fig. 25a with Fig. 25b. Also, Fig. 26a illustrates the difference between uniaxial loading and some triaxial loading.
- The particle stress concentration factor κ^P does not exhibit an asymptotic behavior, in general. It increases with increasing w^P , with decreasing T or with increasing E^P/E . It is weakly sensitive to the matrix hardening exponent.
- Stress concentration in the particle is always greater than that at the interface, as soon as plastic flow sets in. The fact that $\kappa^P > \kappa^I$ is illustrated in Fig. 26b for two values of w^P . The difference between κ^P and κ^I is accentuated by a large particle aspect ratio (Fig. 26b) or an increase in material non-linearity (larger N).
- Both stress concentration factors decrease with increasing triaxiality but not at the same rate. The ratio κ^P/κ^I is a decreasing function of T . Therefore, as T is increased void nucleation will have a greater tendency to occur by interfacial decohesion than by particle fracture.

Analyses of ductile fracture are often based on the view that void nucleation is a continuous process. In the case of particle–matrix debonding, the prediction of an asymptotic behavior for the interfacial stress concentration factor κ^I in Fig. 26 indicates the opposite. What is of particular significance in this regard is the fact that the asymptotic behavior of κ^I is reached at strains smaller than 0.05. This suggests that if decohesion does not take place in the early stages of deformation, it most likely will not occur thereafter.

It is tempting to make use of Lee and Mear’s concentration factors to improve upon the Argon–Beremin criteria. The following concurrent void nucleation conditions are

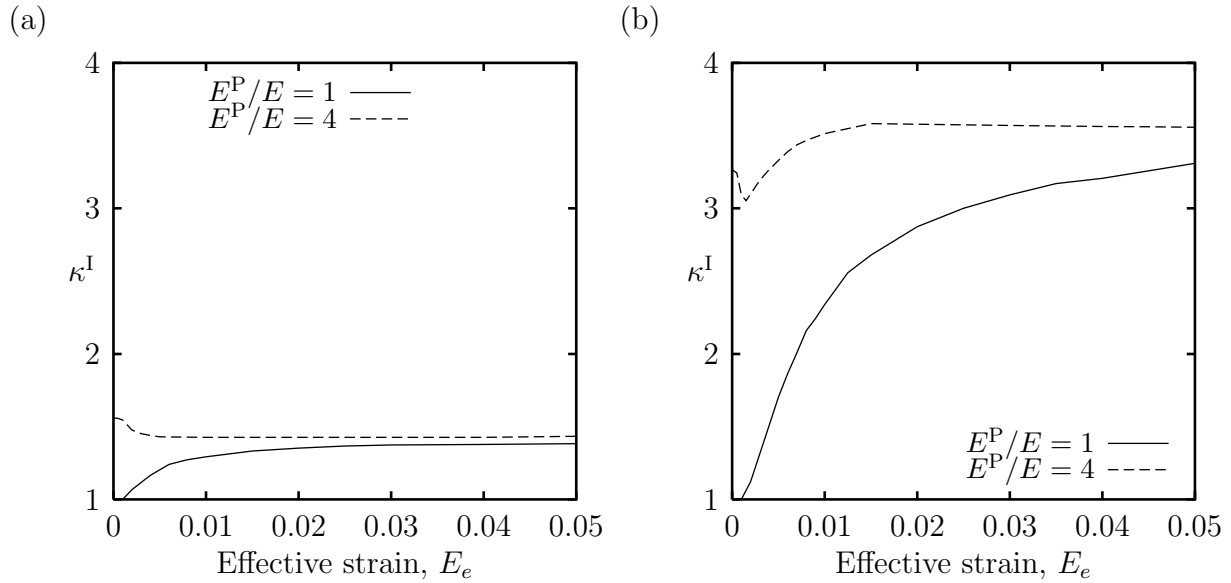


Figure 25: Particle–matrix interface stress concentration factor κ^I in (9) versus effective strain E_e for an elasto-plastic matrix with $N = 0.2$ under remote uniaxial loading and two values of the modulus mismatch E^P/E (a) Spherical particle, $w^P = 1$; and (b) Elongated particle with $w^P = 7$. Adapted from (Lee and Mear, 1999).

formulated:

$$\kappa^I \Sigma_I = \sigma^d \quad \text{versus} \quad \kappa^P \Sigma_I = \sigma^c \quad (10)$$

for interfacial debonding and particle cracking, respectively, whichever occurs first. Predicting the specific mode of void nucleation presents the advantage of identifying the initial void state. As shown in the tomographs of Fig. 7, particle cracking leads to the formation of a penny-shaped crack whereas interfacial debonding leads to the formation of a void having the same volume as that of the inclusion. While criterion (10) is superior in principle to criteria (7) and (8), closed form expressions for the stress concentration factors are not known at present. For practical purposes, the Beremin model provides an adequate micromechanical description of the void nucleation condition. It matches the trends of the Lee–Mear analysis regarding the effect of particle aspect ratio and stress triaxiality. In addition, it accounts for cases of transverse loading and oblate particles, which are not addressed in the Lee–Mear analysis.

When void nucleation is by particle fracture, criteria (8) or $(10)_2$ are adequate since the normal stress is roughly uniform over the meridian plane (Lee and Mear, 1999). However, interfacial debonding is a process with an initiation and a propagation stage, as evidenced by the cell model studies (Needleman, 1987). Depending on the level of triaxiality, void locking by the particle may prevent complete debonding, typically for $T < 2/3$ (Siruguet and Leblond, 2004) (also see Fig. 7b). Even at higher triaxiality, the strain range over which debonding takes place may be significant (Needleman, 1987). Under such circumstances, criterion $(10)_1$ may be adequate for initiation but not for complete void formation. To illustrate this, Fig. 27 shows the distribution of the interfacial

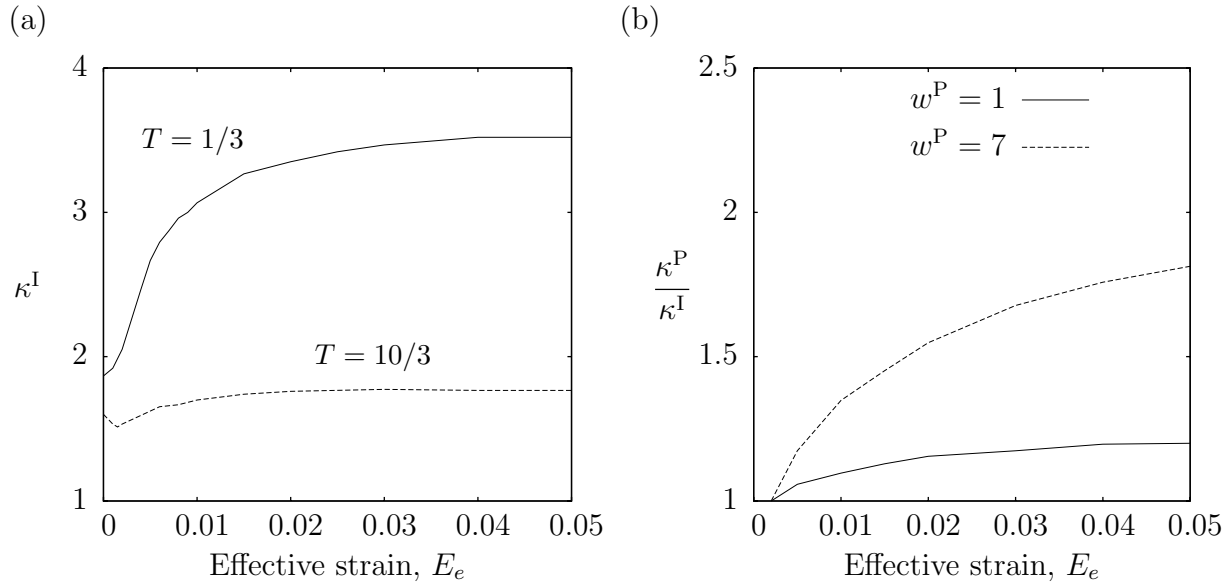


Figure 26: (a) Interface stress concentration factor κ^I versus effective strain E_e for an elasto-plastic matrix containing a prolate particle with $w^P = 7$ using $N = 0.2$ and $E^P/E = 2$ and two values of stress triaxiality T . (b) Ratio of the particle to interface stress concentration factors κ^P/κ^I in (9) versus E_e for uniaxial loading ($T = 1/3$), $N = 0.1$ and $E^P/E = 2$ and two particle aspect ratios. Adapted from (Lee and Mear, 1999).

normal traction as a function of the angle ϕ measured from the x_3 axis, as predicted by Lee and Mear (1999). The results are shown for two values of the particle aspect ratio and two triaxialities. Fig. 28 depicts the distributions qualitatively for ease of visualization. Under uniaxial loading (Fig. 27a), if local debonding initiates it is much more likely to propagate for spherical particles than for elongated ones (also see the sketch in Fig. 28a). For moderate to high remote triaxialities (Fig. 27b), the interfacial normal traction is everywhere tensile and more uniformly distributed, irrespective of the particle aspect ratio. Therefore, once debonding initiates it will likely continue to complete separation.

The effect of particle size, which was long debated, is now understood as the consequence of local particle volume fraction fluctuations leading to increased interactions among particles. Above a certain particle size, there is no absolute particle size effect on the plastic strain required for void nucleation by debonding. This does not mean that particle size does not matter at all. (i) There is a minimum size below which interfacial cracks are no longer energetically favorable (Tanaka et al., 1970; Argon et al., 1975). This critical size was initially estimated at about 25 nm but is likely to be above 100 nm (Montheillet and Gilormini, 1986). (ii) For particle cracking, a size effect is associated with a Weibull-like distribution of defects in the particles affecting their brittle strength. (iii) For very small particles, say below 1 μm , a size effect in debonding by gradual decohesion may emerge because of the cohesive length.

While void nucleation models based on critical stress conditions and stress concentration factors are more basic, some practical difficulties are associated with them. One example is the incomplete decohesion due to stress state or loading orientation. In prac-

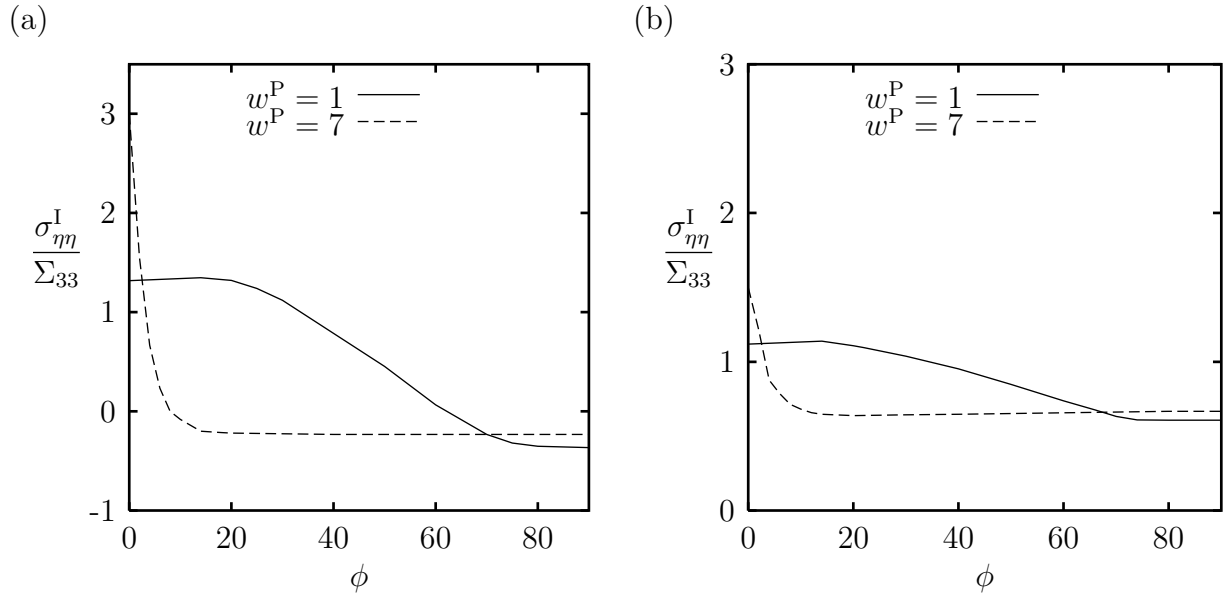


Figure 27: Interfacial normal traction, normalized by remote axial stress Σ_{33} , versus the angle ϕ measured from the x_3 -axis. Results are shown for two particle aspect ratios, $N = 0.1$, $E^P/E = 2$ at an effective strain of $E_e = 0.03$. (a) Uniaxial loading ($T = 1/3$); and (b) $T = 10/3$. Adapted from (Lee and Mear, 1999).

tice, continuum void nucleation models have been developed and gained wide attention (Chu and Needleman, 1980). Their formulation will be better appreciated in the context of porous ductile materials below (Section 6.1.2). Other models have attempted to account for more complex stress state effects, linking in particular the void nucleation condition with the material toughness, albeit on phenomenological grounds (Horstemeyer and Gokhale, 1999).

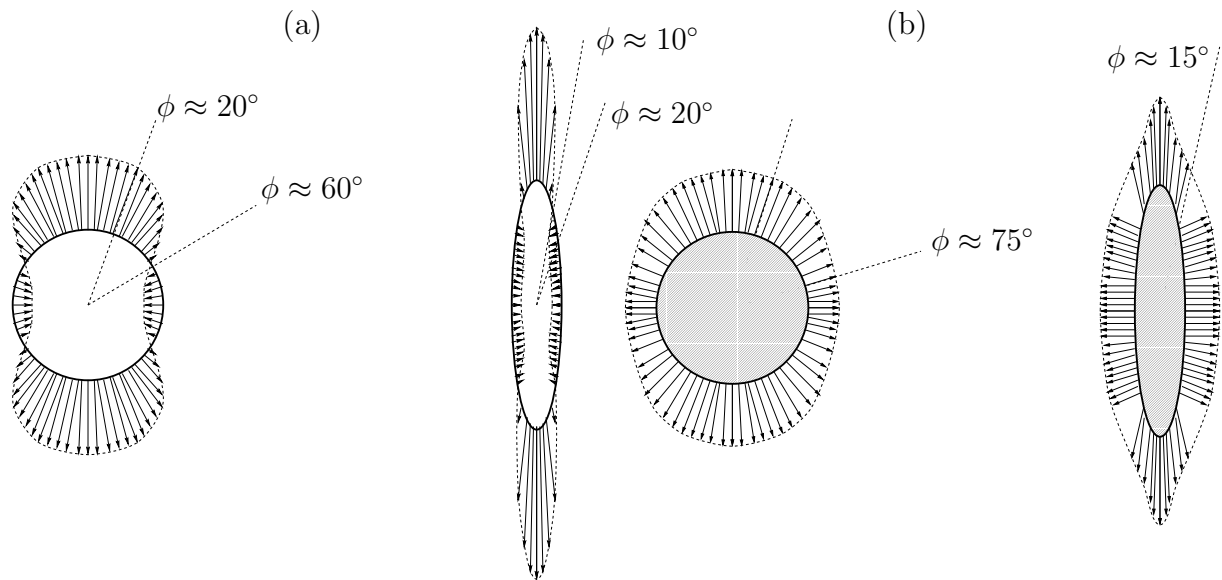


Figure 28: Sketch showing the distribution of the interfacial normal traction for elastic particles in an elasto-plastic matrix with hardening under (a) uniaxial loading ($T = 1/3$) and (b) triaxial loading ($T = 10/3$) for two particle shapes. Special angles indicate either a maximum value, a transition to compressive tractions or a saturation of the traction, consistent with the results in Fig. 27. Traction vectors may not be drawn normal to interfacial regions of high curvature. Adapted from (Benzerga, 2000).

5 Fundamentals for Porous Ductile Solids

Elements from the theories of homogenization and limit analysis are briefly recalled following Leblond (2003). For a comprehensive coverage of these subjects the reader may refer to specialized texts and monographs (Prager and Hodge, 1951; Suquet, 1982; Nemat-Nasser and Hori, 1990). The objective here is to provide the backbone for a unifying description of the continuum models of porous ductile solids, which are covered in Sections 6 and 7. For a given constitutive description at the microscale, i.e., a scale at which each void is resolved, the question addressed is that of what relationship exists between stress and strain at the macroscale, i.e. one which contains many voids. Of particular importance is how microstructural information (usually void population attributes and matrix properties) enters the macroscopic constitutive laws and how it evolves in the context of porous ductile solids.

5.1 Homogenization

Consider a representative volume element (RVE) of a porous ductile solid (Fig. 29) consisting of voids, with traction-free boundaries, embedded in a matrix. Let Ω denote the total domain and ω that occupied by the voids. For notational convenience we shall also use Ω and ω for their volume measures. Assume that none of the voids ends on the external surface $\partial\Omega$ of the domain so that $\partial\Omega \cap \partial\omega = \emptyset$. The void volume fraction, or porosity, is thus $f = \omega/\Omega$. Large plastic deformations accompany cavity enlargement in ductile solids so that a formulation accounting for finite deformations is necessary. We shall adopt a eulerian description with $\boldsymbol{\sigma}$ and \mathbf{d} denoting the Cauchy stress and the rate of deformation, respectively. The results of this section remain valid if other work-conjugate measures of stress and strain are employed.

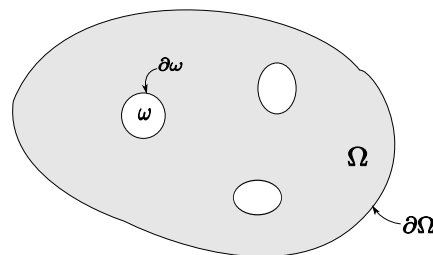


Figure 29: Sketch of a porous representative volume element, Ω , containing voids occupying volume ω .

In the voids, extensions of $\boldsymbol{\sigma}$ and \mathbf{d} are adopted as follows. The stress field is taken to be zero there, consistent with the condition of traction-free boundaries, while the velocity field \mathbf{v} associated with \mathbf{d} is extended in some arbitrary but \mathcal{C}^1 manner.

Presented in what follows are general results from the Hill–Mandel homogenization theory (Hill, 1967; Mandel, 1964). There are two possible approaches, depending on the type of boundary conditions assumed for the RVE. It is worth noting that there are other types of boundary conditions than those considered below, notably periodic boundary conditions and mixed boundary conditions such as those used in the cell model studies. More on this will be discussed in Section 7.

5.1.1 Kinematic Approach

Definitions Kinematic boundary conditions are imposed whereby the RVE is subjected to a uniform rate of deformation on its boundary, i.e.,

$$\forall \mathbf{x} \in \partial\Omega, \quad v_i = D_{ij}x_j \quad (11)$$

where \mathbf{v} is the microscopic velocity field and \mathbf{D} is a specified second-rank symmetric tensor. Such boundary conditions would, for example, follow from a uniform deformation rate within Ω .

Under such circumstances, define the macroscopic stress as the volume average of the microscopic stress $\boldsymbol{\sigma}$:

$$\Sigma_{ij} \equiv \langle \sigma_{ij} \rangle_{\Omega}, \quad (12)$$

where the notation $\langle \cdot \rangle_{\Omega}$ stands for volume averaging over Ω . Note that (12) is equivalent to

$$\Sigma_{ij} = (1 - f) \langle \sigma_{ij} \rangle_{\Omega \setminus \omega}, \quad (13)$$

where f is the porosity as above and $\Omega \setminus \omega$ denotes the domain occupied by the dense matrix.

Integral Expression of \mathbf{D} Using Green's theorem, boundary condition (11) and kinematics, along with the extension of \mathbf{v} in the voids, it is straightforward to show that the imposed boundary deformation rate, \mathbf{D} , is equal to the volume average of the microscopic deformation rate, \mathbf{d} , over the volume of the entire RVE

$$D_{ij} = \langle d_{ij} \rangle_{\Omega} \quad (14)$$

For this reason \mathbf{D} is called the *macroscopic rate of deformation*. Property (14) remains valid regardless of the extension chosen for the velocity field within the voids, provided that the velocity field is continuous across $\partial\omega$. However, an expression similar to (13) cannot be written for \mathbf{D} for it is clear that the porous material is compressible even if the matrix is not. In other terms, the average of \mathbf{d} over the volume of the voids ω is not zero and leads to a dilational component in \mathbf{D} .

Hill–Mandel Lemma Let \mathbf{v} be a kinematically admissible velocity field and $\boldsymbol{\sigma}$ a statically admissible stress field. In the kinematic approach, these conditions mean that \mathbf{v} obeys boundary conditions (11) and that $\boldsymbol{\sigma}$ is a self-equilibrating field (i.e., $\sigma_{ij,j} = 0$ in $\Omega \setminus \omega$) obeying the traction-free boundary conditions $\sigma_{ij}n_j = 0$ on $\partial\omega$, where \mathbf{n} is the unit normal. Adopting the above extensions of these fields into the voids, the following result is established:

$$\langle \sigma_{ij} d_{ij} \rangle_{\Omega} = \Sigma_{ij} D_{ij} \quad (15)$$

In this lemma, $\boldsymbol{\sigma}$ and \mathbf{d} need not be related through a constitutive relation.

Proof: The volume average is given by

$$\begin{aligned}
\frac{1}{\Omega} \int_{\Omega} \sigma_{ij} d_{ij} \, dV &= \frac{1}{\Omega} \int_{\partial\Omega} \sigma_{ij} n_j v_i \, dS && \text{(principle of virtual work)} \\
&= \frac{1}{\Omega} \int_{\partial\Omega} \sigma_{ij} n_j D_{ik} x_k \, dS && \text{(boundary condition (11))} \\
&= \frac{1}{\Omega} \int_{\Omega} (\sigma_{ij} D_{ik} x_k)_{,j} \, dV && \text{(divergence theorem)} \\
&= \frac{1}{\Omega} \int_{\Omega} (\sigma_{ij} D_{ik} \delta_{kj}) \, dV && \text{(equilibrium)} \\
&= \Sigma_{ij} D_{ij} && \text{(definition of } \Sigma)
\end{aligned}$$

Consistent with the extensions of stress and velocity fields in the voids, the Hill–Mandel lemma (15) may also be stated as follows:

$$(1 - f) \langle \sigma_{ij} d_{ij} \rangle_{\Omega \setminus \omega} = \Sigma_{ij} D_{ij} \quad (16)$$

5.1.2 Static Approach

Definitions Static boundary conditions are now considered of the form:

$$\forall \mathbf{x} \in \partial\Omega, \quad \sigma_{ij} n_j = \Sigma_{ij} n_j \quad (17)$$

where \mathbf{n} is the boundary unit normal and Σ is a specified second-rank symmetric tensor. Such boundary conditions would, for example, follow from a uniform stress within Ω .

Under these circumstances, define the macroscopic rate of deformation as the volume average of the microscopic one:

$$D_{ij} \equiv \langle d_{ij} \rangle_{\Omega}, \quad (18)$$

Definition (18) is independent of the chosen extension for \mathbf{v} in the voids since the volume average of \mathbf{d} over Ω is fully determined by values of the velocity on the external boundary $\partial\Omega$, as evidenced by application of the gradient theorem.

Hill–Mandel Lemma Let \mathbf{v} be a kinematically admissible velocity field and $\boldsymbol{\sigma}$ a statically admissible stress field. In the static approach, these conditions mean that \mathbf{v} is in fact arbitrary and that $\boldsymbol{\sigma}$ is a self-equilibrating field (i.e., $\sigma_{ij,j} = 0$ in $\Omega - \omega$) obeying the traction-free boundary conditions $\sigma_{ij} n_j = 0$ on $\partial\omega$ as well as boundary conditions (17). Then,

$$\langle \sigma_{ij} d_{ij} \rangle_{\Omega} = \Sigma_{ij} D_{ij} \quad (19)$$

The result is formally the same as in (15) and may be written in the form (16) as well.

Proof: After applying the principle of virtual power as in the proof of (15) one gets

$$\begin{aligned}
 \frac{1}{\Omega} \int_{\partial\Omega} \sigma_{ij} n_j v_i \, dS &= \frac{1}{\Omega} \int_{\partial\Omega} \Sigma_{ij} n_j v_i \, dS && \text{(boundary condition (17))} \\
 &= \Sigma_{ij} \frac{1}{\Omega} \int_{\partial\Omega} \frac{1}{2} (v_i n_j + v_j n_i) \, dS && \text{(symmetry of } \Sigma) \\
 &= \Sigma_{ij} \frac{1}{\Omega} \int_{\Omega} \frac{1}{2} (v_{i,j} + v_{j,i}) \, dV && \text{(gradient theorem)} \\
 &= \Sigma_{ij} D_{ij} && \text{(definition of } \mathbf{D})
 \end{aligned}$$

Integral Expression of Σ Since lemma (19) holds for any velocity field of class \mathcal{C}^1 it applies in particular to a uniform deformation field $\mathbf{d} \equiv \mathbf{D}$. For such a field, $\Sigma : \mathbf{D} = \langle \sigma \rangle_{\Omega} : \mathbf{D}$. Since this is true for any choice of \mathbf{D} it follows that

$$\Sigma_{ij} = \langle \sigma_{ij} \rangle_{\Omega} \quad (20)$$

Note that, in the kinematic approach, one cannot derive the analogous averaging relation (14) from the Hill–Mandel lemma because a constant stress σ would not be statically admissible.

In summary, volume averaging equalities for Σ and \mathbf{D} are true for both types of boundary conditions, although they hold a different status. For example, (20) is a theorem in the static approach whereas (12) is a definition in the kinematic approach. Regardless, the Hill–Mandel lemma (19), or (15), holds with Σ and \mathbf{D} being volume averages of their microscopic counterparts, consistent with the adopted terminology of macroscopic stress and rate of deformation.

5.2 Limit Analysis

The choice of limit analysis as a framework to derive constitutive equations inevitably restricts the class of microscopic behaviors that can be considered. On the other hand, combined with the above results from homogenization theory, this framework presents the advantage of permitting a scale transition to be effectively operated. It delivers a format for the macroscopic constitutive behavior and provides the signature of microstructural information.

The dense matrix (Fig. 29) is here assumed to be incompressible, rigid–ideal plastic and to obey some yield criterion along with an associated flow rule. An example of such a matrix model would be J_2 flow theory. For a given matrix deformation field \mathbf{d} , the rate of plastic dissipation associated with it is defined as

$$\pi(\mathbf{d}) = \sup_{\sigma^* \in \mathcal{C}} \sigma_{ij}^* d_{ij} \quad (21)$$

the supremum being taken over all microscopic stresses that fall within the microscopic convex domain of reversibility \mathcal{C} . The matrix being incompressible, \mathbf{d} must be traceless, otherwise $\pi(\mathbf{d})$ would be infinite. Consider now a velocity field $\mathbf{v}(\mathbf{x})$ consistent with an arbitrary deviator field $\mathbf{d}(\mathbf{x})$ and kinematically admissible with \mathbf{D} . This means that either (11) or (18) is obeyed, depending on whether a kinematic or static approach is

followed. Also, consider a stress field $\boldsymbol{\sigma}$ in the matrix that is statically admissible with $\boldsymbol{\Sigma}$ and plastically admissible. The first condition means that the matrix stress field obeys (12) or (17) while the second means that $\forall \mathbf{x} \in \Omega, \boldsymbol{\sigma}(\mathbf{x}) \in \mathcal{C}$. By way of consequence, the product $\boldsymbol{\Sigma} : \mathbf{D}$ is bounded from above

$$\forall \mathbf{d}, \quad \boldsymbol{\Sigma} : \mathbf{D} \leq \langle \pi(\mathbf{d}) \rangle_{\Omega}. \quad (22)$$

This follows from application of the Hill–Mandel lemma (15) or (19) and definition (21). Appropriate extensions of stress and deformation fields in the voids were also assumed as in Section 5.1. The inequality above being true for arbitrary matrix deformation fields, a tighter upper bound is:

$$\boldsymbol{\Sigma} : \mathbf{D} \leq \Pi(\mathbf{D}) = \inf_{\mathbf{d} \in \mathcal{K}(\mathbf{D})} \langle \pi(\mathbf{d}) \rangle_{\Omega} \quad (23)$$

where $\mathcal{K}(\mathbf{D})$ denotes the set of kinematically admissible microscopic deformations. For example, in a kinematic approach

$$\mathcal{K}(\mathbf{D}) = \{ \mathbf{d} \mid \forall \mathbf{x} \in \Omega \setminus \omega, d_{kk} = 0 \text{ and } \exists \mathbf{v}, \forall \mathbf{x} \in \Omega, d_{ij} = \frac{1}{2}(v_{i,j} + v_{j,i}) \text{ and } \forall \mathbf{x} \in \partial\Omega, v_i = D_{ij}x_j \} \quad (24)$$

$\Pi(\mathbf{D})$ is called the macroscopic, or effective, plastic dissipation associated with \mathbf{D} .

Next, define \mathcal{C} as the set of *potentially* sustainable macroscopic stresses $\boldsymbol{\Sigma}$, i.e., such that there exists a microscopic stress field $\boldsymbol{\sigma}$ which is statically admissible with $\boldsymbol{\Sigma}$ and plastically admissible. It follows from what precedes that \mathcal{C} lies in the intersection of the semi-spaces defined by $\boldsymbol{\Sigma} : \mathbf{D} \leq \Pi(\mathbf{D})$, \mathbf{D} being a parameter. For a sufficiently broad class of matrix constitutive laws, it can be shown that the two sets are in fact identical, i.e.

$$\mathcal{C} = \{ \boldsymbol{\Sigma} \mid \forall \mathbf{D}, \boldsymbol{\Sigma} : \mathbf{D} \leq \Pi(\mathbf{D}) \} \quad (25)$$

Of particular interest is the boundary of this set, which is denoted $\text{fr}(\mathcal{C})$. The above equation implies that $\text{fr}(\mathcal{C})$ is the envelope of the hyperplanes $\boldsymbol{\Sigma} : \mathbf{D} = \Pi(\mathbf{D})$. Its parametric equations are thus

$$\begin{cases} \boldsymbol{\Sigma} : \mathbf{D} - \Pi(\mathbf{D}) = 0 \\ \boldsymbol{\Sigma} - \frac{\partial \Pi}{\partial \mathbf{D}}(\mathbf{D}) = 0 \end{cases} \quad (26)$$

But since $\Pi(\mathbf{D})$ is positively homogeneous of degree 1, Euler's relation implies that the first equation in (26) is included in the second. Therefore, the parametric equation of $\text{fr}(\mathcal{C})$ reduces to

$$\Sigma_{ij} = \frac{\partial \Pi}{\partial D_{ij}}(\mathbf{D}) \quad (27)$$

It remains to connect the set \mathcal{C} with the macroscopic elastic domain. At this juncture, it is necessary to invoke a classical result of limit analysis asserting that, when normality is obeyed, the set of potentially supportable macroscopic stresses coincides with that of actually sustainable ones. In other terms, every potentially supportable $\boldsymbol{\Sigma}$ can be attained in some actual mechanical evolution prior to possibly reaching a state of plastic collapse. Under these circumstances, it seems logical to identify the macroscopic domain of elasticity

with the set \mathcal{C} , now known to consist of attainable stresses. As a consequence, equation (27) defines the macroscopic, or effective, yield surface of the porous ductile material. In this identification, the macroscopic behavior is considered as purely elastic before $\text{fr}(\mathcal{C})$ is reached, which is only an approximation. In actuality, plastic flow takes place at some points before the overall limit load is attained.

In principle, elimination of \mathbf{D} from the parametric form (27) is possible since $\partial\Pi/\partial\mathbf{D}$ is positively homogeneous of degree 0. The equation of $\text{fr}(\mathcal{C})$ may thus be written as $\Phi(\mathbf{\Sigma}) = 0$ where Φ denotes an effective yield function.

If the microscopic plastic flow obeys Drucker's stability postulate, or equivalently Hill's principle of maximum plastic work, then application of the Hill–Mandel lemma permits to show that the same principle applies at the macroscale. Three classical consequences follow: (i) the macroscopic elastic domain \mathcal{C} is convex; (ii) the plastic rate of deformation belongs to the hypercone of normals to the effective yield surface $\text{fr}(\mathcal{C})$ at the current stress state; and (iii) if $\text{fr}(\mathcal{C})$ is smooth then the macroscopic flow rule obeys normality.

5.3 Viscoplastic Formulation

5.3.1 The Microscopic and Macroscopic Stress Potentials

We now consider some porous, nonlinear viscous material. The sound matrix is assumed to be rigid-viscoplastic and obey the Norton constitutive law without threshold introduced in Section 3.2.2 (equation (4)), rewritten here for convenience in the form

$$\mathbf{d} = \frac{\partial\psi}{\partial\boldsymbol{\sigma}}(\boldsymbol{\sigma}) \quad , \quad \psi(\boldsymbol{\sigma}) \equiv \frac{\sigma_0 \dot{\epsilon}_0}{n+1} \left(\frac{\sigma_{eq}}{\sigma_0} \right)^{n+1} \quad (28)$$

where $\psi(\boldsymbol{\sigma})$ is the *microscopic viscous stress potential*. This constitutive law includes, as special cases, linearly viscous materials for $n = 1$, and rigid-ideal plastic materials for $n = +\infty$.

The homogenization problem consists here of finding the *macroscopic viscous stress potential* $\Psi(\mathbf{\Sigma})$, where $\mathbf{\Sigma}$ denotes the macroscopic stress tensor. General properties of this potential have been stated many times, see for instance (Leblond et al., 1994b), and are as follows. The macroscopic potential is the volume average of the microscopic potential. It is convex and positively homogeneous of degree $n+1$ with respect to $\mathbf{\Sigma}$, just as ψ is convex and positively homogeneous of degree $n+1$ with respect to $\boldsymbol{\sigma}$. It satisfies a variational property analogous to (23), but this property need not be stated here. Once it is known, the macroscopic rate of deformation tensor \mathbf{D} follows from the equation

$$\mathbf{D} = \frac{\partial\Psi}{\partial\mathbf{\Sigma}}(\mathbf{\Sigma}). \quad (29)$$

5.3.2 The Gauge Surface, the Gauge Function and the Gauge Factor

The *gauge surface* \mathcal{S} of the porous material, in the space of macroscopic stress tensors, was defined by Leblond et al. (1994b) as the following isopotential surface:

$$\mathcal{S} \equiv \left\{ \mathbf{S}, \Psi(\mathbf{S}) = \frac{\dot{\epsilon}_0}{(n+1)\sigma_0^n} \right\}. \quad (30)$$

The *gauge function* is any convex function $\bar{\Psi}(\mathbf{S})$ providing the equation of the gauge surface in the form

$$\mathbf{S} \in \mathcal{S} \iff \bar{\Psi}(\mathbf{S}) = 0. \quad (31)$$

The notions of gauge surface and gauge function are interesting in that, as remarked by Leblond et al. (1994b), it is much easier to find a good approximation for the gauge function than for the macroscopic viscous potential. The difficulty with the viscous potential is to respect both its properties of convexity and positive homogeneity. These properties restrict explicit, analytical formulae for the potential to forms which are somewhat too simple to be physically realistic over the whole range of possible values of the geometric and mechanical parameters. In contrast, the sole, much less stringent condition that must be satisfied by the gauge function is convexity.

The *gauge factor* is defined in the following way. Since Ψ is a positively homogeneous function of Σ of degree $n + 1$, for each Σ , there is a scalar $\Lambda(\Sigma)$ called the *gauge factor associated with Σ* , which is a positively homogeneous function of Σ of degree 1, such that

$$\Psi(\Sigma) = \frac{\sigma_0 \dot{\epsilon}_0}{n + 1} \left(\frac{\Lambda(\Sigma)}{\sigma_0} \right)^{n+1}. \quad (32)$$

Defining then the reduced stress

$$\mathbf{S}(\Sigma) \equiv \frac{\Sigma}{\Lambda(\Sigma)}, \quad (33)$$

which is a positively homogeneous function of Σ of degree 0, and using the homogeneity of Ψ and the definition (32) of the gauge factor, one gets

$$\Psi(\mathbf{S}(\Sigma)) = \frac{\Psi(\Sigma)}{(\Lambda(\Sigma))^{n+1}} = \frac{\dot{\epsilon}_0}{(n + 1)\sigma_0^n}. \quad (34)$$

Thus $\mathbf{S}(\Sigma)$ lies on the gauge surface \mathcal{S} , so that it obeys equation (31).

The meaning of the gauge surface, the gauge function and the gauge factor is schematically illustrated in Figure 30.

The notions of gauge surface and gauge function extend those of yield surface and yield function of standard plasticity in the following sense. Assume that $n = +\infty$. It is then clear from equations (29) and (32) that \mathbf{D} is zero if $\Lambda(\Sigma) < \sigma_0$ and infinite if $\Lambda(\Sigma) > \sigma_0$. Hence the material is ideal-plastic, with yield criterion defined by $\Lambda(\Sigma) = \sigma_0$. It follows that if plastic flow does occur, equation (31) for $\mathbf{S}(\Sigma) = \Sigma/\Lambda(\Sigma)$ reads $\bar{\Psi}(\Sigma/\sigma_0) = 0$. Hence, up to some unimportant scaling factor of σ_0 , \mathcal{S} is nothing else than the yield surface, and $\bar{\Psi}$ is nothing else than the yield function.

The flow rule can be nicely expressed in terms of the gauge function. Indeed combination of equations (29) and (32) yields

$$\mathbf{D} = \dot{\epsilon}_0 \left(\frac{\Lambda(\Sigma)}{\sigma_0} \right)^n \frac{\partial \Lambda}{\partial \Sigma}(\Sigma). \quad (35)$$

Now differentiation of equation (31) for $\mathbf{S}(\Sigma)$ with respect to Σ_{ij} yields

$$\frac{\partial \bar{\Psi}}{\partial S_{kl}}(\mathbf{S}(\Sigma)) \left[\frac{\frac{1}{2}(\delta_{ik}\delta_{jl} + \delta_{jk}\delta_{il})}{\Lambda(\Sigma)} - \frac{\Sigma_{kl}}{(\Lambda(\Sigma))^2} \frac{\partial \Lambda}{\partial \Sigma_{ij}} \right] = 0 \implies \frac{\partial \Lambda}{\partial \Sigma}(\Sigma) = \frac{\frac{\partial \bar{\Psi}}{\partial \mathbf{S}}(\mathbf{S}(\Sigma))}{\frac{\partial \bar{\Psi}}{\partial \mathbf{S}}(\mathbf{S}(\Sigma)) : \mathbf{S}(\Sigma)}. \quad (36)$$

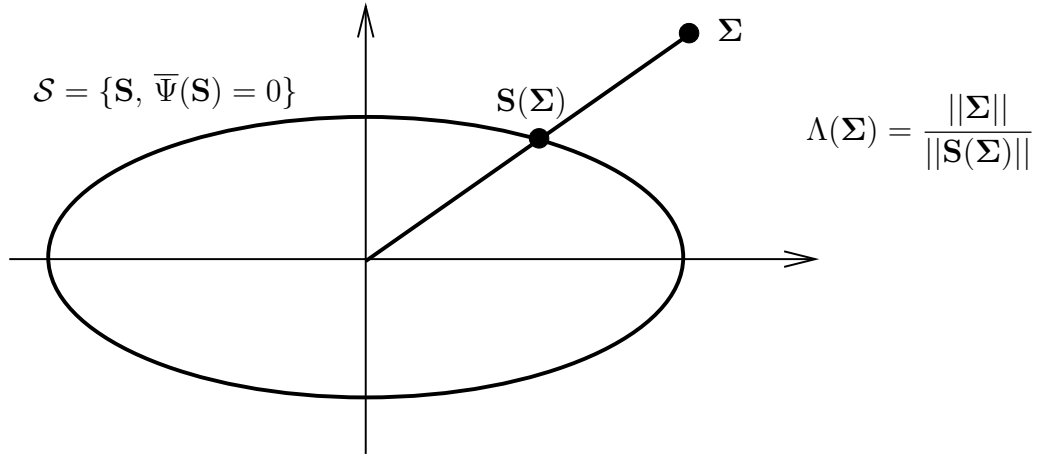


Figure 30: Schematic representation of the gauge surface, the gauge function and the gauge factor in stress space. After (Leblond et al., 1994b).

Combination of equations (35) and (36) then yields

$$\mathbf{D} = \dot{\epsilon}_0 \left(\frac{\Lambda(\boldsymbol{\Sigma})}{\sigma_0} \right)^n \frac{\frac{\partial \bar{\Psi}}{\partial \mathbf{S}}(\mathbf{S}(\boldsymbol{\Sigma}))}{\frac{\partial \bar{\Psi}}{\partial \mathbf{S}}(\mathbf{S}(\boldsymbol{\Sigma})) : \mathbf{S}(\boldsymbol{\Sigma})}. \quad (37)$$

Thus a kind of normality property, analogous to that in standard plasticity, is obeyed with respect to the gauge function.

5.4 Microstructure Evolution

The homogenization procedure outlined for rate-independent materials (Section 5.2) or rate-dependent materials (Section 5.3) applies to a frozen microstructure. Before closing this section, some elements dictating the derivation of evolution laws for microstructural variables are addressed.

A basic microstructural variable consists of the void volume fraction f . Omit for now contributions due to void nucleation so that any change in f can only come from the growth of preexisting voids. The matrix being incompressible, it follows that the change in volume may only originate from that in the volume of the voids, to the neglect of elastic deformations. Hence, $\dot{\omega} = \dot{\Omega}$ so that

$$\dot{f} \equiv \frac{d}{dt} \left(\frac{\omega}{\Omega} \right) = \left(1 - \frac{\omega}{\Omega} \right) \frac{\dot{\Omega}}{\Omega}$$

This may be restated as

$$\dot{f} = (1 - f) D_{kk} \quad (38)$$

For rate-independent plasticity, Eq. (38) becomes

$$\dot{f} = (1 - f) H \frac{\partial \Phi}{\partial \Sigma_m}, \quad (39)$$

where the property of macroscopic normality was used, H being the plastic multiplier and $\Sigma_m = \Sigma_{kk}/3$. The above equation (38) clearly shows that knowledge of the (inelastic) rate of deformation determines the rate of f . Therefore, this rate can be deduced from the macroscopic yield criterion or viscoplastic potential of the porous material, as was first recognized by Gurson (1977), in the rate-independent case, and by Duva and Hutchinson (1984) in the rate dependent case. This possibility is interesting in that it is easier to derive rigorous bounds or approximations for yield functions and viscoplastic potentials—because of their remarkable variational properties—than it is for void growth rates.

Unfortunately, the same is not possible for other microstructural variables, such as the shape of voids or their orientation. This is so because the local, microscopic fields dictate how these variables ultimately evolve. Descriptions based on a single scalar microstructural variable such as porosity are generally sufficient to model an isotropic damage process. However, in the presence of initial anisotropies or large deformation induced anisotropy, rigorous incorporation of additional microstructural variables is desirable. In such circumstances, evolution laws for these are necessary and may be derived based on micromechanics.

6 Void Growth Models

Models that fit within the framework outlined in the previous section are now presented. In the rate-independent case, the macroscopic yield surface is defined by (27) with plastic dissipation Π given by

$$\Pi(\mathbf{D}) = \inf_{\mathbf{d} \in \mathcal{K}(\mathbf{D})} \left\langle \sup_{\boldsymbol{\sigma}^* \in \mathcal{C}} \sigma_{ij}^* d_{ij} \right\rangle_{\Omega} \quad (40)$$

through combination of (21) and (23). Physically, this definition of the yield surface means that among all microscopic modes of plastic deformation, those that result in the smallest average dissipation over the RVE will define “macroscopic” yielding. Equations (27) and (40) represent a variational definition of the effective yield criterion.

First, one has to choose the type of boundary conditions, kinematic versus static. Generally speaking, the space of kinematically admissible velocity fields is smaller in the former case, with the consequence that the corresponding function $\Pi(\mathbf{D})$ is greater, hence the macroscopic domain \mathcal{C} is larger. Formally, this can be summarized as $\mathcal{C}_{\mathbf{v}=\mathbf{D}\mathbf{x}} \supset \mathcal{C}_{\boldsymbol{\sigma}\mathbf{n}=\boldsymbol{\Sigma}\mathbf{n}}$ using obvious shorthand subscript notations. Although no formal proof is available, it is likely that the true yield locus $\text{fr}(\mathcal{C})$ lies between the other two, as sketched in Fig. 31 (solid lines). In other terms,

$$\mathcal{C}_{\mathbf{v}=\mathbf{D}\mathbf{x}} \supset \mathcal{C} \supset \mathcal{C}_{\boldsymbol{\sigma}\mathbf{n}=\boldsymbol{\Sigma}\mathbf{n}} \quad (41)$$

For specified geometry and matrix yield criterion, variational problem $\{(27), (40)\}$ can be solved numerically, e.g., using the finite element method in combination with convex optimization tools (Pastor et al., 2009). However, closed-form solutions generally derive from approximations. One notorious approximation consists of using a reduced set of trial velocity fields, i.e., a subset of $\mathcal{K}(\mathbf{D})$.

In doing so, one will only calculate an upper bound $\Pi^+(\mathbf{D})$ for the plastic dissipation, based on some partial minimization over the restricted set of velocity fields. As a consequence, the boundary $\text{fr}(\mathcal{C})$ will be interior to the hypersurface defined as per equation (27) but with Π replaced with Π^+ . In other terms, the obtained, approximate yield locus will be exterior to the true one. This is illustrated in Fig. 31 where approximate yield surfaces are sketched as dashed lines. The inclusion $\mathcal{C}^{\text{app}} \supset \mathcal{C}$ holds for both types of boundary conditions. Thus, use of a restricted set of velocity fields results in an upper-bound approach to the exact yield locus for given boundary conditions. Ultimately, the appropriateness of the chosen velocity fields may be checked *a posteriori* by comparing the yield locus derived in closed form with that obtained numerically.

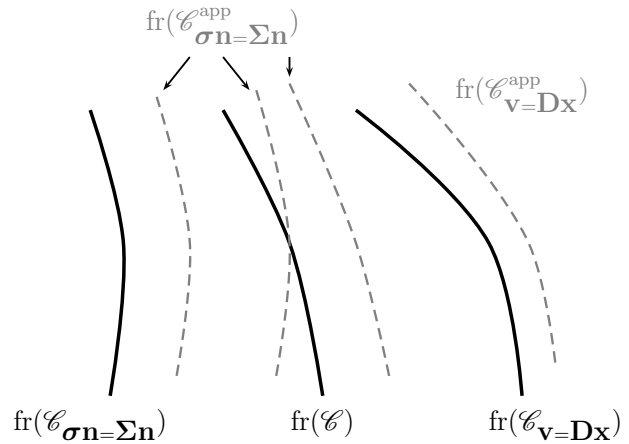


Figure 31: Schematic representation of yield loci relative configurations in stress space. Solid lines: exact loci for given boundary conditions. Dashed lines: approximate yield loci of the kinematic and static approaches. Three possible positions of the surface $\text{fr}(\mathcal{C}_{\boldsymbol{\sigma}\mathbf{n}=\boldsymbol{\Sigma}\mathbf{n}}^{\text{app}})$, are represented, interior to $\text{fr}(\mathcal{C})$, exterior to it, or intersecting it.

From what precedes, it follows that a kinematic approach is preferred to a static approach, for the following reasons. First, the space of velocity fields being smaller, the search for a good approximation of the infimum in (40) should be easier. Most importantly, the use of a static approach does not necessarily preserve its lower-bound character when trial velocity fields are employed. Indeed, one has

$$\mathcal{C}_{\boldsymbol{\sigma}\mathbf{n}=\boldsymbol{\Sigma}\mathbf{n}}^{\text{app}} \supset \mathcal{C}_{\boldsymbol{\sigma}\mathbf{n}=\boldsymbol{\Sigma}\mathbf{n}},$$

which, combined with (41), does not tell where the approximate locus lies with respect to the true one. To illustrate this, Fig. 31 depicts three possibilities for the former. By way of contrast, in the kinematic approach one also has

$$\mathcal{C}_{\mathbf{v}=\mathbf{D}\mathbf{x}}^{\text{app}} \supset \mathcal{C}_{\mathbf{v}=\mathbf{D}\mathbf{x}},$$

which now combined with (41) does ensure that

$$\mathcal{C}_{\mathbf{v}=\mathbf{D}\mathbf{x}}^{\text{app}} \supset \mathcal{C}.$$

The latter inclusion means that the use of a kinematic approach does preserve the upper-bound character of the closed-form yield locus (Fig. 31).

Actual derivation of the effective yield criterion $\{(27),(40)\}$ requires that the following be specified: (i) the geometry of the RVE; (ii) a micro-scale plasticity model, i.e., the boundary of \mathcal{C} with the flow rule being necessarily associative; and (iii) kinematically admissible microscale velocity fields defining a subset of $\mathcal{K}(\mathbf{D})$. It is through one, at least, of these basic ingredients that the models below differ from each other. In the literature, models derived within a kinematic approach include the Gurson model and its various extensions. Fewer models have been derived within a static approach (Hsu et al., 2009). The commonality among all models outlined below is that they share the kinematic approach character.

6.1 Gurson Model

6.1.1 Synopsis of Derivation

In the Gurson model, the basic ingredients entering homogenization problem $\{(27),(40)\}$ are as follows. (i) The RVE consists of a hollow sphere of outer radius b containing a concentric spherical void of radius a (Fig. 32a); the porosity $f = a^3/b^3$ is thus the only microstructural variable. (ii) Plastic flow in the matrix is taken to obey J_2 flow theory with an associated flow rule. (iii) The trial velocity field consists of two components: an incompressible, isotropic expansion field and a linear field corresponding to a uniform deformation field.

Specifically, the microscopic yield criterion and flow rule are written as:

$$\sigma_{\text{eq}} \equiv \sqrt{\frac{3}{2} \boldsymbol{\sigma}' : \boldsymbol{\sigma}'} \leq \bar{\sigma}, \quad \mathbf{d} = \frac{3}{2} \frac{d_{\text{eq}}}{\bar{\sigma}} \boldsymbol{\sigma}', \quad d_{\text{eq}} = \sqrt{\frac{2}{3} \mathbf{d} : \mathbf{d}} \quad (42)$$

where the prime stands for the deviatoric part of a tensor and $\bar{\sigma}$ is the yield stress of the material. For such a material model, the microscopic plastic dissipation in (21) takes the form

$$\pi(\mathbf{d}(\mathbf{x})) = \begin{cases} \bar{\sigma} d_{\text{eq}}(\mathbf{x}) & (\text{in the matrix}) \\ 0 & (\text{in the voids}) \end{cases} \quad (43)$$

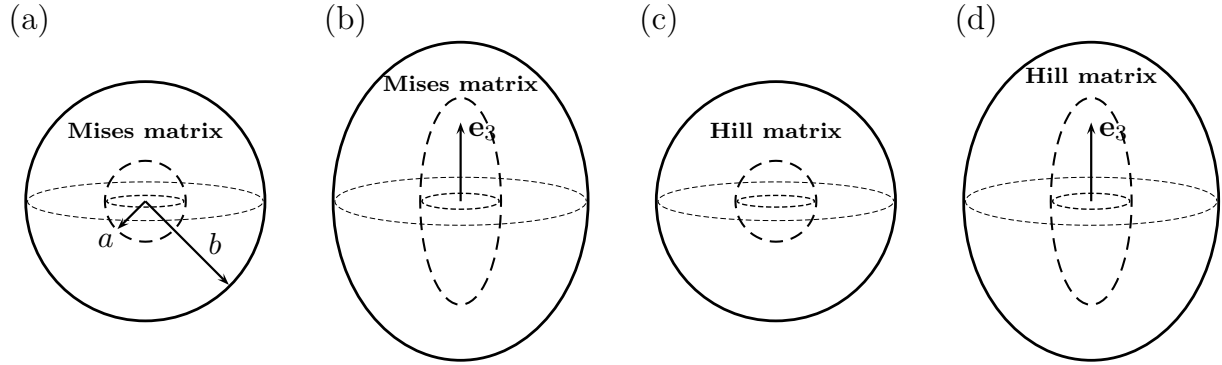


Figure 32: Representative volume elements considered in the models of (a) Gurson, (b) Gologanu–Leblond–Devaux, (c) Benzerga and Besson, and (d) Keralavarma and Benzerga.

Also, the trial velocity field is given by

$$\forall \mathbf{x} \in \Omega \setminus \omega, \quad v_i(\mathbf{x}) = A v_i^A(\mathbf{x}) + \beta_{ij} x_j, \quad \mathbf{v}^A(\mathbf{x}) = \frac{1}{r^2} \mathbf{e}_r \quad (44)$$

where both Cartesian and spherical coordinates are used. The scalar A and the symmetric tensor $\boldsymbol{\beta}$ are parameters. Matrix incompressibility requires that the latter be a pure deviator ($\beta_{kk} = 0$). Thus, \mathbf{v} leads to an inhomogeneous deformation field, \mathbf{d}^A , responsible for isotropic void expansion, and a homogeneous field $\boldsymbol{\beta}$. Boundary condition (11) at $\mathbf{x} = b\mathbf{e}_r$ yields:

$$A = b^3 D_m, \quad \text{and} \quad \boldsymbol{\beta} = \mathbf{D}' \quad (45)$$

where $D_m \equiv D_{kk}/3$. With \mathbf{D} specified through the boundary conditions, the velocity field is thus completely determined. This means that the set of restricted velocity fields is reduced to one field only. Therefore, the calculation of the macroscopic dissipation $\Pi(\mathbf{D})$ will not require any minimization, only evaluation of the value of the function Π in (40) for the above velocity field. The steps for doing so are as follows. First, in view of (43) and denoting $\mathcal{S}(r)$ the sphere of radius r with area $\mathcal{S}(r) = 4\pi r^2$, one has

$$\Pi(\mathbf{D}) = \bar{\sigma}(1-f) \langle d_{\text{eq}} \rangle_{\Omega \setminus \omega} = \frac{\bar{\sigma}}{\Omega} \int_a^b \mathcal{S}(r) \langle d_{\text{eq}} \rangle_{\mathcal{S}(r)} dr, \quad (46)$$

which can be bounded from above by

$$\Pi(\mathbf{D}) = \frac{\bar{\sigma}}{\Omega} \int_a^b \mathcal{S}(r) \langle d_{\text{eq}}^2 \rangle_{\mathcal{S}(r)}^{1/2} dr \quad (47)$$

using the Cauchy–Schwartz inequality and keeping the same notation for Π for convenience. Rewriting d_{eq} in terms of the fields \mathbf{d}^A and $\boldsymbol{\beta}$ of the assumed velocity field (44), we get

$$\langle d_{\text{eq}}^2 \rangle_{\mathcal{S}(r)} = A^2 \langle d_{\text{eq}}^{A^2} \rangle_{\mathcal{S}(r)} + \beta_{\text{eq}}^2 + \frac{4}{3} A \langle \mathbf{d}^A \rangle_{\mathcal{S}(r)} : \boldsymbol{\beta} \quad (48)$$

with

$$\mathbf{d}^A = \frac{b^3}{r^3} D_m [-2\mathbf{e}_r \otimes \mathbf{e}_r + \mathbf{e}_\theta \otimes \mathbf{e}_\theta + \mathbf{e}_\varphi \otimes \mathbf{e}_\varphi], \quad d_{\text{eq}}^{A^2} = 4D_m^2 \frac{b^6}{r^6}, \quad \beta_{\text{eq}}^2 = D_{\text{eq}}^2 \quad (49)$$

where use was made of (45). Here and subsequently, the meaning of subscript “eq” is consistent with definition (42)₃ for deformation related quantities. Since $\langle \mathbf{e}_i \otimes \mathbf{e}_i \rangle_{\mathcal{S}(r)} = 1/3$ for any spherical base vector \mathbf{e}_i the last term in (48) drops out rigorously and the macroscopic plastic dissipation can be written in the form:

$$\Pi(\mathbf{D}) = \frac{\bar{\sigma}}{b^3} \int_{\xi}^{\xi f} \sqrt{1+u^2} \frac{du}{u^2} \quad (50)$$

after operating the change of variable

$$u = \xi \frac{b^3}{r^3}; \quad \xi \equiv \frac{2D_m}{D_{eq}}$$

Integration of (50) permits the determination of the parametric equations of the yield locus (27). More precisely, the latter is written in terms of the deviatoric and hydrostatic components of the macroscopic stress tensor, Σ_{eq} and Σ_m , the meaning of subscript “eq” being consistent with definition (42)₁ for stress related quantities³. Subsequent elimination of D_m and D_{eq} from the parametric equations thus obtained leads to the well known Gurson yield function:

$$\Phi^{GT}(\Sigma; f) \equiv \frac{\Sigma_{eq}^2}{\bar{\sigma}^2} + 2q_1 f \cosh \left(\frac{3}{2} q_2 \frac{\Sigma_m}{\bar{\sigma}} \right) - (1 + q_1^2 f^2) \quad (51)$$

for $q_1 = q_2 = 1$.

The yield condition $\Phi^{GT} = 0$ defines a smooth yield surface $\text{fr}(\mathcal{C}^{GT})$. Therefore, the theorem enunciated at the end of Section 5.2 applies and plastic flow is normal to the yield surface. Yield criterion (51) is thus supplemented with the normality flow rule and an evolution equation for the porosity. This evolution law is given by (39), which by elimination of the plastic multiplier H may be written as:

$$\frac{\dot{f}}{1-f} = \left(\frac{\partial \Phi}{\partial \Sigma_m} / \frac{\partial \Phi}{\partial \Sigma_{eq}} \right) D_{eq} \quad (52)$$

In the Gurson model, the porosity f is the only microstructural variable.

6.1.2 Heuristic Extensions

Several extensions of the Gurson model are needed to implement it in finite element codes and make comparisons with experiments. In its minimal form, the Gurson model includes yield criterion (51), an associated flow rule, evolution law (52) for the porosity (with D_{eq} replaced with D_{eq}^p) and some expression for the elastic part of the rate of deformation. The latter is typically obtained using a heuristic weak-elasticity (i.e., hypoelastic) law; see Appendix B.

In an extended form, the Gurson model includes some representation of strain hardening and void interaction effects. Isotropic hardening of the matrix material is introduced

³Note that Σ_{eq} is exactly Σ_e in (1) but $\int D_{eq} dt$ and E_e in (5) differ from each other by an elastic contribution to the latter. For convenience, therefore, we use Σ_{eq} and Σ_e interchangeably, depending on the context

by replacing the constant $\bar{\sigma}$ in (51) with the function $\bar{\sigma}(\bar{\varepsilon})$ that gives the true (Cauchy) stress as a function of effective plastic strain, $\bar{\varepsilon}$, the latter being identified with the logarithmic plastic strain in a uniaxial tension test. $\bar{\varepsilon}$ represents the effective strain of some fictitious matrix material that would deform uniformly. In actuality, the matrix does not strain-harden uniformly in the presence of voids. Gurson's original approach, which is widely employed in current usage, is purely phenomenological and identifies the plastic dissipation of the real material (matrix with spatially fluctuating hardness and voids) with that of the fictitious material (matrix with uniform hardness and voids). This identification results in the following evolution law for the effective plastic strain:

$$(1 - f)\bar{\sigma} \dot{\bar{\varepsilon}} = \boldsymbol{\Sigma} : \mathbf{D}^p \quad (53)$$

This is a simple, yet elegant proposal for the evolution of $\bar{\varepsilon}$. It also happens to capture the physical aspect of that part of strain hardening that results from the mean part of \mathbf{D}^p . In a porous material indeed, the hydrostatic part of the loading can lead to plastic flow at the microscale.

Based on a bifurcation study, Tvergaard (1982b) introduced factors q_1 and q_2 in Gurson's criterion (51). A possible interpretation of these factors is that they allow to represent void interaction effects. Perrin and Leblond (1990) derived an estimate for q_1 assuming $q_2 = 1$ based on an analytical solution of a hollow sphere with a porous matrix loaded hydrostatically. Using a self-consistent scheme they obtained $q_1 = 4/e = 1.47$, which is close to the value of 1.5 proposed by Tvergaard (1982b). Subsequent cell model studies have indicated that the values assigned to q_1 and, as a matter of fact also q_2 , significantly vary with geometry and loading conditions (Koplik and Needleman, 1988; Gao et al., 1998). Such variations indicated that the introduction of the q_i factors may not be simply associated with a physical interaction effect, but are likely to reflect some inaccuracies in the Gurson model itself.

Granted such extensions, the Gurson constitutive equations can be integrated for specified loading paths. Figure 33 shows the predictions of the Gurson model for various values of the imposed stress triaxiality ratio T , as defined in (1). The data used in the calculations correspond to those used in the cell model studies of Fig. 16. In particular, $f_0 = 0.001$ and the power law hardening equation (3) is used with $N = 0.1$. Comparison with the cell model results, Fig. 33, indicates that the Gurson model captures well the important effect of stress triaxiality on void growth. In particular, the prediction is quantitatively excellent in the range $1 \leq T \leq 3$ using a value of $q_1 = 1.3$ for the Tvergaard parameter (also $q_2 = 1$). Extensive comparisons of that kind were performed by Koplik and Needleman (1988). However, for $T = 1/3$ and other low triaxialities the Gurson model overestimates the rate of void growth.

The good performance of the Gurson model can be rationalized by considering the rate of increase of porosity f . Combining (52) and (51) one gets:

$$\frac{\dot{f}}{1 - f} = \frac{3}{2} f \frac{\bar{\sigma}}{\Sigma_{eq}} \sinh \left(\frac{3}{2} T \frac{\Sigma_{eq}}{\bar{\sigma}} \right) D_{eq}^p \quad (54)$$

which shows the exponential effect of stress triaxiality on void growth, a well known trend since Rice and Tracey (1969).

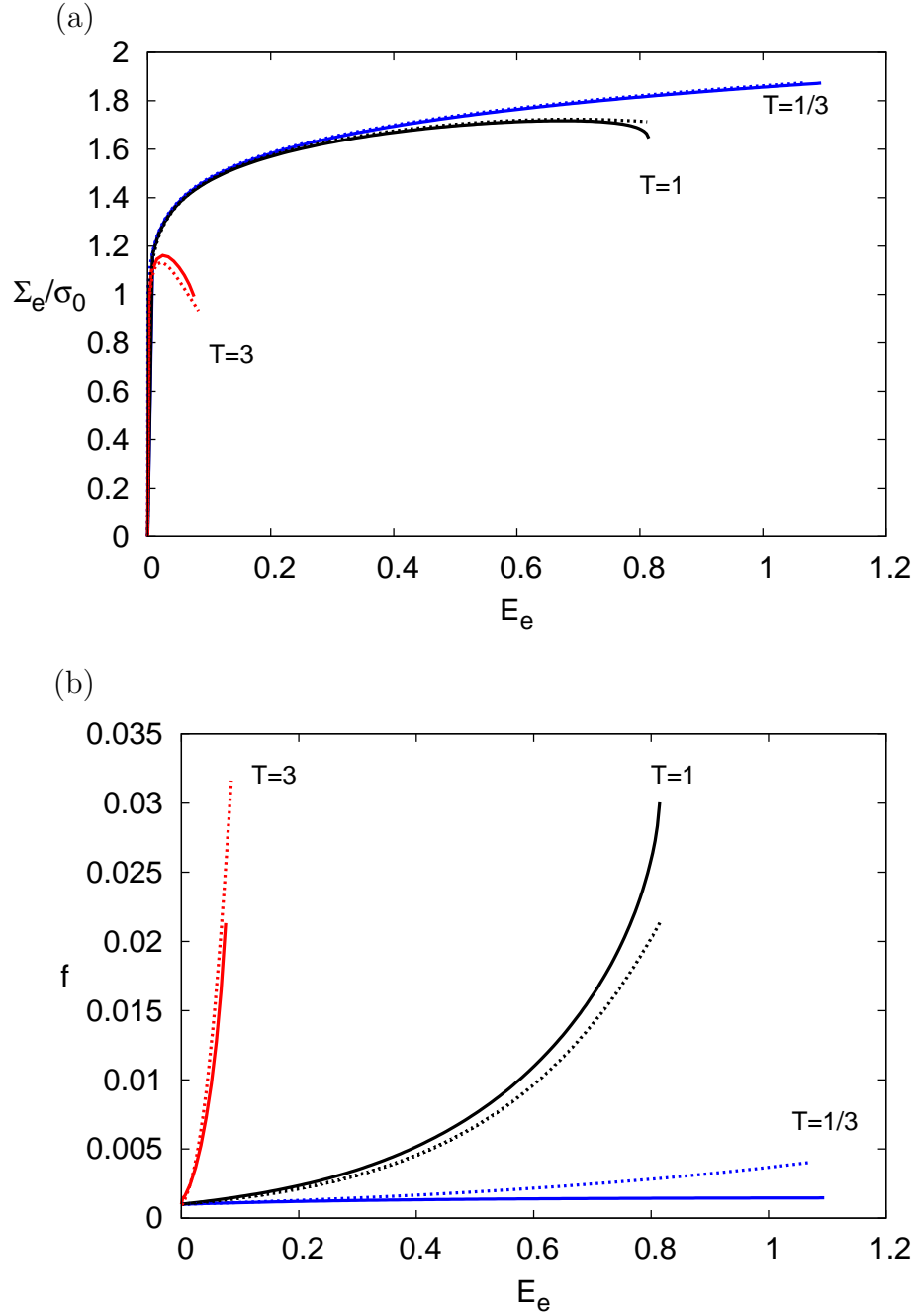


Figure 33: Comparison of predictions using the Gurson–Tvergaard model (dashed lines, $q_1 = 1.3$) with results of unit-cell calculations (solid lines) for an initially spherical void in an isotropic matrix for $T = 1/3, 1$ and 3 . (a) Effective stress, Σ_e , normalized by the matrix yield stress, versus effective strain, E_e . (b) void volume fraction versus E_e .

In spite of that, the Gurson model does not capture well strain hardening effects on the evolution of porosity. This is deeply rooted in the nonuniform nature of strain-hardening when voids are present. An improved model accounting for strain hardening effects was developed by Leblond et al. (1995) where the reader can find further details about this particular aspect. Mear and Hutchinson (1985) have also proposed an extension of Gurson's criterion to incorporate kinematic hardening.

Other extensions of the model include void nucleation and void coalescence. The latter will be addressed more specifically in Section 7. A continuum model of void nucleation that has been used quite extensively in conjunction with the Gurson model assumes that the total rate of porosity is the sum of two terms (Chu and Needleman, 1980)

$$\dot{f} = \dot{f}_g + \dot{f}_n \quad (55)$$

The first term is associated with the growth of pre-existing voids and is therefore given by (38) specialized to (54). The second term represents the rate of nucleation of new voids. In some general formulation, it consists of two terms:

$$\dot{f}_n = \mathcal{A} \dot{\bar{\epsilon}} + \mathcal{B} (\dot{\Sigma}_{eq} + c \dot{\Sigma}_m) \quad (56)$$

the first one representing strain-controlled nucleation, the second stress-controlled nucleation, with the requirement that $\dot{\Sigma}_{eq} + c \dot{\Sigma}_m > 0$. The factor c is introduced here based on findings by Needleman (1987) using cell model analyses. Chu and Needleman (1980) suggested that \mathcal{A} and \mathcal{B} are functions of $\bar{\epsilon}$ and $\Sigma_{eq} + c \Sigma_m$, respectively, and that they follow a normal distribution. For example,

$$\mathcal{A}(\bar{\epsilon}) = \frac{f_N}{s_N \sqrt{2\pi}} \exp \left[-\frac{1}{2} \left(\frac{\bar{\epsilon} - \epsilon_N}{s_N} \right)^2 \right] \quad (57)$$

where f_N represents the volume fraction of void-nucleating particles, ϵ_N is some average nucleation strain and s_N is a standard deviation.

At a more fundamental, yet practically relevant scale, an energy criterion is necessary for void nucleation (see Section 4). When this criterion is satisfied, a sufficient condition may be formulated in terms of a stress-based criterion. On the other hand, attainment of a critical strain is neither necessary nor sufficient for void nucleation. In addition, a strain-controlled criterion does not capture the dependence of void nucleation upon stress triaxiality, a fact that is inferred from both experiments and analysis (Needleman, 1987; Lee and Mear, 1999). It would also predict an increasing rate of void nucleation with decreasing stress triaxiality, simply because of the larger amounts of accumulated plastic strain. In practice, however, use of a strain-controlled nucleation may be a convenient way of representing the outcome of a more basic stress-based criterion. An example in this regard was discussed by Needleman (1987); see Section 3.1 around Fig. 14. Analyses of localization carried out within the framework of Rice (1977) indicated that strain-controlled and stress-controlled nucleation can lead to quite different predictions of macroscopic ductility, interpreted as the onset of a bifurcation in the set of governing partial differential equations⁴. Of particular significance is that the hydrostatic stress dependence of \dot{f}_n in (56) entails non-symmetry of the tangent matrix, which favors early flow localization.

⁴It may be remarked that such a definition generally leads to an overestimation of experimental or cell-model ductility.

6.2 GLD Model

The Gologanu–Leblond–Deviaux (GLD) model extends the Gurson model to account for void shape effects. In the GLD model, the basic ingredients entering homogenization problem $\{(27), (40)\}$ are as follows. (i) The RVE consists of a spheroidal volume containing a confocal spheroidal void (Fig. 32b). The microstructural variables are thus the porosity f , the void aspect ratio, w , and the void axis, \mathbf{e}_3 . (ii) The microscale plasticity model obeys associative J_2 flow theory. (iii) The trial velocity field consists of two components. The linear field in (44) is kept but the isotropic field \mathbf{v}^A is replaced with an expansion field which is constructed from the family of incompressible velocity fields introduced by Lee and Mear (1992)⁵. This field \mathbf{v}^A is axisymmetric about the void axis. It reduces to a spherically symmetric field in the case of a spherical void and to a cylindrically symmetric field in the case of a cylindrical one. Its components in spheroidal coordinates involve doubly infinite series of associated Legendre functions of the first and second kinds. They are omitted here for brevity and can be found in (Gologanu et al., 1997); also see Keralavarma and Benzerga (2010).

Gologanu et al. (1993, 1994a, 1997) carried out a number of limit analyses of such spheroidal RVEs to obtain approximate yield loci in closed form. Most accurate among these is the one derived using four terms of the Lee–Mear expansion field under axisymmetric loadings aligned with the voids. For arbitrary loadings Gologanu et al. (1997) proposed a heuristic extension, which was later justified on rigorous grounds (Gologanu, 1997). The approximate GLD effective yield condition is $\Phi^{\text{GLD}}(\Sigma; f, w, \mathbf{e}_3) = 0$ with

$$\Phi^{\text{GLD}} = C \frac{\|\Sigma' + \eta \Sigma_h \mathbf{Q}\|^2}{\bar{\sigma}^2} + 2q(g+1)(g+f) \cosh \left(\kappa \frac{\Sigma : \mathbf{X}}{\bar{\sigma}} \right) - (g+1)^2 - q^2(g+f)^2 \quad (58)$$

for $q = 1$. Here, $\|\mathbf{T}\| \equiv (3/2 \mathbf{T}' : \mathbf{T}')^{1/2}$ denotes the von Mises norm of tensor \mathbf{T} , \mathbf{Q} and \mathbf{X} are transversely isotropic tensors given by:

$$\mathbf{X} \equiv \alpha_2(\mathbf{e}_1 \otimes \mathbf{e}_1 + \mathbf{e}_2 \otimes \mathbf{e}_2) + (1 - 2\alpha_2)\mathbf{e}_3 \otimes \mathbf{e}_3 \quad (59)$$

$$\mathbf{Q} \equiv -\frac{1}{3}(\mathbf{e}_1 \otimes \mathbf{e}_1 + \mathbf{e}_2 \otimes \mathbf{e}_2) + \frac{2}{3}\mathbf{e}_3 \otimes \mathbf{e}_3, \quad (60)$$

$\Sigma_h \equiv \Sigma : \mathbf{X}$ is a weighted average of the normal stresses along the principal axes of the void and $\mathbf{e}_1, \mathbf{e}_2$ are arbitrarily chosen transverse unit base vectors. Also, κ, α_2, g, C and η are scalar valued functions of microstructural parameters f and w . Their expressions that result from the micromechanical derivation are provided in Appendix A.

Some special cases are worth noting. Criterion (58) reduces to Gurson's criterion (51) in the limit of a spherical void ($w \rightarrow 1$) and to Gurson's criterion for cylindrical cavities in the limit $w \rightarrow \infty$. It also reduces to the standard von Mises yield condition when $f = 0$, but only for prolate voids. In the case of oblate voids, the limit $f \rightarrow 0$ corresponds to a material with a distribution of penny-shaped cracks for which the yield condition is:

$$\Phi^{\text{cracks}} = C \frac{\|\Sigma' + \eta \Sigma_h \mathbf{Q}\|^2}{\bar{\sigma}^2} + 2q(g+1)g \cosh \left(\kappa \frac{\Sigma : \mathbf{X}}{\bar{\sigma}} \right) - (g+1)^2 - q^2g^2 \quad (61)$$

⁵Quite recently, Leblond and Gologanu (2008) derived integral expressions of admissible velocity fields for general ellipsoids.

Since $g = 4\pi c^3/(3\Omega)$ with c the crack radius (see Appendix A) g plays in this case the role of an effective porosity, i.e., that of an “equivalent” spherical void of radius c .

The void shape has in general a direct effect on the rate of void growth. For axisymmetric loadings, Benzerga (2002) has shown that the rate of growth of porosity associated with the GLD criterion is given by

$$\frac{\dot{f}}{1-f} = \frac{\frac{\partial \Phi}{\partial \Sigma_h}}{\frac{\partial \Phi}{\partial \Sigma_{eq}} - \beta \frac{\partial \Phi}{\partial \Sigma_h}} D_{eq}^p \quad (62)$$

where $\beta = 2(\alpha_2 - \frac{1}{3})$. The above equation generalizes (52) and reduces to it in the case of spherical voids since $\beta = 0$ and $\Sigma_h = \Sigma_m$ then. The void shape enters (62) mostly through parameters α_2 and κ , the leading term in $\partial \Phi / \partial \Sigma_h$ being the exponential term $\sinh(\kappa \Sigma_h / \bar{\sigma})$.

Figure 34 illustrates typical ranges of variation of κ for values of the microstructural variables f and w within the practical range of interest. In particular, $\kappa = 3/2$ for

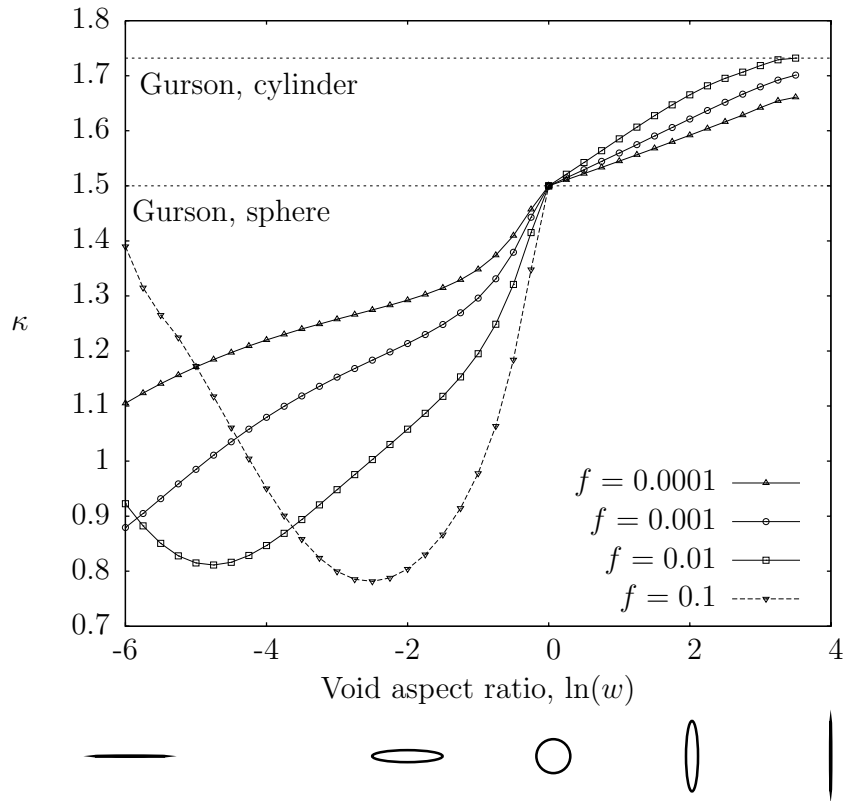


Figure 34: Dependence of κ in (58) on the void aspect ratio for various values of the porosity f (Benzerga, 2000).

spherical cavities and $\kappa = \sqrt{3}$ for cylindrical ones, irrespective of the value taken by f . These special cases correspond to the Gurson models and are indicated by dashed lines in Fig. 34. For prolate voids κ takes values in between the above limits. For oblate voids, however, the variations of κ are more significant with lowest values slightly above 0.75.

Figure 35 shows the dependence of parameter α_2 upon f and w . For spherical voids

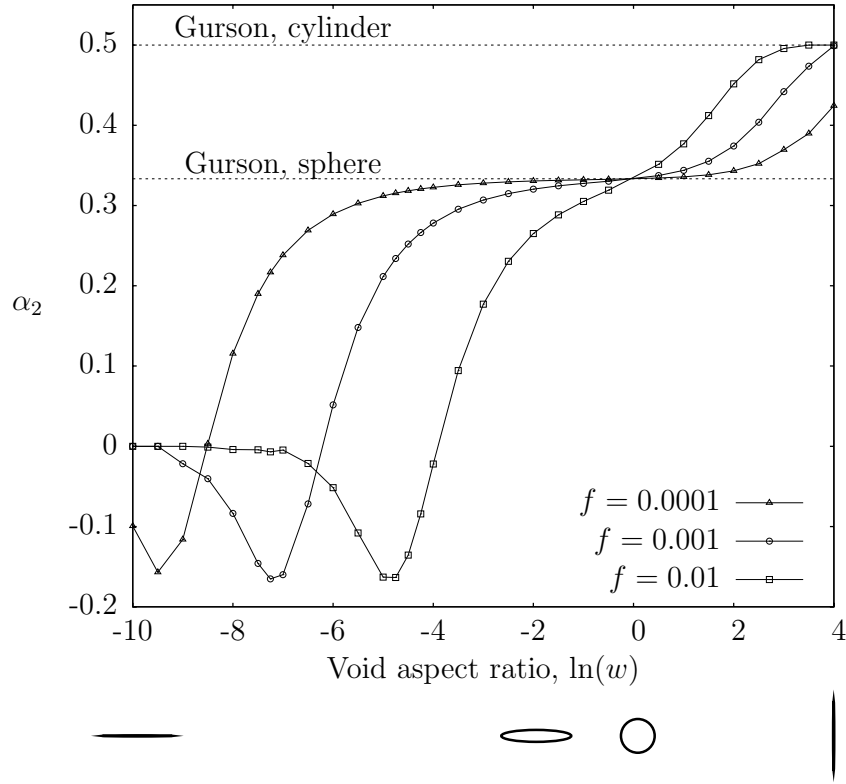


Figure 35: Dependence of α_2 in (58) and (59) on the void aspect ratio for various values of the porosity f (Benzerga, 2000).

$\alpha_2 = 1/3$ so that Σ_h reduces to the mean normal stress Σ_m , whereas for cylindrical voids $\alpha_2 = 1/2$, which is consistent with the fact that void growth of cylindrical cavities is only sensitive to the mean lateral stress and not to the axial stress. These special cases are also indicated in Fig. 35.

Gologanu et al. (1997) supplemented yield criterion (58) with evolution laws for the microstructural variables. That of f is given by (39), which specializes to equation (62) under axisymmetric loadings. The evolution law of the void aspect ratio, in its basic form, was obtained by averaging the trial deformation field over the void boundary $\partial\omega$. The final form was based on the notion of Eshelby-like concentration tensors (Ponte Castañeda and Zaidman, 1994; Garajeu et al., 2000) and heuristic corrections based on numerically estimated rates of w . Introducing the void shape parameter $S \equiv \ln w$, the evolution law reads:

$$\dot{S} = \frac{3}{2} \left[1 + \left(\frac{9}{2} - \frac{T^2 + T^4}{2} \right) (1 - \sqrt{f})^2 \frac{\alpha_1 - \alpha_1^G}{1 - 3\alpha_1} \right] \mathbf{e}_3 \cdot \mathbf{D}'^p \cdot \mathbf{e}_3 + \left(\frac{1 - 3\alpha_1}{f} + 3\alpha_2 - 1 \right) \mathbf{I} : \mathbf{D}^p \quad (63)$$

where the term $[\cdot]$ is the result of fits to numerical calculations, T is the stress triaxiality ratio and α_1 and α_1^G are given in Appendix A. Finally, assuming that the voids rotate with the material, the evolution of the void axis \mathbf{e}_3 is given by

$$\dot{\mathbf{e}}_3 = \mathbf{W} \cdot \mathbf{e}_3 \quad (64)$$

where \mathbf{W} is the total material spin. Experimental evidence supports the general form (64) if the loading axes are initially aligned with the void axes (Benzerga, 2000). An improved evolution law was developed by Kailasam and Ponte Castaneda (1998) using reference elastic solutions and a nonlinear variational principle due to Ponte Castaneda (1991). This law was tested successfully by Scheyvaerts (2008) using 3D cell model calculations. A succinct description of this formulation may be found in (Keralavarma and Benzerga, 2010).

The performance of the GLD model has been studied quite extensively by Benzerga (2000). Granted some heuristic extensions similar to those adopted for the Gurson model, comparisons with cell model calculations can also be carried out. The extensions include incorporation of elasticity, strain hardening and void interaction effects through the parameter q already included in (58). Sovik and Thaulow (1997) performed a series of micromechanical unit cell analyses and compared their results with predictions by an earlier version of the GLD model (Gologanu et al., 1993, 1994a). They found that the model did not pick up well the effect of initial void shape on void growth rates. This drawback was remedied in the later version of Gologanu et al. (1997) which is the one described above. Figure 36 shows some comparisons between the GLD model and the cell model analyses shown in Fig. 18. A value of $q = 1.5$ was used in all model simulations. The origin of the improved performance is rooted in two aspects: first in the use of four terms in the expansion velocity field \mathbf{v}^A of the limit analysis instead of only two terms in the earlier versions; and second in the improved evolution law (63) for the void shape. Pardoen and Hutchinson (2000) carried out detailed comparisons between GLD model and cell model predictions. They proposed alternative heuristics for the function $h_T(T)$ appearing in (63) in an attempt to improve the quantitative predictions of the model across wide ranges of variation for microstructural parameters (f_0 , w_0 , λ_0), stress triaxiality T and matrix hardening exponent N . Also, see (Scheyvaerts et al., 2010) for more recent comparisons.

Remark: On account of the variations of key model parameters κ and α_2 (Figs. 34 and 35), it might be surprising at first glance that the GLD model works. Indeed, both κ and α_2 are monotonically increasing functions of the void aspect ratio within the ranges explored in all of the above cell model calculations. Since κ enters the cosh term of criterion (58) one would expect that a higher aspect ratio w , hence larger values of κ would enhance void growth, not slow it down. Yet the opposite is seen in Fig. 36. As discussed by Benzerga (2000), this paradox is lifted by examining the rate of void growth for small porosities. For axisymmetric loadings, the rate of increase of porosity f given by (62) can be simplified into:

$$\frac{\dot{f}}{(1-f)D_{\text{eq}}^p} = (g+f) \frac{\kappa \bar{\sigma}}{\Sigma_{\text{eq}}} \sinh \left(\kappa (T - \beta) \frac{\Sigma_{\text{eq}}}{\bar{\sigma}} \right) + C\eta + \mathcal{O}(f^2) \quad (65)$$

The approximate relation (65) shows that the competition between the increase in κ and that in α_2 (i.e. β) affects ultimately the growth rate of porosity with small microstructural evolutions leading to significant variations, consistent with the predictions in Fig. 36. By the same account, relation (65) clearly shows that above a certain triaxiality this competitive effect is swamped (T dominating over the β term inside the cosh). In other words, it is the “effective triaxiality” $T - \beta$ that plays a key role, not the actual triaxiality.

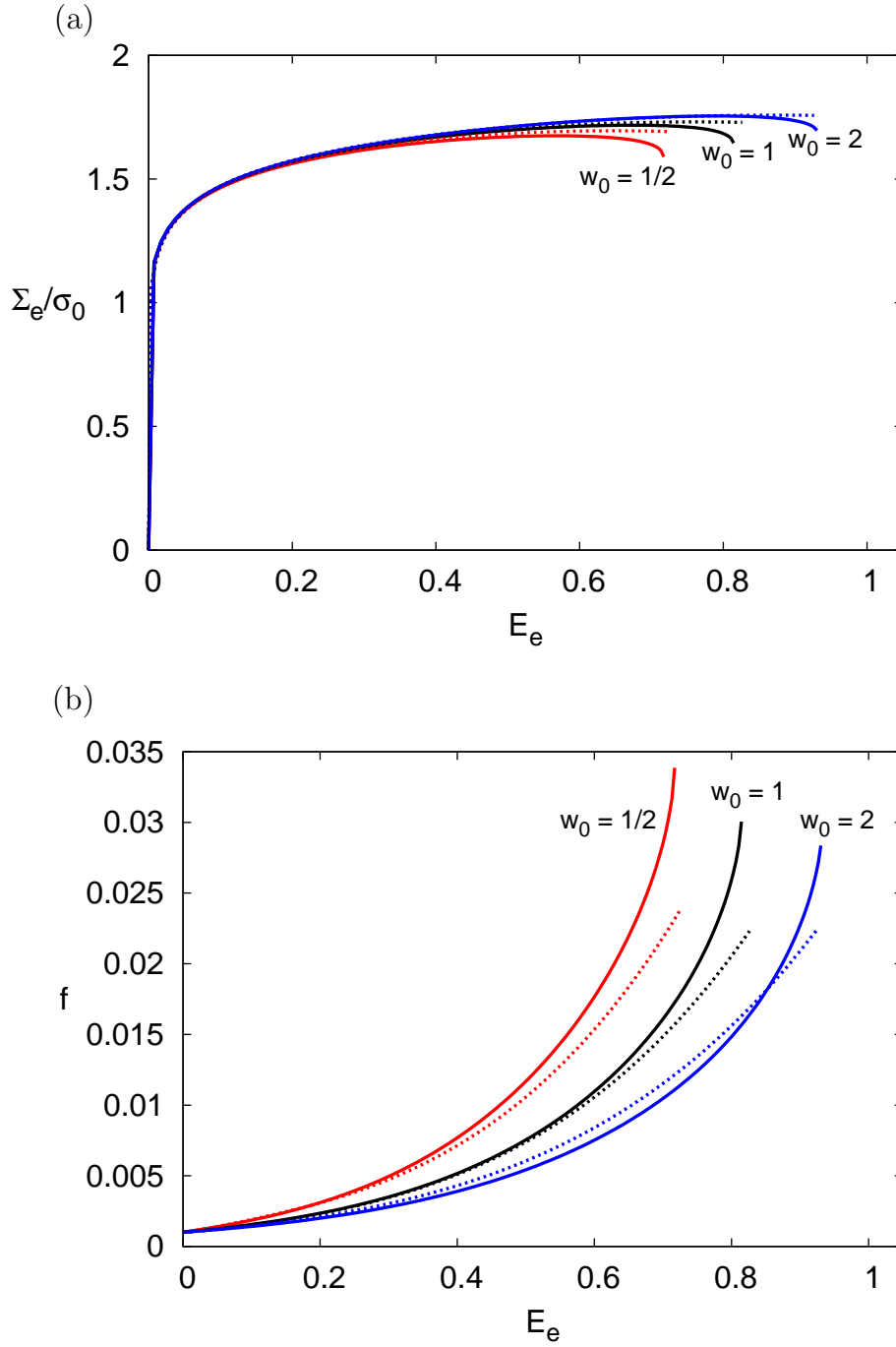


Figure 36: Comparison of predictions using the GLD model (dashed lines, $q = 1.5$) with results of unit-cell calculations (solid lines) for various values of the initial void aspect ratio w_0 and $T = 1$. (a) Effective stress, Σ_e , normalized by the matrix yield stress, versus effective strain, E_e . (b) void volume fraction versus E_e .

The fact that void growth is not equally sensitive to all normal components of the stress tensor is emphasized again. For example, the axial stress would not matter in the growth of an elongated cavity just as the lateral normal stresses would not affect the initial growth of a penny-shaped crack. More in-depth analysis reveals that in narrow ranges of w_0 , such

as in Fig. 36, the “secondary porosity” g and the term $C\eta$ play a role in the case of oblate and prolate voids, respectively. Of particular importance in equation (65) is the term g , which is usually slightly larger than f for oblate cavities.

For spherical voids and axisymmetric loadings with one major normal stress, the prediction of the Gurson model matches that of the GLD model at sufficiently high triaxiality levels. For an initial void volume fraction $f_0 = 0.0009$, this occurs for $T \geq 4/3$ as illustrated in Fig. 37a. For lower values of T the Gurson model overestimates the rate of void growth. In particular, the prediction for uniaxial loading ($T = 1/3$) is erroneous. By way of contrast, the GLD model predicts no net increase in the porosity under uniaxial loading, in keeping with the cell model prediction in Fig. 16b. The zero growth rate of f is due to microstructural evolution, namely to a continuous elongation of the cavity (Fig. 37b) and to the absence of a lateral normal stress. Figure 37b shows the evolution

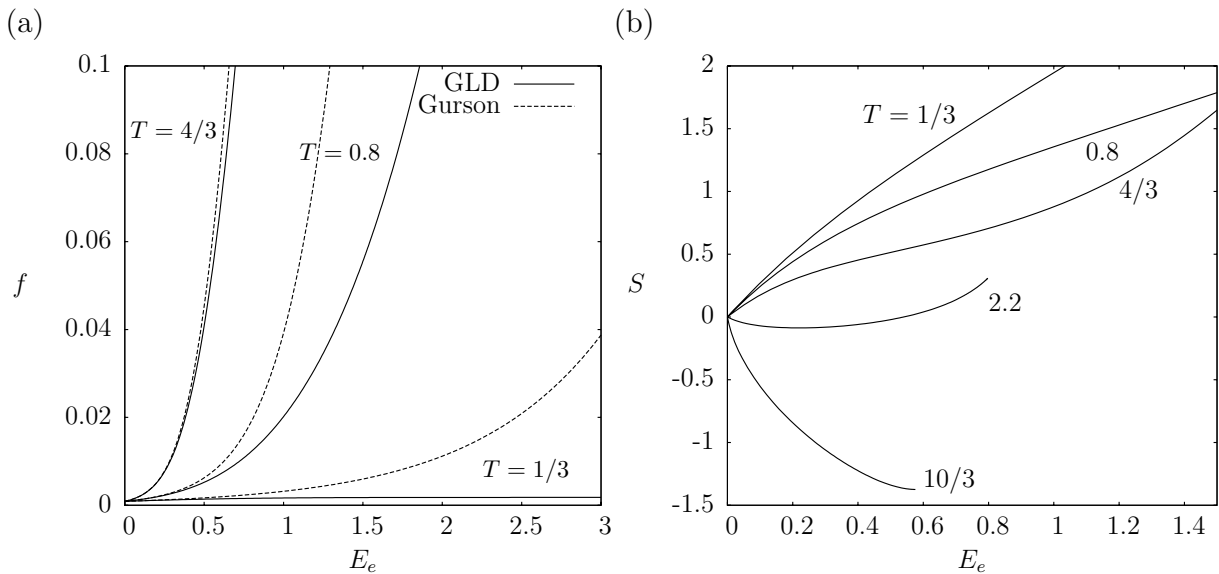


Figure 37: Comparison of predictions using the Gurson and GLD models for initially spherical voids ($f_0 = 0.0009$) at various triaxialities. (a) Void volume fraction versus effective strain, E_e . (b) Void aspect ratio, $S = \ln w$, versus E_e . Adapted from (Benzerga, 2000)

of the void aspect ratio predicted by the GLD model over a wider range of triaxialities. The latter range from $1/3$ (uniaxial tension) to $10/3$, a value that would prevail ahead of a blunted crack tip in a strain-hardening material. The void shape is predicted to change from prolate at low T values to oblate at higher values of T . The transition is found to take place for T between 1.8 and 2.2. Within this range, the initially spherical void roughly retains its equiaxed shape. Using a simpler model and a point definition of the void aspect ratio, Budiansky et al. (1982) predicted that such a transition would occur for $T \approx 1.5$. The evolution of the void toward an oblate shape at $T > 2.2$, while the major stress is axial, is a typically nonlinear effect. It has been confirmed by the many cell model studies published to date.

Yet the main advantage of the GLD model is its ability to represent initial anisotropy when considering nonspherical voids. Benzerga (2000) has evaluated the predictions of this model for triaxial loadings with a major normal stress parallel or perpendicular to

the void axis. The latter is referred to as transverse loading. In this case, the voids would actually develop into ellipsoidal cavities for which two void aspect ratios are needed. As a first approximation, the GLD model may be used by replacing the current void shape by an equivalent spheroid. Figure 38 shows typical predictions for the evolution of microstructure for $f_0 = 0.0009$ and highly elongated cavities with $S_0 = 2.5$ (roughly an aspect ratio above 10). For uniaxial tension ($T = 1/3$), void growth is predicted un-

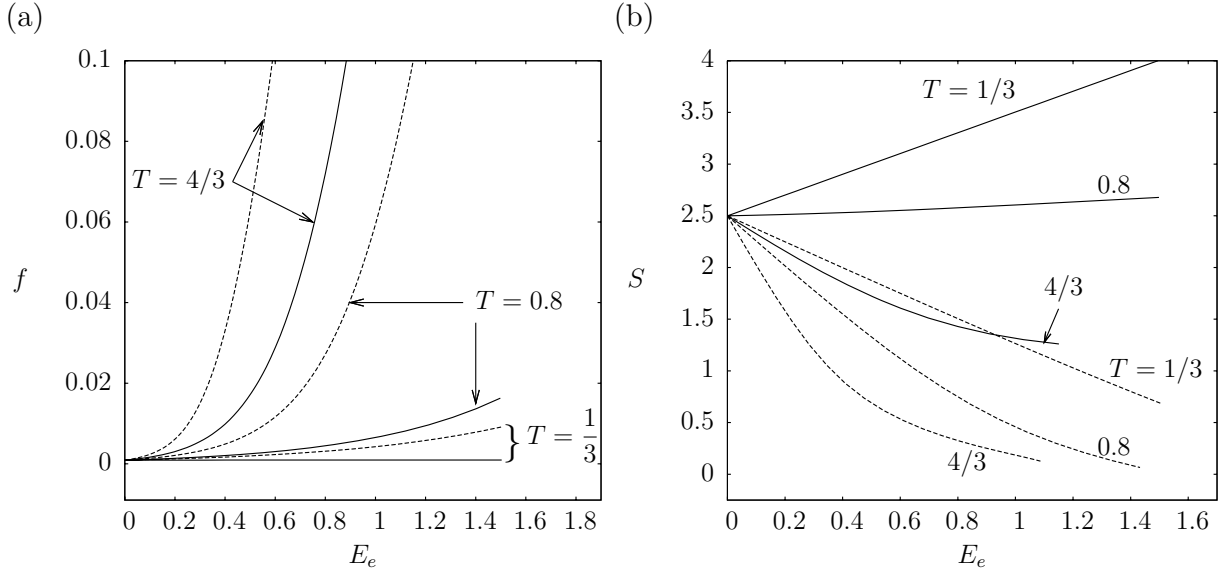


Figure 38: Prediction of ductile damage anisotropy using the GLD model for $f_0 = 0.0009$ and initially elongated voids ($S_0 = 2.5$) at various stress triaxialities and loading parallel to the voids (solid lines) and transverse to the voids (dashed lines). (a) Void volume fraction versus effective strain, E_e . (b) Void aspect ratio, $S = \ln w$, versus E_e . Adapted from (Benzerga, 2000)

der loading perpendicular to the voids, which is qualitatively reasonable. Anisotropy in the void growth process is predicted with the growth rate of porosity being larger under transverse loading. The difference in ductility between the two loading orientations decreases with increasing stress triaxiality but remains significant at all levels of T considered here. 3D cell model studies are needed to assess the model predictions under such circumstances.

Finite element implementations of the GLD model were carried out by Benzerga et al. (1998), Benzerga (2000) and more recently by Gao and Kim (2006). Two-dimensional (plain strain and axisymmetric) computations (Benzerga et al., 2002) as well as fully 3D computations (Benzerga et al., 2004b) were performed using this model.

On the basis of all the analyses mentioned above, it appears that the GLD model gives a reasonably accurate representation of void shape effects in ductile porous solids. More challenging is the comparison with experiments. Elements of such a comparison will be provided in Sections 8 and 9.

6.3 Benzerga & Besson Model

The Benzerga & Besson model is an extension of the Gurson model accounting for plastic anisotropy effects. In this model, the basic ingredients entering homogenization problem $\{(27),(40)\}$ are as follows. (i) The RVE consists of a hollow sphere containing a concentric spherical void (Fig. 32c). (ii) Plastic flow in the matrix is taken to obey Hill's associative plasticity model (Hill, 1948), which is the simplest extension of J_2 flow theory to anisotropic media. (iii) The trial velocity field consists of the same two components used by Gurson in (44). The microscopic yield criterion and flow rule are written as:

$$\sigma_{\text{eq}} \equiv \sqrt{\frac{3}{2} \boldsymbol{\sigma} : \mathbb{p} : \boldsymbol{\sigma}} = \sqrt{\frac{3}{2} \boldsymbol{\sigma}' : \mathbb{h} : \boldsymbol{\sigma}'} \leq \bar{\sigma}, \quad \mathbf{d} = \frac{3}{2} \frac{d_{\text{eq}}}{\bar{\sigma}} \mathbb{p} : \boldsymbol{\sigma}, \quad d_{\text{eq}} = \sqrt{\frac{2}{3} \mathbf{d} : \hat{\mathbb{h}} : \mathbf{d}} \quad (66)$$

Here and in the following section, the meaning of subscript “eq” is consistent with Hill's equivalent quantities, and $\bar{\sigma}$ is the yield stress of the material in a reference direction. Also, \mathbb{p} denotes Hill's anisotropy tensor, \mathbb{h} is the anisotropy tensor in the space of stress deviators, and $\hat{\mathbb{h}}$ is a formal inverse of \mathbb{h} defined through the identities:

$$\mathbb{p} = \mathbb{J} : \mathbb{h} : \mathbb{J}, \quad \hat{\mathbb{p}} \equiv \mathbb{J} : \hat{\mathbb{h}} : \mathbb{J}, \quad \mathbb{p} : \hat{\mathbb{p}} = \hat{\mathbb{p}} : \mathbb{p} = \mathbb{J} \quad (67)$$

where $\mathbb{J} \equiv \mathbb{I} - \frac{1}{3} \mathbf{I} \otimes \mathbf{I}$ with \mathbb{I} and \mathbf{I} the fourth and second order identity tensors, respectively. \mathbb{J} is the deviatoric projector, e.g., $\mathbb{J} : \boldsymbol{\sigma} = \boldsymbol{\sigma}'$. Both \mathbb{h} and $\hat{\mathbb{h}}$ are symmetric positive definite. In the frame of material orthotropy, they may be expressed as diagonal 6×6 matrices using Voigt's condensation. The six Hill coefficients, i.e., the diagonal elements of \mathbb{h} , are then denoted h_i , $i = 1, 6$. For such a material model, Benzerga et al. (1997) have shown that the microscopic plastic dissipation is formally given by the same equation (43) but with the appropriate definition (66)₃ for d_{eq} . They then obtained a rigorous upper bound for the macroscopic plastic dissipation, which is formally given by (50) with $\xi \equiv h D_{\text{m}} / D_{\text{eq}}$, h being an invariant of tensor \mathbb{h} . Details may be found in (Benzerga and Besson, 2001). Their effective yield function reads

$$\Phi^{\text{BB}}(\boldsymbol{\Sigma}; f, \mathbb{h}) \equiv \frac{3}{2} \frac{\boldsymbol{\Sigma}' : \mathbb{h} : \boldsymbol{\Sigma}'}{\bar{\sigma}^2} + 2qf \cosh \left(\frac{3}{h} \frac{\Sigma_{\text{m}}}{\bar{\sigma}} \right) - (1 + q^2 f^2) \quad (68)$$

for $q = 1$. In axes pointing toward the principal directions of matrix orthotropy, the invariant h admits the following expression:

$$h = 2 \left[\frac{2}{5} \frac{h_1 + h_2 + h_3}{h_1 h_2 + h_2 h_3 + h_3 h_1} + \frac{1}{5} \left(\frac{1}{h_4} + \frac{1}{h_5} + \frac{1}{h_6} \right) \right]^{\frac{1}{2}} \quad (69)$$

In the case of an isotropic matrix, $\mathbb{h} = \mathbb{I}$ so that $h = 2$ and the Gurson yield function is retrieved. In the case of a dense matrix ($f = 0$) criterion (68) reduces to Hill's quadratic criterion. Note that the appearance of the mean normal stress Σ_{m} in the exponential term of (68) comes from the fact that the chosen velocity field is spherically symmetric. The exact velocity field is in general not so, because of plastic anisotropy of the matrix.

Matrix plastic flow anisotropy has in general a direct effect on the rate of void growth. Formally, equation (52) applies for the anisotropic model with equivalent quantities Σ_{eq}

and D_{eq} defined according to Hill as in (66). On that basis, Benzerga and Besson (2001) have shown that the rate of growth of porosity associated with their criterion is given by

$$\frac{\dot{f}}{f(1-f)} = \frac{3}{h} \frac{\bar{\sigma}}{\Sigma_{\text{eq}}} \sinh \left(\frac{3}{h} \frac{\Sigma_{\text{m}}}{\bar{\sigma}} \right) D_{\text{eq}}^{\text{p}} \quad (70)$$

Therefore, matrix anisotropy affects void growth in two ways: through the scalar h and the ratio $\Sigma_{\text{eq}}/D_{\text{eq}}^{\text{p}}$. Note that small variations in the anisotropy factor h are significant because of the exponential dependence in (70). Different materials will generally have different values of the anisotropy factor h . Benzerga (2000) has tabulated the values of h for over 30 thin and thick-sheet engineering materials. For the materials considered h was found to vary between 1.6 and 2.4. For the special case of planar isotropy, as considered for example in the cell model calculations in Figs. 20 and 21, Fig. 39 shows typical variations of the anisotropy factor with the plastic strain ratios R (in-plane) and R_h (off-axes and out of plane). For a given material, the magnitude of h will affect the

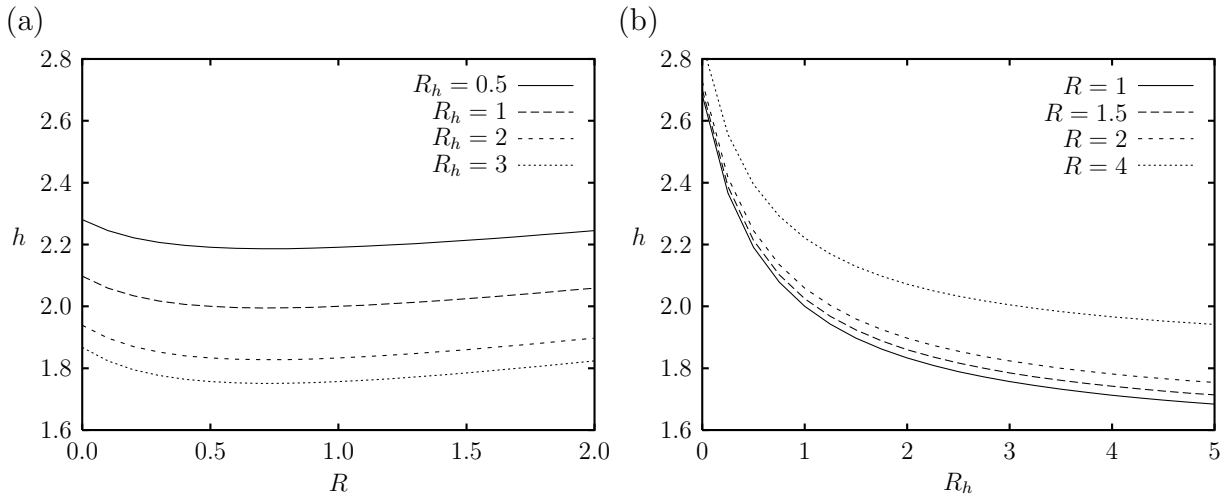


Figure 39: Variation of anisotropy factor h in (69) in the special case of planar isotropy. (a) h versus in-plane strain ratio R . (b) h versus off-axes strain ratio R_h . (Benzerga and Besson, 2001).

average rate of void growth. On the other hand, the ratio $\Sigma_{\text{eq}}/D_{\text{eq}}^{\text{p}}$ will eventually lead to damage anisotropy since the value taken by Σ_{eq} depends on the loading orientation.

Benzerga and Besson (2001) carried out a series of comparisons between cell model results and predictions by their model. Elasticity and hardening were incorporated in the same way as in the previous sections. Figure 40 shows the performance of their model using $q = 1.3$ and material parameters from Table 2 for matrices endowed with transversely isotropy about an axis \mathbf{e}_3 , as in Section 3.2. The results are shown at a stress triaxiality of $T = 3$ but similar trends were obtained at other triaxialities ($T \geq 1$) using the same value of q . The cell model results were shown earlier in Fig. 20c-d, including the void coalescence stage. The value of $T = 3$ is chosen here to emphasize the fact that plastic anisotropy effects persist at high triaxialities. The value of the Tvergaard

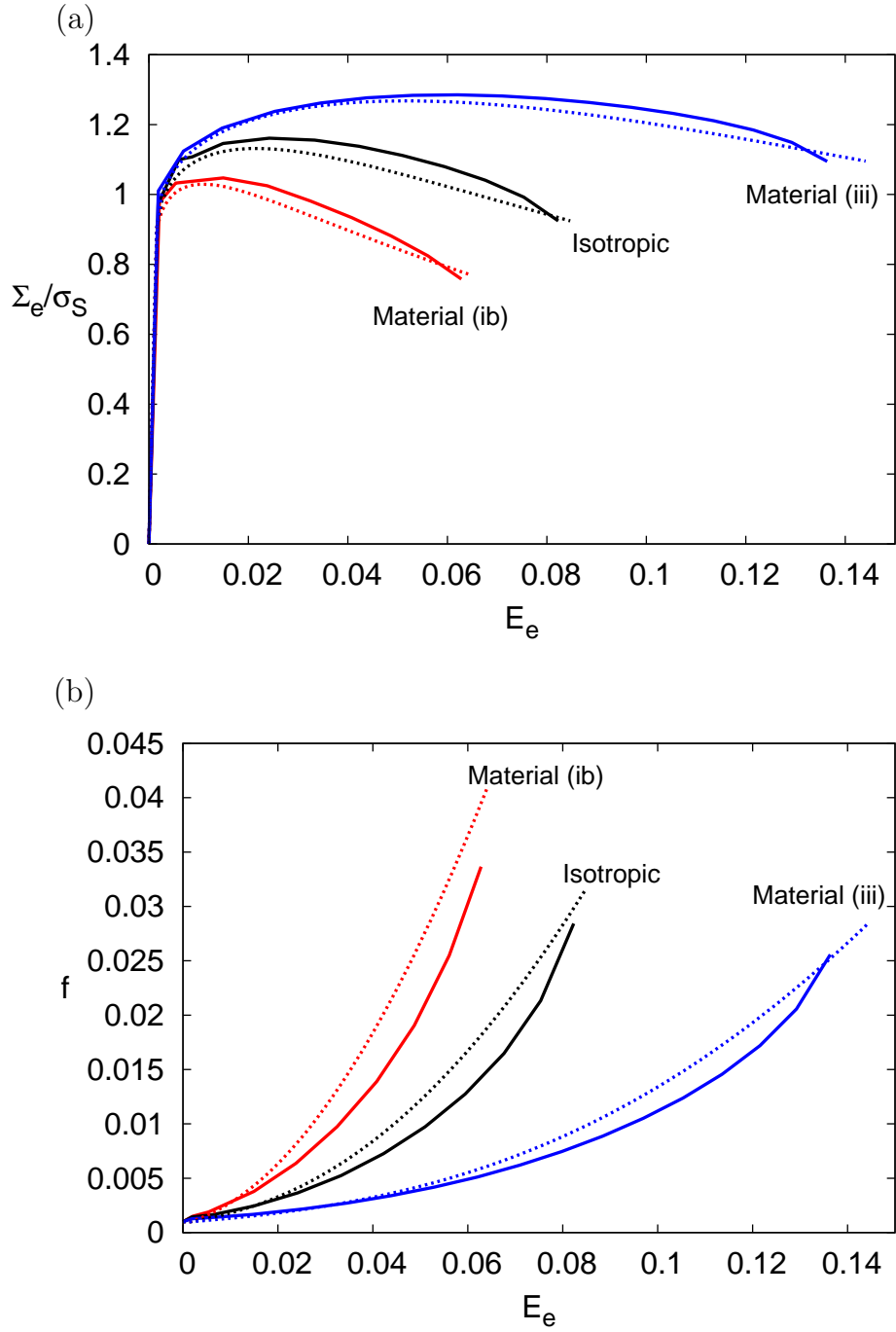


Figure 40: Comparison of predictions using the Benzerga and Besson model (dashed lines, $q = 1.3$) with results of unit-cell calculations (solid lines) for an initially spherical void in a transversely isotropic matrix (Table 2) and $T = 3$. (a) Effective stress, Σ_e , normalized by the matrix yield stress in loading along \mathbf{e}_S , versus effective strain, E_e . (b) void volume fraction versus E_e .

parameter $q = 1.3$ was chosen so as to obtain a good correspondence between the model predictions and the cell model results in the case of an isotropic matrix. Note that this is the same value used for assessment of the Gurson model in Fig. 33. The results in Fig. 40

indicate that the Benzerga and Besson model predicts very well the plastic anisotropy effects on the stress-strain curve and on void growth for both materials considered.

Benzerga and Besson (2001) also generalized Gurson's criterion for cylindrical cavities to transversely isotropic matrix materials. In the case of planar isotropy ($h_1 = h_2 = h_6$) their cylindrical criterion reduces to the model of Liao et al. (1997), which was developed under plane stress conditions.

6.4 Combined Plastic Anisotropy and Void Shape Effects

The continuum models described above capture separately void shape effects and plastic anisotropy effects reasonably well. When both are present in the same material, the combined effect is, however, not necessarily the superposition of the two effects. Even for mild forms of anisotropy, cell model studies have illustrated such nontrivial couplings; see Fig. 21. The homogenization problem combining the two kinds of anisotropies has been addressed by a number of authors in recent years. Thus, Monchiet et al. (2006, 2008) developed a solution based on consideration of the velocity fields used by Gologanu et al. (1993, 1994a) in their earlier versions of the GLD model, and Keralavarma and Benzerga (2008) developed an improved solution using the richer Lee–Mear fields used by Gologanu et al. (1997). The latter model is, however, restricted to axisymmetric loadings and microstructures for which the void axis is aligned with one direction of material orthotropy.

Quite recently, Keralavarma and Benzerga (2010) have developed a new approximate yield function applicable to *non-axisymmetric* loadings and to circumstances where the void axis \mathbf{e}_3 is no longer constrained to be aligned with a principal direction of orthotropy. In this model, the basic ingredients entering homogenization problem $\{(27), (40)\}$ are: (i) spheroidal RVEs (oblate or prolate) similar to those considered in the GLD model (Fig. 32d); (ii) Hill's plasticity model (66) for the matrix with L, T and S referring to the principal directions; and (iii) a two-field trial velocity consisting of a linear field and four terms in the Lee–Mear expansion field. In addition, the uniform deformation field β in (44) was not required to be axisymmetric. The approximate yield condition derived is of the form $\Phi^{\text{KB}}(\Sigma; f, w, \mathbf{e}_3, \mathbb{h}) = 0$ with

$$\Phi^{\text{KB}} = C \frac{3}{2} \frac{\Sigma : \mathbb{H} : \Sigma}{\bar{\sigma}^2} + 2(g+1)(g+f) \cosh \left(\kappa \frac{\Sigma : \mathbf{X}}{\bar{\sigma}} \right) - (g+1)^2 - (g+f)^2 \quad (71)$$

where the macroscopic anisotropy tensor \mathbb{H} is related to the microscopic one \mathbb{h} through:

$$\mathbb{H} \equiv \mathbb{J} : \mathbb{h} : \mathbb{J} + \eta(\mathbf{X} \otimes \mathbf{Q} + \mathbf{Q} \otimes \mathbf{X}) \quad (72)$$

Here, \mathbf{X} and \mathbf{Q} are defined as in (60) and criterion parameters κ , C and η are scalar valued functions of microstructural parameters (f and w) and of \mathbb{h} , whereas α_2 and g are only functions of f and w . The independence of α_2 upon plastic anisotropy is an approximation. The latter is relaxed in a version of the model valid only for axisymmetric loadings. The complete expressions of the criterion parameters can be found in (Keralavarma and

Benzerga, 2010). For example, a simplified expression of κ is

$$\kappa = \begin{cases} \frac{3}{h} \left\{ 1 + \frac{h_t}{h^2 \ln f} \ln \frac{1 - e_2^2}{1 - e_1^2} \right\}^{-1/2} & \text{(p)} \\ \frac{3}{h} \left\{ 1 + \frac{(g_f - g_1) + \frac{4}{5}(g_f^{5/2} - g_1^{5/2}) - \frac{3}{5}(g_f^5 - g_1^5)}{\ln(g_f/g_1)} \right\}^{-1} & \text{(o)} \end{cases} \quad (73)$$

where (p) and (o) stand for prolate and oblate, respectively, and $g_x \equiv g/(g + x)$. The dependence of the criterion parameters upon anisotropy tensor \mathbb{h} enters through one invariant, h , and two transversely isotropic invariants, h_t and h_q , of that tensor. When expressed in the basis associated with the principal directions of orthotropy⁶, invariant h is given by (69) while h_t is given by:

$$h_t = \frac{1}{5} \left[-\frac{13}{12}(\hat{h}_L + \hat{h}_T) + \frac{8}{3}\hat{h}_S + 4(\hat{h}_{TS} + \hat{h}_{SL}) - \frac{7}{2}\hat{h}_{LT} \right] \quad (74)$$

Here, the \hat{h}_i are the components of $\hat{\mathbb{h}}$ expressed using Voigt's condensation. Finally, h_q only appears in the expressions of C and η and need not be provided here (it was denoted \hat{h}_q in (Keralavarma and Benzerga, 2010)).

In the special case of an isotropic Von Mises matrix ($\mathbb{h} = \hat{\mathbb{h}} = \mathbb{I}$) the yield condition (71) reduces to the GLD criterion. In the case of spherical voids in a Hill matrix, one obtains $\lim_{w \rightarrow 1} \alpha_2 = 1/3$, $C = 1$ and $\eta = 0$. Also, (73) reduces to $\kappa^{\text{BB}} \equiv 3/h$ and the upper-bound yield criterion of Benzerga and Besson (2001) is recovered. In particular, the Gurson yield function is obtained in the limit of spherical voids in an isotropic matrix since $\mathbb{h} = \mathbb{I}$ implies $\kappa^{\text{BB}} = 3/2$. In the limit of cylindrical voids in a Hill matrix with $\mathbf{e}_S = \mathbf{e}_3$, we have $\lim_{w \rightarrow \infty} \alpha_2 = 1/2$, $C = 1$, $\eta = 0$ and (73) reduces to

$$\kappa^{\text{cyl}} = \sqrt{3} \left[\frac{1}{4} \frac{h_L + h_T + 4h_S}{h_L h_T + h_T h_S + h_S h_L} + \frac{1}{2h_{LT}} \right]^{-\frac{1}{2}} \quad (75)$$

which is the result obtained by Benzerga and Besson (2001). In particular, the Gurson yield function for cylindrical cavities in a Von Mises matrix is recovered with $\kappa^{\text{cyl}} = \sqrt{3}$ in that case.

Keralavarma and Benzerga (2010) supplemented yield criterion (71) with evolution laws for the microstructural variables f , w and the void axis \mathbf{e}_3 . The first two are in essence similar to those used in the GLD model but the latter one employs an Eshelby concentration tensor for the spin following a proposal by Kailasam and Ponte Castaneda (1998).

Because this new model reduces to the GLD model in the case of isotropic matrices, it inherits its predictive capabilities in that case, as shown for example in Figs. 36–38. The new model also captures the quantitative trends shown in Fig. 40 in the case of spherical voids embedded in a Hill matrix. Figure 41 shows some additional comparisons between

⁶In the context of this section, this means replacing indices 1 to 6 in (69) with L, T, S, TS, SL and LT, respectively.

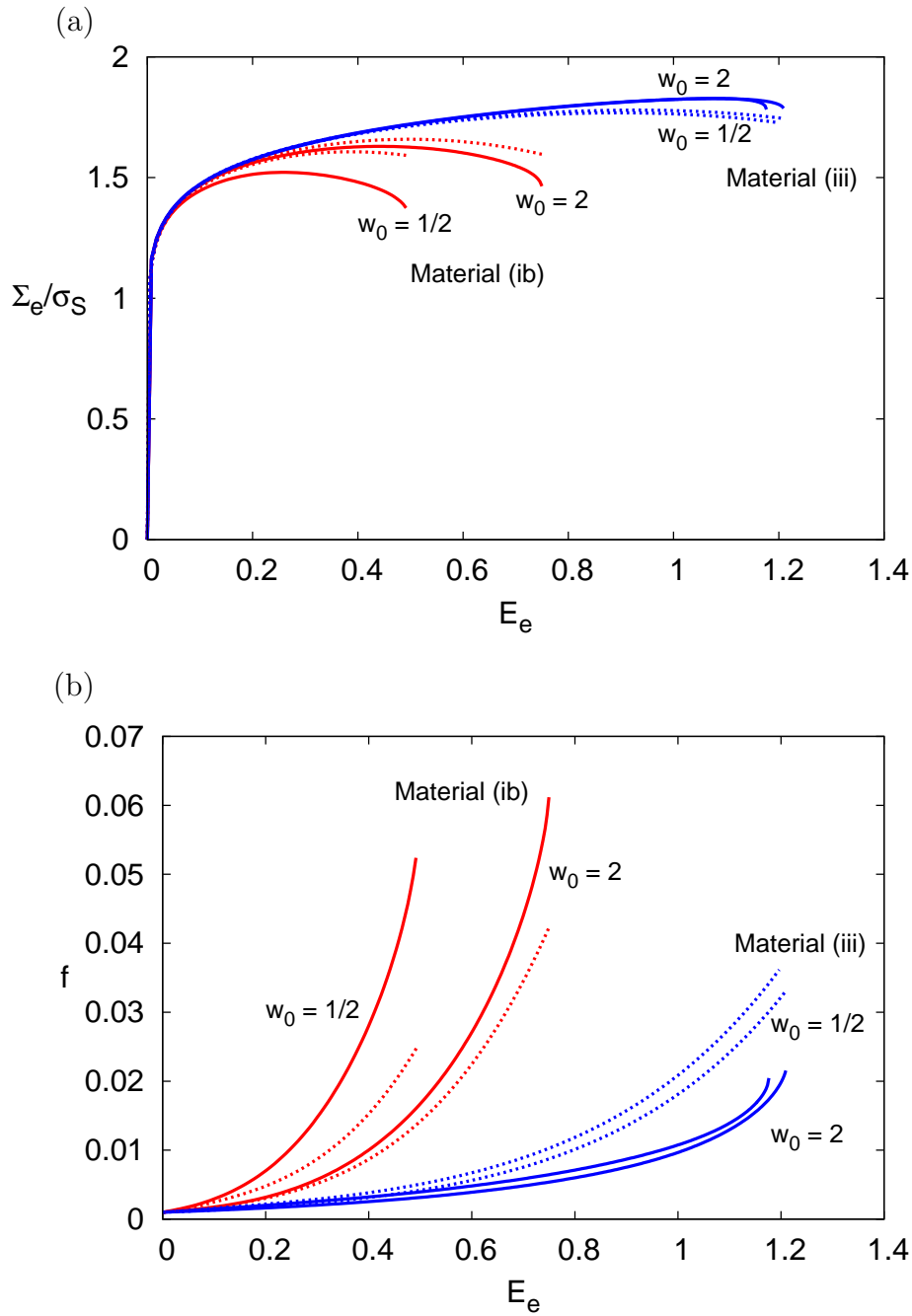


Figure 41: Comparison of predictions using the Keralavarma and Benzerga model (dashed lines, $q = 1.5$) with results of unit-cell calculations (solid lines) for three values of w_0 and two transversely isotropic matrix materials (Table 2) and $T = 1$. (a) Effective stress, Σ_e , normalized by the matrix yield stress in loading along \mathbf{e}_S , versus effective strain, E_e . (b) void volume fraction versus E_e .

the model predictions, with extensions to elasticity and hardening as above, and the cell model response for a triaxiality $T = 1$ and material parameters from Table 2. Using a value of 1.5 for the Tvergaard parameter in all predictions, the model was found to pick up the combined effect of void shape and plastic anisotropy. In particular, the effect of

void shape was found to prevail in the case of material (ib), just like for the isotropic matrix. On the other hand, the effect of void shape was swamped by plastic anisotropy in the case of material (iii). Predictions such as those in Fig. 41 could not be made by simply superposing the GLD model with the Benzerga and Besson model. The reason for the good quantitative performance of the enhanced model can be traced to an equation similar to (65) for the rate of porosity with κ given by (73). Hence, the effect of the scalar invariant h of fourth-order tensor \mathbb{h} , as given by (69), enters through κ .

The results shown above correspond to axisymmetric loadings. For more general loadings, Keralavarma and Benzerga (2010) have determined the yield surfaces corresponding to criterion (71) for various loading orientations with respect to the void axes and the principal directions of orthotropy (L,T,S). They considered two loading cases (L_1 and L_2)

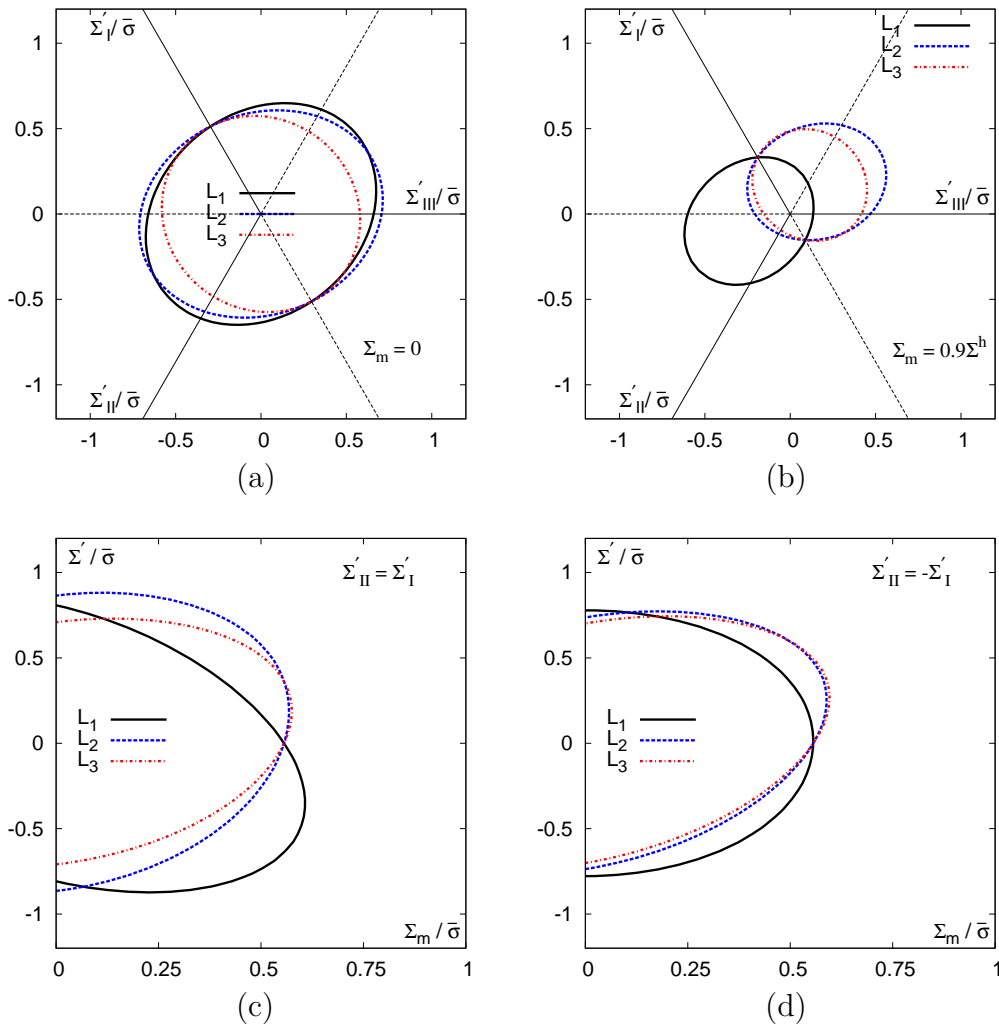


Figure 42: Cross-sections of yield surfaces given by (71) for $f = 0.1$, $w = 1/5$ and material Ti from Table 2 and for three loading orientations L_1 – L_3 (see text). (a) π -plane with $\Sigma_m = 0$, (b) π -plane with $\Sigma_m = 0.9\Sigma^h$, (c) axisymmetric loading, (d) in-plane shear with superposed hydrostatic stress. (Keralavarma and Benzerga, 2010).

where the principal directions of loading, $(\mathbf{e}_I, \mathbf{e}_{II}, \mathbf{e}_{III})$, are aligned with (L,T,S) and one off-axis loading L_3 . Also, the voids were misaligned with respect to the material with

the void axis given by $\mathbf{e}_3 = 1/7(2\mathbf{e}_L + 3\mathbf{e}_T + 6\mathbf{e}_S)$. The results are better illustrated in the case of oblate cavities and a relatively large value of the porosity $f = 0.1$. Various cross-sections of the rather complex yield surfaces are shown in Fig. 42 where the stresses are normalized by the yield stress of the matrix material under uniaxial tension in the \mathbf{e}_S direction of orthotropy. Fig. 42a shows cross-sections in the π -plane at zero hydrostatic pressure for all three loading orientations. The oval shape of the yield surfaces is the result of plastic anisotropy. For a nonzero superposed hydrostatic pressure, the cross-sections of the yield surfaces appear smaller and translated from the origin because of the high distortion (Fig. 42b). In the figure, Σ^h designates the yield stress of the effective medium under pure hydrostatic loading. The apparent translation of the yield surfaces in Fig. 42b is mainly due to the nonspherical void shape, with the direction of the translation depending on the loading orientation. Fig. 42c shows the yield surfaces under axisymmetric loadings of the type: $\Sigma = \Sigma_m \mathbf{I} + \Sigma'/3(-\mathbf{e}_I \otimes \mathbf{e}_I - \mathbf{e}_{II} \otimes \mathbf{e}_{II} + 2\mathbf{e}_{III} \otimes \mathbf{e}_{III})$. Unlike for spherical voids, these yield loci do not exhibit symmetry with respect to either coordinate axis. Finally, Fig. 42d shows the yield surfaces corresponding to in-plane shear loading with a superposed hydrostatic stress, $\Sigma = \Sigma_m \mathbf{I} + \Sigma'/\sqrt{3}(\mathbf{e}_I \otimes \mathbf{e}_I - \mathbf{e}_{II} \otimes \mathbf{e}_{II})$. Note that the Von Mises effective stress $\Sigma_e = |\Sigma'|$. Interestingly, one can show that the rate of growth of porosity is non zero under in-plane or pure shear loadings for non-spherical voids.

6.5 Viscoplastic Model

A number of authors have proposed models analogous to that of Gurson but for rigid nonlinearly viscous materials obeying the Norton law (28). Interesting proposals have notably been made by Duva and Hutchinson (1984), Duva (1986), Cocks (1989), Michel and Suquet (1992) and Licht and Suquet (1988a,b). Duva and Hutchinson (1984)'s model was based on Budiansky et al. (1982)'s approximate study of growth of spherical voids in viscous materials and played the same role with respect to it, within the context of viscoplasticity, as Gurson's model with respect to Rice and Tracey (1969)'s paper in the context of rate-independent plasticity. The potential proposed by Duva (1986) corresponded to a gauge function identical to Gurson's yield function; this approximation is quite good when the Norton exponent n is large, but poor when it is small. Licht and Suquet (1988a,b)'s approximation consisted of an interpolation formula linking up the exact asymptotic expressions of the potential for very small and very large triaxialities. It is a good approximation when n is neither too small nor too large. The proposals of Cocks (1989) and Michel and Suquet (1992) were to adopt a quadratic gauge function; the conditions of validity of this approximation are exactly opposite to those of Duva (1986)'s model.

None of the models just quoted did simultaneously satisfy the three following natural requirements:

- be defined by a macroscopic potential quadratic in Σ for $n = 1$ (as required by linearity in that case);
- reduce to Gurson's criterion and the associated flow rule for an ideal-plastic matrix ($n = +\infty$);

- reproduce the exact solution of a hollow sphere loaded in hydrostatic tension or compression, namely

$$D_m = \frac{\dot{\epsilon}_0}{2} \operatorname{sgn}(\Sigma_m) \left(\frac{3}{2n} \frac{|\Sigma_m|/\sigma_0}{f^{-1/n} - 1} \right)^n \quad (76)$$

where $D_m \equiv \frac{1}{3} \operatorname{tr} \mathbf{D}$ and $\Sigma_m \equiv \frac{1}{3} \operatorname{tr} \mathbf{\Sigma}$. Solution (76) is valid whatever the values of the porosity f and the Norton exponent n .

Leblond et al. (1994b) have proposed a model satisfying these conditions using an heuristic approach based on the notion of gauge surface, factor and function. The approximate gauge function chosen was given by

$$\begin{cases} \bar{\Psi}(\mathbf{S}) & \equiv \left(1 + \frac{2f}{3}\right) Q^2 + f \left[h(M) + \frac{n-1}{n+1} \frac{1}{h(M)} \right] - 1 - \frac{n-1}{n+1} f^2, \\ h(M) & \equiv \left[1 + \frac{1}{n} \left(\frac{3|M|}{2} \right)^{\frac{n+1}{n}} \right]^n. \end{cases} \quad (77)$$

where

$$Q \equiv \frac{\Sigma_{eq}}{\Lambda(\mathbf{\Sigma})} \quad \text{and} \quad M \equiv \frac{\Sigma_m}{\Lambda(\mathbf{\Sigma})} \quad (78)$$

with the notations of Section 5.3. This expression can be checked to not only satisfy

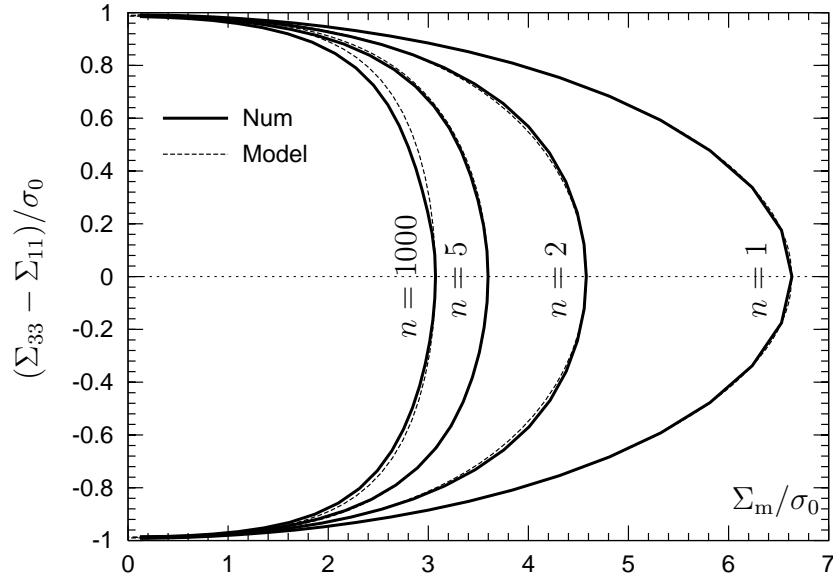


Figure 43: Gauge surfaces for a spherical void and a porosity of 0.01. After (Leblond et al., 1994b).

the three above conditions⁷, but also match, to first order in the porosity, the “nonlinear Hashin–Shtrikman bound” established by Ponte Castaneda (1991), Willis (1991) and Suquet (1992).

⁷For an ideal-plastic material ($n = +\infty$), Gurson’s criterion is retrieved with an additional $1 + \frac{2f}{3}$ factor multiplying Σ_{eq}^2 , which improves its predictions at low triaxialities.

Figure 43 shows the approximate gauge surface proposed by Leblond et al. (1994b) in the case of an axisymmetric loading, for a porosity of 0.01 and several values of the Norton exponent. Results obtained numerically through the variational characterization of the macroscopic stress potential, using a large number of trial velocity fields, are also shown. The model satisfactorily reproduces the numerical, presumably exact gauge surface. Another point of interest is the slight dissymmetry of the numerical gauge surface about the horizontal axis for $n = 1000$ (ideal-plastic material), which was remarked by Gologanu (1997) to denote a small influence of the third invariant of the stress tensor upon the macroscopic yield surface, disregarded by Gurson's approximate expression. This influence, which is related to the effect of the Lode parameter, was already commented upon in Section 3.2 above.

Klöcker and Tvergaard (2003) extended Leblond et al. (1994b)'s model by considering spheroidal voids instead of spherical ones. Their approach was thus similar, except that the "reference model" used in the ideal-plastic case ($n = +\infty$) was the GLD model instead of that of Gurson. However their model violated the nonlinear Hashin-Shtrikman bound in some cases. Flandi and Leblond (2005a) have proposed an alternative model respecting this additional condition.

Figure 44 shows the approximate gauge surface proposed by Flandi and Leblond (2005a) in the case of an axisymmetric loading, for a Norton exponent of 5, a porosity of 0.01 and w -values of $1/5$, 1 and 5, together with the results of some numerical calculations. Flandi and Leblond (2005a)'s model gives quite acceptable results in all cases but the greater difficulty of dealing with oblate voids than with prolate ones is clearly apparent here.

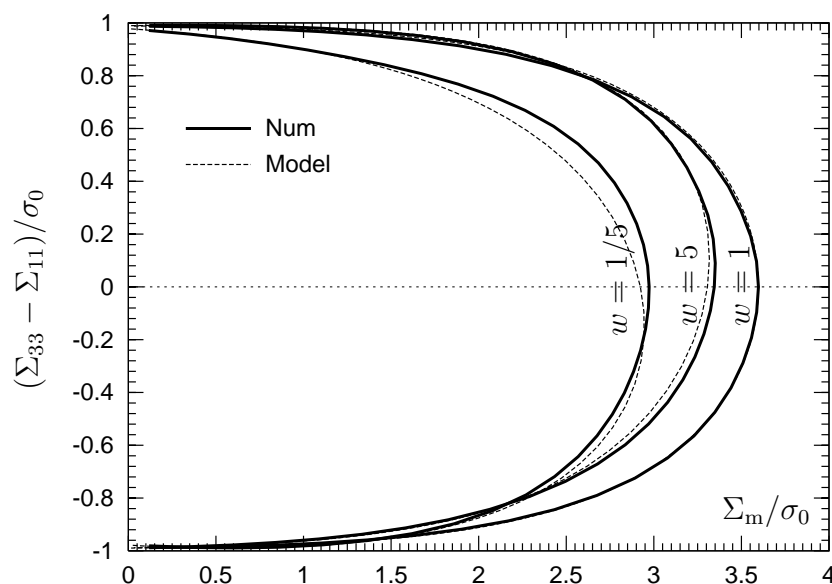


Figure 44: Gauge surfaces for a Norton exponent of 5 and a porosity of 0.01

Finally, Fig. 45 shows the results of some FE micromechanical simulations of the behavior of a cylindrical RVE containing an initially spherical void, already cited in Section 3.2.2 above. The predictions of Flandi and Leblond (2005a)'s model satisfactorily match the numerical results during the pre-coalescence phase. (The correct reproduc-

tion of the coalescence phase requires important modifications of the model sketched in Section 7 below).

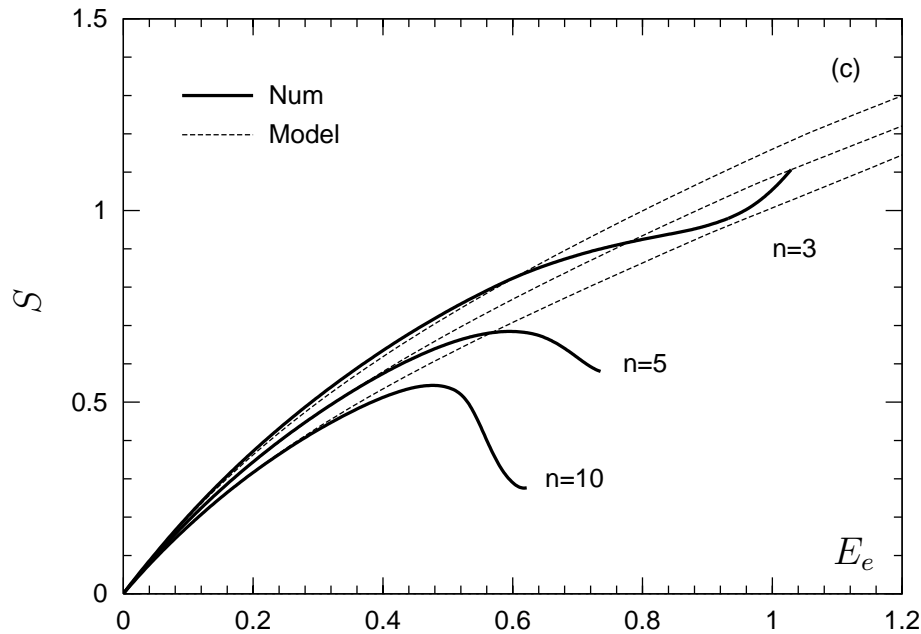


Figure 45: Influence of Norton's exponent. Comparison between cell model results for $T = 1$, $f_0 = 0.0104$ and $w_0 = 1$ and the viscoplastic model of Flandi and Leblond (2005a). Void shape parameter, S versus effective strain, E_e . The effective stress versus E_e and porosity versus E_e were shown earlier in Fig. 23.

7 Void Coalescence Models

It has long been known that stable and diffuse plastic flow in a porous matrix would lead to void impingement at strains that are, in general, far in excess of measured or computed strains to fracture. Ductile failure ultimately takes place because of plastic flow localization in the intervoid matrix. For that reason, the void growth models of the previous section may not be adequate to describe complete material failure. Cell model studies, such as those documented in Section 3, clearly establish the transition from diffuse to localized plastic flow. Substantial void growth and important microstructural changes may precede localization (see e.g. Fig. 16). However, void growth may not be necessary for localization to set in, for instance under remote shear loading, especially when void-particle interactions are taken into account.

The transition to localized plastic flow is conventionally referred to as the onset of void coalescence⁸. As shown in Fig. 16b, the amount of void growth that takes place post localization is much more important than before it. For initial porosities representative of structural materials (between 10^{-5} and 10^{-3}) and a wide variety of other parameter ranges, the porosity at the onset of coalescence is about 0.01 to a few percent whereas the

⁸The abuse of language is apparent here as the usage of the term “coalescence” is distinct from it in other branches of physics, e.g., bubble coalescence.

porosity at complete failure is typically 0.2 or less. In particular, failure criteria that are based on mere attainment of some localization condition are inadequate. At the onset of coalescence, the voids are generally still far apart (e.g. see Fig. 19) and the stress levels are high. Therefore, there is a need for models describing the gradual loss of stress bearing capacity during the post-localization regime.

This section is devoted to models of void growth in the post-localized regime, in brief, to models of void coalescence. Rate-independent models that fit within the framework outlined in Section 5 are presented here. At this juncture, a note on boundary conditions is in order. Boundary conditions of uniform rate of deformation cannot lead to localized plastic flow. On the other hand, the boundary conditions that are typically employed in finite-element cell model studies, i.e., either mixed or periodic, are not conditions of uniform rate of deformation. Therefore, localization is possible with this type of conditions. Under such circumstances, we shall define macroscopic measures of stress and rate of deformation as volume averages of their microscopic counterparts. We shall continue to define the macroscopic yield surface by (27) with plastic dissipation Π given by (40). The exact velocity fields that would emerge from a complete solution, for example using computational limit analysis, would eventually be discontinuous thus indicating the onset of localization and formation of regions of elastic unloading (or rigid zones, depending on the context). The quest for approximate, closed-form solutions entails, however, that the microscopic velocity fields are an input, not an output, of the analysis. One is then content by the fact that the choice of incompressible, kinematically admissible velocity fields leads to an upper bound of the yield locus, for the specified boundary conditions.

Existing models of void coalescence are classified based on the type of localization. When the latter occurs in ligaments perpendicular to one major normal stress, it is referred to as coalescence in layers. This encompasses the most commonly observed mode of void coalescence by internal necking. Other modes include the coalescence in columns and in thin, eventually inclined bands (see Fig. 9 for reference). In this regard, the main effect of the Lode parameter (see Sections 2 and 3) is through the mode of void coalescence.

7.1 Coalescence in Layers

This mode of void coalescence corresponds to a Lode parameter $\mu = -1$. The commonality among all models of coalescence in layers is that the boundary condition is one which is consistent with an overall pure extension of the RVE in the axial x_3 direction, i.e., such that

$$D_{11} = D_{22} = 0 \quad (79)$$

Also, all models assume a Von Mises yield criterion for the matrix. The models differ from each other on at least one of two ingredients: the geometry of the RVE and the microscopic velocity fields.

7.1.1 Thomason's Model

The idea that metals fracture prematurely by a process of internal necking goes back as early as 1855, according to Argon et al. (1975). Apparently, Thomason (1968) was the first to attempt to model the onset of internal necking by attainment of some plastic limit

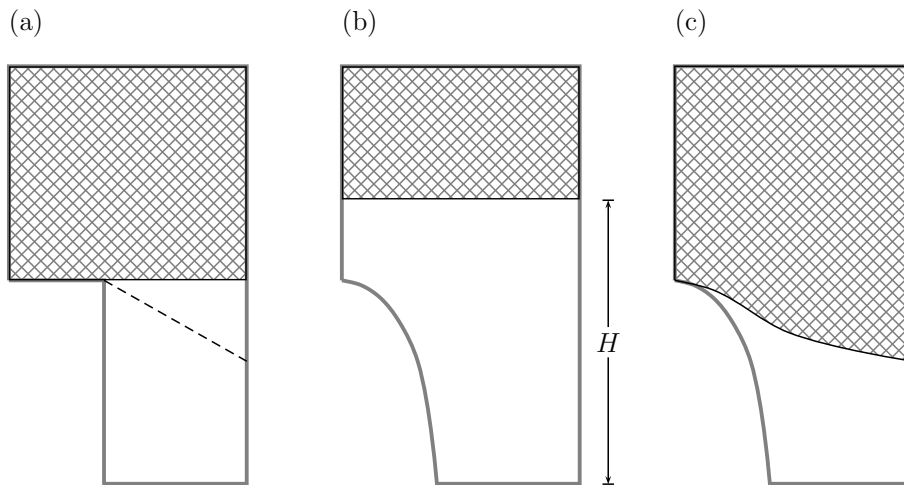


Figure 46: Geometry of representative elements considered in the void coalescence models of (a) Thomason (1985b), Pardoen and Hutchinson (2000); (b) Gologanu (1997), Gologanu et al. (2001b); and (c) Benzerga (2000, 2002).

load in the intervvoid ligament. But his early model was two-dimensional, hence of limited scope. Thomason (1985b) considered a square-prismatic RVE containing a cylindrical void with a square basis. His RVE was made up of rigid zones above and below the void with plastic flow contained in between, as sketched in Fig. 46a. Drawing along the lines of a treatment by Kudo (1960), he then devised two incompressible velocity fields, one “parallel”, the other “triangular”. Both are kinematically admissible, i.e., compatible with boundary condition (79). In the case of a parallel velocity field, the plastic zone is bounded by parallel planes at the top and the bottom. In the case of the triangular field, the plastic zone is limited by inclined planes (dashed line in Fig. 46a). For each case, Thomason calculated an upper-bound estimate for the maximum axial stress, Σ_{33}^{\max} , that would lead to plastic flow in the intervvoid ligaments alone. Approximate analytical expressions were seemingly too complex and were not provided⁹. Little technical detail was given and it is likely that some of the approximations were uncontrolled, i.e., not strictly upper-bound preserving¹⁰. The numerical results were also compared with those adapted from an early work by Kudo (1960) using axisymmetric velocity fields. The two sets of results were found to be very close. Thomason finally proposed a closed-form empirical expression for the limit-load constraint factor C_f^T that provided the best fit to his and Kudo’s numerical results. C_f^T is defined as the maximum axial stress supported by the top surface of the localization zone divided by the matrix yield stress. It strongly depends on the microstructural state. Typically, the values of Σ_{33}^{\max} are two to four times the matrix flow stress.

Benzerga et al. (1999) have evaluated the performance of various versions of Thomason’s model, depending on how microstructure evolution is represented. As in later work (Pardoen and Hutchinson, 2000), the model was heuristically extended to spheroidal voids

⁹The beginner in this field may first examine Kudo’s (1960) solution which contains all the mathematical details.

¹⁰Recently, Benzerga (2010) has developed rigorous upper-bound solutions in closed form.

by identifying the void aspect ratio w with the height-to-diameter ratio of Thomason's cylindrical void. Using the notation of Benzerga et al. (1999) the expression of the limit-load constraint factor C_f^T is:

$$C_f^T \equiv \frac{A}{A_{\text{lig}}} \frac{\Sigma_{33}^{\text{max}}}{\bar{\sigma}} = \alpha \left(\frac{\chi^{-1} - 1}{w} \right)^2 + \beta \sqrt{\chi^{-1}} \quad (80)$$

with $\alpha = 0.1$, $\beta = 1.2$ and $\bar{\sigma}$ the matrix flow stress as above. The ratio A/A_{lig} of top area to ligament area enters (80) because of the precise definition of C_f^T above and χ is the ratio of lateral void diameter to lateral void spacing. Thus, χ is a measure of ligament size ratio so that $\chi = 1$ entails void impingement. It is related to the other independent microstructural variables through

$$\chi = \left[\frac{3}{2} \frac{f}{w} \lambda \right]^{1/3} \quad (81)$$

where f and λ are the porosity and RVE aspect ratio as in Section 3. For a non-hardening matrix and proportional stressing histories at constant triaxiality T , the void coalescence condition writes:

$$(1 - \chi^2) C_f^T = \left(\frac{2}{3} + T \right) \frac{\Sigma_{\text{eq}}}{\bar{\sigma}} \quad (82)$$

Evaluation of this condition requires a void growth model prior to localization, providing the evolution of porosity, void shape and remote stress field. The outcome of the analysis consists of estimates of the strain to coalescence, E_c^c , and the porosity f_c at incipient localization.

Fig. 47b shows the predicted critical porosity f_c as a function of stress triaxiality for various values of the initial void volume fraction f_0 of initially spherical voids. The results were obtained using the Gurson model for the pre-coalescence phase, as proposed earlier by Zhang and Niemi (1994), thus neglecting void shape evolution. The results shown in Fig. 47a correspond to an alternative model of coalescence in layers due to Perrin (1992). The general trends being the same for both models, we shall only discuss the predictions of the adapted Thomason coalescence condition (82). There is some variation of f_c with stress triaxiality. This is qualitatively consistent with findings from cell model studies (Koplik and Needleman, 1988; Brocks et al., 1995; Pardoen and Hutchinson, 2000). At high stress triaxialities, there is a tendency for all curves to asymptote to a value close to 0.015, irrespective of the initial porosity.

There is no length scale in coalescence condition (82). In particular, the criterion is independent of the absolute height of the cylindrical RVE. This is explained by the fact that the height of the rigid zone has no influence on the state of stress in the ligaments. However, the RVE aspect ratio λ enters the criterion through the ligament size ratio χ in (81). Benzerga et al. (1999) have also shown the predictions of criterion (82) for various values of λ_0 , in keeping with cell model results, such as those shown in Fig. 17. These and other results in the literature indicate that while the relative spacing of voids has no effect on void growth prior to localization, it does affect the onset of coalescence to a great extent.

The results shown in Fig. 47 were based on the assumption that voids remained spherical throughout. This is clearly a crude approximation, which leads to a loss of accuracy

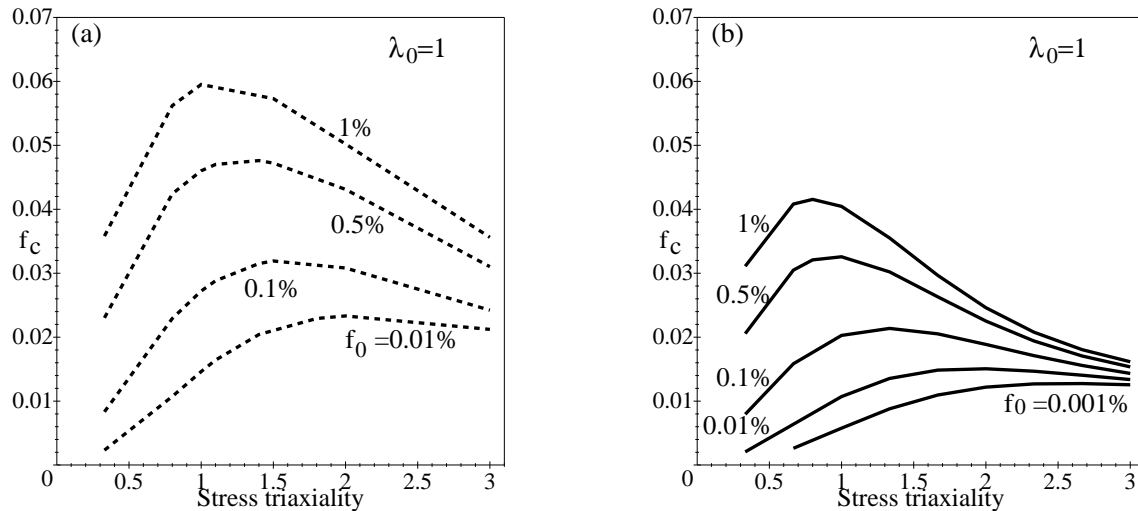


Figure 47: Dependence of the critical porosity f_c on the stress triaxiality T for various values of f_0 : (a) using the Gurson model and a coalescence condition due to Perrin (1992); (b) using the Gurson model and coalescence condition (82). After (Benzerga et al., 1999).

at stress triaxialities lower than, say 1.5 (see Fig. 37). Better predictions are obtained when coalescence condition (82) is used in conjunction with the GLD model presented in Section 6.2. Fig. 48a shows the predicted critical porosity f_c as a function of stress triaxiality for initially spherical voids ($w_0 = 1$) and two extreme values of the initial porosity f_0 . The value used for the q parameter was 1.6. Under uniaxial loading ($T = 1/3$) no void coalescence is predicted when void shape evolution is taken into account. This is in agreement with the cell model predictions (e.g. see Fig. 16) and will be explained further below. By way of contrast, use of the Gurson model predicts that localization is possible. This example illustrates the kind of erroneous trends obtained when neglecting void shape effects. Comparison with the results of Fig. 47b indicates that the predicted values of f_c are generally higher when void shape evolution is taken into account.

It is apparent from Fig. 48a that the correction brought by the GLD model at high stress triaxiality is minute, as expected. More extensive results were obtained in the case of initially spheroidal voids with the major load parallel to the void axis. As shown in Fig. 48b, at a stress triaxiality of 1.33 the effect of initial void shape on the coalescence strain is already important. Results are reported for initial isotropic distributions of voids, as well as for initially anisotropic distributions with $\lambda_0 = 3$. At all stress triaxialities, increasing the vertical to lateral spacing ratio leads to a decrease in ductility. Both the values of f_c and E_e^c are in good to excellent agreement with cell model studies for nonhardening materials (Koplik and Needleman, 1988; Sovik and Thaulow, 1997; Pardoen and Hutchinson, 2000).

The collection of results in terms of macroscopic strains to coalescence and microscopic critical porosities is useful for comparing various materials and analyzing trends. However, the onset of void coalescence may not be an adequate failure criterion. At high stress triaxiality the amount of overall strain accumulated post-localization is comparable with the strain to coalescence, if not larger. Apparently, this point was missed by Thomason

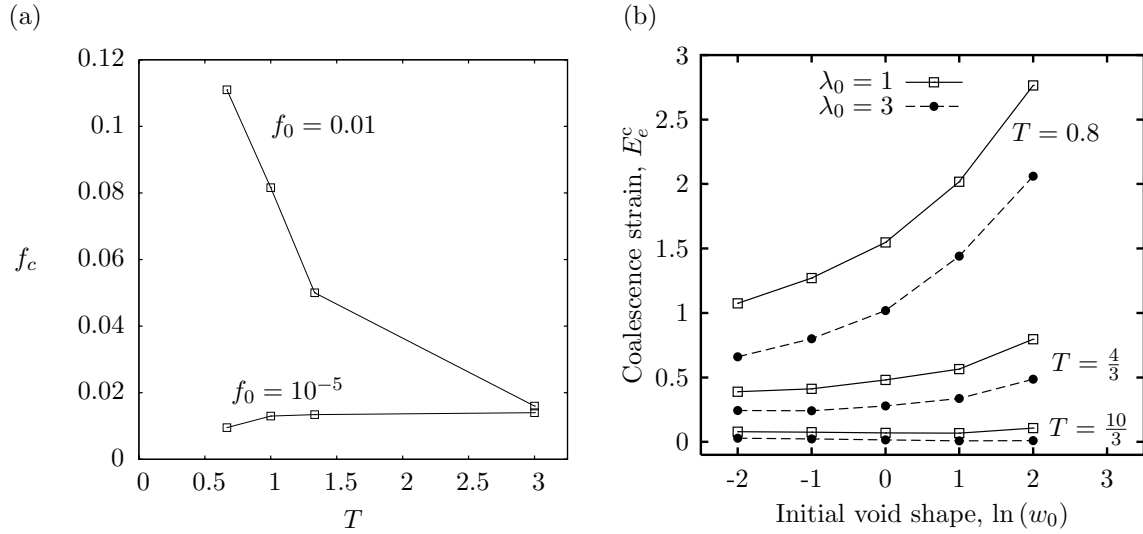


Figure 48: Predictions of coalescence condition (82) used in conjunction with the GLD void growth model accounting for void shape effects. (a) Dependence of the critical porosity on stress triaxiality T for initially spherical voids and two values of f_0 . (b) Dependence of the strain to coalescence, E_e^c , on the initial void shape for three values of T and two values of the void spacing ratio λ_0 . Adapted from (Benzerga et al., 1999).

(1985a) is his analysis of model predictions.

The results in Figs. 48a and 47b along with those of cell model studies also indicate that for initial porosities representative of structural alloys (between 10^{-5} and 10^{-3}) f_c is about one to a few percent. These values are in very good agreement with direct measurements of critical porosities as summarized in Section 2.3. In particular, the void growth ratio at the onset of coalescence may be higher than 10, in contrast with earlier understanding in the experimental literature. This aspect is further evidenced by examining various states at incipient coalescence as was shown in Fig. 19.

Finally, as indicated above, stress levels are still high at incipient coalescence. Therefore, models that are capable of describing the complete loss of stress carrying capacity are needed for numerical simulations of fracture. This task was undertaken by Pardoen and Hutchinson (2000) and completed more recently by Scheyvaerts et al. (2010) using a certain methodology based on Thomason's model adapted for spheroidal voids. Their models bear some resemblances with the model of Benzerga (2000, 2002), which will be presented below along with an important theoretical improvement of the limit-load constraint factor in (80).

7.1.2 Benzerga's Model

Thomason's coalescence condition (80)–(82) presents an obvious theoretical drawback. It predicts that no coalescence would occur in the limit of very flat voids ($w \rightarrow 0$) since the limit-load constraint factor C_f^T in (80) is then unbounded. This is disturbing because flat cavities and penny-shaped cracks loaded normal to their plane are known to be

most harmful. This limitation of Thomason's model, as well as the need for a complete model capable of describing the gradual decay of stress-bearing capacity of the elementary volume prior to void link-up, motivated the model of Benzerga (2000, 2002). This author considered a cylindrical RVE containing a spheroidal void and made up of rigid zones above and below the void with plastic flow contained in between, Fig. 46c. Knowledge of the exact size and shape of the localization zone is not needed for evolving the microstructure.

As pointed out above, in the limit $w \rightarrow 0$ Thomason's limit-load constraint factor, which is given by (80), is such that $C_f^T \rightarrow \infty$, irrespective of the value taken by the ligament size ratio χ . This behavior is illustrated in Fig. 49 (dotted lines). It is due to the

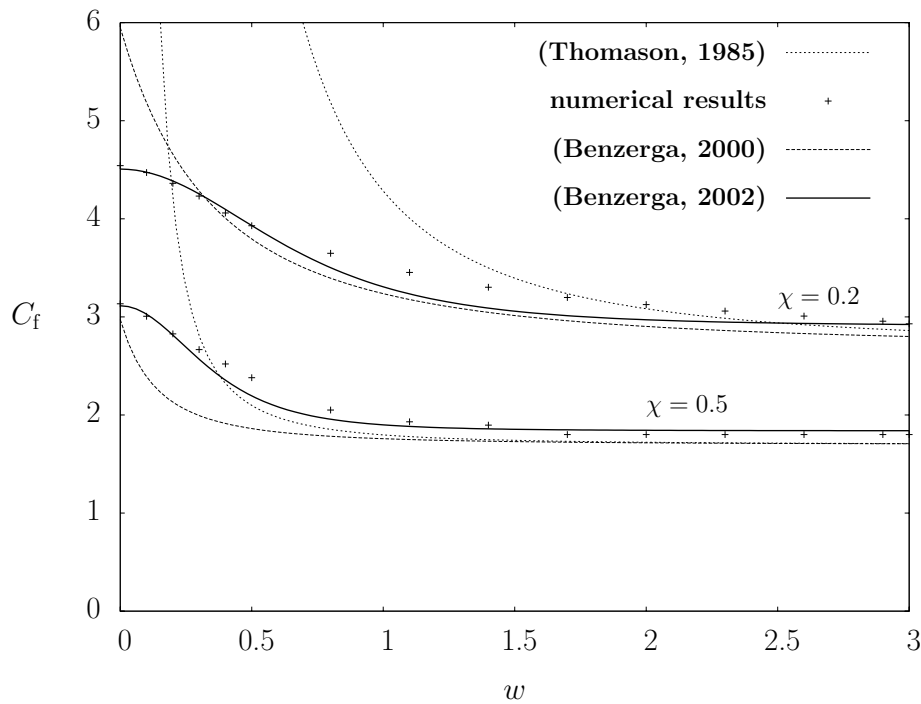


Figure 49: Comparison of different expressions of the limit-load constraint factor C_f as a function of void aspect ratio w for two values of the ligament size parameter χ . Thomason's expression (80) for cylindrical velocity fields (dotted lines) versus expression (83) obtained using spheroidal velocity fields (solid lines). After (Benzerga, 2002).

fact that Thomason only considered cylindrical voids; his velocity fields are well adapted to these but not to penny-shaped cracks. In fact, all of Thomason's velocities diverge for flat cavities. To obviate this drawback, Benzerga (2000, 2002) used improved limit-analysis results employing four axisymmetric velocity fields from the Lee–Mear expansion, following along the lines of Gologanu (1997), but only in the localization zone. The presence of the rigid layers ensures compatibility with boundary condition (79). At fixed values of χ and w , the limit load in the ligaments was computed using an estimate of the plastic dissipation for the above velocity fields. The numerical results are shown as points in Fig. 49. The numerical values of C_f fall below those of Thomason; hence they constitute a better estimate of the upper bound. In particular, the values for very flat cavities are finite. With these numerical estimates as basis, Benzerga (2002) proposed the

following heuristic formula for C_f

$$C_f(\chi, w) = 0.1 \left(\frac{\chi^{-1} - 1}{w^2 + 0.1\chi^{-1} + 0.02\chi^{-2}} \right)^2 + 1.3\sqrt{\chi^{-1}} \quad (83)$$

The quality of the fit to the numerical results may be assessed from Fig. 49, which also shows an earlier proposal by Benzerga (2000).

From a purely theoretical viewpoint, proposal (83) is superior to Thomason's equation (80). In practice, however, the quantitative predictions obtained with the two models are very close, for most cases analyzed, e.g. in the cell model studies. This is quite puzzling at first sight. Indeed, in the pre-localization regime, a model for cylindrical cavities such as Gurson's is so much more restrictive than a model accounting for void shape effects, such as the GLD model. Their predictions are quite far apart and the latter encompasses the former as a special limit case. In the localized regime, however, the highly constrained character of plastic flow swamps the effect of void shape and it is the ligament size ratio χ that plays the dominant role (Fig. 49). The void aspect ratio has an influence if it is typically smaller than unity (oblate shapes) with $\chi \leq 0.3$. Using Eq. (81) this entails that the product $f\lambda$ must be smaller than about 0.02. It turns out that such a condition is not frequently met at the onset of localization. Yet expression (83) is preferred theoretically and will predict localization for closely packed flat cavities when Thomason's criterion will not.

Observing that $\Phi = \Sigma_{33} - \Sigma_{33}^{\max}$ is a possible yield function, Benzerga (2000, 2002) proposed the following yield criterion for the post-localization regime:

$$\Phi^{(c+)}(\Sigma, \chi, w) = \frac{\Sigma_{eq}}{\bar{\sigma}} + \frac{3}{2} \frac{|\Sigma_m|}{\bar{\sigma}} - \frac{3}{2} (1 - \chi^2) C_f(\chi, w) = 0 \quad (84)$$

with Σ_{eq} and Σ_m as above, $\bar{\sigma}$ is the matrix flow stress, C_f is the plastic limit-load factor in (83), χ is the ligament size ratio defined by Eqn (81), and w is the void aspect ratio. Criterion (84) defines a convex domain of reversibility in stress space and is invariant upon a change of sign of stress. It is consistent with the uniaxial straining mode characterizing void coalescence in layers; this may be verified by applying the normality flow rule. The proposed form (84) is strictly valid under axisymmetric loadings, but is applicable to arbitrary orientations of the localization band.

Yield criterion (84) is supplemented with evolution laws of the microstructural variables χ , w and, eventually, λ . An initial value of the relative void spacing λ is needed to initialize χ through (81). χ plays the role of the porosity and hence its evolution law was derived using plastic incompressibility of the matrix and the associated flow rule. The evolution law of the void aspect ratio was derived based on the conjecture that the rigid zones above and below the cavity intercept the latter at its poles. This is all that is needed to evolve w from first principles. In particular, the exact shape or height of the localization zone does not matter. All equations and further details may be found in (Benzerga, 2002).

Figure 50 depicts some yield surfaces in the (Σ_{eq}, Σ_m) plane for axisymmetric loadings. Surfaces of the type $\Phi^{(c+)} = 0$ are given by lines with a slope $-3/2$ in the half-plane $\Sigma_m > 0$. Also shown in the figure are yield surfaces corresponding to the GLD model. At initial yield, the limit-load associated with the GLD model is lower than that resulting

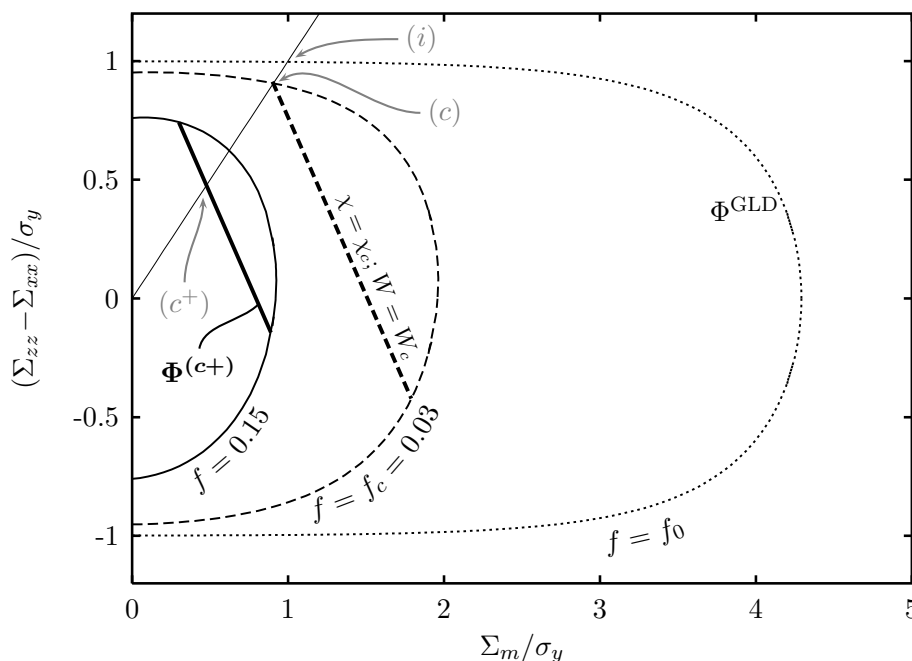


Figure 50: Typical yield surfaces before and after localization for axisymmetric loadings, given by Eqs (58) and (84), respectively. Actual surfaces corresponding to: (i) initial state: $f_0 = 0.001$, $w_0 = 1$ and $\lambda_0 = 1$; (c) incipient coalescence with $\chi_c = 0.46$ and $w_c = 1.85$ at $T = 1$; and (c^+) state during coalescence with $\chi = 0.7$ and $w = 1.5$. After (Benzerga, 2002).

from Eq. (84), which is not shown. At the onset of localization, the two limit-loads are identical. Subsequently, the limit load is smaller with Eq. (84).

Benzerga (2000) implemented the above model in the finite-element code ZéBuLoN along with the GLD model for the pre-coalescence regime. Extensions to include elasticity and hardening were made just like in Section 6. Figure 51 illustrates the type of macroscopic stress-strain response obtained using the full model (a) along with the corresponding evolution of microstructural variables (b)–(d). The sharp drop in the effective stress Σ_e in Fig. 51a is associated with the transition from the pre-coalescence GLD yield surface to the void-coalescence yield surface; see Fig. 50.

The parameter γ represents a shape factor. In fact, equation (81) relating the ligament size ratio χ to f , w and λ is valid for spheroidal voids¹¹. Other shapes may be considered provided that the factor $3/2$ in (81) is replaced with 3γ . For example, $\gamma = 1/2$ for a spheroid and $\gamma = 1$ for a conical void. As shown in Fig. 51, this micromechanical parameter γ has a direct effect on the slope of the stress-strain curve in the softening regime. This effect is due to different evolutions of χ and S . A more conical shape of the void promotes a faster lateral void growth, which results in a faster rate of increase of χ (Fig. 51b) and decrease of S (Fig. 51c). In fact, when the void shape is constrained to remain spheroidal ($\gamma = 1/2$), the void shape decreases at the onset of coalescence, reaches a minimum then increases again. The results shown in Fig. 51 were obtained using an upper cut-off of 0.95 for the ligament size ratio χ , after which the stiffness was ramped

¹¹As illustrated in Section 2.2, void shapes during void coalescence very seldom keep their approximate spheroidal shape.

down to zero. This was done in order to ease the numerical treatment of the very final stages of failure. Without such a heuristics, Σ_e would saturate to a low but non zero value, and correspondingly χ would have saturated to some value greater than $\sqrt{2}/2$ (notice the inflexion point in Fig. 51b). By way of contrast, the use of larger values of γ does lead to complete loss of stress bearing capacity even without using the cut-off for χ . For this reason, it was argued by Benzerga (2002) that the use of a shape factor is necessary to let the stress carrying capacity of the element completely vanish.

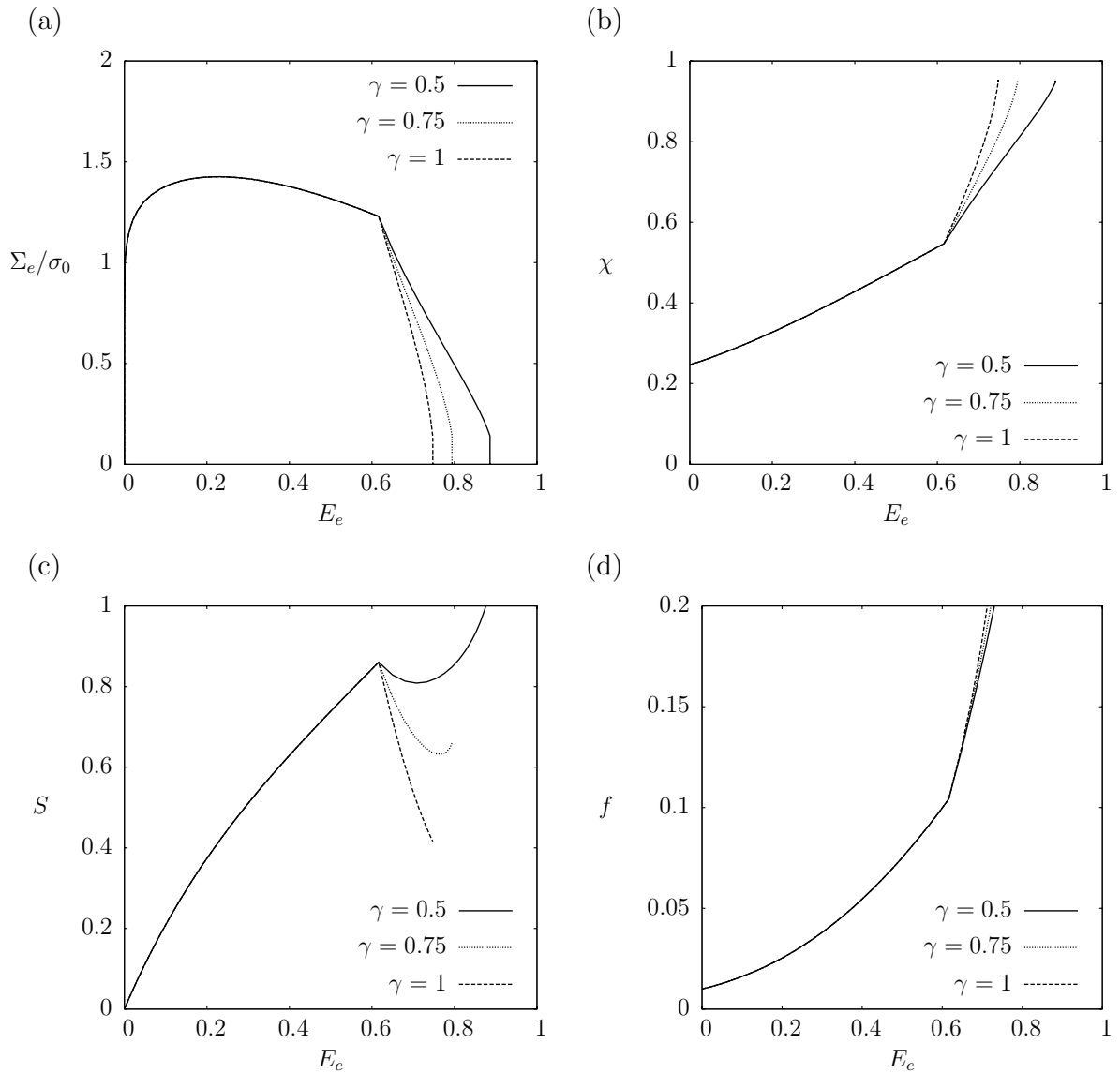


Figure 51: Typical responses obtained using the void coalescence model along with the GLD model for the pre-coalescence phase for $f_0 = 0.01$, $w_0 = 1$ and $\lambda_0 = 1$ at fixed stress triaxiality $T = 1$. (a) Effective stress versus effective strain, E_e . (b) Ligament size ratio versus E_e . (c) Void shape parameter $S \equiv \ln w$ versus E_e . (d) Porosity versus E_e . After (Benzerga, 2000).

This aspect of the model is related to the coupled character of the system of ordinary

differential equations governing the evolution of internal variables. It is not essential for model assessment but may be important in practical numerical simulations of fracture. Interestingly, the exact value of γ has very little influence on the void volume fraction, Fig. 51d.

7.1.3 Coalescence in Combined Tension and Shear

An analytical treatment of coalescence alternative to that of Thomason (1985b) was proposed by Gologanu (1997) and Gologanu et al. (2001b) (borrowing some previous ideas of Perrin (1992)) and extended by Leblond and Mottet (2008). The basic physical idea was identical to that in the work of Thomason. A distinction was thus made between the pre-coalescence phase, during which the plastic rate of deformation is spread over the whole RVE, and the coalescence phase, marked by a sudden concentration of this rate of deformation in the horizontal inter-void ligaments. Limit-analysis was again used to derive conditions for such a localization, the idea being to compare estimates of the global limit-load obtained through two types of trial velocity fields, non-localized and localized, with the selection of that field leading to the lower estimate in view.

The difference between the approach of Thomason (1985b) and that of Gologanu et al. (2001b) and Leblond and Mottet (2008) resided in some additional simplifying hypothesis introduced in the latter works. Instead of defining some localized velocity field in full 3D detail, Gologanu et al. (2001b) and Leblond and Mottet (2008) assumed that the limit-load for such a field could be estimated by replacing the central void-rich region of the RVE, prone to localization of the plastic strain rate, by some “equivalent” homogeneous porous layer obeying Gurson’s homogenized criterion or some variant.

This approximation is illustrated in Figs. 52 and 53 below. Figure 52a shows an elementary region of material prior to any deformation; the distribution of voids is assumed to be periodic and homogeneous in this state. After some deformation, however, this distribution is no longer homogeneous, Fig. 52b, and voids appear as concentrated within horizontal layers, in which the plastic strain rate is bound to concentrate provided suitable conditions are met. The approximation made consists of replacing this complex microstructure by a simple “sandwich” structure illustrated in Fig. 53a, made of alternatively sound (s) von Mises layers and porous (p) Gurson layers. The periodicity of the structure allows to restrict the study to some very simple cell made of three layers only, shown in Fig. 53b.

The major advantage of introduction of this simplifying hypothesis is that the limit-load can then be calculated analytically. This basic simplicity allowed Leblond and Mottet (2008) to extend Gologanu et al. (2001b)’s treatment, limited to loadings including only axial and lateral stresses like in the work of Thomason (1985b), to fully general loads including shear components. (An extension to viscoplasticity was also carried out by Flandi and Leblond (2005a)).

These advantages find their counterpart in the fact that the estimate of the limit-load depends crucially on the thickness $2H$ of the “equivalent” homogeneous porous layer, the choice of which raises some difficulties. Indeed it would seem natural to ascribe it the value $2r$ (the current diameter of the voids), which represents the minimum thickness ensuring that voids intersecting the layer are entirely contained within it. Unfortunately experience shows that this natural choice leads to rather poor predictions, as compared

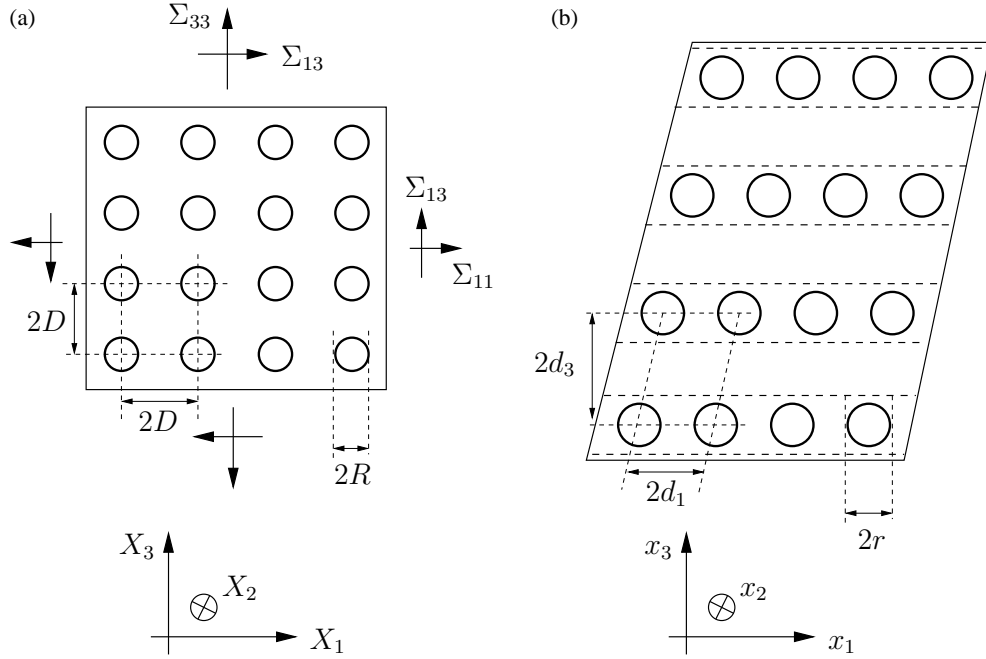


Figure 52: Deformation of a periodically voided material. (a) Initial state. (b) Deformed state. After (Leblond and Mottet, 2008).

with results of FE micromechanical computations. Choices leading to better predictions, but more complex and less natural, are discussed in (Gologanu et al., 2001b) and (Leblond and Mottet, 2008).

The solution of the sandwich problem is elementary and leads to the following macroscopic yield surface of the RVE for localized plastic strain rate:

$$\begin{cases} \frac{|N|}{\bar{\sigma}} - \frac{2}{3}(\zeta + p \sinh \zeta) = 0 \\ \zeta \equiv \arg \cosh \left(-\frac{1}{p} + \sqrt{2 + \frac{2 - 3\|\mathbf{T}\|^2/\bar{\sigma}^2}{p^2}} \right) \end{cases}, \quad \text{where } p \equiv q \frac{f}{c}. \quad (85)$$

The symbols $N \equiv \mathbf{n} \cdot \boldsymbol{\Sigma} \cdot \mathbf{n}$ and $\mathbf{T} \equiv \boldsymbol{\Sigma} \cdot \mathbf{n} - N \mathbf{n}$ here denote the normal and tangential components of the stress vector exerted on the layer of normal \mathbf{n} , q is Tvergaard's usual parameter and c is the volume fraction of the central layer, connected to its half-thickness h (f/c thus represents the local porosity within this layer). With this criterion goes a flow rule obeying normality, as imposed by a general result of limit-analysis. The deformation mode consists of a uniaxial extension in the direction \mathbf{n} combined with a shear.

Finite element micromechanical cell model computations were performed by Leblond and Mottet (2008) to validate the model. These computations were analogous to those discussed in Section 3, except that the loading included a shear component which made it necessary to perform the calculation in 3D, with periodic boundary conditions. Figures 54 and 55 show the results obtained¹² in a typical case, involving an initial porosity of 0.02, a constant triaxiality $T = 1$, and a constant ratio $S \equiv \sqrt{3}|\Sigma_{13}|/\Sigma_e = 0.5$. (This

¹²For two variants of the model which need not be detailed here.

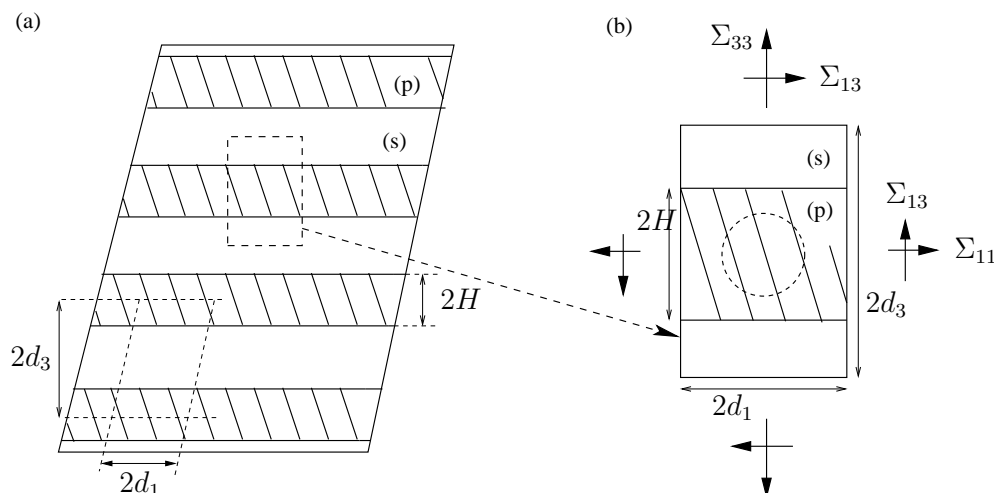


Figure 53: The sandwich model.

ratio lies in the interval $[0, 1]$ and measures the importance of the macroscopic shear stress component). The model can be seen to correctly capture the evolutions of all quantities.

Predictions using a simpler model not accounting for shear effects due to Perrin (1992) were analyzed by Benzerga et al. (1999). Numerical integration of the corresponding constitutive equations for $T = 1, 2$ and 3 has shown a very good agreement with cell model results obtained by Koplik and Needleman (1988). Further results for the critical porosity versus stress triaxiality are shown in Fig. 47a, for a wide range of f_0 values and an initially isotropic void distribution ($\lambda_0 = 1$). The predicted values using the adapted Thomason coalescence condition (82) were found to be always lower than those predicted using Perrin's model.

7.2 Coalescence in Columns

Coalescence “in layers”, as envisaged up to now, basically consists of deformation-induced concentration of voids within thin planar layers. Benzerga (2000) has observed a different type of coalescence “in columns” in which voids were aligned along beads within thin cylindrical regions. Coalescence in columns prevails for a Lode factor $\mu = +1$. It also occurs for $\mu = -1$ and elongated voids.

In Benzerga (2000)'s observations, the peculiar distribution of voids resulted from lamination of a plate; the very prolate voids were generated through decohesion of the metallic matrix around inclusions elongated by the rolling process. A similar distribution of voids may also be generated by application of some axisymmetric macroscopic stress state with predominant lateral rather than axial stress, since the deformation of the RVE will then tend to make it oblate rather than prolate, thus decreasing the intervold distance in the axial direction. The latter case corresponds to $\mu = +1$.

A model for this type of coalescence has been proposed by Gologanu et al. (2001a), using the same kind of ideas as for coalescence “in layers” (Gologanu et al., 2001b). Figure 56 illustrates the principle of the treatment. Figure 56(a) shows a typical cylindrical RVE in a periodic porous material subjected to some axisymmetric loading with predominant

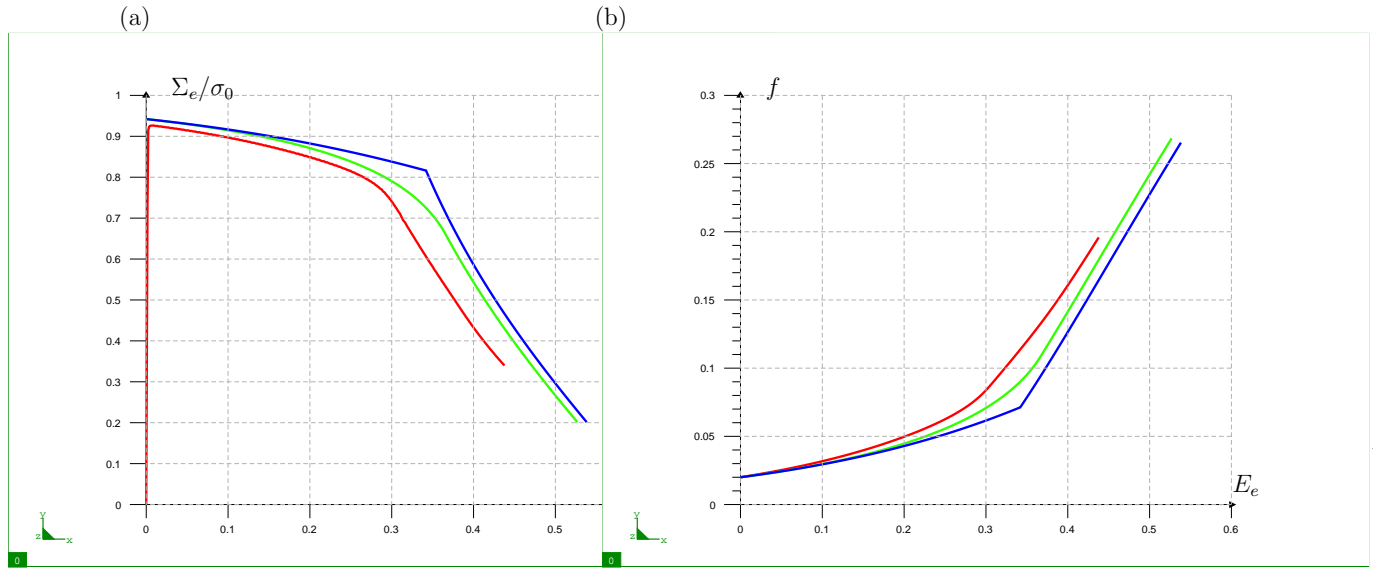


Figure 54: Evolution of (a) the macroscopic equivalent stress and (b) the porosity - $T = 1$, $S = 0.5$. FE results in red, two variants of the model in green and blue. After (Leblond and Mottet, 2008).

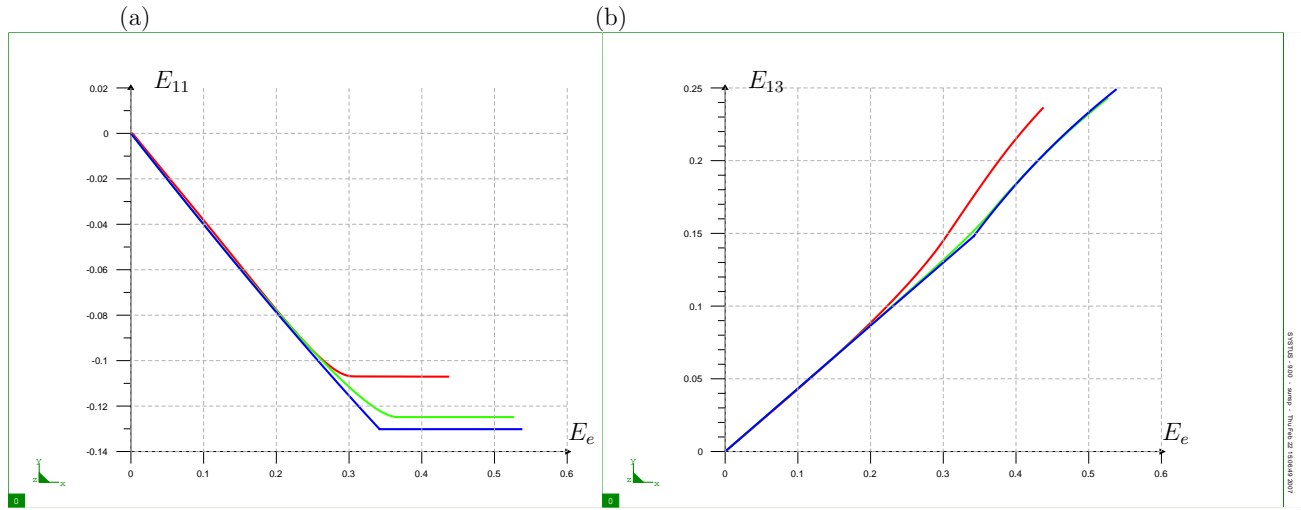


Figure 55: Evolution of (a) the horizontal strain and (b) the shear strain - $T = 1$, $S = 0.5$. FE results in red, two variants of the model in green and blue. After (Leblond and Mottet, 2008).

lateral stress ($\Sigma_{11} = \Sigma_{22} > \Sigma_{33}$). Because of the deformation of this RVE, the voids are closer to each other in the vertical direction than in the horizontal ones, and thus appear to be “concentrated” within vertical columns. Figure 56(b) illustrates the schematization of this microstructure through some composite cylindrical structure made of a central porous (p) cylindrical core embedded in a sound (s) cylindrical envelope. The behavior of the central homogeneous region may be approximately described by the Gurson or GLD

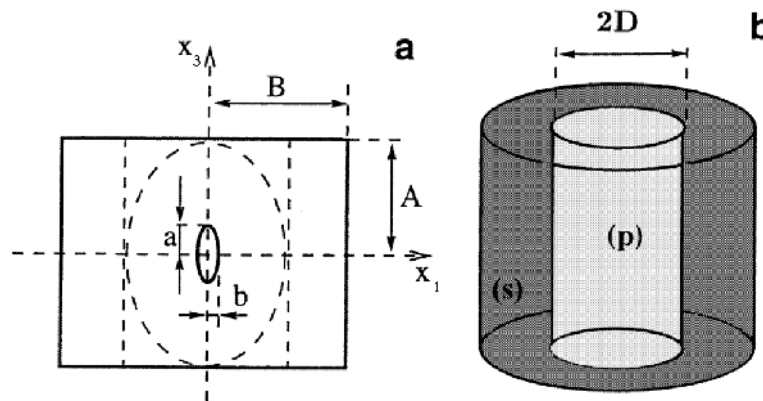


Figure 56: The RVE studied (a) and its schematization as a composite cylindrical structure (b). After (Gologanu et al., 2001a).

models, while von Mises's model is appropriate for the external zone.

The problem of the composite cylindrical structure may be solved analytically, like that of the sandwich structure described in Section 7.1.3; the treatment closely resembles that of Gurson for a hollow cylinder subjected to some axisymmetric loading under conditions of generalized plain strain. There are however two major differences. First, global flow of the cylindrical structure necessarily implies that it must be entirely plastic; the sound zone may never become rigid like in the sandwich structure, because this would obviously prevent any overall deformation. Second, the rate of deformation and stress fields are inhomogeneous in the external sound cylinder, unlike in the sound layers of the sandwich structure, and this makes the calculation much more involved. For this reason, mathematical expressions will not be shown here; the interested reader may refer to (Gologanu et al., 2001a).

Figure 57 compares the results of some numerical FE micromechanical simulations of coalescence in columns with the predictions of Gologanu et al. (2001a)'s model. The RVE considered is a cylinder with equal initial radius and height, containing an initially spherical void; the initial porosity is 0.0104 and the loading is axisymmetric with predominant lateral stress, with a constant triaxiality of $1/3$, $2/3$, 1 or 2 . The model can be seen to reproduce the numerical results quite well in all cases.

It may be observed that except for a triaxiality of $1/3$, the numerical curves all exhibit some kind of "coalescence" leading to significantly quicker evolutions of the macroscopic stress and porosity¹³. One notable and interesting difference with respect to coalescence in layers, however, is that here the onset of coalescence can no longer be defined precisely. The explanation is that there is no longer a sharp transition from a phase where both the sound and porous zones are plastic to one where the sound region becomes rigid (or rather elastic in the FE computations), since this second occurrence is impossible in the case considered, as remarked above.

¹³Predictions of the Gurson or GLD models disregarding coalescence, not shown here, would exhibit an equally good agreement with numerical results for small values of the overall deformation, but a much poorer one for larger values.

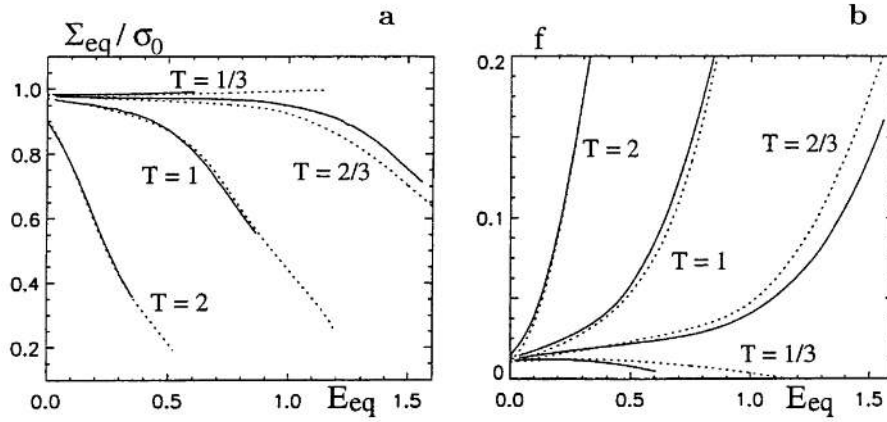


Figure 57: Comparison of numerical FE results (solid lines) and model predictions (dashed lines). (a) Macroscopic equivalent stress versus equivalent strain E_{eq} . (b) Porosity versus E_{eq} . After (Gologanu et al., 2001a).

7.3 Closing Remarks on Void Coalescence

Current understanding of void coalescence is that it is a process that begins with plastic flow localization in the dense intervvoid matrix and ends with void linkage. Fundamentally, it is a void growth process under constrained plastic flow. It is therefore highly anisotropic. With that in mind, a formulation of void growth and coalescence models within a unified framework is possible. To illustrate this, consider the GLD model as the void growth model before the onset of localization, Benzerga’s model as the void “growth” model for localization in layers and the Gologanu model for localization in columns. The intersection of the three corresponding yield surfaces defines a convex yield surface since each of the criteria defines a convex domain of reversibility. This multi-surface representation is illustrated in Fig. 58. The curved parts correspond to branches of the GLD yield surface while the planar parts are from the coalescence model of Benzerga. In this “static” view of the effective yield surface, the latter exhibits some sharp corners, which can be dealt with using, for example, Koiter’s (1953) formulation. Alternatively, in the multi-layer approach of Gologanu et al. (2001b,a) and Leblond and Mottet (2008) the corners are replaced with regions of extreme curvature, but the effective yield surface is smooth everywhere. This feature resulted from their homogenization scheme, since the three layers were modeled from the outset of plastic flow, including the phase prior to localization.

Current practice of void coalescence modeling is still based on a phenomenological approach introduced by Tvergaard and Needleman (1984). With cell model studies as micromechanical reference, they introduced an effective porosity $f^*(f)$ as a function of the true porosity. Prior to localization $f^* = f$; after it, f^* is a multiple of the porosity. This allows to mimic void growth acceleration in the localized regime. In both regimes, the Gurson yield function is used. Two parameters are thus introduced: a critical porosity f_c beyond which f^* ceases to be identified with the actual porosity, and an acceleration factor δ related to the porosity at complete loss of stress bearing capacity, f_f . In the literature, this methodology is widely known as the Gurson–Tvergaard–Needleman (GTN) model,

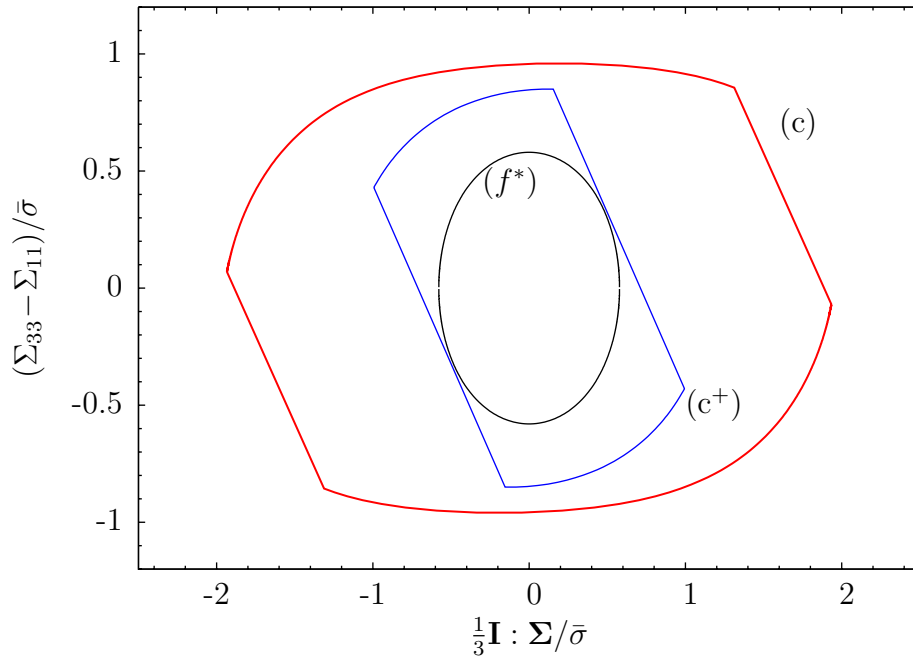


Figure 58: Effective yield surfaces for axisymmetric loadings resulting from the intersection of yield domains defined by (87) and (95). Stages (c) at the onset of coalescence with $f = 0.04$, $w = 5$ and $\chi = 0.34$; (c^+) post-localization with $f = 0.15$, $w = 2.2$ and $\chi = 0.75$. Also shown is the GTN yield surface with $f^* = 0.42$ tangent to the (c^+) yield surface at the current loading point. Conditions correspond to an initial state with $f_0 = 0.00075$ and $w_0 = 15$, and a stress triaxiality ratio $T \approx 2$.

and includes Tvergaard's q parameter and continuum models of void nucleation.

Progress achieved over the past decade in the micromechanics modeling of void coalescence resolves a number of issues associated with the GTN approach. One issue has to do with transferability of model parameters from a laboratory specimen to a component, or even from one specimen geometry to another; e.g. see (Brocks et al., 1995). On this count, the micromechanical models presented in this section naturally account for stress state effects. In the GTN model, the effect of microstructure (initial void volume fraction, shape and distribution of voids) can only be taken into account through calibration to experimental results, with no guarantee of uniqueness of the parameter set in the identification procedure. On the other hand, the micromechanical models naturally account for microstructural effects, initial and induced. Also, in the GTN approach the attempt is made to capture void growth acceleration during the coalescence phase through the effective porosity f^* , which is the only feature of the localization regime. Fundamentally speaking, void acceleration is only a consequence of constrained plastic flow and it is the yield locus itself that changes during void coalescence. Figure 58 illustrates this difference in that the GTN approach exaggerates the shrinkage of the yield surface to obtain the same decrease in load bearing capacity. One practical consequence of the GTN approximation is that the porosity level at complete loss of stress bearing capacity is $1/q_1 \approx 0.66$. This value is much higher than what is predicted using the micromechanical studies, where porosity levels at vanishing macroscopic stress roughly range between 0.15 and 0.30. Fi-

nally, the effective GTN yield surface is smooth whereas the effective yield surface of a multi-surface model either exhibits sharp corners or regions of extreme curvature. Clearly, such differences will have a strong influence on the propensity to plastic flow localization at a scale greater than that of the representative volume element. An example of such occurrence was discussed by Benzerga et al. (2002).

8 Top-Down Approach to Ductile Fracture

The ideal framework for modeling ductile fracture is one that has a good representation of polycrystalline plastic deformation combined with the ability to predict void nucleation, growth and coalescence in various competing modes. “Bottom-up” approaches which use chemistry and physics to link the atomic scale to the macroscopic aspects of deformation and fracture are unlikely to be developed with adequate accuracy in the foreseeable future, given the complexity of the microscopic mechanisms in structural material systems. By way of contrast, “top-down” approaches to fracture have emerged over the past few decades as most promising (Hutchinson and Evans, 2000; Pineau, 2006). In a top-down approach, experiments are generally used to provide calibration of fracture at the smallest scale of relevance.

From the elementary micromechanisms of ductile damage a key concept emerged for modeling ductile fracture: void growth and coalescence, on one hand, and matrix plasticity, on the other hand, are inherently coupled. Physically, void growth is but an *expression* of plastic deformation of the surrounding material. Therefore, in principle one only needs to calibrate parameters that affect the plastic behavior. In particular, there is basically no need to calibrate any fracture parameter, provided that the models are quantitative enough. For example, one does not need to adjust the critical porosity if micromechanics-based models of void coalescence are used. We emphasize that this sets a paradigm for predictive modeling, a direction for improving existing methodologies and a way to discover the inherent limitations of existing models. All models remain perfectible, especially when usage does not cloud their formulation with excessive empiricism and unnecessary heuristics.

8.1 Synopsis of Integrated Model

Various strategies may be used for integrating models from the previous sections and their finite element implementation. Here we outline one such methodology for which some examples are demonstrated in the following section. Within a finite deformation framework, we used a co-rotational formulation of the constitutive equations as in (Benzerga et al., 2004b). The total rate of deformation \mathbf{D} is written as the sum of an elastic and a plastic part with elasticity included through a hypoelastic law (see Appendix B). The plastic part of the rate of deformation, \mathbf{D}^p , is obtained by normality from the gauge function:

$$\phi = \sigma_\star - \bar{\sigma}(\bar{\varepsilon}) \quad (86)$$

where $\bar{\sigma}$ is the matrix flow stress, $\bar{\varepsilon}$ is the effective plastic strain and σ_\star is an effective matrix stress which is implicitly defined through an equation of the type $\mathcal{F}(\boldsymbol{\Sigma}, f, S, \mathbf{e}_3, \mathbb{H}, \sigma_\star) = 0$ with f the porosity, S the shape parameter (logarithm of the void aspect ratio w), \mathbf{e}_3 the

void axis and \mathbb{H} Hill's tensor (equal to \mathbb{h} in this section). For a rate-independent material (standard plasticity), plastic flow occurs for $\phi = 0$ and $\dot{\phi} = 0$. For a rate-dependent material (viscoplasticity), one has $\phi > 0$ during plastic flow. This strategy corresponds to the way in which many other plastic or viscoplastic constitutive equations are implemented in ZéBuLoN (Besson and Foerch, 1997). The potential \mathcal{F} admits two different expressions, $\mathcal{F}^{(c-)}$ and $\mathcal{F}^{(c+)}$, prior to and after the onset of coalescence, respectively.

Void Growth

The flow potential prior to coalescence is given by $\mathcal{F}^{(c-)}(\boldsymbol{\Sigma}, f, S, \mathbb{H}, \sigma_*)$ with

$$\mathcal{F}^{(c-)} = C \frac{\|\boldsymbol{\Sigma}' + \eta \Sigma_h \mathbf{Q}\|_{\mathbb{H}}^2}{\sigma_*^2} + 2q_w(g+1)(g+f) \cosh\left(\frac{\kappa}{h} \frac{\boldsymbol{\Sigma} : \mathbf{X}}{\sigma_*}\right) - (g+1)^2 - q_w^2(g+f)^2 \quad (87)$$

where $()'$ refers to the deviator and $\|\cdot\|_{\mathbb{H}}$ denotes the Hill norm of a tensor as in (66). Also,

$$\mathbf{X} \equiv \alpha_2(\mathbf{e}_1 \otimes \mathbf{e}_1 + \mathbf{e}_2 \otimes \mathbf{e}_2) + (1 - 2\alpha_2)\mathbf{e}_3 \otimes \mathbf{e}_3 \quad (88)$$

$$\mathbf{Q} \equiv -\frac{1}{3}(\mathbf{e}_1 \otimes \mathbf{e}_1 + \mathbf{e}_2 \otimes \mathbf{e}_2) + \frac{2}{3}\mathbf{e}_3 \otimes \mathbf{e}_3, \quad (89)$$

\mathbf{e}_1 and \mathbf{e}_2 being arbitrarily chosen transverse unit base vectors and $\Sigma_h \equiv \boldsymbol{\Sigma} : \mathbf{X}$ in (87). Also, h is a scalar invariant of Hill's anisotropy tensor given in terms of Hill's coefficients

$$h = 2 \left[\frac{2}{5} \frac{h_L + h_T + h_S}{h_L h_T + h_T h_S + h_S h_L} + \frac{1}{5} \left(\frac{1}{h_{TS}} + \frac{1}{h_{SL}} + \frac{1}{h_{LT}} \right) \right]^{\frac{1}{2}} \quad (90)$$

Also, κ , α_2 , g , C and η are scalar valued functions of microstructural parameters f and S . Their expressions are provided in Appendix A. Finally, q_w is a void-shape dependent factor that was determined by Gologanu et al. (1997) to fit unit-cell results:

$$q_w = 1 + (q - 1)/\cosh S \quad (91)$$

where $q = 1.6$ is the value taken by q_w for a spherical void.

The evolution laws of the microstructural variables prior to coalescence are given by

$$\dot{f} = (1 - f) \mathbf{I} : \mathbf{D}^p, \quad (92)$$

$$\dot{S} = \frac{3}{2} \left[1 + \left(\frac{9}{2} - \frac{T^2 + T^4}{2} \right) (1 - \sqrt{f})^2 \frac{\alpha_1 - \alpha_1^G}{1 - 3\alpha_1} \right] D'_{33} + \left(\frac{1 - 3\alpha_1}{f} + 3\alpha_2 - 1 \right) \mathbf{I} : \mathbf{D}^p \quad (93)$$

Here, T is the stress triaxiality ratio and α_1 and α_1^G are given in Appendix A. Assuming that voids rotate with the material, the evolution of void orientation is given by

$$\dot{\mathbf{e}}_3 = \dot{\boldsymbol{\Omega}} \cdot \boldsymbol{\Omega}^T \cdot \mathbf{e}_3 \quad (94)$$

where $\boldsymbol{\Omega}$ is the rotation used in the co-rotational formulation; see Appendix B, Eq. (B.4).

Void Coalescence

The flow potential after the onset of coalescence is given by

$$\mathcal{F}^{(c+)}(\boldsymbol{\Sigma}, \chi, S, \mathbb{H}, \sigma_*) = \frac{\|\boldsymbol{\Sigma}\|_{\mathbb{H}}}{\sigma_*} + \frac{1}{2} \frac{|\mathbf{I} : \boldsymbol{\Sigma}|}{\sigma_*} - \frac{3}{2}(1 - \chi^2) C_f(\chi, S) \quad (95)$$

where χ is the ligament size ratio defined with respect to the principal axes of loading. and C_f is given by

$$C_f(\chi, S) = 0.1 \left(\frac{\chi^{-1} - 1}{w^2 + 0.1\chi^{-1} + 0.02\chi^{-2}} \right)^2 + 1.3\sqrt{\chi^{-1}}; \quad w = e^S \quad (96)$$

For an arbitrary void shape between a spheroid and a cone, χ is exactly related to the void spacing ratio, λ , through a shape factor γ as

$$\chi = \begin{cases} \left[3\gamma \frac{f}{w} \lambda \right]^{1/3} & \text{(P)} \\ w \left[3\gamma \frac{f}{w} \lambda \right]^{1/3} & \text{(T)} \end{cases} \quad (97)$$

where (P) and (T) are a shorthand notation for parallel and transverse loading, respectively. The function $\gamma(\chi)$ was introduced in Benzerga (2002) to represent the actual non-spheroidal void shapes observed during coalescence (see Fig. 9). As $\chi \rightarrow 1$ the material loses all stress carrying capacity. At the onset of coalescence we have $\mathcal{F}^{(c-)} = \mathcal{F}^{(c+)} = 0$.

After the onset of coalescence the relevant microstructural variables are λ , χ and w . Their evolution laws are given by

$$\dot{\lambda} = \frac{3}{2} \lambda D_{\text{eq}}^p, \quad (98)$$

$$\dot{\chi} = \frac{3}{4} \frac{\lambda}{w} \left[\frac{3\gamma}{\chi^2} - 1 \right] D_{\text{eq}}^p + \frac{\chi}{2\gamma} \dot{\gamma}, \quad (99)$$

which results from plastic incompressibility of the matrix material, and

$$\dot{w} = \frac{9}{4} \frac{\lambda}{\chi} \left[1 - \frac{\gamma}{\chi^2} \right] D_{\text{eq}}^p - \frac{w}{2\gamma} \dot{\gamma} \quad (100)$$

A fully implicit time integration procedure was used for the local behavior in conjunction with an iterative Newton–Raphson method. The consistent tangent matrix was computed as detailed in the case of prolate voids by Benzerga et al. (2002). Figure 59 shows some typical responses obtained using the full integrated model in the case of initially penny-shaped cracks. Two loading cases are considered, parallel (the axial stress being normal to the crack) versus transverse. In each case, the stress–strain response and the evolution of porosity are compared with their counterparts when only the GLD model is used. The results illustrate the rapid decrease in load carrying capacity due to void coalescence and the anisotropy in damage evolution and fracture.

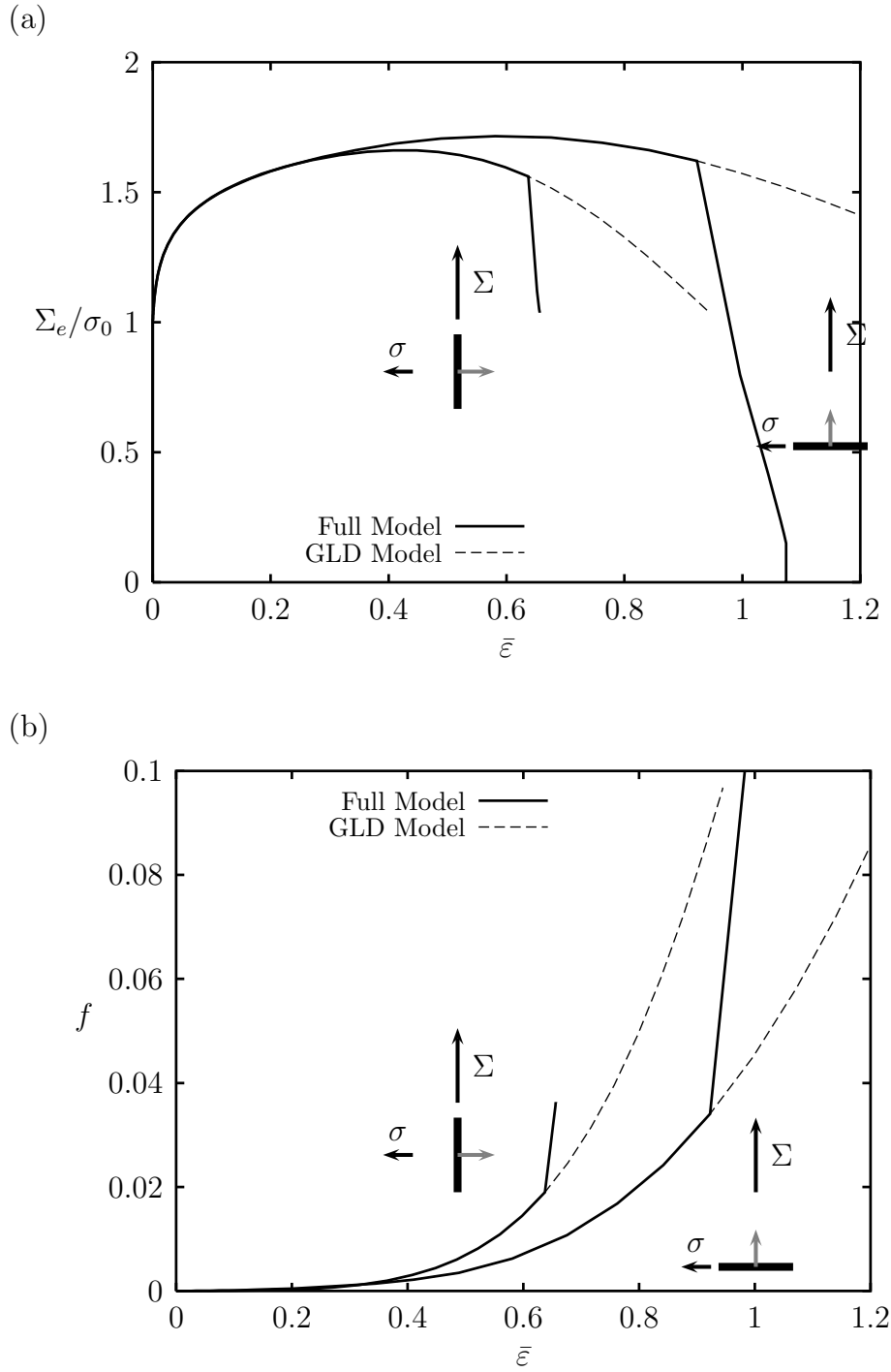


Figure 59: Typical responses obtained using the integrated model for initially penny-shaped cracks using $f_0 = 10^{-8}$, $S_0 \equiv \ln w_0 = -8$ and $\lambda_0 = 1$ under axisymmetric loading at fixed stress triaxiality $T = 1$. (a) Effective stress versus matrix effective strain, $\bar{\epsilon}$. (b) Porosity versus $\bar{\epsilon}$. Normal to crack is shown as a grey arrow; axial (Σ) and lateral (σ) stresses are shown as black arrows. After (Benzerga, 2000).

8.2 Material Parameter Identification

The micromechanical model streamlined above enables to implement a top-down approach to ductile fracture. The paradigm of this approach is that only deformation related pa-

rameters need to be calibrated on experiments. Inasmuch as a phenomenological model, such as a Voce-type hardening law, adequately captures the large strain plastic behavior of the matrix material, the calibration procedure should deliver as good a description as possible of that behavior, including any possible initial or emergent plastic anisotropy. In principle, there is no fracture parameter *per se* to be calibrated on experiments. Examination of constitutive equations (86)–(100) reveals no adjustable fracture parameter. The coupled damage–plasticity constitutive equations are now at such a level of sophistication that one can truly view fracture as the end of an evolution process with initial conditions and driving forces. In particular, path dependency, stress state effects and the signature of microstructure would all be natural outcomes of a modeling framework adopting such a constitution.

8.2.1 Standard Procedure

The hardening response of the matrix is first determined using uniaxial testing with appropriate measurements of neck geometry evolution to extrapolate the hardening curve beyond the onset of instability. If transverse cross-sections are observed to develop into oval shapes, as is the case in materials in wrought form, a complete characterization of plastic flow anisotropy is needed. This is common in the metal forming community although it is often restricted to two-dimensional measurements. Within the confines of the integrated model above, this first step will deliver the basic hardening curve $\bar{\sigma}(\bar{\epsilon})$ as well as the anisotropy tensor \mathbb{H} . Although other plasticity models may require different input, the type of tests to be conducted would hardly change. These will basically consist of tension and compression tests along various directions with appropriate measurements made. The minimal set of tests to be conducted in the case of 3D orthotropy of thick plates was discussed by Benzerga (2000) and Benzerga et al. (2004a).

In the standard procedure, voids are considered to be present from the outset of plastic deformation. This is a good assumption for ductile materials with weakly bonded or elongated inclusions. In other materials, the predicted ductility would need to be augmented by an appropriate amount of nucleation strain, which could be either measured or estimated from void nucleation models (see Section 4). Next, exploratory experiments should be conducted followed by metallographic examination of damage processes to identify clearly the damage initiation sites. Without this step the initial conditions of the evolution problem cannot be known or, at least, bounded. For example, in C–Mn steels, sulfides and oxides are the damage initiation sites (typically, manganese sulfides and alumina particles). Carbides play virtually no role in damage other than through the plastic flow properties of the matrix. In multiphase material systems where damage initiates in a brittle phase or at the interface between two phases, some difficulties arise due to a stronger coupling between damage and plasticity in that case. The standard procedure is better suited for materials systems with inclusions and second-phase particles occupying a volume fraction no more than a percent. This encompasses many structural alloys, including steels and aluminum alloys. The condition of a low volume fraction allows to identify without difficulty the plastic flow response of the matrix material with that of the alloy itself.

With the basic flow properties of the matrix calibrated and the damage initiation sites identified, the final step is to determine the initial state of the microstructure. By

that we mean the volume fraction, aspect ratio and relative spacing of inclusions, in the average sense. Practically, this can be achieved by examining three perpendicular cross-sections in optical microscopy, carrying out the needed two-dimensional measurements using digital image analysis, and finally operating standard stereology transformations to infer their 3D counterparts. The outcome of this step in the case of relatively equiaxed or spheroidal particles is the set of parameters f_0 , w_0 and λ_0 needed to initialize the state of the microstructure in constitutive equations (86)–(100).

8.2.2 Accounting for 3D Aspects

In the integrated model, voids are represented by spheroids and their spatial distributions by a square-prismatic or circular-cylindrical RVE. In material systems where the spatial distribution of void-nucleating second-phase particles exhibits some anisotropy, for example due to processing, the 3D distribution is approximated by a cylinder, dependent on the loading (Figs. 60a and b) orientation. Also, the plate-like particle is approximated by a spheroid. A difficulty arises in the case of the spatial distribution. One cannot rigorously infer the 3D relative spacings λ from the 2D measurements. Dirichlet networks, which are typically used to infer the 2D λ 's, are not endowed with stereological properties allowing to operate the transition to 3D in a straightforward manner. The development of high-resolution tomography may solve this problem in the future. At present, the 3D λ can only be a rough approximation.

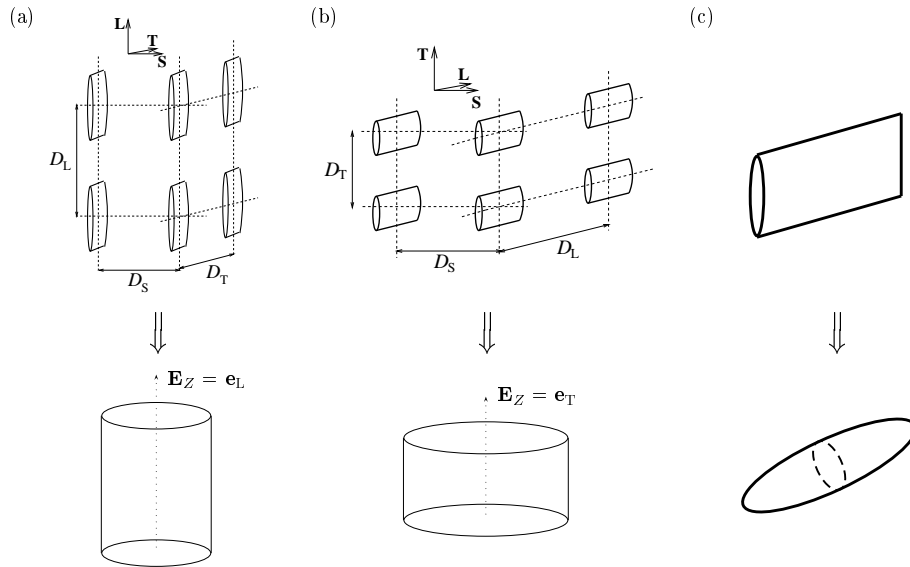


Figure 60: Schematic for the treatment of initial anisotropy in two steps. Step 1: the unit cell of the aggregate of inclusions is approximated by a cylinder whose axis is the loading axis: (a) major stress parallel to L; (b) major stress parallel to T. Step 2: the void nucleated on a MnS inclusion is approximated by an equivalent spheroid as shown in (c).

Another difficulty may be encountered in material systems with two or more populations of inclusions, e.g., having a different shape. In many steels, MnS inclusions are elongated while oxides are equiaxed. Voids nucleate at both but the onset of void coalescence may involve only one population, depending on the loading orientation. While it is

possible to develop a more sophisticated model accounting for such aspects, a simpler way consists of adapting the initial microstructural state to the loading orientation. In any case, an integrated model such as the one presented above may be employed to analyze and discuss various scenarios and deliver bounds on the path-dependent fracture locus.

8.2.3 Accounting for Void Nucleation

In material systems where the strain to nucleation is either large or represents a good fraction of the total strain to fracture, it is important to devise a procedure for identification of the material parameters involved. If void nucleation is modeled using the approach outlined in Section (6.1.2) and Eqn. (56) then there are five parameters: f_N , ϵ_N and s_N and the counterparts of the last two for the stress-controlled nucleation. f_N is typically taken as the void volume fraction of void-nucleating second phase particles. In particular, the integral of \dot{f}_n over the strain history should not exceed f_N for it is clear that the source term is limited by the available damage sites. Next, ϵ_N may be inferred from pre-straining experiments such as those of Le Roy et al. (1981); Pardoen et al. (1998). There is no direct way to identify s_N . The authors are not aware of any experimental work where these parameters were fully identified. In practice, the function \mathcal{A} is taken as a constant, e.g., Joly et al. (1990).

If stress-based micromechanical models of void nucleation are used (see Section 4) then the parameters to be identified are the brittle strength of the particles and the interfacial strength, both interpreted as effective properties of the particle and interface, respectively. Upon attainment of any of the two concurrent criteria (10), one would initialize the void volume fraction to the average particle volume fraction. A variant of this procedure has recently been used by Lassance et al. (2006).

9 Crack Initiation and Growth

Applications of the top-down approach to the modeling and simulation of crack initiation and propagation are presented for the various specimen geometries of Fig. 2. Focus is on predictions based on full solutions of boundary-value problems using the finite element method. Unless otherwise noted, the integrated model of Section 8 is used. Attention is given to both macroscopic and microscopic aspects of the fracture process. Comparisons of model predictions with macroscopic properties and, when available, with microscopic measurements are discussed.

9.1 Round Smooth Bars

Cup-cone fracture in round tensile bars involves both the initiation and growth of a crack. It has been analyzed by Tvergaard and Needleman (1984) using the Gurson model and incorporating void nucleation and void coalescence through the $f^*(f)$ function with $f_c = 0.15$ and $\delta \approx 5.2$ (GTN model). Initially, the bar is smooth. Subsequent to necking, the stress triaxiality increases inside the neck where voids nucleate and grow. The coalescence of voids at the center of the specimen leads to the initiation of a crack, which propagates first as a “flat” crack, then goes “slant” as it approaches the free surface. Thus, the

Gurson model captures the essence of the cup and cone rupture of a round tensile bar. Also, a zig-zag growth prior to formation of the shear lips was simulated. As noted by Tvergaard and Needleman (1984), mesh design plays an important role in the simulation of cup-cone and other crack growth problems.

Besson et al. (2001) carried out a thorough finite-element investigation of cup-cone fracture using both the GTN model and the Rousselier model. They analyzed the effects of mesh design, element type, material strain-rate sensitivity and constitutive damage parameters. Fig. 61 depicts the simulated phenomenology of cup-cone formation in a round tensile bar. Element-level localization indicators were particularly useful for interpreting the results. Rice's (1977) localization condition was used in the case of rate-independent plasticity while a localization indicator based on a linear perturbation analysis (Barbier et al., 1998) was used in the rate-dependent (viscoplastic) case. Cup-cone fracture was successfully simulated when the mesh was fine enough to resolve the localization zone, provided that the elements were not too flat when the crack initiated. What is meant by mesh refinement is the density of degrees of freedom, not only the element size. In particular, the zig-zag growth was found to be a result of symmetry assumptions. No zig-zag was obtained with the full specimen meshed.

Appropriate meshing (mesh density and element aspect ratio) emerged as a necessary condition to obtain the cup-cone formation in the calculations of Besson et al. (2001). However, it was not sufficient. A judicious choice of constitutive parameters had to be made. In particular, use of the f^* function with $f_c = 0.005$ was found to inhibit cup-cone formation and flat fracture was obtained. Further analysis aided by the localization indicators has shown that this behavior is due to the discontinuity of the derivative of the f^* function with respect to the porosity. The value $f_c = 0.005$ was used, along with $\delta = 3$, since it provided the best fit to experimental data on a high strength steel¹⁴. This finding is important because it documents the fact that use of critical porosities inferred from the micromechanical models of Section 7 in conjunction with the f^* approach would prohibit cup-cone formation. Since these models predict quite well the values computed from cell model analyses, taken as reference, it follows that the f^* approach for modeling void coalescence may not be adequate for modeling cup-cone fracture with realistic values of the micromechanical parameters.

In order to remedy this, Besson et al. (2001) suggested two alternative options: (i) use a larger value of $q_2 = 1.15$ instead of the commonly used value of 1; or (ii) introduce strain-controlled nucleation of a secondary porosity using Eqn. (56) with a constant $\mathcal{A} = 0.2$. Both options led to formation of cup-cone rupture. None of these options is however fully satisfactory from the physical point of view. The approach consisting of fitting q_1 and q_2 , as advocated for example by Gullerud et al. (2000) and Faleskog et al. (1998), is inelegant and could be justified if a better void growth model were not available. Use of the GLD model for instance is obviously a better alternative. Option (ii), on the other hand, is not consistent with the expectation based on the micromechanical void nucleation model that continuous void nucleation is unlikely to be physical, especially for debonding (see Section 4 and Fig. 26). In addition, the carbides invoked as secondary sites of nucleation are unlikely to nucleate voids of such significance.

¹⁴Incidentally, this value of f_c is close to what would be predicted based on the micromechanically based void coalescence model for an initial porosity of $f_0 = 10^{-5}$ at a stress triaxiality of 0.5; see Fig. 48.

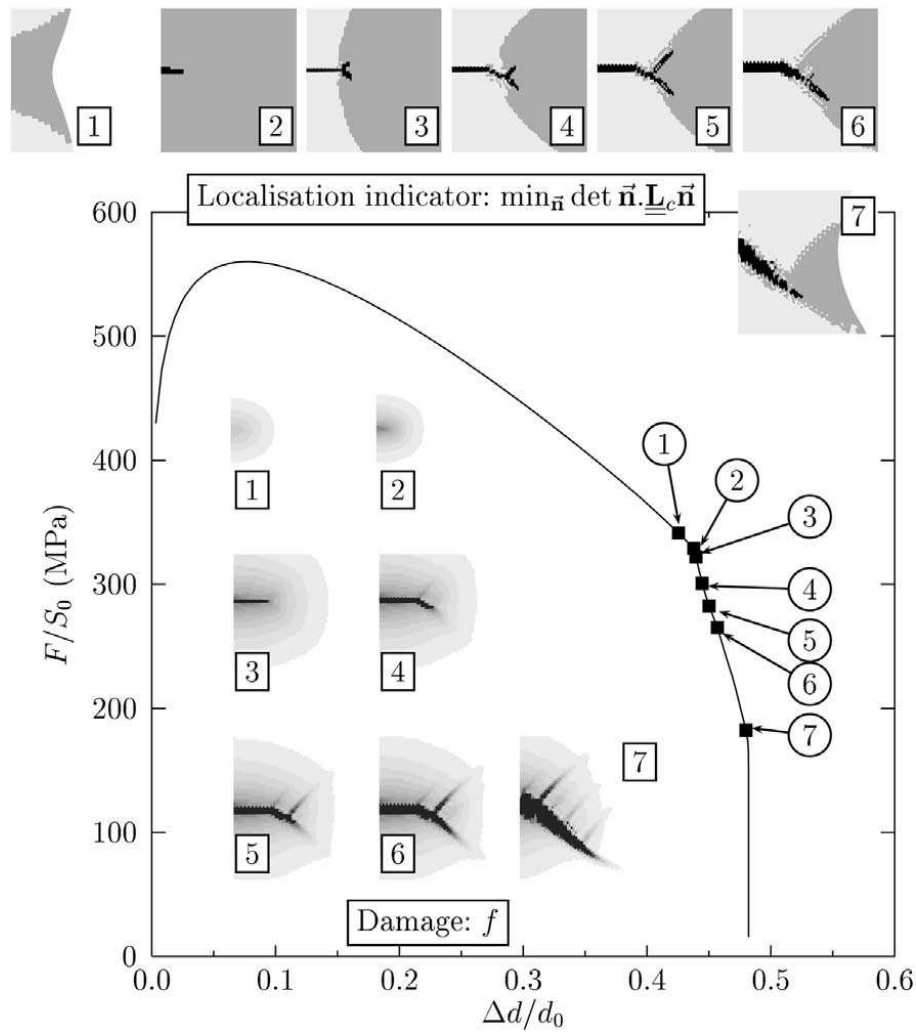


Figure 61: Phenomenology of cup-cone formation in an initially smooth round bar, simulated using the GTN model. Reprinted from (Besson et al., 2001) with permission from Elsevier.

In summary, the GTN model has the ability to capture qualitatively the simulation of cup-cone fracture in round smooth bars. However, it cannot do so with realistic values of the micromechanical parameters. Also, it is worth noting that the Gurson model will predict some void growth prior to necking (see Fig. 33) and will overestimate void growth after it because of the low stress triaxialities involved ($0.3 \leq T \leq 0.6$). By way of contrast, the GLD model will predict no void growth prior to necking (see Fig. 37), which is the correct trend. Therefore, what is of particular importance regarding cup-cone fracture is that the GLD model alone will not suffice to simulate fracture in smooth bars. But the integrated model (GLD supplemented with the micromechanical void coalescence model) holds the promise of resolving the above issues with the GTN model. Analyses of the type of Besson et al's using the integrated model are still lacking.

9.2 Plane Strain Bars

Experimental evidence has shown that fracture in plane strain bars exhibits a macroscopically slant character. Conditions for the localization of plastic flow at macroscopic scales have been examined notably by Tvergaard (1982b) and Saje et al. (1982) under plane strain loading conditions. In general, macroscopic localization is favored in numerical simulations when at least one of the following is included: continuous void nucleation; porosity-induced softening (provided large porosity levels); large kinematic hardening leading to high yield surface curvatures; deviations from normal plastic flow; thermal softening at high strain-rates and presence of a vertex in the yield surface. In the context of porous ductile solids, analyses based on variants of the GTN model have successfully modeled plastic flow localization in finite-deformation settings and discussed rather complex shear band patterns depending on details of the constitutive formulation and choices of damage parameters. The reader is referred to the previous review by Tvergaard (1990) for more details.

More recently, fracture in plane strain bars was also investigated by Besson et al. (2003) who carried out a series of analyses using the GTN model. Systematic examination of the effects of mesh design and refinement and of constitutive damage parameters was conducted and localization indicators were evaluated throughout the calculations. The conclusions of their analyses were similar to those of their earlier studies on round bars (Besson et al., 2001). In particular, use of the f^* function to model void coalescence was found to favor flat fracture when f_c takes values of about 0.01. These analyses are consistent with the trends of all previous studies (Tvergaard, 1990), but point out the need for better models capable of more quantitative predictions.

Indeed, assume for the time being that void nucleation occurs and is terminated at some stage of plastic flow, well before the onset of a macroscopic crack in the bar. Under such circumstances, a finite element simulation of a plane strain bar using the Gurson (or GLD model) with the f^* function and an isotropically hardening matrix material will predict flat fracture so long as the values used for f_c are about one percent (Benzerga, 2000). Given that the above assumption on void nucleation is a reasonable expectation for structural steels and some other alloys, and that values much higher than a few percent for f_c would not be realistic, one is led to conclude that the GTN model has some but not all of the ingredients needed to model plane strain fracture.

Thus, the fundamental question examined here is that of what conditions are sufficient for the formation of slant fracture under plane strain, when continuous void nucleation is deactivated. Only conditions that are true to the physics and micromechanics of ductile fracture are sought. This question was examined by Benzerga et al. (2002) in a combined experimental–computational investigation. They used the integrated model of Section 8.1, i.e., the GLD model for void growth and Benzerga’s (2002) model for void coalescence. Both models included the heuristic extension to plastic anisotropy apparent in (87) and (95).

The ductile fracture process in the plane strain bar was found to take place as follows. Initially, the bar has uniform thickness with porosity $f_0 = 0.0075$. In the reference case, the voids were assumed to be initially spherical $w_0 = 1$ and their spatial distribution statistically isotropic $\lambda_0 = 1$. Also, the matrix was modeled as a power-law hardening material with plastic anisotropy. Unlike in round bars, some void growth takes place

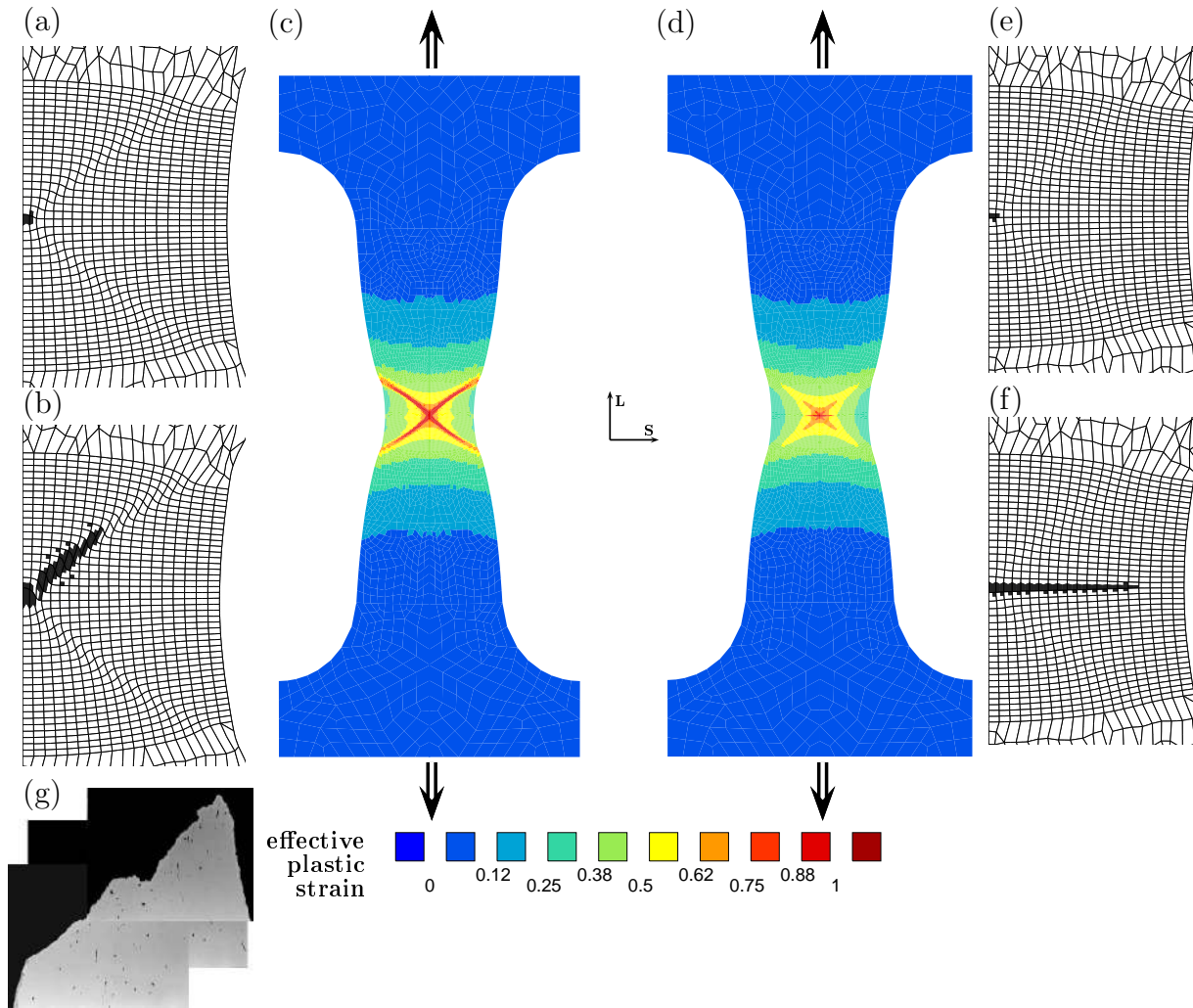


Figure 62: Macroscopic plastic flow localization in plane strain bars. (a)–(c) Using the integrated model of Section 8.1. (d)–(f) Using the GLD model and isotropic plasticity for the matrix. Elements that have undergone coalescence are painted black. (g) Cross-section of a plane strain steel bar after fracture. Adapted from (Benzerga et al., 2002).

before necking because the stress triaxiality is initially about 0.55 and increases to about 0.6 at the onset of necking. Then necking occurs, and subsequently voids grow faster in the central region of the neck, where increased triaxial tension develops ($0.6 \leq T \leq 1.0$). Fig. 62 shows the distribution of porosity at two stages: at the onset of coalescence in the center of the neck (a) and at a later stage (b). More stages were shown in the quoted paper. In particular, no shear band had formed before the onset of coalescence in the central element. In other words, it is the onset of coalescence that triggered localization and the formation of two intersecting shear bands, as may be appreciated from Fig. 62c. Damage then concentrates in one of the two bands.

This phenomenology of fracture is quite different from what was reported by Tvergaard (1990) using the GTN approach and continuous void nucleation. There, strain localization

takes place prior to fracture by void coalescence. The opposite is seen here. Benzerga et al. (2002) also reported that when plastic anisotropy was not accounted for, a flat fracture mode was obtained (Figs. 62d-f). Additional subsequent analyses have indicated that this behavior was probably due to the finite elements being too flat in the neck region. As discussed by Besson et al. (2003) appropriate mesh design is important in localization predictions. Also, the calculations reported by Benzerga et al. (2002) were carried out using a Jaumann rate of Cauchy's stress in the co-rotational formulation of the constitutive equations (see Appendix B). The effect of the type of objective stress rate has not been investigated. For isotropically hardening materials, the plastic spin was found to play a secondary role on the onset of plastic flow localization by Tvergaard and Van der Giessen (1991).

Synergistic effects of plastic anisotropy and void coalescence are possibly important in discussing fracture mode in plane strain. For example, plastic anisotropy can be a destabilizing factor for plastic flow even in the absence of porosity (Steinmann et al., 1994). However, the main finding illustrated in Fig. 62 and subsequent unpublished work is the role of void coalescence as a precursor to shear-band formation, provided that a micromechanical model is used instead of the phenomenological f^* approach. The results of Benzerga et al. (2002) can be interpreted based on the presence of a vertex in the effective yield surface of the porous ductile material, as illustrated in Fig. 63. The vertex has a clear physical meaning: it corresponds to the onset of void coalescence. The use of

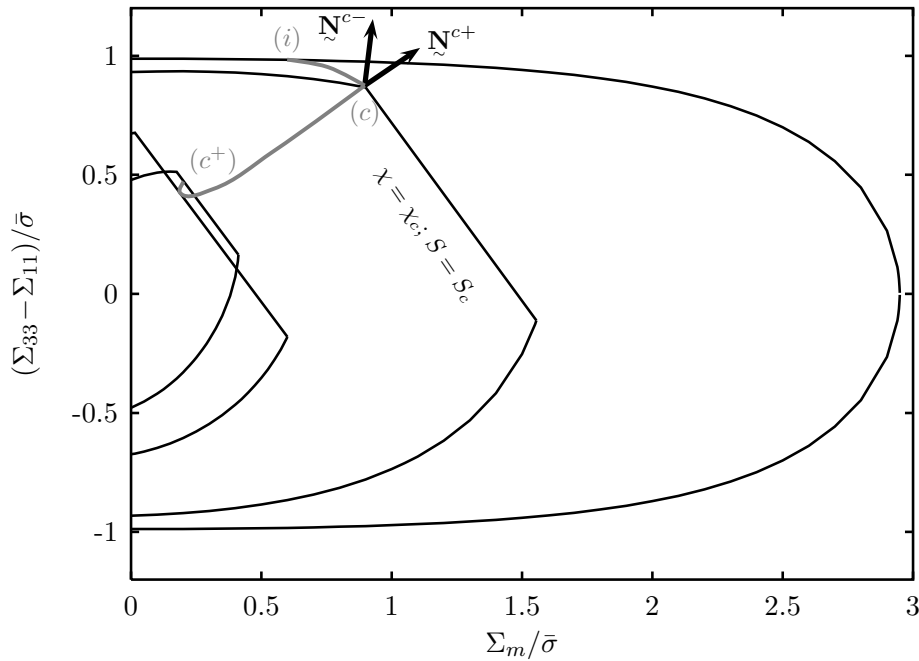


Figure 63: Effective yield surfaces before and after localization. The loading path is that experienced inside the neck of the plane-strain specimen: (i) initial state: $f_0 = 0.0075$, $S_0 = 0$ and $\lambda_0 = 1.5$; (c) state at the onset of coalescence with $\chi_c = 0.47$, $S_c = 1.1$ and $f_c = 0.05$; (c^+) two states post-localization with $(\chi = 0.82, S = 1.3)$ and $(\chi = 0.80, S = 2)$ respectively. In all cases, matrix plasticity is isotropic. After (Benzerga et al., 2002).

the f^* -approach along with the Gurson model entails that there is no difference in the

shape of the yield surface before and after the onset of coalescence; only the porosity rate is subject to some “acceleration” after a given critical porosity is reached. In other words, because such yield surfaces are smooth, the normal to the yield surface varies a little from before to after coalescence. On the other hand, in the present theory, the yield surface during coalescence differs in essence from the one prior to coalescence and the onset of the latter is accompanied by an abrupt change in the direction of plastic flow, i.e., from \mathbf{N}^{c-} to \mathbf{N}^{c+} , as depicted in Fig. 63.

The predicted slant fracture phenomenology is consistent with detailed microscopic examination of fracture surfaces. An example is shown in Fig. 62g. It is clear from the cross-section that the crack proceeded in a flat mode to some extent prior to forming the shear lips. In fact, this view conciliates the phenomenologies of plane strain and round smooth bars, except that the formation of the shear lips takes place much earlier in plane strain bars. An other example was shown in Fig. 5c. Also, the fracture surfaces of a wide variety of internally pressurized thick-walled tubes exhibit a visible central line parallel to the tube axis (Fig. 6). In a current section normal to the tube, the line shrinks to a ‘point’ (actually to a narrow segment) which is clearly identified as the location of fracture initiation, just as in Fig. 62g. This observation sheds some light on the phenomenon under investigation. In both the plane-strain tensile specimen and pressurized cylinders, the macroscopic shear-like fracture mode is subsequent to crack initiation at the center, which occurs by void coalescence through internal necking. An important implication of this finding is that plane strain ductility should not be much different from that measured in a round (notched) bar of comparable stress state triaxiality. This was indeed shown to be approximately the case in Fig. 4¹⁵. In this regard, care should be taken in comparing experimental ductilities based on area reductions at fracture. The reason for this is that the amount of overall strain accumulated during crack propagation in a notched bar may be a significant fraction of the total ductility (e.g. see Fig. 10). On the contrary, that strain is generally negligible in smooth bars, round or plane strain.

9.3 Notched Bars

While the prediction of cup-cone and slant fractures in smooth bars constitutes a good qualitative test of models for porous ductile solids, the prediction of fracture in notched bars with various notch radii may be considered as the ultimate quantitative test. Notched bars present some advantages over smooth bars in that the fracture process is decoupled from plastic instabilities such as necking and shear banding, the stress triaxiality range can be made wider by varying the notch radius, and crack propagation can be controlled in the experiments, thus providing an ideal tool for model assessment. A thorough assessment of the Gurson model against notched bar experiments was made by Becker et al. (1988). Their study centered on a compacted iron powder so that the material contained some initial porosity. Here, focus is laid on structural materials.

The top-down approach of Section 8 has been applied to predict ductile fracture in round notched bars by Benzerga (2000) and Benzerga et al. (2004b). The material was a low alloy steel studied by Benzerga et al. (2004a). This steel exhibited, like many

¹⁵An additional contribution may come from the effect of the third invariant of the stress tensor, i.e., a Lode parameter effect.

others, some anisotropy in plastic deformation and a strong anisotropy in the fracture properties (ductilities and toughness). For material parameter identification, the standard procedure of Section 8.2.1 was essentially followed. In particular, voids were found to initiate at relatively low amounts of plastic strain from elongated MnS inclusions and equiaxed alumina particles. The initial volume fraction, void aspect ratios and void spacing ratios were determined using quantitative metallography, then transformed into equivalent quantities, as explained in Section 8.2.2.

Fig. 64a shows a typical force (P) versus diameter-reduction ($\Delta\Phi$) response for a bar with a shallow notch subject to transverse loading. Quadratic quadrilateral elements were employed in these calculations using reduced integration. Gauss points that have shifted to the void coalescence regime, i.e., equations (95)–(100), are said to be in the post-localization regime. Various snapshots of this regime are highlighted in Fig. 64b. Corresponding stages of the post-coalescence regime (i.e., after complete loss of stress carrying capacity) are shown in Fig. 64c. It is important to distinguish the localization indicator in Fig. 64b from that shown in Fig. 61 based on the work of Besson et al. (2001). The former corresponds to micro-scale localization associated with the physical process of void coalescence.

In Fig. 64a diameter reduction is given along two perpendicular directions, as an evidence for the anisotropy of deformation. Fig. 64b also shows the anisotropy of damage accumulation, here measured by the number of elements that undergo the post-localized behavior, while Fig. 64c depicts the subsequent anisotropy in crack growth.

Before the stage marked **A** in Fig 64a plastic flow at the current loading point is normal to the smooth GLD-like yield surface with the evolution of the microstructure being determined by (92) and (93) for the porosity and void aspect ratio, respectively. As long as the current loading point lies on the pre-coalescence yield surface, there is no effect of the spacing ratio λ . Rapid void growth occurs at the center of the bar and is accompanied by a steady decrease in the void aspect ratio, which under T-loading, corresponds to the void opening up. Correspondingly, the ligament size ratio, χ , increases exponentially from a relatively high initial value ($\chi_0 \approx 0.1$) that reflects an unfavorable loading configuration. This increase in χ (i.e. decrease of local ligament area) strongly affects the limit-load constraint factor C_f in (96). When for the first time the combined decrease of both ligament area and C_f outweighs the increase in the axial stress the mode of deformation shifts toward the uniaxial straining mode. Because of this (micro-scale) localization, for a small increase of deformation the loading point now lies on the planar part of the effective yield surface; see Fig. 58. This shift in the deformation mode first occurs at the center of the bar as shown in Fig 64b at stage **A**. As a consequence the global force drops quite abruptly although there is no crack yet in the specimen. When a crack has nucleated at stage **B** (see Fig 64c) the number of elements undergoing coalescence has very much increased.

In addition to the essential features above, anisotropy in crack growth was successfully simulated. The crack clearly advances faster in the L direction than in the S direction. In the simulations, this is attributed to plastic anisotropy, not to the fact that voids are longer along L in the plane of coalescence. The latter fact cannot be captured by the current formulation of the model. Similarly, the simulation of shear lips would require a much finer mesh, with no consequence on the predictions of ductility.

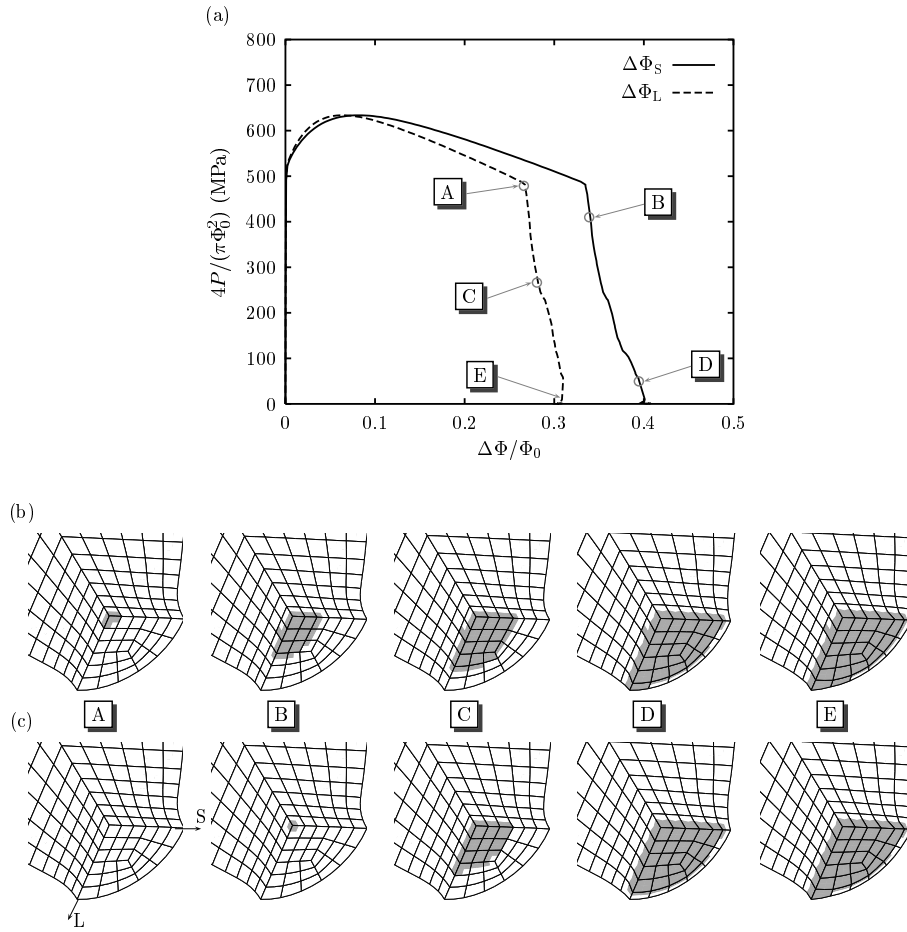


Figure 64: 3D simulation of ductile fracture in a notched bar using the integrated model of Section 8.1. (a) Normalized load versus diameter reduction along two perpendicular transverse directions (rolling direction, $\Delta\Phi_L$, and through-thickness direction, $\Delta\Phi_S$). (b) Elements undergoing void coalescence are painted gray. (c) Failed elements are painted gray. After (Benzerga et al., 2004b).

Figure 65 shows some actual comparisons with experimental data. For two loading orientations, transverse T and longitudinal L, the mean strains to crack initiation, as defined in Section 2, are plotted against the stress triaxiality ratio at the center of the notched bar, roughly averaged over the entire deformation history. Error bars account for the spread in experimental measurements. What is of importance here is that the predictions contained no adjustable factor regarding damage and fracture modeling. As explained in Section 8.2.1, calibration was made for the plastic flow properties only. Promising comparisons between experiments and model predictions for microstructural variables at the onset of cracking were also discussed by Benzerga et al. (2004b).

9.4 Cracked Specimens

Global approaches to fracture, which are based on attainment of a critical value for a global indicator such as the J integral or the crack-tip opening angle, have been and

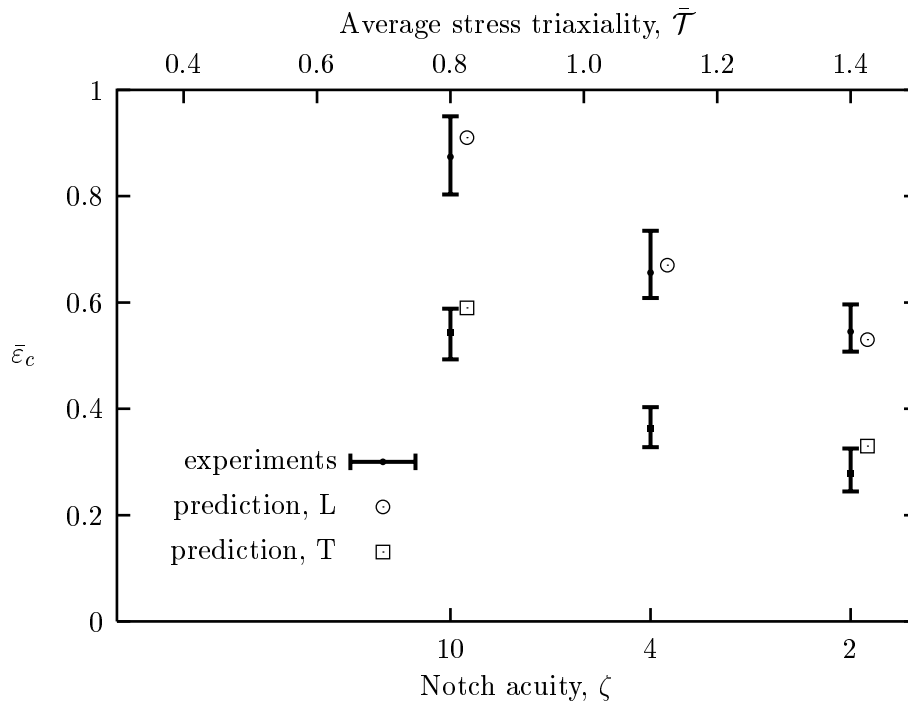


Figure 65: Comparison between measured and predicted average strains to failure initiation in notched bars for two loading orientations. After (Benzerga et al., 2004b).

remain useful to engineers. Their connection to microstructure is, however, weak. By way of contrast, an approach that employs a local fracture criterion, i.e., in the near-tip region, directly tackles the microstructural effects on fracture properties (Pineau, 1992). This is important since the driving forces in fracture are mechanical but the material resistance basically depends on the microstructure.

Material located in the vicinity of a crack tip is subject to much stronger gradients in the mechanical fields than is the case in notched bars. Yet, the top-down approach provides a unifying framework for treating both types of problems. This is so because the fundamental mechanisms, which are generically the same, are incorporated in the material models.

Rice and Johnson (1970) and later McMeeking (1977) *de facto* employed a top-down approach to estimate the critical crack-tip opening displacement for crack growth under small scale yielding at a mode I plane strain crack. Both studies used a local fracture criterion based on void growth (Rice and Tracey, 1969), evaluated at a critical distance from the crack-tip, along with either slip-line or full finite-element solutions; see also (D'Escatha and Devaux, 1979) who, in addition, used a node-release technique for propagation. Some later studies have modeled explicit voids ahead of the crack tip with some criteria for final ligament failure; see (Gao et al., 2005) and references therein. Other studies employed Gurson-like constitutive relations either to describe natural loss of stress bearing capacity, e.g., (Needleman and Tvergaard, 1987; Xia et al., 1995), or to inform a cohesive-surface model (Tvergaard and Hutchinson, 1992).

In all of these studies, the results are typically used to compute the J -resistance curve (J versus crack extension Δa) and estimate the tearing modulus dJ/da . Subsequently,

the critical value J_{Ic} for the onset of crack growth is determined by back extrapolation using the slope given by the tearing modulus. When conditions of small-scale yielding are obeyed, the critical value of the stress intensity factor, or fracture toughness, is evaluated from

$$K_{Ic} = \left(\frac{J_{Ic} E}{1 - \nu^2} \right)^{\frac{1}{2}} \quad (101)$$

Under more general conditions, e.g., (Xia et al., 1995), J_{Ic} is taken as a measure of initiation toughness. If crack growth is simulated over sufficiently large distances then a steady-state regime is reached, which is characterized by a steady-state toughness. At present, however, predictions of the latter have only been made using a cohesive-zone approach (Tvergaard and Hutchinson, 1992) or the computational cell model approach of Xia and Shih (1995).

The major advantage of this type of studies is that they directly draw a connection between microstructure and toughness. However, when comparisons are made with experiments, the quantitative character of the predictions ultimately resides in the robustness of the failure criterion that was employed for crack growth. In general, predictions based on the Rice–Tracey void growth model tend to overestimate the critical conditions (Tvergaard, 1990). In fact, the same could be said of predictions by the GTN model, unless specific void nucleation model parameters are used. The latter are difficult to identify based on experiments and, when the particle volume fraction f_N is smaller than say 0.001, they do not affect the predictions much. In addition, some of the experiments reported by McMeeking (1977) and subsequently used by several authors concerned C–Mn steels with MnS inclusions, just like those discussed in the previous section, and loaded in the transverse direction. Under such circumstances, fracture is essentially coalescence-controlled so that the use of an appropriate void coalescence criterion is critical for obtaining quantitative predictions.

While detailed analyses of the type presented for notched bars is still lacking some work has been done employing the integrated model of Section 8.1 or variants thereof. Thus, Gao and Kim (2006) have used the GLD void growth model, along with the f^* approach for void coalescence, in a three-dimensional analysis of crack growth in thin aluminum panels, Fig. 66a. Because the initial microstructure was not characterized experimentally, these authors proposed a calibration procedure based on CT specimens (Fig. 66b) then offered good predictions for the middle-crack tension M(T) specimens. However, the value of 0.02 used for the initial porosity is likely much higher than the real value, since not all second-phase particles in Al alloys nucleate voids. In addition, the effect of plastic anisotropy was not accounted for. Anisotropy, which is usually important in these materials, would lead to accelerated void growth.

In an other study, Pardoen and Hutchinson (2003) have discussed trends for the prediction of initiation toughness using the top-down approach of Section 8. They employed the GLD void growth model along with an enhanced void coalescence model (Pardoen and Hutchinson, 2000). The latter is based on Thomason’s limit-load constraint factor in its original form, Eqn. (80), heuristically modified to account for strain hardening effects¹⁶, along with evolution laws for the microstructural variables, similar to those presented in

¹⁶The factors α and β in expression (80) were taken to depend on the strain hardening exponent N . Expressions for functions $\alpha(N)$ and $\beta(N)$ were then obtained based on fits to cell model results.

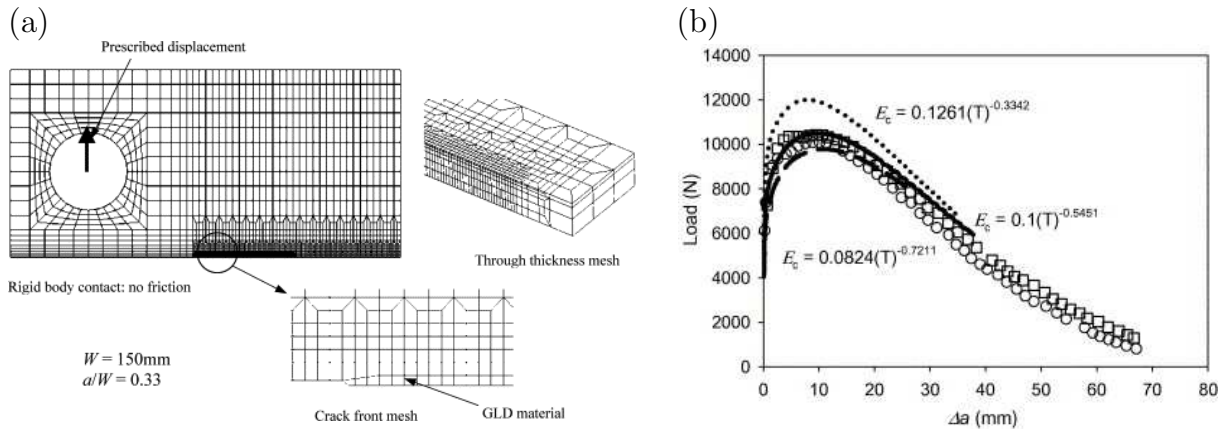


Figure 66: (a) 3D finite-element mesh of a CT specimen. (b) Experimental and computed curves of load versus crack extension for Al alloy. After (Gao and Kim, 2006).

Section 8.1. Pardoen and Hutchinson (2003) systematically investigated the effect of material flow properties (yield stress σ_0/E and hardening exponent N) for initial porosities spanning 4 orders of magnitude. They also investigated the effects of initial void shape and relative spacing. Their results allowed to discuss effects of microstructure, beyond the particle void volume fraction, on the initiation toughness. For example, J_{Ic} was found to vary by a factor of 2 when the initial aspect ratio w_0 goes from 0.1 (flat voids) to 3 (long voids). Some earlier predictions using the GTN model were within a factor of two of experimental values Tvergaard (1990). This indicates that much variability among experimental values of toughness may be traceable to microstructural variations.

As indicated earlier, crack-tip fields are characterized by steep gradients. As a consequence, a characteristic length scale plays a much more important role in the presence of cracks. This length scale, say X_0 , enters all of the above studies. Physically, X_0 is usually associated with the mean inclusion or void spacing. In the conventional implementations using the GTN model or the integrated model of Section 8.1, X_0 is typically taken as the size of the finite element mesh. This is so because numerical simulations involving these damage models suffer from mesh-sensitivity of the results. While somewhat practical, this approach is not satisfactory considering the fact that the mesh affects the direction of crack propagation.

From a fundamental point of view, an approach that incorporates the length scale X_0 in the constitutive formulation is, in principle, required. A common characteristic of all damage material models employed in failure analysis is the softening behavior inherent to the degradation of mechanical properties (de Borst, 1987). It has long been recognized that introduction of such softening in a constitutive law raises problems on both mathematical and physical grounds (Bazant and Pijaudier-Cabot, 1988; Leblond et al., 1994a; Peerlings et al., 2001). The major mathematical drawback is that softening leads to bifurcations with an infinite number of bifurcated branches, which raises the problem of selecting the relevant one and thus yields a pathological mesh-sensitivity in numerical simulations. The main physical drawback is the phenomenon of strain localization, which results in a vanishing dissipated energy at failure, a paradox. While the introduction of

viscosity leads to some regularization (Needleman, 1988) it does not remove the pathological mesh-dependence. By this we mean that, when the discretization grid element is fine enough to resolve field gradients, fracture predictions exhibit strong dependence vis-a-vis mesh refinement.

Within this context, attempts have been made to introduce “localization limiters” or regularization techniques. The most physical among these is one based on the nonlocal concept, whereby the damage variable is delocalized over a volume through a convolution integral, thus introducing a characteristic length. Application of this concept yields satisfactory results in the presence of moderate gradients of the macroscopic fields (Leblond et al., 1994a; Tvergaard and Needleman, 1995; Enakoutsa et al., 2007; Hu and Ghosh, 2008). However, this relatively simple regularization method does not solve the mesh-dependency problem when strong gradients are present such as near crack tips. Other robust methods were introduced in recent years by Mediavilla et al. (2006). Unfortunately, the damage models used have nearly no physical grounding with respect to the ductile fracture phenomena of void growth to coalescence. An alternative, perhaps more fundamental solution to this problem was proposed by Gologanu et al. (1997). They used the framework of Section 5 to account for nonuniform boundary conditions at the scale of the elementary volume. The outcome of their analysis was a Gurson-like model with higher order stresses and a length scale, which naturally represents a void spacing. Preliminary finite element calculations of cracked specimens using this model were recently carried out by Enakoutsa and Leblond (2008). The results are promising in terms of mesh-insensitivity. However, more work is needed in this area.

10 Discussion

The material models for porous plastic solids that were available at the time of the previous review (Tvergaard, 1990) were already quite powerful. This stems from their grounding in micromechanics. Because the generic micromechanisms of ductile fracture are well known, micromechanics is a natural framework for its modeling. The basic mechanisms involve some observables and the microstructural parameters that describe damage are measurable.

This review did not do justice to alternative micromechanical models based on non-linear variational principles (Ponte Castaneda, 1991). While earlier versions of this line of models (Ponte Castañeda and Zaidman, 1994; Kailasam and Ponte Castaneda, 1998) suffered from drawbacks at high stress triaxialities, recent developments have proven promising (Danas and Ponte Castañeda, 2009; Vincent et al., 2009). Granted sufficient assessment against experiments, it is likely that these approaches will gain increased use in practical applications.

The review did not consider a class of material models derived within the framework of continuum thermodynamics. This framework may set constraints on evolution paths and bounds on constitutive parameters. Eventually, it allows the structure of constitutive equations to be discussed. However, models abound within its confines and no review could be all inclusive. What is important is that thermodynamic consistency is not enough for a material model to be accurate and predictive. In thermoelasticity, for example, thermodynamic considerations lead to bounds on the elastic constants. However, the latter can only be predicted using atomistics or, given their long-range character, obtained by macroscopic measurements. Similarly, plastic flow and fracture properties, which are less intrinsic and so much more microstructure-dependent, cannot be predicted using continuum thermodynamics. By way of contrast, the material models reviewed here have an inherent predictive capability, thanks to scale transition operations. The evolving variables are microstructural, as opposed to internal state “hidden” variables. Their evolution is often set by physical considerations. For example, the porosity evolves directly from a conservation principle and the equation of continuity.

The mechanics of porous ductile solids leads to robust constitutive equations. At the microscopic scale, the matrix is typically modeled as fully dense, plastically incompressible, obeying J_2 flow theory and perfectly plastic (hardening is incorporated *a posteriori*). Of the general properties obtained for the macroscopic constitutive relations, some are worth noting. At the macroscale, the material is compressible, has an evolving density and it is not perfectly plastic. Plastic flow obeys normality and, for a class of models where it is constrained to be isotropic, it is dependent upon all three invariants of the stress tensor, although the third one does not come out of current averaging procedures. For a broader, more accurate class of models, the overall behavior is anisotropic and this is a direct consequence of microstructure evolution. If the matrix itself is anisotropic, this anisotropy translates to the macroscopic scale in rather intricate ways, as reflected in the highly distorted yield surfaces in the rate-independent case. One peculiar feature of this distortion is the apparent “kinematic” hardening seen in Fig. 42b. This kinematic-like hardening, i.e., displacement of the center of the yield surface, in the π -plane under a superimposed hydrostatic stress, is also a pure microstructural effect.

A number of interesting developments have taken place in the area of ductile frac-

ture over the past two decades. Perhaps the two main theoretical developments are with respect to incorporation of anisotropy in the constitutive laws and to the modeling of void coalescence. The lack of representation of anisotropy in previous models was emphasized as a limitation in the review by Tvergaard (1990). This problem is now solved, but only to some extent. Void shape effects have been incorporated for spheroidal voids only and plastic anisotropy has been modeled using quadratic criteria of orthotropy. One may argue that the material models are already too sophisticated to be used by engineers. On the other hand, without fully three-dimensional models one cannot avoid the gymnastics adopted in the procedure for material parameter identification in some cases (Section 8.2.2). Some 3D models have been developed within an alternative micromechanical framework (Kailasam and Ponte Castaneda, 1998; Danas and Ponte Castañeda, 2009). One mathematical challenge for all anisotropic void growth models is to account for strongly nonlinear effects, such as cavity flattening at high stress triaxiality. Currently, this aspect is either missing (Danas and Ponte Castañeda, 2009) or dealt with in a heuristic way (Gologanu et al., 1997; Keralavarma and Benzerga, 2010).

The micromechanical modeling of void coalescence is the other major development. Accurate modeling does require that microstructure evolution, hence the induced anisotropy, be adequately captured. Our current understanding of the phenomenon is that it is that stage of void growth taking place while plastic flow is highly constrained by material regions undergoing elastic unloading. A good example, for which analytical solutions have become available, is that of internal necking of the intervoid ligament. While this microscopic phenomenon has long been known in the materials science community, only in recent years has its mathematical formulation been properly posed. Within this framework, the onset of void coalescence is identified with the onset of localization within the elementary volume.

Current level of understanding allows to make important distinctions between localization of plastic flow at microscopic and macroscopic scales. Localization is typically not predicted in an isotropic elastic–plastic material with a positive hardening modulus, when subjected to remote homogeneous deformation. This is the result of either bifurcation studies carried out within the classical framework of Hadamard (1903), Hill (1962), Mandel (1966) and Rice (1977) or using full numerical solutions of boundary-value problems accounting for finite-strain effects (Tvergaard, 1990). Localization of plastic flow in macroscopic shear bands that lead to shear-like fractures is typically predicted using constitutive equations for porous ductile solids, under certain circumstances (see Section 9.2). On the other hand, in the presence of microvoids, plastic flow localization can occur at the microscale between voids even if the matrix is modeled as a hardening elastic–plastic matrix. What is of particular importance is that a necking instability generally precedes the Hadamard–Rice localization condition, when checked at the micro-scale.

There are some interesting consequences to these new developments, which are of both theoretical and practical significance. A framework for modeling the constitutive response of porous ductile solids combining Gurson-like constitutive models with models that account for the different response during micro-scale localization can itself be used to analyze flow localization at macroscopic scales, i.e., once the homogenized response is obtained at the scale of the elementary volume. An application was discussed in Fig. 62.

An other important distinction allowed by current understanding is between void co-

alescence and void interaction. Void coalescence refers to a process beginning with the onset of localization in some intervvoid ligament and ending with void link-up. In particular, there is no length scale in the continuum models that are currently available. The micromechanical models involve dimensionless parameters, the most important of which being the void size relative to void spacing. The absolute void size does not enter the formulation. On the other hand, void interaction, in its deepest physical meaning, involves a concept of non-locality. Accounting for that supposes that judicious boundary conditions are considered for the representative elementary volume. Appropriate boundary conditions will have to account for nonuniformity in rates of deformation and tractions on the boundary, as a signature of neighborhood influence. Such a formulation has been posed and developed by Gologanu et al. (1997) and does lead to a length scale in the final constitutive equations.

On the experimental side, the most important development of the last two decades may be the advent of X-ray micro-computed tomography. This technique has allowed *in situ* real-time examination of micro-scale ductile damage processes in three dimensions. When fully developed, this technique will help avoid destructive, often tedious cross-sectioning of test specimens. The leap that will continue to be made using X-ray tomography can only be compared with that enabled by the advent of scanning electron microscopy toward the second half of the last century. The application of the latter technique to fractography, as pioneered by Crussard and co-workers, has enabled features of dimpled surfaces, among so many others, to become visible. Yet, however powerful fractographs might be, *post mortem* examination of fracture surfaces only reveals one facet of the story. Mere presence of dimples is not informative enough for it is so that fracture surfaces of commercially pure single crystals are dimpled, just as well. At the very end of any ductile fracture process, all interfaces give up as material separation has to take place. By way of contrast, tomography maps the microstructural information in the bulk. However, the time and spatial resolutions of micro-computed tomography are still not high enough to observe nucleation processes from small inclusions and precipitates or sudden processes such as void coalescence. As this technique will continue to develop, the field of ductile fracture, and many others, will benefit immensely.

Are any of these developments going to impact engineering fracture mechanics? It is hard to tell, given how conservative this field has been. While cautious rationales sometimes call for conservative measures—when the integrity of important infrastructure or the safety of transportation vehicles are involved—other synergistic fields such as metal forming and rational material design may benefit more directly from a microstructure-based approach in the nearest future. At the very least, the material models reported on here contribute to much deeper understanding of the complex phenomenon of ductile fracture. An example concerning the engineering fracture community is definitely in order. A simple criterion based on attainment of a critical void growth ratio has shaped the understanding amongst engineers, for quite some time, and maybe still does. According to this criterion, as practiced, materials with a critical void growth ratio of 1.2, 1.5 and 2.0 would be characterized as having respectively poor, average or outstanding ductility and toughness. Progress made over the past two decades suggests that such figures are generally meaningless. At the onset of coalescence, void growth ratios as high as 10 are predicted by cell model studies (Pardoën and Hutchinson, 2000). Growth ratios in excess

of ten were measured in some experiments (see Section 2.3).

Where does the field go from here? In our opinion, there are two major directions which are worth pursuing by the community at large.

Numerical simulations of ductile fracture have benefited from various developments in computational mechanics. Conversely, the challenges posed by ductile fracture modeling have often motivated the development of new methods, an archetype of which is the computational formulation of the cohesive-zone model (Needleman, 1987; Tvergaard and Hutchinson, 1992). In more recent years, robust methods have been developed based on nonlocal damage models that aim at resolving issues associated with pathological mesh-sensitivity in numerical solutions of boundary-value problems, e.g., using the finite element method (Mediavilla et al., 2006; Enakoutsa and Leblond, 2008). Generalized finite element methods are also ideally placed to tackle some of the challenging localization and crack growth problems in ductile fracture, e.g., (Moes et al., 1999; Strouboulis et al., 2001; Huespe et al., 2009). As emphasized in the text, it is not an option to rely on a condition for the onset of coalescence, or any other localization indicator, as a failure criterion. This is so because element-level stresses are still too high at the onset of coalescence. What is particularly attractive in the new material models is that they naturally account for the gradual loss of stress carrying capacity at the element level, while accounting for micro-scale localization. Therefore, what is expected from new developments in computational mechanics is accuracy and robustness of model implementations, and mesh-insensitivity of numerical solutions.

Another area in which active research is needed is the connection to physics-based plasticity models. Current models appear, to some, as overly sophisticated. Yet, their development was based on ideal plasticity. The heuristics involved in incorporating hardening is often based on power laws, clearly not the best approximations of large-strain polycrystalline behavior. Effects of temperature and strain-rate are often superposed *ad hoc*, at least in the micromechanical approaches. The connection to physics-based plasticity models is particularly needed when multiple physical length scales are involved. One example is the brittle to ductile transition. The length scale is nanoscopic in the brittle regime (dislocations, fine precipitates) but is microscopic in the ductile regime (inclusion spacing). Another even more challenging problem is in radiation embrittlement where nanoscale voids and microscale voids co-exist while being governed by different physics.

Meanwhile more incremental, but important advances are needed to improve certain mathematical aspects of current models. New applications, including to old challenging problems, are likely to emerge, given the pace at which new structural materials are developed. One cannot emphasize enough the need for critical and fair comparisons with clean, discriminating experiments. What is important is that model predictions should not be biased against experiments. Otherwise, the efforts put into developing top-down approaches will be undermined, opening the door for excessive empiricism.

Acknowledgments

AAB acknowledges stimulating discussions with Mr. Keralavarma and support from the National Science Foundation of the United States of America.

Appendix A. GLD Criterion Parameters

There are six parameters which depend on the microstructural variables f and w : C , g , κ , η and α_2 , listed by order of appearance in criterion (58) and α_1 , which mainly appears in the evolution law of w .

$$g = 0 \quad (\text{p}); \quad g = \frac{e_2^3}{\sqrt{1-e_2^2}} = f \frac{e_1^3}{\sqrt{1-e_1^2}} = f \frac{(1-w^2)^{\frac{3}{2}}}{w} \quad (\text{o}) \quad (\text{A.1})$$

where (p) and (o) are a shorthand notation for prolate and oblate, respectively. We recall that e_1 and e_2 are the eccentricities of the void and the outer boundary of the RVE, respectively. Both are implicit functions of f and w .

$$\kappa = \begin{cases} \left[\frac{1}{\sqrt{3}} + \frac{1}{\ln f} \left((\sqrt{3}-2) \ln \frac{e_1}{e_2} \right) \right]^{-1} & (\text{p}) \\ \frac{3}{2} \left[1 + \frac{(g_f - g_1) + \frac{4}{5}(g_f^{5/2} - g_1^{5/2}) - \frac{3}{5}(g_f^5 - g_1^5)}{\ln \frac{g_f}{g_1}} \right]^{-1} & (\text{o}) \end{cases} \quad (\text{A.2})$$

where

$$g_f \equiv \frac{g}{g+f}, \quad g_1 \equiv \frac{g}{g+1}$$

$$\alpha_2 = \begin{cases} \frac{(1+e_2^2)}{(1+e_2^2)^2 + 2(1-e_2^2)} & (\text{p}) \\ \frac{(1-e_2^2)(1-2e_2^2)}{(1-2e_2^2)^2 + 2(1-e_2^2)} & (\text{o}) \end{cases} \quad (\text{A.3})$$

$$\eta = -\frac{2}{3} \frac{\kappa Q^*(g+1)(g+f)\text{sh}}{(g+1)^2 + (g+f)^2 + (g+1)(g+f)[\kappa H^*\text{sh} - 2\text{ch}]}, \quad (\text{A.4})$$

$$C = -\frac{2}{3} \frac{\kappa(g+1)(g+f)\text{sh}}{(Q^* + \frac{3}{2}\eta H^*)\eta}, \quad \text{sh} \equiv \sinh(\kappa H^*), \quad \text{ch} \equiv \cosh(\kappa H^*)$$

where $H^* \equiv 2(\alpha_1 - \alpha_2)$ and $Q^* \equiv (1-f)$.

$$\alpha_1 = \begin{cases} [e_1 - (1-e_1^2) \tanh^{-1} e_1] / (2e_1^3) & (\text{p}) \\ [-e_1(1-e_1^2) + \sqrt{1-e_1^2} \sin^{-1} e_1] / (2e_1^3) & (\text{o}) \end{cases} \quad (\text{A.5})$$

Finally, the parameter α_1^G which enters the evolution law (93) of the void shape parameter is given by:

$$\alpha_1^G = \begin{cases} 1/(3-e_1^2) & (\text{p}) \\ (1-e_1^2)/(3-2e_1^2) & (\text{o}) \end{cases} \quad (\text{A.6})$$

Appendix B. Finite Element Formulation

The following formulation was used in all the finite element computations reported in the text using the object oriented code ZéBuLoN (Version 8.2 in Section 3 and Version 7 in Section 9). The weak form of the principal of virtual work is written as

$$\int_V \mathbf{S} : \delta \mathbf{E} dV = \int_S \mathbf{T} \cdot \delta \mathbf{u} dS + \int_V \mathbf{f} \cdot \delta \mathbf{u} dV \quad (\text{B.1})$$

with

$$\mathbf{S} = J \mathbf{F}^{-1} \cdot \boldsymbol{\Sigma} \cdot \mathbf{F}^{-T}, \quad \mathbf{E} = \frac{1}{2} (\mathbf{F}^T \mathbf{F} - \mathbf{I}) \quad (\text{B.2})$$

where \mathbf{S} is the second Piola–Kirchhoff stress, \mathbf{E} is the Green–Lagrange strain, \mathbf{F} is the deformation gradient, $\boldsymbol{\Sigma}$ is the Cauchy stress, $J = \det(\mathbf{F})$, \mathbf{T} and \mathbf{f} are, respectively, the surface tractions and body forces if any, \mathbf{u} is the displacement vector and V and S are the volume and surface of the body in the reference configuration. An updated Lagrangian formulation is used which employs objective space frames with the reference configuration being either chosen at the beginning of the increment or at the end of the increment.

For plastic or viscoplastic constitutive equations, the total rate of deformation \mathbf{D} is written as the sum of an elastic part, \mathbf{D}^e , and a plastic part, \mathbf{D}^p . Assuming small elastic strains and isotropic elasticity, a hypoelastic law is expressed using the rotated stress \mathbf{P}

$$\mathbf{D}^e = \mathbb{C}^{-1} : \dot{\mathbf{P}} \quad (\text{B.3})$$

$$\mathbf{P} = J \boldsymbol{\Omega}^T \cdot \boldsymbol{\Sigma} \cdot \boldsymbol{\Omega} \quad (\text{B.4})$$

where \mathbb{C} is the rotated tensor of elastic moduli. $\boldsymbol{\Omega}$ is an appropriate rotation tensor; it is identified with the rotation \mathbf{R} resulting from the polar decomposition of \mathbf{F} if the Green–Naghdi rate of $\boldsymbol{\Sigma}$ is used and $\dot{\boldsymbol{\Omega}} \cdot \boldsymbol{\Omega}^T = \mathbf{W}$ if the Jaumann rate is used, \mathbf{W} being the spin tensor.

The plastic part of the rate of deformation is context dependent; it is provided in the main text. With respect to the integrated model of Section 8.1, both forms (87) and (95) of the plastic potential \mathcal{F} define σ_\star with the remarkable property

$$\frac{\partial \sigma_\star}{\partial \boldsymbol{\Sigma}} : \boldsymbol{\Sigma} = \sigma_\star, \quad (\text{B.5})$$

so that, assuming equality of macroscopic plastic work rate and matrix dissipation, the viscoplastic strain rate is written as

$$\mathbf{D}^p = -(1 - f) \dot{\bar{\epsilon}} \left(\frac{\partial \mathcal{F}}{\partial \sigma_\star} \right)^{-1} \frac{\partial \mathcal{F}}{\partial \boldsymbol{\Sigma}} \quad (\text{B.6})$$

In the rate-independent case, the evolution law of $\bar{\epsilon}$ is obtained from (53). In the viscoplastic case, $\bar{\epsilon}$ is obtained through a Norton law, written as

$$\dot{\bar{\epsilon}} = \left(\frac{\langle \phi \rangle}{K} \right)^n = \left(\frac{\langle \sigma_\star - \bar{\sigma} \rangle}{K} \right)^n \quad (\text{B.7})$$

where ϕ is the gauge function and $\langle \cdot \rangle$ denote McCauley's brackets to ensure positivity of the argument. The above equation is a variant of eqn.(4) with a threshold ($\bar{\sigma} \neq 0$) and

with strain hardening. Hardening is included through a uniaxial stress–strain relation having the form

$$\bar{\sigma}(\bar{\epsilon}) = \sigma_L \left[1 + \frac{\bar{\epsilon}}{\epsilon_0} + Q \left(1 - e^{-\bar{\epsilon}/\epsilon_1} \right) \right] \quad (\text{B.8})$$

Above, K and n are material dependent constants, σ_L is the longitudinal yield stress and Q , ϵ_0 and ϵ_1 are material constants. Eqns. (B.7) and (B.8) were used for example in the simulations of Section 9.3 with material parameters calibrated on experiments and negligible rate-sensitivity. In the limit of a rate independent material with σ_\star replaced everywhere by $\bar{\sigma}$, $\mathcal{F} \leq 0$ defines a convex elastic domain. The advantage of using the gauge function ϕ in (86) is precisely to allow a unified implementation of plastic and viscoplastic versions of the integrated model.

References

- Achon, P., 1994. Comportement et ténacité d'alliages d'aluminium à haute résistance. Ph.D. thesis, Ecole des Mines de Paris.
- Agarwal, H., Gokhale, A. M., Graham, S., Horstemeyer, M. F., 2002. Anisotropy of intermetallic particle cracking damage evolution in an Al-Mg-Si base wrought aluminum alloy under uniaxial compression. *Metallurgical and Materials Transactions A*. 33, 3443–3448.
- Argon, A. S., 1976. Formation of Cavities from Nondeformable Second-Phase Particles in Low Temperature Ductile Fracture. *Journal of Engineering Materials and Technology* 18, 60–68.
- Argon, A. S., Im, J., 1975. Separation of Second Phase Particles in Spheroidized 1045 Steel, Cu-0.6pct Cr Alloy, and Maraging Steel in Plastic Straining. *Metallurgical Transactions* 6A, 839–851.
- Argon, A. S., Im, J., Safoglu, R., 1975. Cavity Formation from Inclusions in Ductile Fracture. *Metallurgical Transactions* 6A, 825–837.
- Asserin-Lebert, A., Besson, J., Gourgues, A.-F., 2005. Fracture of 6056 aluminum sheet materials: Effect of specimen thickness and hardening behavior on strain localization and toughness. *Materials Science and Engineering* 395, 186–194.
- Babout, L., Bréchet, Y., Maire, E., Fougères, R., 2004a. On the competition between particle fracture and particle decohesion in metal matrix composites. *Acta Materialia* 52, 4517–4525.
- Babout, L., Maire, E., Fougères, R., 2004b. Damage initiation in model metallic materials: X-ray tomography and modelling. *Acta Materialia* 52, 2475–2487.
- Bao, Y., Wierzbicki, T., 2004. On fracture locus in the equivalent strain and stress triaxiality space. *International Journal of Mechanical Sciences* 46 (81), 81–98.
- Barbier, G., Benallal, A., Cano, V., 1998. Relation théorique entre la méthode de perturbation linéaire et l'analyse de bifurcation pour la prédiction de la localisation des déformations. *C. R. Acad. Sci. Paris* 326, 153–158.
- Barsoum, I., Faleskog, J., 2007a. Rupture mechanisms in combined tension and shear—Experiments. *International Journal of Solids and Structures* 44, 1768–1786.
- Barsoum, I., Faleskog, J., 2007b. Rupture mechanisms in combined tension and shear—Micromechanics. *International Journal of Solids and Structures* 44, 5481–5498.
- Bazant, Z., Pijaudier-Cabot, G., 1988. Non local continuum damage. localization, instability and convergence. *Journal of Applied Mechanics* 55, 287–294.
- Becker, R., Needleman, A., Richmond, O., Tvergaard, V., 1988. Void growth and failure in notched bars. *Journal of the Mechanics and Physics of Solids* 36, 317–351.

- Becker, R., Smelser, R. E., Richmond, O., 1989. The effect of void shape on the development of damage and fracture in plane-strain tension. *Journal of the Mechanics and Physics of Solids* 37, 111–129.
- Benzerga, A. A., 1999. Unpublished research.
- Benzerga, A. A., 2000. Rupture ductile des tôles anisotropes. Ph.D. thesis, Ecole Nationale Supérieure des Mines de Paris.
- Benzerga, A. A., 2002. Micromechanics of Coalescence in Ductile Fracture. *Journal of the Mechanics and Physics of Solids* 50, 1331–1362.
- Benzerga, A. A., 2010. Limit analysis of constrained plastic flow in ductile porous solids. In Preparation.
- Benzerga, A. A., Besson, J., 2001. Plastic potentials for anisotropic porous solids. *European Journal of Mechanics* 20A, 397–434.
- Benzerga, A. A., Besson, J., Batisse, R., Pineau, A., 1998. Anisotropic Ductile Rupture. ECF 12: Fracture From Defects, Vols. I-III, 715–720.
- Benzerga, A. A., Besson, J., Batisse, R., Pineau, A., 2002. Synergistic effects of plastic anisotropy and void coalescence on fracture mode in plane strain. *Modelling and Simulation in Materials Science and Engineering* 10, 73–102.
- Benzerga, A. A., Besson, J., Pineau, A., 20–23 May 1997. Modèle couplé comportement–endommagement ductile de tôles anisotropes. In: Peseux, B., Aubry, D., Pelle, J. P., Touratier, M. (Eds.), *Actes du 3^{ème} Colloque National en Calcul des Structures*. Presses Académiques de l’Ouest, pp. 673–678.
- Benzerga, A. A., Besson, J., Pineau, A., 1999. Coalescence–Controlled Anisotropic Ductile Fracture. *Journal of Engineering Materials and Technology* 121, 221–229.
- Benzerga, A. A., Besson, J., Pineau, A., 2004a. Anisotropic ductile fracture. Part I: experiments. *Acta Materialia* 52, 4623–4638.
- Benzerga, A. A., Besson, J., Pineau, A., 2004b. Anisotropic ductile fracture. Part II: theory. *Acta Materialia* 52, 4639–4650.
- Benzerga, A. A., Keralavarma, S. M., 2009. Finite–element analyses of combined void shape and plastic anisotropy effects in ductile fracture. In: 12th International Conference on Fracture. National Research Council of Canada, pp. 10 in CD–ROM.
- Beremin, F. M., 1980. Elasto–plastic calculations of circumferentially notched specimens using the finite element method. *J. Mécanique Appliquée* 4, 307–325.
- Beremin, F. M., 1981a. Cavity formation from inclusions in ductile fracture. *Metallurgical Transactions* 12A, 723–731.

- Beremin, F. M., 1981b. Experimental and numerical study of the different stages in ductile rupture: application to crack initiation and stable crack growth. In: Nemat-Nasser, S. (Ed.), *Three-Dimensional Constitutive relations of Damage and Fracture*. Pergamon press, pp. 157–172.
- Berveiller, M., Zaoui, A., 1979. An extension of the self-consistent scheme to plastically-flowing polycrystals. *J. Mech. Phys. Solids* 26, 325–344.
- Besson, J., Foerch, R., 1997. Large scale object oriented finite element code design. *Computer Methods in Applied Mechanics and Engineering* 142, 165–187.
- Besson, J., Steglich, D., Brocks, W., 2001. Modeling of crack growth in round bars and plane strain specimens. *International Journal of Solids and Structures* 38, 8259–8284.
- Besson, J., Steglich, D., Brocks, W., 2003. Modeling of plane strain ductile rupture. *International Journal of Plasticity* 19, 1517–1541.
- Borvik, T., Hopperstad, O. S., Langseth, M., Malo, K. A., 2002. Perforation of 12mm thick steel plates by 20mm diameter projectiles with flat, hemispherical and conical noses Part I: Experimental study. *International Journal of Impact Engineering* 27, 19–35.
- Borvik, T., Langseth, M., Hopperstad, O. S., Malo, K., 1999. Ballistic penetration of steel plates. *International Journal of Impact Engineering* 22, 855–885.
- Bourcier, R. J., Koss, D. A., Smelser, R. E., Richmond, O., 1986. The influence of porosity on the deformation and fracture of alloys. *Acta Metallurgica* 34 (12), 2443–2453.
- Brocks, W., Sun, D. Z., Hömig, A., 1995. Verification of the transferability of micromechanical parameters by cell model calculations with visco-plastic materials. *International Journal of Plasticity* 11 (8), 971–989.
- Budiansky, B., Hutchinson, J. W., Slutsky, S., 1982. Void growth and collapse in viscous solids. In: Hopkins, H. G., Sowell, M. J. (Eds.), *Mechanics of Solids, The Rodney Hill 60th Anniversary Volume*. Pergamon press, Oxford, pp. 13–45.
- Bugat, S., 2000. Comportement et endommagement des aciers austéno-ferritiques vieillis: une approche micromécanique. Ph.D. thesis, Ecole des Mines de Paris.
- Chae, D., Koss, D. A., 2004. Damage accumulation and failure in hsla-100 steel. *Materials Science and Engineering* 366 A, 299–309.
- Chu, C., Needleman, A., 1980. Void nucleation effects in biaxially stretched sheets. *Journal of Engineering Materials and Technology* 102, 249–256.
- Cocks, A. C. E., 1989. Inelastic deformation of porous materials. *Journal of the Mechanics and Physics of Solids* 37, 693–715.
- Cox, T. B., Low, J. R., 1974. An Investigation of the Plastic Fracture of AISI 4340 and 18 Nickel–200 Grade Maraging Steels. *Met. Trans.* 5, 1457–1470.

- Danas, K., Ponte Castañeda, P., 2009. A finite-strain model for anisotropic viscoplastic porous media: I–Theory. *European Journal of Mechanics* 28, 387–401.
- de Borst, R., 1987. Computation of Post–Bifurcation and Post–Failure Behavior of Strain–Softening Solids. *Computers and Structures* 25 (2), 211–224.
- Decamp, K., Bauvineau, L., Besson, J., Pineau, A., 1997. Size and geometry effects on ductile rupture of notched bars in a C–Mn steel: Experiments and modelling. *International Journal of Fracture* 88, 1–18.
- D’Escatha, Y., Devaux, J. C., 1979. ASTM STP 668. American Society for Testing and Materials, Ch. Numerical study of initiation, stable crack growth and maximum load with a ductile fracture criterion based on the growth of holes, pp. 229–248.
- Duva, J. M., 1986. A constitutive description of nonlinear materials containing voids. *Mechanics of Materials* 5, 137–144.
- Duva, J. M., Hutchinson, J. W., 1984. Constitutive potentials for dilutely voided nonlinear materials. *Mechanics of Materials* 3, 41–54.
- Edelson, B. I., Baldwin, W. M., J., 1962. The effect of second phases on the mechanical properties of alloys. *Trans. ASM* 55, 238–250.
- Enakoutsa, K., Leblond, J.-B., 2008. Numerical implementation and assessment of the glpd micromorphic model of ductile rupture. *European Journal of Mechanics* 28, 445–460.
- Enakoutsa, K., Leblond, J. B., Perrin, G., 2007. Numerical implementation and assessment of a phenomenological nonlocal model of ductile rupture. *Computer Methods in Applied Mechanics and Engineering* 196, 1946–1957.
- Eshelby, J., 1957. The determination of the elastic field of an ellipsoidal inclusion, and related problems. *Proc. Roy. Soc A* 241, 357–396.
- Fabregue, D., Pardoen, T., 2008. A constitutive model for elastoplastic solids containing primary and secondary voids. *Journal of the Mechanics and Physics of Solids* 56, 719–741.
- Faleskog, J., Gao, X., Shih, C. F., 1998. Cell model for nonlinear fracture analysis – I. Micromechanics calibration. *International Journal of Fracture* 89, 355–373.
- Flandi, L., Leblond, J.-B., 2005a. A new model for porous viscoplastic solids incorporating void shape effects – I: Theory. *European Journal of Mechanics* 24, 537–551.
- Flandi, L., Leblond, J.-B., 2005b. A new model for porous viscoplastic solids incorporating void shape effects – II: Numerical validation. *European Journal of Mechanics* 24, 552–571.
- Fleck, N. A., Hutchinson, J. W., Tvergaard, V., 1989. Softening by void nucleation and growth in tension and shear. *Journal of the Mechanics and Physics of Solids* 37, 515–540.

- Gao, X., Faleskog, J., Shih, C. F., 1998. Cell model for nonlinear fracture analysis – II. Fracture-process calibration and verification. *International Journal of Fracture* 89, 375–398.
- Gao, X., Kim, J., 2006. Modeling of ductile fracture: Significance of void coalescence. *International Journal of Solids and Structures* 43, 6277–6293.
- Gao, X., Wang, T., Kim, J., 2005. On ductile fracture initiation toughness: Effects of void volume fraction, void shape and void distribution. *International Journal of Solids and Structures* 42, 5097–5117.
- Garajeu, M., Michel, J. C., Suquet, P., 2000. A micromechanical approach of damage in viscoplastic materials by evolution in size, shape and distribution of voids. *Computer Methods in Applied Mechanics and Engineering* 183, 223–246.
- Garrison, W. M., Moody, N. R., 1987. Ductile fracture. *J. Phys. Chem. Solids* 48 (11), 1035–1074.
- Gologanu, M., 1997. Etude de quelques problèmes de rupture ductile des métaux. Ph.D. thesis, Université Paris 6.
- Gologanu, M., Leblond, J.-B., Devaux, J., 1993. Approximate models for ductile metals containing non-spherical voids – case of axisymmetric prolate ellipsoidal cavities. *Journal of the Mechanics and Physics of Solids* 41 (11), 1723–1754.
- Gologanu, M., Leblond, J.-B., Devaux, J., 1994a. Approximate Models for Ductile Metals Containing Non-spherical Voids — Case of Axisymmetric Oblate Ellipsoidal Cavities. *Journal of Engineering Materials and Technology* 116, 290–297.
- Gologanu, M., Leblond, J.-B., Devaux, J., 1994b. Numerical and Theoretical Study of Coalescence of Cavities in Periodically Voided Solids. In: Noor, A. K., Needleman, A. (Eds.), *Computational Material Modeling*. Vol. AD-42/PVP-294. ASME, New York, pp. 223–244.
- Gologanu, M., Leblond, J.-B., Devaux, J., 2001a. Theoretical models for void coalescence in porous ductile solids – II: Coalescence in “columns”. *International Journal of Solids and Structures* 38, 5595–5604.
- Gologanu, M., Leblond, J.-B., Perrin, G., Devaux, J., 1997. Recent extensions of Gurson’s model for porous ductile metals. In: Suquet, P. (Ed.), *Continuum Micromechanics, CISM Lectures Series*. Springer, New York, pp. 61–130.
- Gologanu, M., Leblond, J.-B., Perrin, G., Devaux, J., 2001b. Theoretical models for void coalescence in porous ductile solids – I: Coalescence in “layers”. *International Journal of Solids and Structures* 38, 5581–5594.
- Gullerud, A., Gao, X., Dodds, R. H., Haj-Ali, R., 2000. Simulation of ductile crack growth using computational cells: Numerical aspects. *Engineering Fracture Mechanics* 66, 65–92.

- Gurson, A. L., 1977. Continuum Theory of Ductile Rupture by Void Nucleation and Growth: Part I– Yield Criteria and Flow Rules for Porous Ductile Media. *Journal of Engineering Materials and Technology* 99, 2–15.
- Hadamard, J., 1903. *Leçons sur la propagation des ondes et les équations de l'hydrodynamique*. Librairie Scientifique, A. Hermann, Paris, Ch. 6.
- Hancock, J. W., MacKenzie, A. C., 1976. On the mechanisms of ductile failure in high-strength steels subjected to multi-axial stress states. *Journal of the Mechanics and Physics of Solids* 24, 147–169.
- Hill, R., 1948. A theory of yielding and plastic flow of anisotropic solids. *Proceedings of the Royal Society of London A* 193, 281–297.
- Hill, R., 1956. New horizons in the mechanics of solids. *Journal of the Mechanics and Physics of Solids* 5, 66.
- Hill, R., 1962. Acceleration waves in solids. *Journal of the Mechanics and Physics of Solids* 10, 1–16.
- Hill, R., 1967. The essential structure of constitutive laws for metal composites and polycrystals. *Journal of the Mechanics and Physics of Solids* 15, 79–95.
- Horstemeyer, M. F., Gokhale, A. M., 1999. A void-crack nucleation model for ductile metals. *International Journal of Solids and Structures* 36, 5029–5055.
- Horstemeyer, M. F., Lathrop, J., Gokhale, A. M., Dighe, M., 2000. Micromechanical finite element calculations of temperature and void configuration effects on void growth and coalescence. *International Journal of Plasticity* 16, 979–1013.
- Hsu, C. Y., Lee, B. J., Mear, M. E., 2009. Constitutive models for power-law viscous solids containing spherical voids. *International Journal of Plasticity* 25, 134–160.
- Hu, C., Ghosh, S., 2008. Locally Enhanced Voronoi Cell Finite Element Model (LE-VCFEM) for Simulating Evolving Fracture in Ductile Microstructures Containing Inclusions. *International Journal of Numerical Methods in Engineering* 76, 1955–1992.
- Huespe, A. E., Needleman, A., Oliver, J., Sánchez, P. J., 2009. A finite thickness band method for ductile fracture analysis. *International Journal of Plasticity* 25, 2349–2365.
- Hutchinson, J. W., Evans, A. G., 2000. Mechanics of materials: Top-down approaches to fracture. *Acta Materialia* 48, 125–135.
- Jablokov, V., Goto, D. M., Koss, D. A., 2001. Damage Accumulation and Failure of HY-100 Steel. *Metallurgical and Materials Transactions A* 32A, 2985–2994.
- James, M. A., Newman Jr., J. C., 2003. The effect of crack tunneling on crack growth: experiments and CTOA analyses. *Engineering Fracture Mechanics* 70, 457–468.

- Joly, P., Cozar, R., Pineau, A., 1990. Effect of crystallographic orientation of austenite on the formation of cleavage cracks in ferrite in an aged duplex stainless steel. *Scripta metall. mater.* 24, 2235–2240.
- Kailasam, M., Ponte Castaneda, P., 1998. A general constitutive theory for linear and nonlinear particulate media with microstructure evolution. *Journal of the Mechanics and Physics of Solids* 46 (3), 427–465.
- Keralavarma, S. M., Benzerga, A. A., 2008. An approximate yield criterion for anisotropic porous media. *Comptes Rendus Mecanique* 336, 685–692.
- Keralavarma, S. M., Benzerga, A. A., 2010. A constitutive model for plastically anisotropic solids with non-spherical voids. *Journal of the Mechanics and Physics of Solids* 58, 874–901.
- Keralavarma, S. M., Hoelscher, S., Benzerga, A. A., 2010. Void growth and coalescence in anisotropic plastic solids. *International Journal of Solids and Structures* Submitted.
- Klöcker, H., Tvergaard, V., 2003. Growth and coalescence of non-spherical voids in metals deformed at elevated temperatures. *International Journal of Mechanical Sciences* 45, 1283–1308.
- Koiter, W. T., 1953. Stress-strain relations, uniqueness and variational theorems for elastic-plastic materials with a singular yield surface. *Quarterly of Applied Mathematics* 11, 350–354.
- Koplik, J., Needleman, A., 1988. Void growth and coalescence in porous plastic solids. *International Journal of Solids and Structures* 24, 835–853.
- Kudo, H., 1960. Some analytical and experimental studies of axi-symmetric cold forging and extrusion—I. *International Journal of Mechanical Sciences* 2, 102–127.
- Kuna, K., Sun, D. Z., 1996. Three-dimensional cell model analyses of void growth in ductile materials. *International Journal of Fracture* 81, 235–258.
- Lassance, D., Scheyvaerts, F., Pardoen, T., 2006. Growth and coalescence of penny-shaped voids in metallic alloys. *Engineering Fracture Mechanics* 73, 1009–1034.
- Lautridou, J.-C., Pineau, A., 1981. Crack initiation and stable crack growth resistance in A508 steels in relation to inclusion distribution. *Engineering Fracture Mechanics* 15 (1-2), 55–71.
- Le Roy, G., Embury, J. D., Edward, G., Ashby, M. F., 1981. A model of ductile fracture based on the nucleation and growth of voids. *Acta Metallurgica* 29, 1509–1522.
- Leblond, J. B., 2003. *Mécanique de la rupture fragile et ductile*. Hermes Science Publications, Lavoisier.
- Leblond, J.-B., Gologanu, M., 2008. External estimate of the yield surface of an arbitrary ellipsoid containing a confocal void. *Comptes Rendus Mecanique* 336, 813–819.

- Leblond, J.-B., Mottet, G., 2008. A theoretical approach of strain localization within thin planar bands in porous ductile materials. *Comptes Rendus Mecanique* 336, 176–189.
- Leblond, J.-B., Perrin, G., Devaux, J., 1994a. Bifurcation Effects in Ductile Metals With Nonlocal Damage. *Journal of Applied Mechanics* 61, 236–242.
- Leblond, J.-B., Perrin, G., Devaux, J., 1995. An improved Gurson-type model for hardenable ductile metals. *European Journal of Mechanics* 14, 499–527.
- Leblond, J.-B., Perrin, G., Suquet, P., 1994b. Exact results and approximate models for porous viscoplastic solids. *International Journal of Plasticity* 10, 213–225.
- Lee, B. J., Mear, M. E., 1992. Axisymmetric deformation of power-law solids containing a dilute concentration of aligned spheroidal voids. *Journal of the Mechanics and Physics of Solids* 40, 1805–1836.
- Lee, B. J., Mear, M. E., 1999. Stress concentration induced by an elastic spheroidal particle in a plastically deforming solid. *Journal of the Mechanics and Physics of Solids* 47, 1301–1336.
- Liao, K.-C., Pan, J., Tang, S. C., 1997. Approximate yield criteria for anisotropic porous ductile sheet metals. *Mechanics of Materials* 26, 213–226.
- Licht, C., Suquet, P., 1988a. The constitutive law of nonlinear viscous and porous materials. *C. R. Acad. Sci. Paris II* 306, 327–330.
- Licht, C., Suquet, P., 1988b. Growth of voids in a nonlinear viscous material at arbitrary void volume fraction: a simple model. *Archives of Mechanics* 40, 741–757.
- Maire, E., Bordreuil, C., Babout, L., Boyer, J. C., 2005. Damage initiation and growth in metals. Comparison between modeling and tomography experiments. *Journal of the Mechanics and Physics of Solids* 53, 2411–2434.
- Mandel, J., 1964. Contribution théorique à l'étude de l'écroutissement et des lois d'écoulement plastique. In: 11th International Congress on Applied Mechanics. Springer, Berlin, pp. 502–509.
- Mandel, J., 1966. Conditions de stabilité et postulat de Drucker. In: Krautchenko, J., Sirieys, P. M. (Eds.), *Rheology and Soil Mechanics*. Springer-Verlag, Berlin, pp. 58–68.
- Marini, B., Mudry, F., Pineau, A., 1985. Experimental study of cavity growth in ductile rupture. *Engineering Fracture Mechanics* 22, 989–996.
- McClintock, F. A., 1968. A criterion for ductile fracture by the growth of holes. *Journal of Applied Mechanics* 35, 363–371.
- McMeeking, R. M., 1977. Finite deformation analysis of crack-tip opening in elastic-plastic materials and implications for fracture. *Journal of the Mechanics and Physics of Solids* 25, 357.

- Mear, M. E., Hutchinson, J. W., 1985. Influence of yield surface curvature on flow localization in dilatant plasticity. *Mechanics of Materials* 4, 395–407.
- Mediavilla, J., Peerlings, R. H. J., Geers, M. G. D., 2006. A nonlocal triaxiality-dependent ductile damage model for finite strain plasticity. *Computer Methods in Applied Mechanics and Engineering* 195, 4617–4634.
- Michel, J. C., Suquet, P., 1992. The constitutive law of nonlinear viscous and porous materials. *Journal of the Mechanics and Physics of Solids* 40, 783–812.
- Moes, N., Dolbow, J., Belytschko, T., 1999. A finite element method for crack growth without remeshing. *International Journal of Numerical Methods in Engineering* 46, 131–150.
- Monchiet, V., Cazacu, O., Charkaluk, E., Kondo, D., 2008. Macroscopic yield criteria for plastic anisotropic materials containing spheroidal voids. *International Journal of Plasticity* 24, 1158–1189.
- Monchiet, V., Gruescu, C., Charkaluk, E., Kondo, D., 2006. Approximate yield criteria for anisotropic metals with prolate or oblate voids. *Comptes Rendus Mecanique* 334, 431–439.
- Montheillet, F., Gilormini, P., 1986. Amorçage de l'endommagement. In: Montheillet, F., Moussy, F. (Eds.), *Physique et mécanique de l'endommagement*. Les éditions de physique, Les Ulis, pp. 122–181.
- Mudry, F., 1982. Etude de la rupture ductile et de la rupture par clivage d'aciers faiblement alliés. Ph.D. thesis, Doctorat d'état, Université de Technologie de Compiègne.
- Needleman, A., 1972a. A numerical study of necking in circular cylindrical bars. *Journal of the Mechanics and Physics of Solids* 20, 111–127.
- Needleman, A., 1972b. Void Growth in an Elastic–Plastic Medium. *Journal of Applied Mechanics* 39, 964–970.
- Needleman, A., 1987. A continuum model for void nucleation by inclusion debonding. *Journal of Applied Mechanics* 54, 525–531.
- Needleman, A., 1988. Material rate dependence and mesh sensitivity in localisation problems. *Comput. Methods. Appl. Mech. Eng.* 67, 69–85.
- Needleman, A., Tvergaard, V., 1987. An analysis of ductile rupture modes at a crack tip. *Journal of the Mechanics and Physics of Solids* 35, 151–183.
- Nemat-Nasser, S., Hori, M., 1990. *Micromechanics: Overall Properties of Heterogeneous Materials*. North Holland.
- Newman Jr., J. C., James, M. A., Zerbst, U., 2003. A review of the CTOA/CTOD fracture criterion. *Engineering Fracture Mechanics* 70, 371–385.

- Orsini, V. C., Zikry, M. A., 2001. Void growth and interaction in crystalline materials. *International Journal of Plasticity* 17, 1393–1417.
- Pardoen, T., Delannay, F., 1998a. Assessment of Void Growth Models from Porosity Measurements in Cold-Drawn Copper Bars. *Metallurgical Transactions* 29A, 1895–1909.
- Pardoen, T., Delannay, F., 1998b. On the coalescence of voids in prestrained notched round copper bars. *Fatigue Fract. Engng. Mater. Struct.* 21, 1459–1472.
- Pardoen, T., Doghri, I., Delannay, F., 1998. Experimental and numerical comparison of void growth models and void coalescence criteria for the prediction of ductile fracture in copper bars. *Acta mater.* 46 (2), 541–552.
- Pardoen, T., Hachez, F., Marchioni, B., Blyth, H., Atkins, A. G., 2004. Mode I fracture of sheet metal. *Journal of the Mechanics and Physics of Solids* 52, 423–452.
- Pardoen, T., Hutchinson, J. W., 2000. An extended model for void growth and coalescence. *Journal of the Mechanics and Physics of Solids* 48, 2467–2512.
- Pardoen, T., Hutchinson, J. W., 2003. Micromechanics-based model for trends in toughness of ductile metals. *Acta Materialia* 51, 133–148.
- Pastor, F., Loute, E., Pastor, J., 2009. Limit analysis and convex programming: A decomposition approach of the kinematic mixed method. *International Journal of Numerical Methods in Engineering* 78, 254–274.
- Peerlings, R. H. J., Geers, M. . G. D., de Borst, R., Brekelmans, W. A. M., 2001. A critical comparison of nonlocal and gradient-enhanced softening. *Int J Solids Struct* 38, 7723–7746.
- Perrin, G., 1992. Contribution à l'étude théorique et numérique de la rupture ductile des métaux. Ph.D. thesis, Ecole Polytechnique.
- Perrin, G., Leblond, J.-B., 1990. Analytical study of a hollow sphere made of plastic porous material and subjected to hydrostatic tension— application to some problems in ductile fracture of metals. *Int. J. Plasticity* 6 (6), 677–699.
- Pineau, A., 1992. Global and local approaches of fracture. transferability of laboratory test results to components. In: Argon, A. S. (Ed.), *Topics in Fracture and Fatigue*. Springer-Verlag, pp. 197–234.
- Pineau, A., 2006. Development of the local approach to fracture over the past 25 years: theory and applications. *International Journal of Fracture* 138, 139–166.
- Plateau, J., Henry, G., Crussard, C., 1957. Quelques nouvelles applications de la microfractographie. *Revue de Métallurgie* 54, 200–216.
- Ponte Castañeda, P., Zaidman, M., 1994. Constitutive models for porous materials with evolving microstructure. *Journal of the Mechanics and Physics of Solids* 42, 1459–1495.

- Ponte Castaneda, P., 1991. The effective mechanical properties of nonlinear composites. *Journal of the Mechanics and Physics of Solids* 39, 45–71.
- Potirniche, G. P., Hearndon, J. L., Horstemeyer, M. F., Ling, X. W., 2006. Lattice orientation effects on void growth and coalescence in fcc single crystals. *International Journal of Plasticity* 22, 921–942.
- Prager, W., Hodge, P. G., 1951. *Theory of perfectly plastic solids*. Wiley, New York.
- Prat, F., Grange, M., Besson, J., Andrieu, E., 1998. Behavior and rupture of hydrided ZIRCALOY-4 tubes and sheets. *Metallurgical and Materials Transactions A*. 29A, 1643–1651.
- Rice, J., 1977. The localization of plastic deformation. In: Koiter, W. (Ed.), 14th Int. Cong. Theoretical and Applied Mechanics. North-Holland, Amsterdam, pp. 207–220.
- Rice, J. R., 1968. A path independent integral and the approximate analysis of strain concentration by notches and cracks. *Journal of Applied Mechanics* 35, 379–386.
- Rice, J. R., Johnson, M. A., 1970. The role of large crack tip geometry changes in plane strain fracture. In: Kanninen, M. F. et al. (Ed.), *Inelastic behavior of solids*. Mc Graw Hill, New York, pp. 641–672.
- Rice, J. R., Tracey, D. M., 1969. On the enlargement of voids in triaxial stress fields. *Journal of the Mechanics and Physics of Solids* 17, 201–217.
- Riks, E., 1979. An incremental approach to the solution of snapping and buckling problems. *Int. J. Solids Structures* 15, 529–551.
- Rivalin, F., Besson, J., Pineau, A., Di Fant, M., 2001. Ductile tearing of pipeline-steel wide plates. I. Dynamic and quasi-static experiments. *Engineering Fracture Mechanics* 68, 329–345.
- Rousselier, G., 1981. Finite deformation constitutive relations including ductile fracture damage. In: Nemat-Nasser (Ed.), *Three-Dimensional Constitutive equations of Damage and Fracture*. Pergamon press, North Holland, pp. 331–355.
- Rousselier, G., 1987. Ductile fracture models and their potential in local approach of fracture. *Nucl. Eng. Design* 105, 97–111.
- Saje, M., Pan, J., Needleman, A., 1982. Void nucleation effects on shear localization in porous plastic solids. *International Journal of Fracture* 19, 163–182.
- Scheyvaerts, F., 2008. Ph.D. thesis, Université Catholique de Louvain.
- Scheyvaerts, F., Pardoën, T., Onck, P. R., 2010. A New Model for Void Coalescence by Internal Necking. *International Journal of Damage Mechancis* 19, 95–126.
- Shabrov, M. N., Needleman, A., 2002. An analysis of inclusion morphology effects on void nucleation. *Modelling and Simulation in Materials Science and Engineering* 10, 163–183.

- Shabrov, M. N., Sylven, E., Kim, S., Sherman, D. H., Chuzhoy, L., Briant, C. L., Needleman, A., 2004. Void nucleation by inclusion cracking. *Metallurgical and Materials Transactions A* 35A, 1745–1755.
- Siruguet, K., Leblond, J.-B., 2004. Effect of void locking by inclusions upon the plastic behavior of porous ductile solids—I: theoretical modeling and numerical study of void growth. *International Journal of Plasticity* 20, 225–254.
- Sovik, O., Thaulow, C., 1997. Growth of spheroidal voids in elastic–plastic solids. *Fatigue Fract. Engng. Mater. Struct.* 20, 1731–1744.
- Steglich, D., Brocks, W., Heerens, J., Pardoen, T., 2008. Anisotropic Ductile Fracture of Al 2024 Alloys. *Engineering Fracture Mechanics* 75, 3692–3706.
- Steinmann, P., Miehe, C., Stein, E., 1994. On the localization analysis of orthotropic hill-type elastoplastic solids. *Journal of the Mechanics and Physics of Solids* 42 (12), 1969–1994.
- Strouboulis, T., Copps, K., Babuska, I., 2001. The generalized finite element method. *Computer Methods in Applied Mechanics and Engineering* 190, 4081–4193.
- Suquet, P., 1982. Plasticité et homogénéisation. Ph.D. thesis, Université Pierre et Marie Curie – Paris VI.
- Suquet, P., 1992. On bounds for the overall potential of power law materials containing voids with arbitrary shape. *Mechanical Research Community* 19, 51–58.
- Tanaka, K., Mori, T., Nakamura, T., 1970. Cavity formation at the interface of a spherical inclusion in a plastically deforming matrix. *Philosophical Magazine* 21, 267–279.
- Tanguy, B., Besson, J., Piques, R., Pineau, A., 2005. Ductile-to-brittle transition of an A 508 steel characterized by Charpy impact test. Part I: Experimental results. *Engineering Fracture Mechanics* 72, 49–72.
- Thomason, P. F., 1968. A theory for ductile fracture by internal necking of cavities. *J. Inst. Metals* 96, 360.
- Thomason, P. F., 1985a. A three-dimensional model for ductile fracture by the growth and coalescence of microvoids. *Acta Metallurgica* 33, 1087–1095.
- Thomason, P. F., 1985b. Three-dimensional models for the plastic limit-loads at incipient failure of the intervold matrix in ductile porous solids. *Acta Metallurgica* 33, 1079–1085.
- Thomson, R. D., Hancock, J. W., 1984. Local stress and strain fields near a spherical elastic inclusion in a plastically deforming matrix. *International Journal of Fracture* 24, 209–228.
- Tvergaard, V., 1981. Influence of voids on shear band instabilities under plane strain conditions. *International Journal of Fracture* 17, 389–407.

- Tvergaard, V., 1982a. Influence of void nucleation on ductile shear fracture at a free surface. *Journal of the Mechanics and Physics of Solids* 30, 399–425.
- Tvergaard, V., 1982b. On localization in ductile materials containing spherical voids. *International Journal of Fracture* 18, 237–252.
- Tvergaard, V., 1990. Material failure by void growth to coalescence. *Advances in Applied Mechanics* 27, 83–151.
- Tvergaard, V., 1998. Interaction of very small voids with larger voids. *International Journal of Solids and Structures* 39, 3989–4000.
- Tvergaard, V., 2009. Behaviour of voids in a shear field. *International Journal of Fracture* 158, 41–49.
- Tvergaard, V., Hutchinson, J. W., 1992. The relationship between crack growth resistance and fracture process parameters in elasticplastic solids. *Journal of the Mechanics and Physics of Solids* 40, 1377–1397.
- Tvergaard, V., Needleman, A., 1984. Analysis of the cup–cone fracture in a round tensile bar. *Acta Metallurgica* 32, 157–169.
- Tvergaard, V., Needleman, A., 1995. Effects of nonlocal damage in porous plastic solids. *International Journal of Solids and Structures* 32 (8/9), 1063–1077.
- Tvergaard, V., Van der Giessen, E., 1991. Effect of plastic spin on localization predictions for a porous ductile material. *Journal of the Mechanics and Physics of Solids* 39, 763–781.
- Vincent, P. G., Monerie, Y., Suquet, P., 2009. Porous materials with two populations of voids under internal pressure: I. Instantaneous constitutive relations. *International Journal of Solids and Structures* 46, 480–506.
- Weck, A., Wilkinson, D. S., Maire, E., Toda, H., 2008. Visualization by X-ray Tomography of Void Growth and Coalescence Leading to Fracture in Model Materials. *Acta Materialia* 56, 2919–2928.
- Willis, J. R., 1991. On methods for bounding the overall properties of nonlinear composites. *Journal of the Mechanics and Physics of Solids* 39, 73–86.
- Wilner, B., 1988. Stress analysis of particles in metals. *Journal of the Mechanics and Physics of Solids* 36 (2), 141–165.
- Woodward, R. L., 1984. The interrelation of failure modes observed in the penetration of metallic targets. *International Journal of Impact Engineering* 2, 121–129.
- Xia, L., Shih, C. F., 1995. Ductile crack growth. I: A numerical study using computational cells with microstructurally based length scales. *Journal of the Mechanics and Physics of Solids* 43, 233–259.

- Xia, L., Shih, C. F., Hutchinson, J. W., 1995. A computational approach to ductile crack growth under large scale yielding conditions. *Journal of the Mechanics and Physics of Solids* 43, 389–413.
- Yerra, S. K., Tekoglu, C., Scheyvaerts, F., Delannay, L., van Houtte, P., Pardoen, T., 2010. Void Growth and Coalescence in Single Crystals. *International Journal of Solids and Structures* 47, 1016–1029.
- Zhang, H., Ravi-Chandar, K., 2006. On the dynamics of necking and fragmentation – I. Real-time and post-mortem observations in Al6061-O. *International Journal of Fracture* 142, 183–217.
- Zhang, H., Ravi-Chandar, K., 2009. Dynamic fragmentation of ductile materials. *Journal of Applied Physics* 42, 1–16.
- Zhang, K. S., Bai, J. B., Francois, D., 2001. Numerical analysis of the influence of the Lode parameter on void growth. *International Journal of Solids and Structures* 38, 5847–5856.
- Zhang, Z. L., Niemi, E., 1994. Analyzing ductile fracture using dual dilational constitutive equations. *Fat. Frac. Eng. Mater. Structures* 17, 695–707.